HYBRID EXCITED SYNCHRONOUS MOTOR: ANALYSIS, DESIGN AND CONTROL

Design and control algorithm

LUCA CINTI

MCCXXII

Department of Industrial Engineering
University of Padova

November 2023 – version 2.0

UNIVERSITÀ
DEGLI STUDI
DI PADOVA

University of Padova
Department of Industrial Engineering

Ph.D. Course in
Electrical Energy Engineering

XXXVI CYCLE

EDLab
Padova

HYBRID EXCITED SYNCHRONOUS MOTOR: ANALYSIS, DESIGN AND CONTROL

Candidate LUCA CINTI

Supervisor PROF. NICOLA BIANCHI

Ph.D. School Coordinator PROF. GIULIO ROSATI

Curriculum Coordinator PROF. LUIGI ALBERTI

If you are not part of the solution, you are the part of the problem.

— Eldridge Cleaver

ABSTRACT

This dissertation includes many research activities in the field of analysis, design and control of Electrically Excited Synchronous Motors (EESM) and Hybrid Excited Permanent Magnet Motors (HEPM) drives. EESM and HEPM motors are promising machine configurations for variable speed applications thanks to their high torque and power density, high capabilities in a wide speed range and low amount of permanent magnets. Different architectures of these motors are analysed and different tests under various operating conditions are carried out and described in the thesis. Structural and thermal limits are also taken into account.

In Part I, some basic background theory of electrical machines is reported, focusing on EESM and HEPM motors. Their general architectures is examined, including series and parallel configurations. The performance under no-load and load conditions are analyzed and different comparative studies between PMs motors, EESM and HEPM motors with the same size are presented. Finally, structural and thermal issues affecting rotor winding machines are discussed.

Part II moves the focus on theoretical and effective design. Analytical techniques are used to calculate the machine parameters, for given requirements of maximum torque at low speed and flux weakening operating speed range. EESM and HEPM motors are detailed designed and optimised to achieve the required performance. A novel fluid rotor geometry and the combination of excitation windings and permanent magnets are explained. This part concludes in illustrating the procedure to select an optimum motor geometry, followed by the prototype construction and the description of a series of experimental tests.

Finally, Part III examines the , the innovative electrical control strategies employed for HEPM motors, covering control techniques such as maximum torque per Amps control, sensorless control and flux weakening operation control. It also considers an extension of implicit Model Predictive Control to include voltage and current constraints.

This dissertation reports analytical, finite element and experimental validation, providing valuable insights into the design and control of EESM and HEPM motors, highlighting their advantages and disadvantages.

SOMMARIO

Questa tesi comprende numerose attività di ricerca nel campo dell'analisi, della progettazione e del controllo di motori sincroni ad eccitazione rotorica Electrically Excited Synchronous Motor (EESM) e di motori a magneti permanenti ad eccitazione ibrida Hybrid Excited Permanent Magnet (HEPM). I motori EESM e HEPM sono effettivamente una configurazione di motore promettente per applicazioni elettriche, infatti esse hanno un'elevata densità di coppia e di potenza, ottime prestazioni ad alta velocità e richiedono una bassa quantità di magneti permanenti (PM). Per questi motori vengono presentate diverse architetture e test in diverse condizioni, tenendo conto delle limitazioni strutturali e termiche.

Nella Parte I, vengono riportate alcune nozioni teoriche di base sulle macchine elettriche, in particolare sui motori EESM e HEPM. Questa sezione esamina le loro architetture generali, le configurazioni in serie e in parallelo. Vengono poi analizzate le prestazioni a vuoto e a carico e viene presentato uno studio comparativo tra motori EESM e HEPM di dimensioni identiche. Infine, vengono discussi i problemi strutturali e termici che interessano le macchine a rotore avvolto.

La Parte II sposta l'attenzione sulla progettazione teorica ed effettiva. Vengono utilizzate tecniche analitiche per calcolare i parametri della macchina, tenendo conto delle regioni di funzionamento in cui opera. Ed esempio la zona della coppia massima per ampere (MTPA) e dell'indebolimento del flusso (FW). Partendo da questo, i motori EESM e HEPM vengono quindi progettati nel dettaglio e ottimizzati per ottenere le prestazioni richieste. Viene spiegata una nuova geometria del rotore fluido e la combinazione di avvolgimenti di eccitazione e magneti permanenti. Questa parte culmina nella selezione della geometria ottimale del motore, accompagnata dalla costruzione di un prototipo e da test sperimentali su banco.

Infine, la Parte III esamina le innovative strategie di controllo impiegate per i motori HEPM, utilizzando tecniche di controllo come il controllo MTPA, il controllo senza sensori e il controllo FW ad alta velocità. E' stato inoltre studiata un'estensione del controllo predittivo implicito del modello (MPC) che includa i vincoli di tensione e corrente.

Dunque, questa tesi riporta la validazione analitica, agli elementi finiti (FE) e sperimentale, fornendo preziose indicazioni sulla metodologia di progettazione e sul controllo dei motori EESM e HEPM, evidenziandone vantaggi e svantaggi.

CONTENTS

LIST OF FIGURES

LIST OF TABLES

LISTINGS

ACRONYMS

AC	Alternative Current
DC	Direct Current
EV	Electric Vehicle
SyPM	Permanent Magnet Synchronous Motor
PM	Permanent Magnet
PMSM	Permanent Magnet Synchronous Motor
SPM	Surface Permanent Magnet
IPM	Interior Permanent Magnet
IM	Induction Motor
MSPM	Normal-Saliency Permanent Magnet
PMARel	Permament Magnet Assisted Reluctance
REL	Reluctance
EESM	Electrically Excited Synchronous Motor
HEPM	Hybrid Excited Permanent Magnet
WR	Wound Rotor
PMaEXC	Permanent Magnet assisted Excitation
EMF	Electromotive Force
MTPA	Maximum-Torque-per-Ampere
FW	Flux Weakening
MTPV	Maximum Torque-per-Voltage
FE	Finite Element
MPC	Model Predictive Control
MCL	Minimum Copper Losses
QP	Quadratic Program
LPM	Linear Piecewise Method
ETM	Equivalent Tangent Method

1

INTRODUCTION

The industry is undergoing a significant transformation with the rise of electric device and the need for highly efficient and powerful electric motor technologies. The focus of this work is on meeting the high torque and power requirements of EVs across a wide speed range, while also addressing the challenges associated with motor design, optimization, and control.

Induction motors (IMs), showed in Fig. 1.1, have been widely utilized in the last few decades due to their ease manufacturing and straightforward control. Some companies, as evidenced by research conducted by Audi [3] and showed in Fig. 1.2, continue to employ these motors while enhancing their performance in the EVs industry. However, the primary trend has been led by synchronous machines (SyMs), which are gaining increasing popularity due to their numerous advantages. These advantages include exceptional efficiency across a broad operational spectrum, a high power factor, sustained torque up to the base speed, impressive torque density, rapid response dynamics and simple control algorithms. Electric motor technology is populated by several configurations [90].

The most used electric SyMs are supplied on the rotor with permanent magnet (PM). SyMs have replaced the induction motors, firstly due to their higher efficiency and the advent of power electronics. Moreover, up to now, SyMs have fulfill the market due to their high torque density, easily manufactured and control.

Main SyPM configurations are: surface permanent magnet (SPM) [86] and interior permanent magnet (IPM). Both rotor configurations are shown in Fig. 1.3a and Fig. 1.3b.

As illustrated in Fig. 1.3a, the SPM geometry exhibits the PM, showed in green, glued on the rotor surface and directly faced on the stator. Fig. 1.3b reported the IPM motor geometry. Here PMs, are buried in-

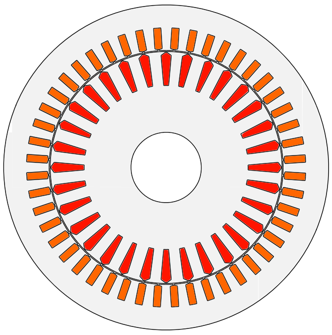

Figure 1.1: Induction Motor sketch configuration.

Figure 1.2: Induction Motor developed by Audi [3].

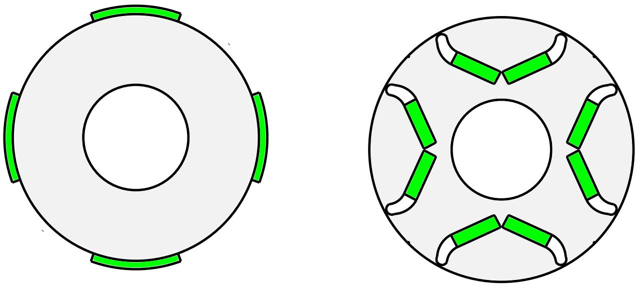

(a) SPM configuration.

(b) IPM configuration.

Figure 1.3: SPM and IPM configuration.

side the rotor. The PMs used are composed by rare earth materials like Neodimium or Samarium-Cobalt.

However, in applications with lower to moderate power requirements, the use of rare-earth materials can be cost-prohibitive. In such cases synchronous reluctance (SyRel) motors are preferable.

SyRel motors do not required rare earth PMs, as shown in Fig. 1.4a, but they use the rotor barrier to delivering torque.

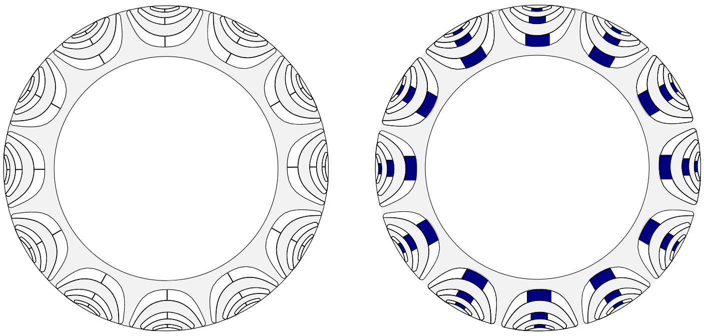

(a) SyRel configuration.

(b) PMaRel configuration.

Figure 1.4: SyRel and PMaRel configuration.

Sometimes, the torque produced is not enough for the application. For this reason the rotor can be assisted by some ferrite PMs, as shown in Fig. 1.4b. The SyRel are called Permanent Magnet assisted

Reluctance (PMaRel) motor, where the main flux is due to the rotor barrier contribution than the PMs.

In high power applications, as power plant generator, other possible solutions are suitable also without PMs.

Electrically excited synchronous motor (EESM) is used for in these cases. Up to now, it has been used in the high power electricity generations but in the last years EESM has been applied to automotive industry by Renalut Zoe and ZF[83, 110]. ZF EESM rotor is showed in Fig. 1.5.

Figure 1.5: EESM developed by ZF [110].

Mainly two EESMs rotor topology can be arranged: the cylindrical and salient pole [82]. Fig. 1.6a and Figs. 1.6b show the cylindrical and salient pole rotor geometries corresponding. Both rotor are supplied by a direct current in the rotor winding represented in orange. The main difference between the two configuration is that the cylindrical has a isotropic rotor while the salient pole has a pole that exit by rotor. EESMs are without PM, and like SyREL and PMaRel motor, has lower torque density compared to IPM motors.

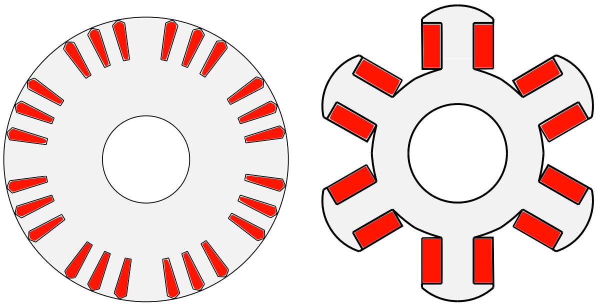

(a) Cylindrical EESM configuration.

(b) Salient Pole EESM configuration.

Figure 1.6: Cylindrical and Salient Pole EESM configurations.

To fill this gap, an interesting compromise is represented by hybrid excited permanent magnet (HEPM) motors, which combine the benefit of EESM and PM motors. [8, 61]. HEPM motor are starting to be used in high torque high speed applications. One example is developed by MAHLE as shown in Fig. 1.7.

Figure 1.7: HEPM Synchronous Motor configuration developed by MAHLE [61].

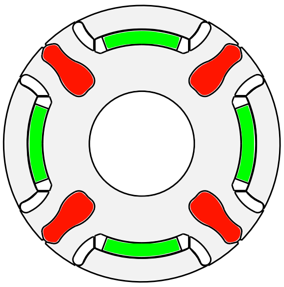

Figure 1.8: HEPM Synchronous Motor sketch configuration.

That is why hereafter the focus will move on HEPM motor [30] and EESM [84]. In HEPM machine, rotor is modified so that not only PMs are buried in the rotor structure, but also an excitation winding is adopted to regulate the rotor flux, as shown in Fig. 1.8. In the resulting structure, the rotor contains both PMs and Rotor Excitation Coils, so that it is referred to as a synchronous HEPM machine. The aim of this rotor arrangement is to get the possibility to change the rotor flux during the operation of the motor, so as to achieve a wider speed range.

Different rotor geometries will be investigated to get a proper utilization of the inverter power ratings without increasing the motor size.

The HEPM machine combines the advantages of PM machines and wound field machines. In the IPM motor, the PMs produce the total rotor flux, but this flux is constant. In the wound field motor, the flux can be varied but an excitation current is always required. The HEPM motor allows the rotor flux to be reduced or increased by means of a minimum excitation current, which depends on the requirements of the application.

The modulation of the rotor flux, according to the operating speed, yields an increase of the motor performance.
In particular:

- the torque increases during the flux-weakening operations,
- the power increases accordingly,

- the motor efficiency remains high for a wider speed range.

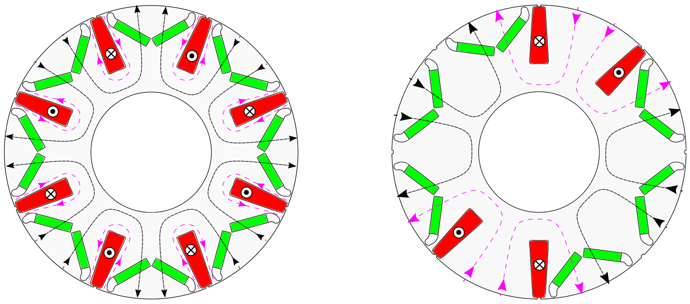

(a) Series HEPM sketch (b) Parallel HEPM sketch

Figure 1.9: Series and Parallel HEPM motor configurations.

To highlight the benefit of the HEPM machine, some comparisons will be reported in the next Chapters .

Series and parallel architecture of HEPM motors, reported in Fig. 1.9, are investigated, designed and compared to IPM motor with the same size. In series configurations, the flux produced by the excitation coils flow through the PMs, while in parallel configurations the flux produced by PMs and by excitation coils has different paths [7, 8].

Others HEPM motors deal with innovative motors like a synchronous motor used for Biaxial Excitation Generator for Auto-mobiles (BEGA) [21, 26], demonstrating that BEGA has a very large constant power speed range.

Also Wang [100] studied that hybrid configuration, focusing mainly on flux switching motor [25]. Finally, HEPM motor configurations are compared to conventional IPM motors in terms of torque and speed capabilities [30, 36].

Moreover, the fundamental equations applied for HEPM motor will be described and the analysis of the steady-state operation of the IPM and HEPM motors exceeding base speed will be readily carried out using the circle diagram theory [69]. It consists in reporting in the (i_d, i_q) plane the constant current, voltage and torque loci, to point

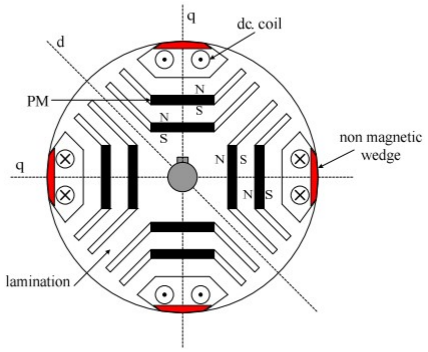

Figure 1.10: BEGA rotor geometry [21].

out the operation limits and to individuate the most suitable current vector control.

The model is sufficiently accurate for a prediction of the motor performance in different working conditions and suitable for the motor design. The motor performances obtained analytically can be compared with those of a Finite Element (FE) model. The results are generally in satisfactory agreement with the whole operating speed range [73].

So far, the synchronous motor model theoretical study with suitable control schemes has been provided. Furthermore, the EESM and HEPM motor variants exhibit interesting and comparable performance to IPM motor. Moving forward, the discussion will focus on them, extending the mathematical model and adopting a precise procedure design and control methodology to HEPM motor and EESM.

1.1 OUTLINE OF THE THESIS

Hereinafter the dissertation structure is briefly presented.

PART I presents the background knowledge on electrical machines and the EESM and HEPM motor analysis:

- Chapter 2 presents an overview of the three-phase a synchronous permanent magnet motor, focusing on the EESM and HEPM motor general architectures and operating points.
- Chapter 3 analyses different preliminary HEPM motors configurations under no-load condition. This involves a systematic comparison of different series and parallel configurations. Each solution exhibits some advantages and drawbacks of each arrangement.
- Chapter 4 analyses HEPM motors configurations under load performance considering MTPA and FW regions.
- Chapter 5 reports a comparison between the EESM and HEPM motors, both sharing identical dimensions.
- Chapter 6 discusses the structural and thermal limits that affected the rotor winding machines.

PART II resumes the contributions in the area of HEPM and EESM design followed by test bench validation, highlighting the potential and drawbacks of these motors. It is structured in four main Chapters:

- Chapters 7 presents some relevant contributions on analytical design technique. The design is obtained considering MTPA and FW operating region requirements and yields the machines parameter that the motor has to have.
- Chapter 8 focuses on the EESM motor effective design and analysis, considering the relationship between pole configurations.
- Chapter 9 focuses on the HEPM motor effective design considering the relationship adding of the PM on the rotor pole.
- Chapter 10 investigates the most promising configuration with a selection of an optimal geometry. A prototype building and methodical experimental testing are carried out.

PART III reports Hybrid Excited Permanent Magnet motors electric control testing on the prototype. The part is divided in five main Chapters:

- Chapters 11 reports the PM control strategies used in literature.

- Chapter 12 discuss the HEPM motor model considering the non-linearity that affected the machine.
- Chapter 13 describes low speed technique as: MTPA technique and sensorless control.
- Chapter 14 presents high speed algorithm during FW region.
- Chapter 15 reports the discussion of an extension of the implicit MPC current control, considering the voltage and currents constraints.

At the end, Chapter 16 deal with the conclusion.

Part I

ELECTRICALLY EXCITED AND HYBRID EXCITED PERMANENT MAGNET: BACKGROUND KNOWLEDGE AND ANALYSIS

This part begins with an overview of three-phase asynchronous permanent magnet motors, discussing the general architectures and operating points of EESM and HEPM motors. Subsequently, it delves into the analysis of various preliminary HEPM motor configurations under both no-load and load conditions, including comparisons between series and parallel configurations. Additionally, it presents a comparative analysis between IPM and HEPM motor and EESM and HEPM motors sharing identical dimensions. Lastly, structural and thermal limitations affecting rotor winding machines are reported.

2

PERMANENT MAGNET SYNCHRONOUS MOTORS: GENERALITIES AND OPERATING POINTS

This Chapter aims to introduce the Permanent Magnet Synchronous Motor technology, which is a valid alternative to the IM for electric drive, for their easy control, construction and high efficiency. A PM motor is a type of electric motor that use permanent magnet on the rotor. Different rotor topology can be obtained but in general they can be divided in four main categories:

1. SPM motor
2. IPM motor
3. EESM motor
4. HEPM motor.

The first three PM motor are established technology. While, the HEPM motor, is a new technology, that will be analyzed in details.

2.1 SPM AND IPM MOTOR

A schematic representation of the structure of three-phase a synchronous PM motor, two-poles configuration, is shown in Fig. 2.1. The electromechanical conversion follows the principle of operation of the electrodynamic systems which is based on the interaction between stator conductors and magnetic fields created by other conductors or permanent magnets. The stator winding is three-phase type.

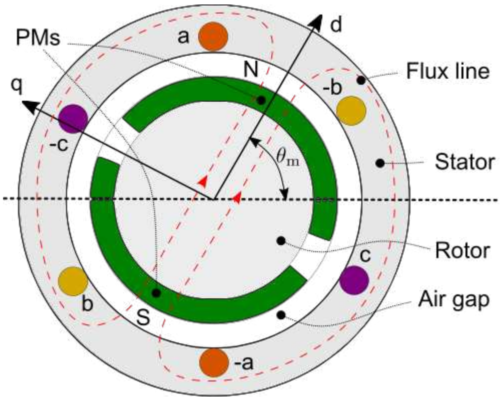

Figure 2.1: Three-phase synchronous permanent magnet motor structure.

The voltage equation, in abc reference system :

$$\begin{cases} v_a(t) = R_s i_a(t) + \frac{d\lambda_a(t)}{dt} \\ v_b(t) = R_s i_b(t) + \frac{d\lambda_b(t)}{dt} \\ v_c(t) = R_s i_c(t) + \frac{d\lambda_c(t)}{dt} \end{cases} \tag{2.1}$$

Where i_a, i_b, i_c are the phase current, $\lambda_a, \lambda_b, \lambda_c$ are the flux linkage with abc phases and R_s is the stator phase resistance.

Assuming no iron saturation, the flux linkage with the phases abc can be divided in:

$$\begin{cases} \lambda_a(t) = \lambda_{a,PM}(t) + \lambda_{a,i}(t) \\ \lambda_b(t) = \lambda_{b,PM}(t) + \lambda_{b,i}(t) \\ \lambda_c(t) = \lambda_{c,PM}(t) + \lambda_{c,i}(t) \end{cases} \tag{2.2}$$

where $\lambda_{a,b,c,PM}$ are PM flux linkage and $\lambda_{a,b,c,i}$ are the stator current flux linkage with stator phases respectively.

To simplify the model, the standard d-q synchronous reference system is adopted [59]. This reference system rotates synchronously with the rotor and has the direct axis fixed to the main rotor flux component and the quadrature axis components at 90 electrical degrees. In SyPM motors, the main component is given by the PM flux. To adopt this reference, it is necessary to know the initial electrical position ϑ_m^e and to measure the position by means of some sensors by estimation observers. In these hypotheses, it is possible to write the d-q voltage equations as:

$$\begin{cases} v_d = R_s i_d + \frac{d\lambda_d}{dt} - \omega_m^e \lambda_q \\ v_q = R_s i_q + \frac{d\lambda_q}{dt} + \omega_m^e \lambda_d \end{cases} \tag{2.3}$$

where for SPM and IPM the d-q flux linkage λ_q, λ_q are developed as:

$$\begin{cases} \lambda_d = \Lambda_{PM} + L_d i_d \\ \lambda_q = L_q i_q \end{cases} \tag{2.4}$$

Symbols i_d, i_q represent the direct and quadrature stator current, Λ_{PM} is the PM flux linkage with stator and L_d, L_q are the direct and quadrature inductances.

The main difference between SPM and IPM motor is the position of the PMs on the rotor, as shown in Fig. 2.2a and 2.2b. The air gap reluctance, is about constant for each rotor position in Fig. 2.2a. In this case the d-axis inductance (L_d) is equal to q-axis inductance (L_q), and therefore are equal to synchronous inductance L. While, the IPM motor architecture, has a variable air gap reluctance, and it is possible to distinguish the inductance L_d and L_q. Usually, the q-axis inductance is higher to d-axis inductance ($L_q > L_d$).

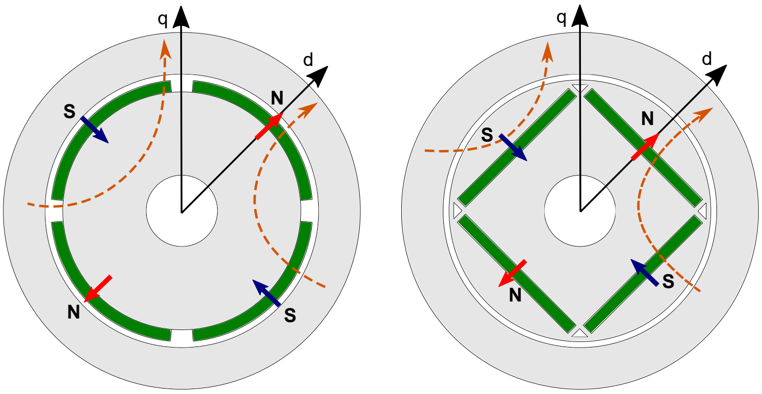

(a) SPM (b) IPM

Figure 2.2: SPM and IPM motors

Applying the energy balance to (2.3) can be easily computed (2.5) and then it is possible to obtain the torque equation.

$$\underbrace{\frac{3}{2}(v_d i_d + v_q i_q)dt}_{\text{Instantaneous energy (d W)}} = \underbrace{\frac{3}{2}R_s\left(i_d^2 + i_q^2\right)dt}_{\text{Joule Losses energy}(dW_j)} + \underbrace{\frac{3}{2}\left(i_d\frac{d\lambda_d}{dt} + i_q\frac{d\lambda_q}{dt}\right)dt}_{\text{Magnetic stored energy }(dW_{mag})}$$
$$+ \underbrace{\frac{3}{2}\omega_m^e(\lambda_d i_q + \lambda_q i_d)dt}_{\text{Electromechanical energy }(dW_{em})} \tag{2.5}$$

The first terms represents the instantaneous energy absorbed by the motor. The second term is linked to the losses energy (for Joule effects). The third term is the power absorbed, positive or negative, engaged in producing the variations of the magnetic energy connected with the field magnetic produced by phase currents. Consequently, the last term represents the electromechanical energy or the electrical energy that is converted into mechanical energy.

The torque can be computed equalizing the electromechanical energy $dW_{em} = T\omega_m dt$ that yields:

$$T = \frac{3}{2}\omega_m^e(\lambda_d i_q + \lambda_q i_d). \tag{2.6}$$

Substituting, (2.4), the IPM motor torque can be computed as:

$$T = \frac{3}{2}p\Lambda_{PM}i_q + \frac{3}{2}p(L_q - L_d)i_d i_q. \tag{2.7}$$

The SPM motor architecture presents $L_d = L_q = L$, and therefore the torque expression:

$$T = \frac{3}{2}p\Lambda_{PM}i_q. \tag{2.8}$$

2.2 EESM MOTOR

The EESM architecture follows the same laws but with the main difference that this geometry avoids PMs and adds a rotor coil. This winding permits to adjust the rotor flux according to the control strategy. The excitation winding changes the air gap flux density produced by the rotor also according to the rotor current.

A sketch of EESM motor is reported in Fig. 2.3.

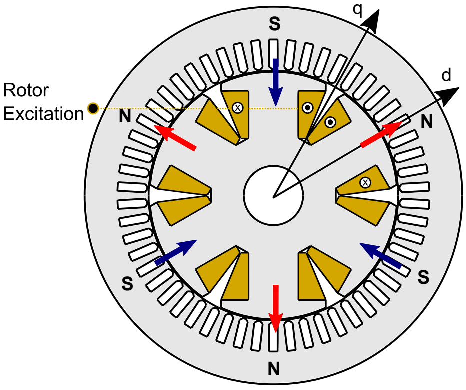

Figure 2.3: Basic architecture of EESM motor

The stator voltage equations are equal to SPM and IPM motors (2.3) with the adding of the rotor equation:

$$v_e = R_e i_q + \frac{d\lambda_{e,rot}}{dt} \tag{2.9}$$

where $\lambda_{e,rot} = L_e \frac{di_e}{dt} + \frac{3}{2} M_e \frac{di_d}{dt}$, L_e is the rotor leakage inductance and M_e the mutual inductance linkage with the stator winding.

The rotor flux linkage with the stator is composed just by the rotor excitation flux $\lambda_e = M_e i_e$ and therefore the flux linkage equations are:

$$\begin{cases} \lambda_d = \lambda_e + L_d i_d \\ \lambda_q = L_q i_q \end{cases} \tag{2.10}$$

where $\lambda_e = M_e i_e$ is the rotor excitation flux contribute, that can be positive or equal to zero. The torque equation can be computed adopting the same energy balance of (2.5) that returns:

$$T = \frac{3}{2} p \lambda_e i_q + \frac{3}{2} p (L_q - L_d) i_d i_q. \tag{2.11}$$

2.3 HEPM MOTOR

Lastly, the HEPM motor combines a field excitation rotor winding with PM. Unlike the IPM and SPM motor and similar to EESM, with

HEPM motor architecture it is possible adjust partially the rotor flux in according to the control strategy. HEPM motor geometry is reported in Fig. 2.4.

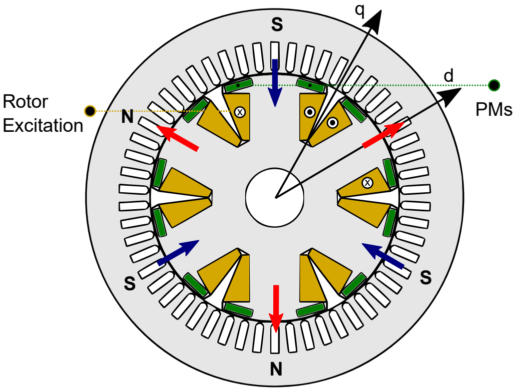

Figure 2.4: Basic architecture of HEPM motor

The voltage equations are the same of (2.3) and (2.9). In this cases, the rotor flux is composed of two terms, PM flux and rotor excitation flux, and therefore the flux linkage equations are:

$$\begin{cases} \lambda_d = (\Lambda_{PM} + \lambda_e) + L_d i_d \\ \lambda_q = L_q i_q \end{cases} \tag{2.12}$$

Where λ_e it is the rotor flux, witch can be positive or negative according to the rotor excitation current direction. The term $\lambda_{he} = \Lambda_{PM} + \lambda_e$ is the total flux linkage due to the rotor and the torque:

$$T = \frac{3}{2} p \lambda_{he} i_q + \frac{3}{2} p (L_q - L_d) i_d i_q. \tag{2.13}$$

In steady-state operations, PMSMs have certain operating limits that will be analyzed. Electrical quantities in the next section are assumed to be constant (steady state condition) and denoted with big symbols $V_d, V_q, I_d, I_q, \Lambda_d, \Lambda_q$. Under these hypotheses the voltage equation became:

$$\begin{cases} V_d = R_s I_d - \omega_m^e \Lambda_q \\ V_q = R_s I_q + \omega_m^e \Lambda_d \end{cases} \tag{2.14}$$

2.4 OPERATING LIMITS

Electrical machines are influenced by thermal and electrical insulation limits, which impose restrictions on both current and voltage.

$$\begin{cases} I_N^2 \leqslant I_d^2 + I_q^2 \\ V_N^2 \leqslant V_d^2 + V_q^2 \end{cases} \tag{2.15}$$

where V_N and I_N are the rated voltage and current of the motor winding. Assuming that the resistance voltage drop $R_s\sqrt{I_d^2 + I_q^2}$ is negligible compared to the motion term $\omega_m^e\sqrt{(\Lambda_d^2 + \Lambda_q^2)}$, the voltage equation can be simplified as:

$$\begin{cases} V_d = -\omega_m^e \Lambda_q \\ V_q = \omega_m^e \Lambda_d. \end{cases} \tag{2.16}$$

Then, in steady state condition, IPM synchronous motor equations (2.16) become:

$$\begin{cases} V_d = -\omega_m^e L_q I_q \\ V_q = \omega_m^e (\Lambda_{PM} + L_d I_d) \end{cases} \tag{2.17}$$

When the d-axis inductance is equal to q-axis inductance, $L_d = L_q = L$ particular case of the SPM motor, the equation is simplified as shown below:

$$\begin{cases} V_d = -\omega_m^e L I_q \\ V_q = \omega_m^e (\Lambda_{PM} + L I_d) \end{cases} \tag{2.18}$$

2.4.1 *SPM motor*

In $I_d - I_q$ plane, the current limit, represents a circumference. While, substituting the equation 2.18 in 2.15 the voltage curve in $I_d - I_q$ plane is obtained. The SPM equations current and voltage limits are:

$$\begin{cases} I_N \geqslant I_d^2 + I_q^2 \\ \dfrac{V_N^2}{\omega_m^{e2} L^2} \geqslant \left(\dfrac{\Lambda_{PM}}{L} + I_d\right)^2 + I_q^2. \end{cases} \tag{2.19}$$

The center of the limit voltage circumference represents the short circuit current, and it is equal to $I_{dcc} = -\Lambda_{PM}/L$.
SPM current and voltage limits are shown in Fig. 2.5

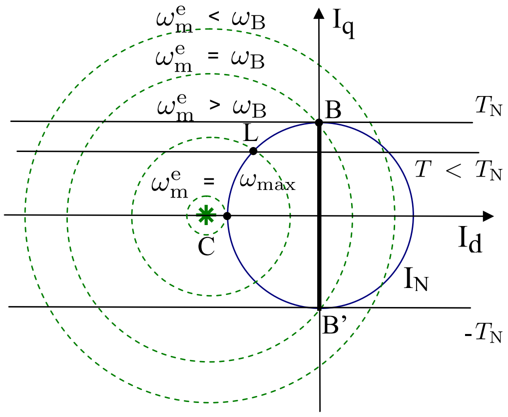

Figure 2.5: SPM motor operating range

The blue circle represents the current limit, while the green circles represent the voltage constraints that change according to the motor speed. The voltage limit decreases as the speed increases.

The torque curves are depicted by solid black lines, which, for SPM motors, are straight lines that are just function of the I_q current.

2.4.2 *IPM motor*

Unlike the SPM motors, the d-axis inductance L_d is not equal to q-axis inductance L_q. The current and voltage limits change into:

$$\begin{cases} I_N \geqslant I_d^2 + I_q^2 \\ \dfrac{V_N^2}{\omega_m^{e2} L_d^2} \geqslant \left(\dfrac{\Lambda_{PM}}{L_d} + I_d\right)^2 + \left(\dfrac{L_q}{L_d} I_q\right)^2 \end{cases} \tag{2.20}$$

In this case, the d-axis short circuit current, is equal to $I_{dcc} = -\Lambda_{PM}/L_d$ and the voltage limit curve becames an ellipse.
IPM motor architecture operating region is shown in Fig. 2.6.

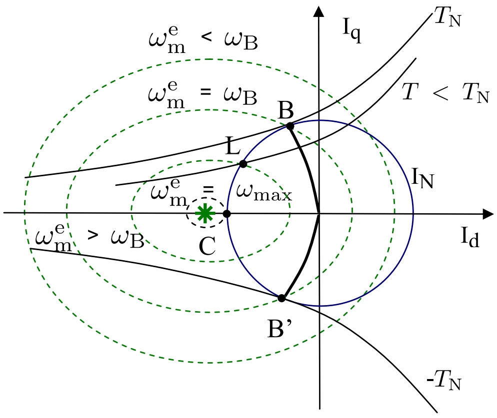

Figure 2.6: IPM motor operating range

In Fig. 2.6 the blue circle represents the current limit, while the green curves represent the voltage constraints that changes with motor speed. The voltage constraint is represented by an ellipse with the horizontal semi-axis greater than the vertical one. This is because inductances $L_q > L_d$. The torque curves are hyperbolic curves that depend on both I_d and I_q currents.

2.4.3 *EESM motor*

As mentioned above, rotor excitation coil adjusts the air gap flux. The rotor current control permits to extend the operating range and improve the performance of the machine in FW operation. An example of operating range, for EESM configuration, is reported in Fig. 2.7.

The center of the voltage limit ellipse $I_{dcc} = -\Lambda_e/L_d$, in this case, is not constant. The operating limits equations are reported:

$$\begin{cases} I_N \geqslant I_d^2 + I_q^2 \\ \dfrac{V_N^2}{\omega_m^{e2} L_d^2} \geqslant \left(\dfrac{\Lambda_e}{L_d} + I_d\right)^2 + \left(\dfrac{L_q}{L_d} I_q\right)^2 . \end{cases} \tag{2.21}$$

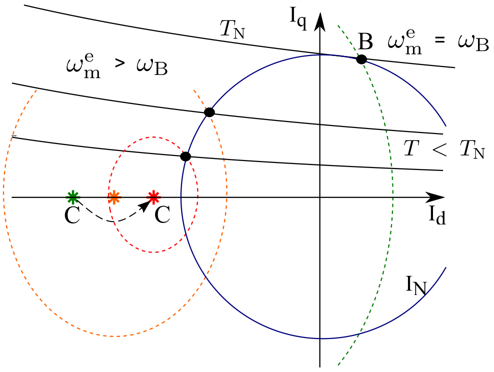

Figure 2.7: EESM operating range.

Similar to IPM motor, the blue circle represents the current limit, while the green, orange and red circles represent the voltage constraints that changes according to the motor speed and the rotor excitation current.

The voltage constraint is represented as an ellipse with the horizontal semi-axis smaller than the vertical one. This is because $L_d > L_q$.

Also here, the torque curves are hyperbolic curves that depend on both I_d and I_q currents.

2.4.4 *HEPM motor*

As for the EESM, HEPM motor can operate in a wide range and improve the performance of the machine during FW operation. An example of operating range, for HEPM motor, is reported in Fig. 2.8. The center of the voltage limit ellipse $I_{dcc} = -\Lambda_{he}/L_d$ is variable with the excitation current. The operating limits equations are:

$$\begin{cases} I_N \geqslant I_d^2 + I_q^2 \\ \dfrac{V_N^2}{\omega_m^{e2} L_d^2} \geqslant \left(\dfrac{\Lambda_{he}}{L_d} + I_d\right)^2 + \left(\dfrac{L_q}{L_d} I_q\right)^2 \end{cases} \tag{2.22}$$

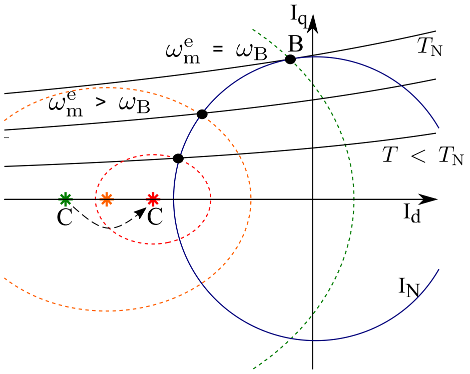

Figure 2.8: HEPM motor operating range

The voltage constraint is represented as an ellipse with the horizontal semi-axis higher than the vertical one. This is because $L_q > L_d$.

Also here, the torque curves are hyperbolic curves that depend on both I_d and I_q currents.

Moving forward, the possibility of modifying the rotor flow makes HEPM and EESM very interesting, adding a degree of freedom in the machine operating range. For this reason a detailed study will be carried out, starting with an analysis of different types of configurations.

3

HEPM MOTOR ANALYSIS: NO LOAD

In this Chapter various HEPM configurations are compared under no-load conditions.
Six-pole architecture has been selected for all the geometries. The machines are evaluated in terms of flux density, flux linkage, and electromotive force (EMF). The results are obtained through finite element (FE) analysis.
The analyzed geometries consider both series and parallel architectures. Additionally, it's important to note that these geometries are presented in their preliminary design state and are not optimized, yet. The aim of this part is to establish the proof of concept for identifying the optimal configuration that can effectively achieve a higher rotor flux increment, a more sinusoidal EMF and an improved flux density.

3.1 HEPM MOTOR: SERIES ROTOR COIL

Series configuration with six Rotor Coils (SRC-6) sketch is shown in Fig. 3.1a. This machine is the combination of a Vshape IPM motor having the excitation current on the rotor. The reluctance of the pole $\mathcal{R}_{\text{pole}}$ (i.e. the reluctance corresponding to $N_e I_e$ generator only) is mainly due to the reluctance of the permanent magnet $\mathcal{R}_{\text{PM}}$(i.e. $\mathcal{R}_{\text{PM}}/2$ in Fig. 3.1b). Fig. 3.1b shows the corresponding magnetic circuit.

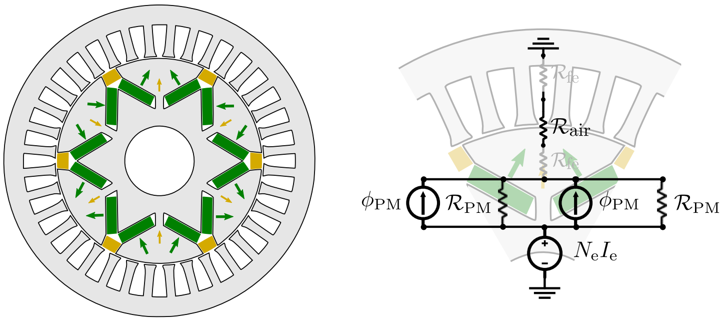

(a) Motor geometry (b) Magnetic circuit

Figure 3.1: SRC-6 configuration: geometry and magnetic circuit

The rotor data geometry is summarized in Tab.1.

3.1.1 *Air gap flux density controlled by the rotor excitation current*

The air gap flux contribution due to excitation is reduced because of the high reluctance $\mathcal{R}_{\text{pole}}$. When the rotor circuit is supplied, the

Table 1: IPM and SRC-6 rotor geometry

PM thickness	t_m	6	mm
PM width	h_m	21	mm
Slot excitation area	$S_{slot,exc}$	80	mm^2
Rotor current density	J_{exc}	15	$A\,mm^{-2}$

average air gap flux density B_g increases or decreases according to the rotor current direction positive or negative respectively.
It is shown in Fig. 3.2a . The red curve shows the distribution of B_g with positive excitation current, the dark curve shows the distribution of B_g without any excitation current, and the blue curve is obtained with negative excitation current. The waveform of air gap flux density remains similar to that with only the PMs that is about a trapezoidal wave.

3.1.2 *Flux linkage and electromotive force*

The no-load stator flux linkage, in abc and dq reference system, produced by this air gap flux density are reported in Fig. 3.2b. Fig. 3.2c reports the behavior of the EMF as a function of the rotor position and the related fundamental component. Therefore, the excitation current does not modify the harmonic content of the air gap flux density.

The electro-motive force, can be obtained as:

$$e = -\frac{d\lambda_{he}(t)}{dt} = -\omega_m^e \frac{d\lambda_{he}(\vartheta_m^e)}{d\vartheta_m^e} \tag{3.1}$$

The no-load flux linkages are not perfectly sinusoidal. They can be expressed by means of Fourier series as:

$$\lambda_{he}(\vartheta_m^e) = \sum_{k=1}^{\infty} \left(a_k \cdot \cos(k\vartheta_m^e) + b_k \cdot \sin(k\vartheta_m^e)\right) \tag{3.2}$$

Deriving the no-load flux linkage with respect the time, the various harmonics are multiplied by the corresponding harmonic order k. The EMF harmonics result to be amplified with respect the flux linkage harmonics.

Fig. 3.2d shows the difference between the actual and the fundamental harmonic of the EMF.

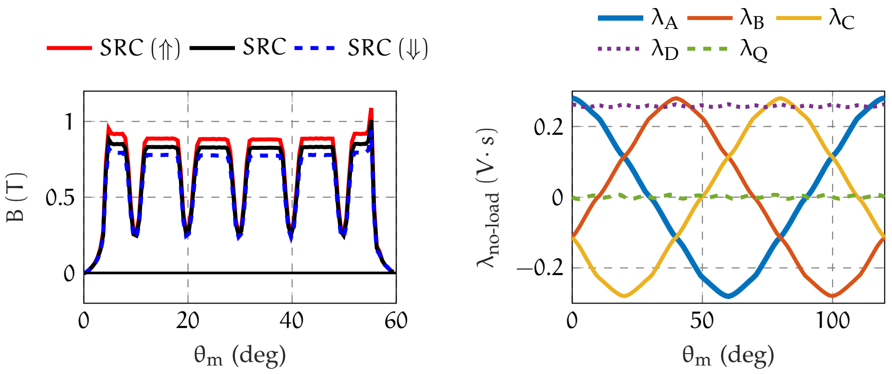

(a) Air gap flux density distribution versus rotor position

(b) No-load stator flux linkage versus rotor position

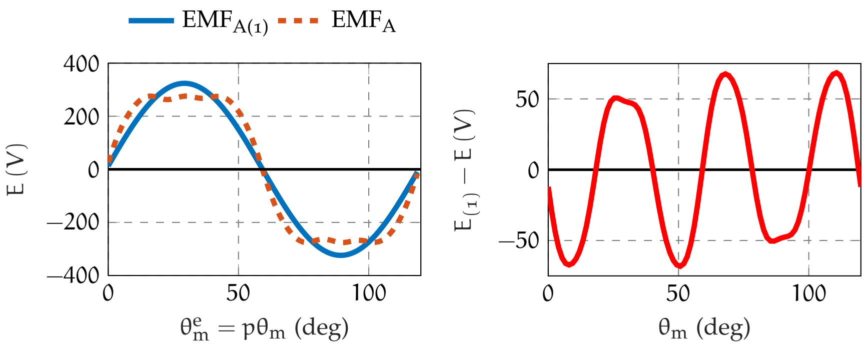

(c) Fouries series of electro-magnetic force versus rotor position

(d) Difference between actual and main EMF harmonic versus rotor position

Figure 3.2: Flux density, electro-magnetic force and linkage flux of the SRC-6 machine

3.2 PARALLEL ROTOR COIL: POLE ADDITION

The Parallel configuration with six Rotor Coils (PRC-6) is shown in Fig. 3.3a. The magnetic circuit is shown in Fig. 3.3b.

Unlike the SRC-6 machine, the PRC-6 configuration is characterized by a lower $\mathcal{R}_{\text{pole}}$ because there is an iron path in parallel to the PM path. Therefore the impact of the rotor current on the flux variation is significantly higher. Also here, there is a rotor coil for each PM, then the air gap flux density distribution is equal under each pole.

The rotor data geometry is summarized in Tab.2.

3.2.1 *Air gap flux density modulated by the rotor excitation current*

In the PRC-6 machine the contribution of the flux density excitation modifies significantly the flux density distribution in the air gap. The air gap flux density distribution, for PRC-6 configuration, is shown in Fig. 3.4a. The red line represents the HEPM motor with a positive

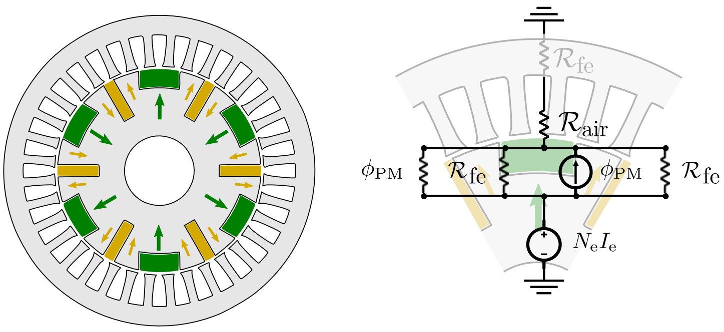

(a) PRC-6 geometry (b) Magnetic circuit

Figure 3.3: PRC-6 configuration: geometry and magnetic circuit

Table 2: PRC-6 rotor geometry

PM thickness	t_m	10	mm
PM width	h_m	22	mm
Slot excitation area	$S_{\mathrm{slot,exc}}$	138	mm^2
Rotor current density	J_{exc}	10	$\mathrm{A\,mm}^{-2}$

current, dark line the motor with the excitation current equal to zero, instead the blue line the flux density at the air-gap when the flux due to excitation current is opposite to the PM flux. Fig. 3.4a shows a flux density waveform closer to the sine wave when the current is positive. The contribution of the excitation flux is higher in this configuration than in SRC-6 motor, due to the low reluctances in the magnetic circuit.

This architecture brings a wider regulation of average air gap flux density. In addiction, compared to SRC configuration, the magnetic voltage drop on the PM is limited, reducing the risk of demagnetizing the PM.

3.2.2 *Flux linkage and electromotive force*

Fig. 3.4b shows the no-load stator flux linkage, they are not perfectly sinusoidal, but compared to the SRC-6 the waves are close to sinusoidal waves and this yields a reduction of harmonics content. Fig. 3.4c shows the electro-magnetic force EMF behaviour versus positions. The excitation current gives close contribution in the reduction of the harmonic content linked by the stator windings.

3.3 PARALLEL ROTOR COIL: POLE SUBSTITUTION

The last geometry analyzed has been built, starting from an IPM motor geometry this PRC-2 configuration is obtained when two PMs are

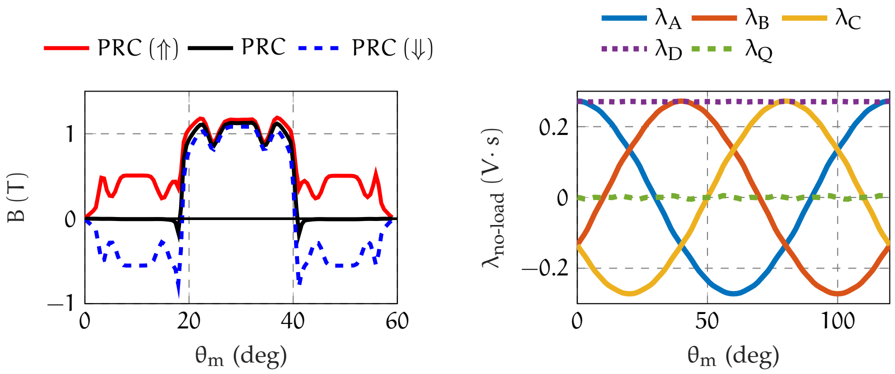

(a) Air gap flux density distribution versus rotor position

(b) No-load stator flux linkage versus rotor position

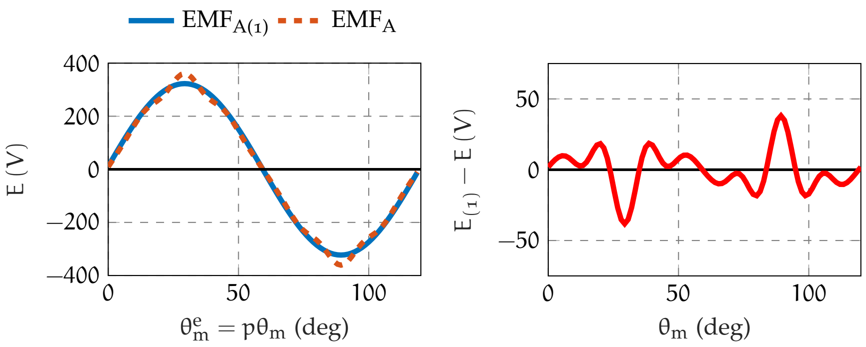

(c) Electro-magnetic force versus rotor position

(d) Difference between actual and main EMF harmonic versus rotor position

Figure 3.4: Flux density, electro magnetic force and flux linkage of PRC-6 machine.

replaced by two rotor coils, as shown in Fig. 3.5a. The magnetic circuit is shown in Fig. 3.5b and rotor data geometry is summarized in Tab.3.

Table 3: PRC-2 rotor geometry

PM thickness	t_m	10	mm
PM width	h_m	32	mm
Slot excitation area	$S_{\text{slot,exc}}$	206.5	mm^2
Rotor current density	J_{exc}	10	A mm^{-2}

3.3.1 *Air gap flux density controlled by the rotor excitation current*

Fig. 3.6a shows the air-gap flux density in three conditions: red-line refers to the excitation currents producing a flux that replaces a PM flux, dark-line refers to the case with zero excitation currents and

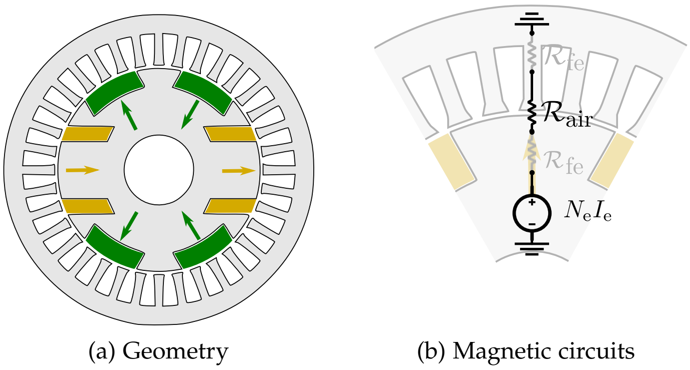

(a) Geometry (b) Magnetic circuits

Figure 3.5: PRC-2 configuration: geometry and magnetic circuit

blue-line refers to the case with negative current, that is when excitation flux is opposite to the PM flux. Red-line shows that the excitation current develops a flux with the same average value to the PMs. Blue-line shows that the average flux is mainly negative on the rotor pole where the coil is located. It is worth noticing that the rotor current produce a flux density variation only in a portion of the air-gap (according to the position of the coils), while the flux remains the same in front of the rotor PM. However, since the stator winding is distributed, a variation of the total flux linkage is obtained.

3.3.2 *Flux linkage and electromotive force*

Fig. 3.6b shows the no-load stator flux linkages. They are not perfectly sinusoidal, but similar to the SRC-6, the EMF are not a sinusoidal waveform and there are several EMF harmonics, compared to PRC-6 machine. Fig. 3.6c shows the electro-magnetic force behavior as a function of the rotor position at rated speed. The excitation current gives a high contribution substituting the PM, but there is a high harmonic content in the EMF waveforms.

3.4 DISCUSSION

Three Hybrid Excitation PM machines are analyzed: the first one with series configuration and two other machines with parallel configuration. Advantages and drawbacks are shown for all of them.

The HEPM motor with series configuration results to be not convenient. It exhibits limited performance if compared to the parallel configurations. There is a limited rotor flux variation even for a high rotor excitation current. This is because the flux produced by the excitation winding flows through the permanent magnets, which exhibit a high magnetic reluctance.

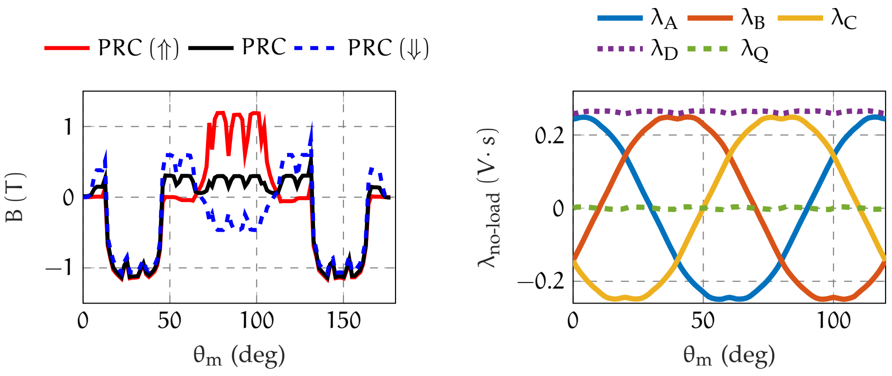

(a) Air gap flux density distribution versus rotor position

(b) No-load stator flux linkage versus rotor position

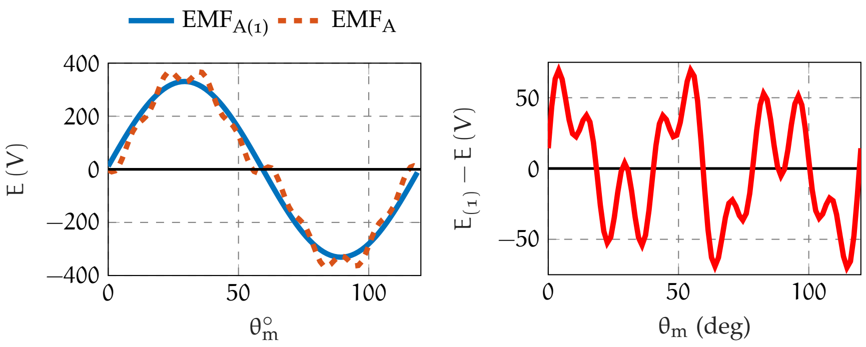

(c) Fouries series of electro-magnetic force versus rotor position

(d) Difference between actual and main EMF harmonic versus rotor position

Figure 3.6: Flux density, electro-magnetic force and flux linkage of PRC-2 machine.

The PRC-2 HEPM motor exhibits a proper variation of the flux. Moreover the harmonic content is limited. This issue has been verified by a magnetic network according to the position of the excitation coils and the rotor geometry, a low reluctance is obtained in parallel to the PM one.

At the end, the PRC-6 HEPM motor exhibits the same advantages of the previous PRC-2 motor, but a lower harmonic content in electromotive force. Moreover, distributing the excitation winding on 6 poles, the current density to obtain the flux variation of less than PRC-2.

This study has been conducted using preliminary geometries and has solely focused on no-load analysis.

In the upcoming Chapter, load analysis will be conducted, involving changes in pole pairs and a comparison with IPM motors suitable for high-power, high-torque applications. The geometries will be finalized and optimized to enable a meaningful comparative assessment.

4

HEPM MOTOR ANALYSIS: LOAD

This Chapter presents a load performance comparison between an IPM motor and three different configurations of HEPM motors [6, 8, 112]. The aim is to evaluate different HEPM motor configurations. The most promising will be selected and used as a benchmark for an IPM motor.

The motor performance of HEPM machines can be predicted using analytical models, which are based on mathematical equations that describe the behavior of the motor. These models are considered to be sufficiently accurate for a prediction of the motor performance in different working conditions and are suitable for the motor design. The motor performances obtained analytically can be compared with those of a FE model, which is a numerical simulation technique that can provide detailed information about the behavior of the motor[35]. The results of these two models are generally in satisfactory agreement in the whole operating speed range.

In addition to the improved performance, HEPM machines also offer other advantages. By controlling the rotor flux, these machines allow to operate over a wide speed range. Furthermore, HEPM machines are more efficient than traditional PM machines, mainly due to the increase of the output power. In fact, the HEPM machines exhibit a high power, which remains at its maximum value during all flux weakening operations. The main focus of this part is given to the motor performance during FW operations, highlighting the potential of HEPM machines to reduce the rotor flux at high speeds.

Hybrid excitation offers an additional degree of freedom with a lower use of magnetic material. This degree of freedom is the hybridization ratio κ, which is the ratio of the rotor winding excitation flux linkage Λ_e to the PM flux linkage Λ_{PM}. Their sum gives the total rotor flux linkage $\Lambda_{he} = \Lambda_{PM} + \Lambda_e$. Finally, there is another advantage adopting the HEPM motor. In the event of a short circuit fault, it is possible to reduce the rotor flux linkage Λ_{he} so as to limit the short circuit current and the corresponding braking torque [93].

4.1 FLUX LINKAGE CONTROL STRATEGY

The load analysis of HEPM rotor configurations requires a modulating rotor flux acting on the excitation control system. This is achieved starting from the steady state equation system as follows:

$$T_N = \frac{3}{2} p \left[\Lambda_{he} I_q + L_d (1 - \xi) I_d I_q \right] \tag{4.1}$$

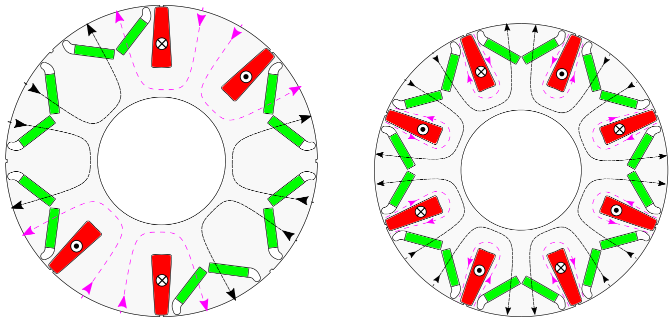

(a) HEPM PRC-2$^{(\Updownarrow)}$ motor (b) HEPM PRC-8$^{(\Downarrow)}$ motor

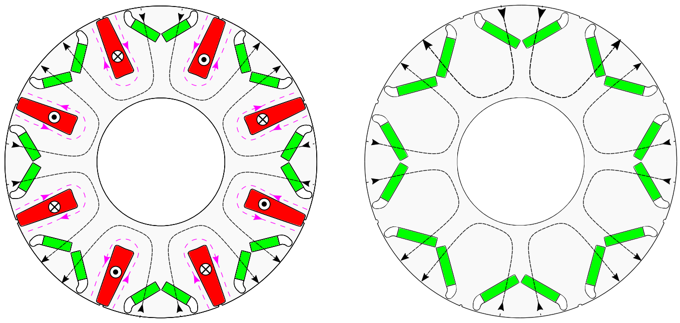

(c) HEPM PRC-8$^{(\Updownarrow)}$ motor (d) IPM V-shape motor

Figure 4.1: IPM and HEPM motor configurations.

$$V_N^2 = \omega_m^{e^2} \left[(\Lambda_{he} + L_d I_d)^2 + (\xi L_d I_q)^2 \right] \tag{4.2}$$

$$I_N^2 = I_d^2 + I_q^2 \tag{4.3}$$

The equations determine the maximum current (I_N) and voltage (V_N) given the rated torque (T_N) and specific machine parameters, such as the saliency ratio ξ and d-axis inductance L_d. The hybrid flux linkage Λ_{he}, which is the sum of the permanent magnet (Λ_{PM}) and excitation (Λ_e) flux linkage, can be formulated to maximize torque, as explained in [35, 56, 84]. At low speed the flux linkage is kept at its maximum value, while at high speed (ω_{FW} higher than rated speed) the rotor flux linkage is regulated as described in [67], the optimal rotor flux linkage is computed as:

$$\Lambda_{he} = \frac{\xi \, (\omega_{FW} \; L_d \; I_N)^2 + V_N^2}{\omega_{FW} \sqrt{(\xi \; \omega_{FW} \; L_d \; I_N)^2 + V_N^2}} \tag{4.4}$$

where the electrical speed is ω_{FW}, the saliency ratio ξ, the inductance L_d, as well as current and voltage limits I_N and V_N, respectively.

4.2 HEPM MOTORS: WORKING HYPOTHESES

Hereafter a detailed study is described comparing the performance of three HEPM motors (Fig. 4.1a, Fig. 4.1b and Fig. 4.1c) to an IPM

motor with V-shaped configuration (Fig. 4.1d). The rotor flux component is shown as a dark line if this component is given by the PM alone. If the component is given by the rotor excitation winding, it is reported with light magenta lines.
All motors analyzed exhibit the same nominal rotor flux linkage. In HEPM motors, the rotor flux linkage is regulated according to the designed configuration. The machine performance is evaluated during FW operations at speeds ranging from the rated speed (n_N = 3000 rpm) to 5 times n_N (15000 rpm) and under short-circuit conditions. Average torque, losses, and efficiency are computed for HEPM motors and compared to the IPM motor. The primary machine data are presented in the Tab.4.

Table 4: Characteristic shared by all machines

Rated working point operations and PM characteristics			
Stator RMS current density	J_{lim}	10	$A\,mm^{-2}$
Maximum values of voltage DC bus	V_{dc}	600	V
PM Type	NdFeB	-	-
PM Coercivity	H_c	850	$kA\,m^{-1}$
PM Relative permeability	$\mu_x = \mu_y$	1.049	-
PM Electrical conductivity	σ	0,667	$MS\,m^{-1}$
Stator winding and geometry			
Slot conductors	n_c	8	-
Machine parallel	n_{pp}	1	-
Rated current	I_N	49.7	A
Air gap	g	0.89	mm
Number of poles	$2p$	8	-
Outer diameter	D_e	200	mm
Inner diameter	D_s	130.86	mm
Axial length	L_{stk}	135.4	mm
Slot opening height	h_{so}	1	mm
Slot height	h_s	19.25	mm
Slot opening width	w_{so}	1.88	mm
Slot stator area	S_{slot}	70	mm^2
Number of slots	Q_s	48	-
Shaft diameter	D_{sh}	53	mm

The comparison aims to evaluate which configuration exhibits higher capability in FW operations, lower losses, a lower amount of PM, copper material, and better demagnetization resistance capability. Vari-

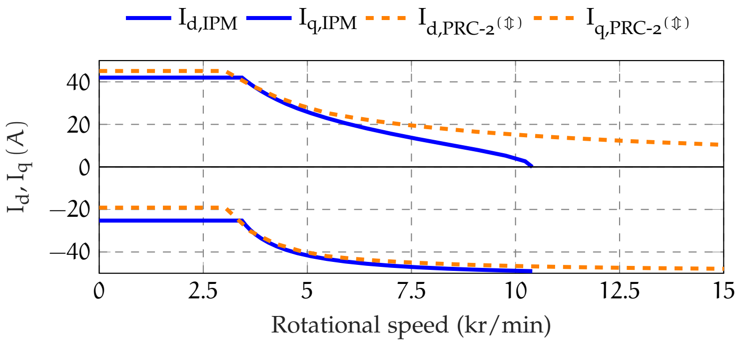

Figure 4.2: Stator current in IPM and HEPM motors in HEPM motor with PRC -2 configuration.

Table 5: IPM and PRC-2 rotor geometry

	IPM V-shape		
IPM PM thickness	t_m	4	mm
IPM PM width	h_m	16	mm
	PRC-2$^{(\Updownarrow)}$		
PRC-2 PM thickness	t_m	4	mm
PRC-2 PM width	h_m	16	mm
Slot excitation area	$S_{slot,e}$	174	mm^2
Rotor current density	J_e	7.5	A/mm^2

ous acronyms are used throughout the text, such as "P" (parallel configuration), "RC" (Rotor Coils), $\Updownarrow$ and $\Downarrow$ (double arrowhead and single arrowhead respectively) which refers to the use of excitation coils to increase and reduce the total rotor flux.

4.3 PRC-2 HEPM MOTOR (CONFIGURATION WITH TWO PARALLEL ROTOR COILS)

The first HEPM motor is obtained from PM motor where two coils replace two PMs and is labeled PRC-2. It is shown in Fig. 4.1a, while the original IPM motor is shown in Fig. 4.1d. Rotor data are reported in Tab.5. The symbol $^{(\Updownarrow)}$ indicates that the excitation current can flow in both directions so as to increase as well as to decrease the flux in the pole.

The winding substitution increases the apparent inductance L_d decreasing the saliency ratio $\xi = L_q/L_d$, since iron path is added to the d-axis as shown in Tab.6. This reduction increases the stator flux linkages developed by the excitation rotor currents but decreases the reluctance torque component. However this machine exhibits interesting capability at high speeds, as it will be shown later.

Table 6: IPM V-shape and PRC-2 Motor Parameters

IPM V-shape	
PM flux linkage	$\Lambda_{PM} = 0.1892\,V \cdot s$
Saliency ratio	$\xi = 2.3$
Direct inductance	$L_d = 2.3\,mH$
PRC-2$^{(\Updownarrow)}$	
PM flux linkage	$\Lambda_{PM} = 0.1419\,V \cdot s$
Excitation flux linkage	$\Lambda_e = 0.0473\,V \cdot s$
Saliency ratio	$\xi = 1.77$
Direct inductance	$L_d = 2.8\,mH$

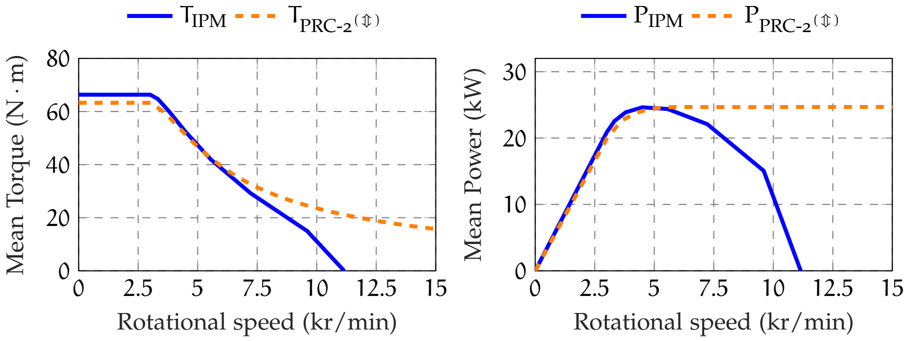

(a) Torque versus speed

(b) Power versus speed

Figure 4.3: Torque and Power developed by the HEPM motor with PRC-2 configuration, compared with those of the corresponding IPM motor.

By utilizing (4.1), (4.2), and (4.3) and taking into account the flux linkage Λ_{he} (4.4) to maximize torque during FW operation, appropriate stator currents I_d and I_q along with rotor current I_e can be obtained at any speed. This procedure will be used to analyze the HEPM machine. The stator currents I_d and I_q can be observed in Fig. 4.2. Notably, the I_q current in the HEPM motor remains significantly higher than in the IPM motor at high speeds. The surge in the HEPM stator current I_q is due to the decline of the rotor flux with speed. This enhances the mean torque and output power, as shown in Fig. 4.3a and Fig. 4.3b.

The outcomes show a different behavior in FW operations. The IPM motor displays a restricted FW working range with a maximum speed of $(3.5 \times n_N)$, while the HEPM motor demonstrates greater torque and power throughout the entire operating range. The maximum torque values are $63\,N \cdot m$ for the HEPM motor and $66\,N \cdot m$ for the IPM motor. The dissimilar rated torque at rated speed of the

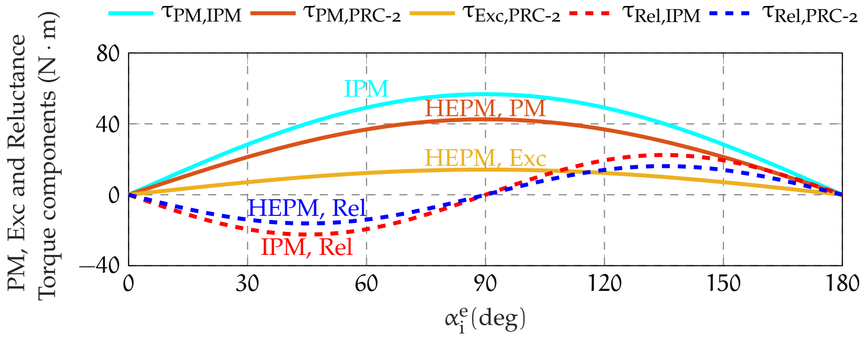

Figure 4.4: PM and Reluctance torque components developed by IPM and HEPM PRC-2 configuration with rated current I_N.

motors is due to the varied contribution of the reluctance torque component, as depicted in Fig. 4.4.

Fig. 4.4 illustrates the torque components in terms of the current vector angle α_i^e (and constant current amplitude). From (14.3), two simulations are carried out changing the sign of the d-axis current. This reverse the sign of the reluctance torque only. Comparing the two results (with positive and negative I_d) the two torque components can be recognised [17]. The solid lines depict the cylindrical torque components, with the IPM motor demonstrating a PM torque with a maximum value of $55\,\mathrm{N \cdot m}$, while the HEPM motor displays a PM torque component of $45\,\mathrm{N \cdot m}$ and a torque component due to the excitation current of $15\,\mathrm{N \cdot m}$. The dashed lines represent the reluctance torque components, with the IPM motor exhibiting a maximum value of $23\,\mathrm{N \cdot m}$, and the HEPM motor demonstrating a maximum value of $16\,\mathrm{N \cdot m}$.

The IPM motor torque drops down to zero at $11\,000\,\mathrm{r/min}$, on the contrary HEPM motor exhibits $22\,\mathrm{N \cdot m}$ at that speed. The IPM machine reaches the maximum power of $25\,\mathrm{k}W$ at a speed close to $5250\,\mathrm{r/min}$, while the HEPM PRC-2 the maximum power of $25\,\mathrm{k}W$ remains constant for all speeds higher than $5250\,\mathrm{r/min}$. Thanks to the Λ_{he} control, the HEPM motor power remains about constant along the whole FW speed range. The behavior of the excitation current is shown in Fig. 4.5. This excitation current I_e starts reduce the flux for speed higher than $5250\,\mathrm{r/min}$. The values of $N_e I_e$ moves from $500\,\mathrm{A}$ to $-150\,\mathrm{A}$. This wide range is due to the presence of only two excitation coils in the rotor. Fig. 4.5 also shows the difference between the variation of the rotor current as a function of the motor speed as achieved analytically by means of the rotor flux linkage Λ_{he} given in (4.4) and numerically by means of a FE analysis. The difference is due to the different saturation that affects the machine in the various working points, that is, L_d and L_q are not constant.

Other aspects have to be considered as the efficiency and the losses, as shown hereafter. Fig. 4.6 shows that the sum of HEPM motor losses

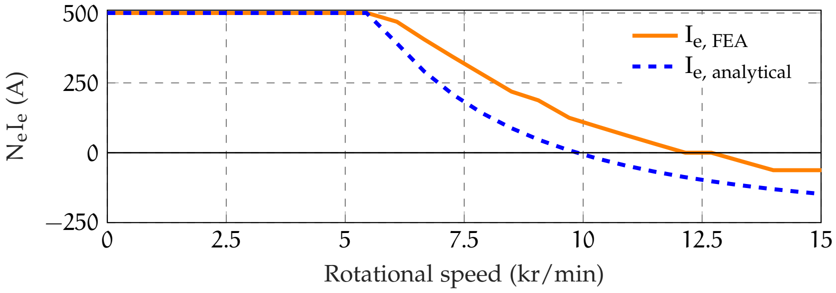

Figure 4.5: Rotor current in HEPM motor with PRC -2 configuration at different rotor speeds.

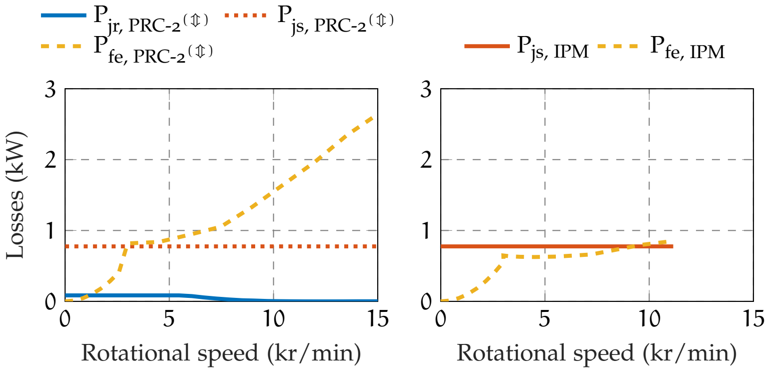

(a) HEPM losses

(b) IPM losses

Figure 4.6: Iron losses, joule stator losses and joule rotor losses in IPM and HEPM PRC-2 motor.

are always higher than the equivalent IPM motor. The joule stator losses of the two motors are the same and always constant neglecting the AC additional losses. The rotor joule losses in the two rotor coils are lower than $P_{jr} = 85\,W$. They are of minor importance compared to the maximum values of P_{fe} and P_{js} that are $P_{js} = 778\,W$ and $P_{fe} = 2600\,W$, respectively. The latter are the main losses at the higher speeds in HEPM motor. As shown in Fig. 4.7, this increase of the losses is due to the stator flux remains high (mainly in the back iron), and thus the iron losses increase during FW operations as remarked in Fig. 4.6a and Fig. 4.6b. This is the main drawback of the HEPM motor with PRC-2 configuration.

4.4 PRC-8 HEPM MOTOR (EIGHT PARALLEL ROTOR COILS)

PRC-8 motor configuration has been studied considering two different geometries reported in Fig. 4.1b and in Fig. 4.1c. The geometry reported in Fig. 4.1b is similar to the IPM configuration adding the excitation windings on the rotor. The other PRC-8 configuration, showed in Fig. 4.1c, is characterized by lower amount of PM than the first one allowing a higher width for the flux flowing in parallel to the PM

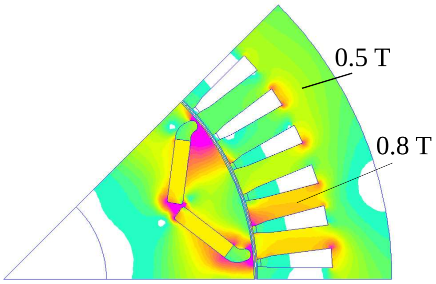

(a) IPM V-shape motor

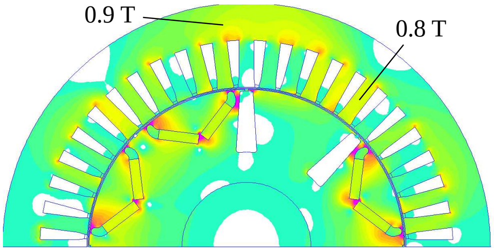

(b) HEPM PRC-2$^{(\Updownarrow)}$ motor

Figure 4.7: IPM and HEPM PRC-2 motor flux maps when operating at $n = 10000$ r/min.

flux. In addition, in this second geometry the rotor excitation current helps the PM to increase and decrease the rotor flux. Differently from the PRC-2 motor all PMs are supported by the flux of the excitation coils. This machine is referred to as PRC-8 (Eight Parallel Rotor Coil) HEPM motor. Again, the flux of the excitation coils flows through different paths with respect to the flux due to the PMs, that is, on the lateral edges of the PMs. These motors are analysed according to two different excitation modes:

- The excitation winding is used only to reduce the flux due to the PMs (a single arrow is used to highlight the unidirectional flux in Fig. 4.1b). This configuration is referred to as PRC-8 $^{(\Downarrow)}$.
- The excitation winding is used both to increase and to reduce the rotor flux. A double arrowhead is used in Fig. 4.1c, and this motor will be referred to as PRC-8$^{(\Updownarrow)}$.

The motors analyzed have different PM geometry as reported in Tab.7 but the excitation winding is the same. As remarked before the control of the excitation winding is different. The range of operating speed is kept constant for both the machines. Both the configurations are compared in term of rated torque and speed, power and efficiency, as for the previous configuration.

In the PRC-8$^{(\Downarrow)}$ HEPM motor the excitation winding is used only to reduce the rotor flux. Fig. 4.8a shows that the excitation current is zero up to 4800 r/min. On the contrary, in the PRC-8$^{(\Updownarrow)}$ HEPM motor

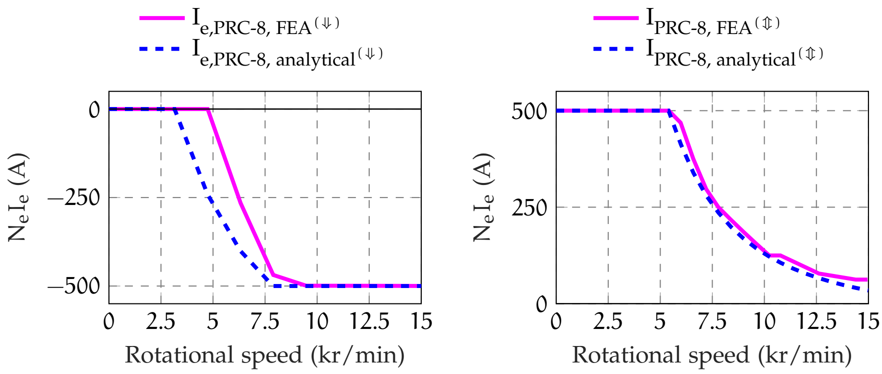

(a) Excitation current versus speed in PRC-8$^{(\Downarrow)}$ configuration motor that just reduces the rotor flux.

(b) In this example I_e remains positive even at high speed, but for higher speed it could become negative.

Figure 4.8: Rotor excitation current in PRC-8$^{(\Downarrow)}$ and PRC-8$^{(\Updownarrow)}$ machines.

Table 7: PRC-8 rotor geometries

	PRC-8$^{(\Downarrow)}$		
PM thickness	t_m	4	mm
V-PM width	h_m	16	mm
	PRC-8$^{(\Updownarrow)}$		
PM thickness	t_m	4	mm
V-PM width	h_m	12	mm
	PRC-8$^{(\Downarrow)}$ & PRC-8$^{(\Updownarrow)}$		
Slot excitation area	$S_{slot,e}$	174	mm^2
Rotor current density	J_e	7.5	A/mm^2

the excitation current is used to increase and reduce the PM flux as shown in Fig. 4.8b.

The advantages are the similar to the ones described in the previous section. At the beginning of the FW operations, the rotor flux is kept to its maximum value: the excitation current is set to zero in PRC-8$^{(\Downarrow)}$ as shown in Fig. 4.8a and the excitation current is set to the maximum value for PRC-8$^{(\Updownarrow)}$ as reported in Fig. 4.8b. At speed higher than the rated speed, the HEPM rotor flux is reduced, so that the stator currents become different so as to achieve the highest torque for both the machines. Fig. 4.8a shows that at speed higher than 4800 r/min the excitation current I_e starts to decrease to develop a flux opposite to the PM flux, while in PRC-8$^{(\Updownarrow)}$ the excitation current I_e starts to be reduced at 5500 r/min. The figures also show the difference between the analytical and the numerical values, adopted in FE analysis. The difference is due to the high saturation of the iron developed by the high current density, while the inductances are considered constant in

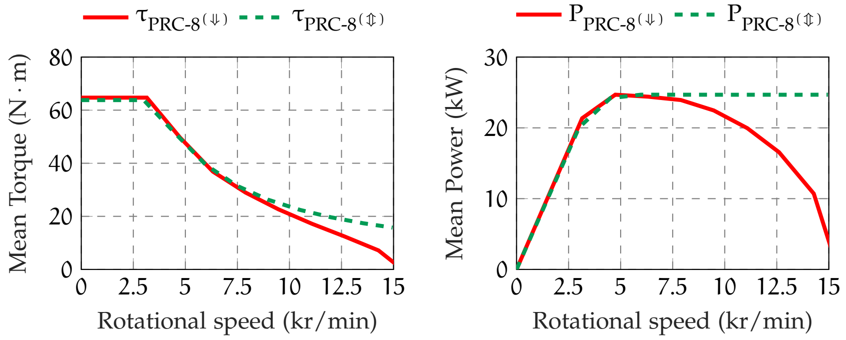

(a) Torque versus speed of PRC-8$^{(\Downarrow)}$ and PRC-8$^{(\Updownarrow)}$ configuration motor

(b) Mechanical power versus speed of PRC-8$^{(\Downarrow)}$ and PRC-8$^{(\Updownarrow)}$ configuration motor

Figure 4.9: Torque and power versus speed.

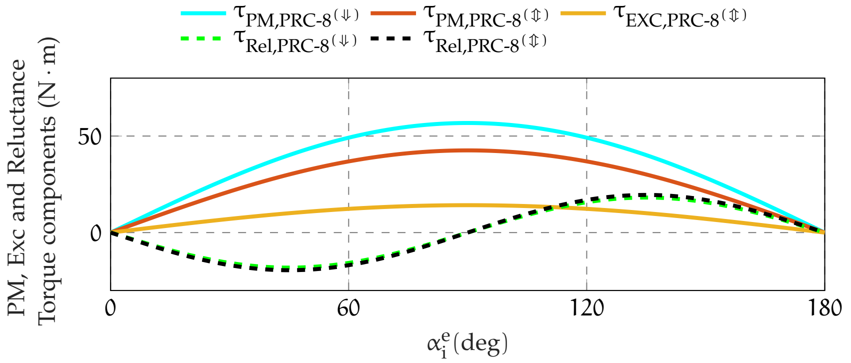

Figure 4.10: PM and Reluctance torque components developed by HEPM PRC-8$^{(\Downarrow)}$ and PRC-8$^{(\Updownarrow)}$ configuration with rated current I_N.

the analytical equation for any working conditions. In the non-linear model the excitation current I_e is slightly higher in all the operating speed range.

The flux reduction allows the average torque and power to be increased, as shown in Fig. 4.9a and Fig. 4.9b. Also in this case, there is a satisfactory performance of both HEPM motors. The results show a different behavior in FW operation. The PRC-8$^{(\Downarrow)}$ motor exhibits a limited performance compared to the PRC-8$^{(\Updownarrow)}$ motor which reaches a higher torque and power delivered.

The maximum values of the torque are 66 N · m in PRC-8$^{(\Updownarrow)}$ and 65 N · m in PRC-8$^{(\Downarrow)}$ motor at rated speed. The different rated torque is due to the different contribution of the reluctance torque component as shown in Fig. 4.10. The rated torque of the motors varies due to the varying contribution of the reluctance torque component. The figure illustrates the comparison of the excitation and PM torque components with the reluctance torque component for both motors. The operation speed range is covered by both motors, but with different torque and power. The PRC-8$^{(\Downarrow)}$ machine reaches a maximum power

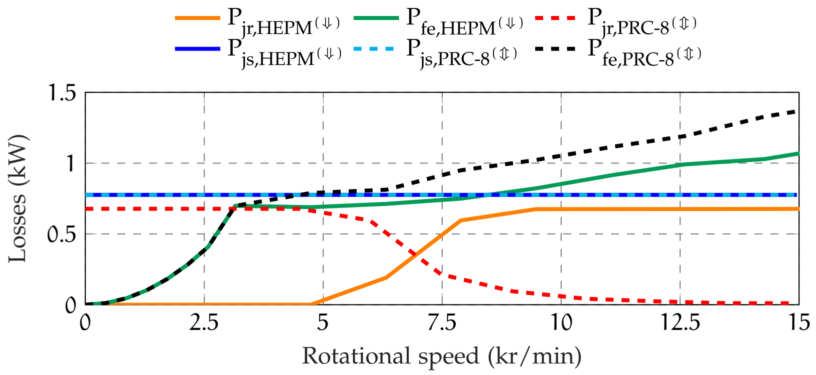

Figure 4.11: Losses component of PRC-8$^{(\Downarrow)}$ and PRC-8$^{(\Updownarrow)}$ motor.

of 25 kW at a given speed (5500 r/min), the PRC-8$^{(\Updownarrow)}$ machine has a maximum power of 25 kW that is kept quite constant for any speed higher than 5500 r/min. Thanks to the Λ_{he} control, the HEPM motor power remains about constant along the whole FW speed range. The curves are not perfectly constant in FW operation due to high saturation of the machine.

The corresponding losses are reported in Fig. 4.11. In both machines the stator joule and iron losses are similar compared to rotor joule losses at low speed. The maximum value of these rotor joule losses is $P_{jr} = 670\,W$ because there are 8 coils instead of 2 in PRC-8$^{(\Updownarrow)}$. In PRC-8$^{(\Downarrow)}$, at low speed they are lower compared to the values of P_{fe} and P_{js}, while at high speed their importance increase compared to the maximum values of P_{fe} and P_{js} that reach $P_{js} = 778\,W$ and $P_{fe} = 1400\,W$. Moreover, the rotor copper losses in PRC-8$^{(\Downarrow)}$ are higher than PRC-8$^{(\Updownarrow)}$ at high speed. In PRC-8$^{(\Updownarrow)}$ motor the Joule losses are similar to the other components at low speed. The iron losses remain limited and much lower in comparison to the PRC-2$^{(\Updownarrow)}$ motor described in the previous section.

The flux maps of both motors are reported in Fig. 4.12. The pictures underlined the different saturation that affects the iron in both PRC-8 configurations at the speed of 10000 r/min. The PRC-8$^{(\Downarrow)}$ exhibits a lower back iron and teeth saturation compared to the PRC-8$^{(\Updownarrow)}$, therefore the PRC-8$^{(\Downarrow)}$ iron losses are lower. This advantage is deleted by a higher risk of demagnetization compared to the PRC-8$^{(\Updownarrow)}$ motor, because the iron paths parallel to the PMs have a low width, that is easy to saturate. In the PRC-8$^{(\Updownarrow)}$ the parallel paths are more extended and guarantee privileged paths for the rotor flux excitation component.

4.5 PERFORMANCE ASSESSMENT

In this section motor parameters such as PM flux linkage, excitation flux linkage, saliency ratio and direct inductance are computed for different configurations. Comparisons are made between IPM and

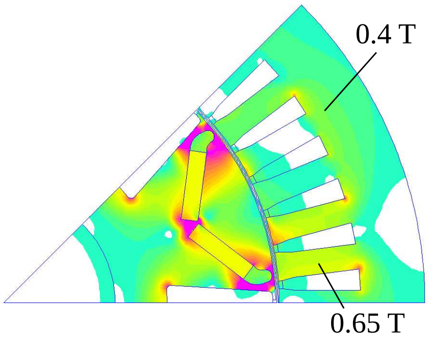

(a) HEPM PRC-8$^{(\Downarrow)}$ motor

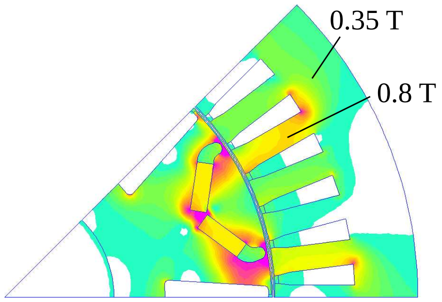

(b) HEPM PRC-8$^{(\Updownarrow)}$ motor

Figure 4.12: PRC-8$^{(\Downarrow)}$ and PRC-8$^{(\Updownarrow)}$ motor flux maps when operating at speed n = 10000 r/min.

HEPM motors in terms of short-circuit current, power, torque and efficiency at various speeds has been reported. Moreover, the flux maps of different motor configurations are also shown, highlighting their saturation characteristics.

4.5.1 *Short circuit fault and PM demagnetization*

The fault reliability is necessary in PM synchronous motor operations, for this reason a PM demagnetization analysis is compulsory during the design of the motor. During a 3-phase short circuit fault of a synchronous PM machine, the terminal voltage is equal to zero and the stator current are subjected to an uncontrolled free evolution.
The equations during this fault are:

$$\begin{cases} \dfrac{di_d}{dt} = \dfrac{\omega_m^e L_q i_q - R_s i_d}{L_d} \\ \\ \dfrac{di_q}{dt} = \dfrac{-\omega_m^e L_d i_d - \omega_m^e \Lambda_{he} - R_s i_q}{L_q} \end{cases} \tag{4.5}$$

where ω_m^e is the electrical speed, R_s is the stator resistance that is equal to $0.2154\,\Omega$ for all machines. At the end of the transitory the machine works with almost only I_d current, whose value is almost $-\Lambda_{he}/L_d$ where Λ_{he} is the rotor flux linkage and L_d is the direct axis

Table 8: PRC-8 motor parameters

PRC-8$^{(\Downarrow)}$	
PM flux linkage	$\Lambda_{PM} = 0.1892\,V\cdot s$
Excitation flux linkage	$\Lambda_e = 0.0278\,V\cdot s$
Saliency ratio	$\xi = 2.1$
Direct inductance	$L_d = 2.2\,mH$
PRC-8$^{(\Updownarrow)}$	
PM flux linkage	$\Lambda_{PM} = 0.1419\,V\cdot s$
Excitation flux linkage	$\Lambda_e = 0.0473\,V\cdot s$
Saliency ratio	$\xi = 2$
Direct inductance	$L_d = 2.6\,mH$

inductance. For the classical PM machine Λ_{he} is equal to Λ_{PM} that is the PM rotor flux linkage, instead for the HEPM motor Λ_{he} is the Λ_{he} that is regulated by means of the excitation current control.

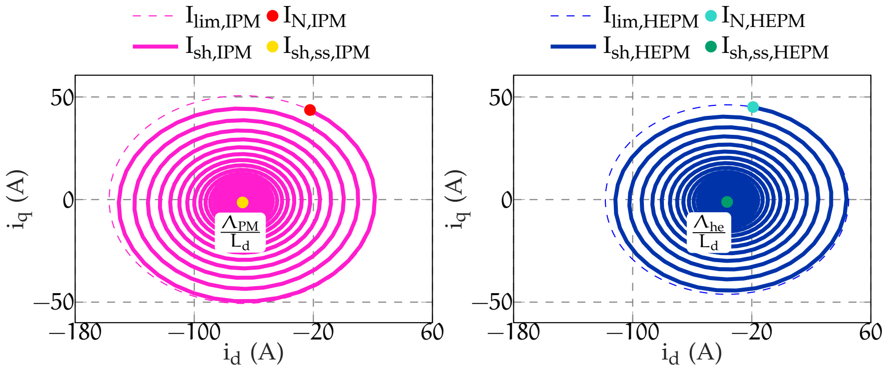

Figure 4.13: IPM (left) and HEPM (right) motor dynamic short circuit current, calculated at a speed equal to 10000 r/min.

In this way it is possible to reduce Λ_{he} in case of fault. The rotor flux linkage components are reported in Tab.6 and Tab.8. Fig. 4.13 shows the dynamic behavior considering the IPM and the HEPM PRC-8$^{(\Downarrow)}$ motors. The maximum current that affects the HEPM motor is 30% lower than the IPM machine. This yields a lower demagnetization of the PMs that are in both motor and a safer condition in case of fault.

A comparison of all the configurations is carried out in terms of power in Fig. 4.14a, torque in Fig. 4.14b and efficiency in Fig. 4.15. It is possible to recognize that at low speeds the IPM motor exhibits slightly better performance due to the lower iron losses and no rotor joule losses. However, at speed higher than the rated speed its benefit disappears and the HEPM motor shows a higher torque and power behaviour.

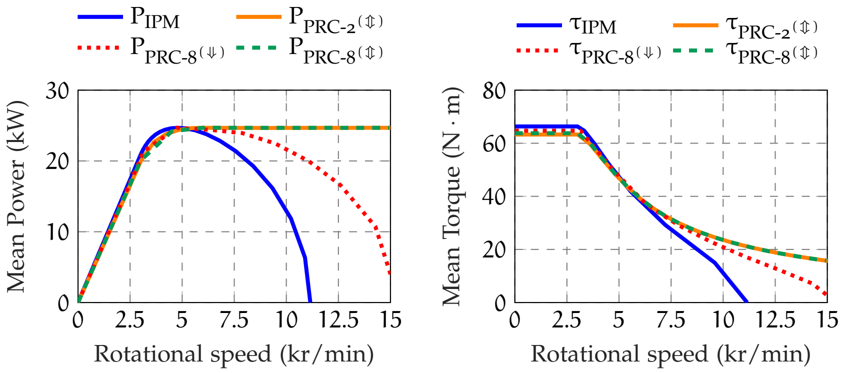

(a) Power comparison versus speed.

(b) Overall torque comparison versus speed.

Figure 4.14: Power and torque comparison versus speed.

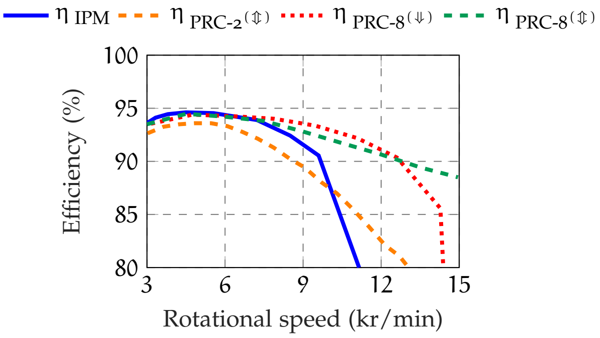

Figure 4.15: Overall efficiency comparison.

To verify that performance, the flux map of each machine has been reported in Fig. 4.7 and Fig. 4.12 at the speed of $10\,000\,\mathrm{r/min}$. The IPM V-shape motor shows a low saturation compared to the other HEPM motors. This aspect is due to the different stator current supplied to reach the same speed. The highest saturation in the back iron is found in the PRC-2 $^{(\Updownarrow)}$ that thus exhibits higher losses.

One aspect to consider is the force distribution in the PRC-2 $^{(\Updownarrow)}$ motor, which is not equally distributed despite the machine periodicity. In contrast, the PRC-8 $^{(\Downarrow)}$ and PRC-8 $^{(\Updownarrow)}$ motors have a uniform symmetry pole by pole. At 10000 r/min, the flux map shows low saturation for the PRC-8 $^{(\Downarrow)}$, but this increases with the rotor joule losses. However, there is a range of speeds where this machine achieves higher efficiency, even though the power delivered and excitation winding flux contribution may be lower.

Instead, PRC-8 $^{(\Updownarrow)}$ motor flux map shows a good trade-off of iron saturation achieving a very good efficiency. The motor symmetry is respected and the amount of PM is lower than IPM motor. The PM magnetization safety is always in the limits of demagnetization in particular at high speed. The control of the excitation current can help avoiding PM demagnetization and reducing the impact of a short-circuit current in the event of a fault. Indeed the dynamic fault response comparison exhibits a reduction of the 30% of maximum short circuit current for the PRC-8 $^{(\Updownarrow)}$ configuration compared to IPM. The maximum efficiency reached by PRC-8 is 95% and in the whole speed range is always higher than 88%. In HEPM motors the power delivered is almost constant along all the operating region once reached the maximum power. In IPM motor the power decreases quickly once overcome the maximum power speed. With the possibility to increase and to reduce the rotor flux, the PRC-8 $^{(\Updownarrow)}$ HEPM motor configuration exhibits the highest performance, in comparison with the other solutions described above. In addition, this configuration is characterized by lower PM and Copper volume, making it a suitable and convenient choice.

4.6 DISCUSSION

The analysis presented here exhibits the benefits and limitations of various HEPM motor configurations in comparison to a conventional PM motor. These motors are designed with equivalent rotor flux linkage and size. It is evident that the HEPM motor, regardless of the configuration, has a greater capacity to operate over a broader range of speeds than an IPM motor and increased resilience to failure.

The IPM motor is characterised by a given PM flux. It exhibits a speed limit and a risk of demagnetization in the event of a short-circuit fault. The HEPM motor has higher speed limit. It has been analyzed up to a speed five times the rated speed.

The losses of the IPM motor is slightly lower at speed lower than rated speed, but this advantage decreases at higher speeds. On the contrary, the HEPM motors reach an efficiency from 95% to 88% in the whole speed range.

Furthermore, the comparison presented above is based on continuous current rating in the rotor winding. As for wound rotor machines, an overload current can be supplied in the rotor winding for a short time. Therefore there is the advantage of an even higher transient torque at low speed.

Summing up all these aspects the HEPM motor results to be a valid alternative to IPM motor, guaranteeing good performance in a wide speed range with a lower overall losses percentage.

Among the various topologies of HEPM motor that have been analyzed, the solution characterized by one coil per pole and reduced PM width exhibits the better performance. The main advantage of this configuration is that the symmetry remains the same in any operating conditions. In addition, the bidirectional excitation current yields a better modulation of the rotor flux.

Until now, the excitation flux was designed to support the PM flux, which was the main component. In the upcoming Chapter, the PMs will enhance the excitation flux, which will become the primary component and will be compared with a similar configuration lacking PMs. A performance comparison will be discussed.

5

EESM AND HEPM MOTOR: PERFORMANCE COMPARISON

In this Chapter a performance comparison between EESM and HEPM motor is carried out. The main focus here is on the real advantages and disadvantages that the addition of a small amount of PM can have, rather than the use of excitation current alone. EESM is characterized by a classical salient pole rotor geometry, while the HEPM motor is a improved version of the EESM including two PMs buried in each salient pole. The magnets helps the rotor flux, for this reason this configuration is called Permanent Magnet assisted Excitation (PMaExc). Fig. 5.1 shows both machine geometries. The overall rotor flux can be either increased or decreased supplying an proper excitation current. The EESM magnetization flux is produced only by the excitation current, while PMaExc motor benefits from both excitation current and PM contribution.

This initial part shows requirements and motor geometric parameters. The DC bus voltage is assumed equal to $350\,V$ and the inverter Volt-Ampere rating is $S = 138\,kV\,A$. Moreover, the rated speed n_N should be in the range between $4000\,r/min$ and $5000\,r/min$.

The PMaExc geometry has been optimized through the differential evolution algorithm illustrated in [4]. Optimization objectives were to maximize the mean torque and minimize the torque ripple. Main parameters were pole shaping and PM position and tilt.

The EESM geometry is assumed exactly identical to the PMaExc one, simply replacing PMs with iron core. Final geometries and parameters of Fig. 5.1a and Fig. 5.1b are described by data of Tab.10 and Tab.11. The choice of both PMaExc and EESM rotor current density $J_{exc} = 4.5\,A/mm^2$ is limited by thermal considerations. In fact, the goal is to avoid excessive rotor core overheating.

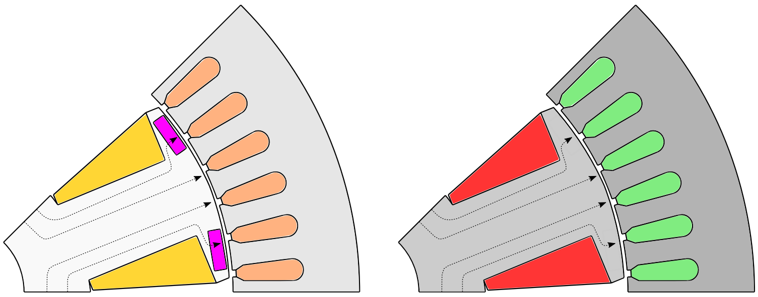

(a) PMaExc motor.

(b) EESM motor.

Figure 5.1: Geometries design.

Table 9: Motor performance requirements.

Parameter	Symbol	Value	Unit
DC bus voltage inverter	V_{dc}	350	V
Rated torque	T_N	230	$N \cdot m$
Speed base	n_N	4100	r/min
Phase stator current	I_N	456	A
Continuous excitation current	I_e	90	A

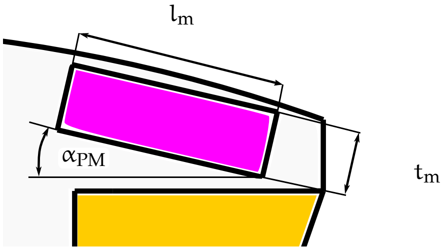

Figure 5.2: Geometry design.

Differently, the stator current density $J_{lim} = 12\,A/mm^2$ is much higher than J_{exc}. Indeed, a water cooling system is assumed for both motors.

The geometry of the stator of both EESM and PMaExc motor analyzed above is reported in Tab.10.

The rotor geometry is reported in Tab.11 according to the geometry details in Fig. 5.2. Pole shaping, PM dimensions and position of the PMaExc motor are the result of an optimization achieved through a differential evolution algorithm. Optimization objectives were to maximize the average torque and to minimize the torque ripple.

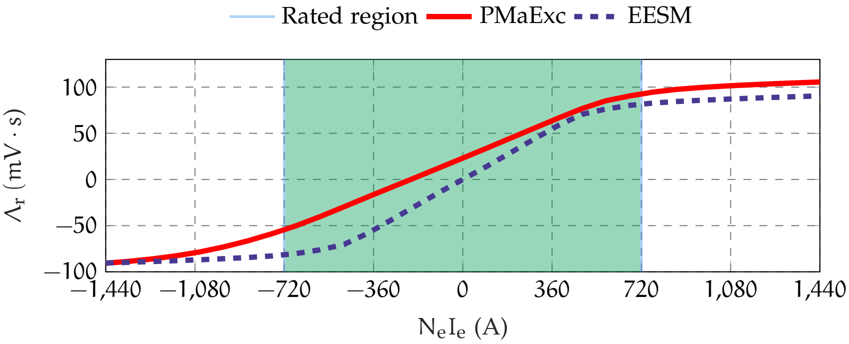

Figure 5.3: Flux linkages linked by EESM (red solid lines), PMaExc (blue dashed lines) machines and the operating region analysed (yellow fill area).

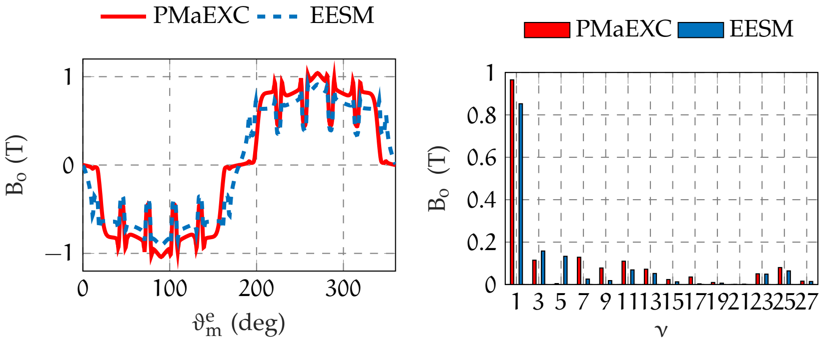

(a) No-load flux-density versus electrical angle.

(b) No-load Fourier harmonic magnitude versus harmonic order.

Figure 5.4: No-load flux-density of PMaExc (red solid line) and EESM (blue dashed line) motor.

5.1 NO LOAD ANALYSIS

The electromagnetic study of both motors is carried out through finite element analysis. 2D magneto static simulations are carried out. The no-load characterization consists in the motor analysis when stator windings are open-circuited. In particular, the main goal is to compute flux linkages and air gap flux density due to the rotor considering both PM and excitation contribution. The second goal is the evaluation of the EMF. No-load results are represented for a pole pair of both PMaExc and EESM motor, thanks to their periodicity.

Fig. 5.3 shows the computed no-load flux linkages of PMaExc and EESM motor with respect to the ampere turns $N_e I_e$. The flux linkages have been analysed considering a current density up to $J_{exc} = 9\,A/mm^2$ ($N_e I_e = 1440\,A$), in order to validate the potential advantages and drawback of the configurations studied. However, both motors performance have been evaluated employing a current density of $J_{exc} = 4.5\,A/mm^2$ ($N_e I_e = 720\,A$) to avoid overheating. Consequently, the operating region is limited to the shaded yellow area. The no-load flux linkage is higher for PMaExc than EESM, along all the operating region. In particular, PMaExc motor flux linkage is 14% higher than the EESM motor flux linkage when the excitation current $N_e I_e$ is equal to 720 A. The additional contribute of the PM flux linkage is shown at $N_e I_e$ equal to 0 A, and it represents the offset of $0.023\,V \cdot s$ between the two machines.

Starting from these considerations the air-gap flux density has been computed supplying a rotor excitation current $N_e I_e$ of 720 A. In this point benefits and drawbacks of the additional PMs can be estimated, in particular their effect on the fundamental and harmonic components. Fig. 5.4 compares the PMaExc (red solid line) and EESM (blue dashed line) air gap flux density. As reported in Fig. 5.4a, waveforms are different: PMaExc flux density has a higher peak value and, at first sight, it seems to have a less sinusoidal shape but a higher fundamental harmonic amplitude. Fig. 5.4b displays the harmonic content achieved by means of Fourier series analysis of both waveforms, up to twenty seventh-order harmonic. PMaExc motor exhibits a higher third and seventh harmonic components, but a lower fifth harmonic magnitude. Adding PMs the flux density fundamental harmonic increases of approximately 13 %.

Therefore, the PMaExc motor torque is expected to be higher than the EESM torque.

Table 10: Stator geometry

Parameter	Symbol	Value	Unit
Pole number	$2p$	8	-
Outer diameter	D_e	210	mm
Inner diameter	D_s	130	mm
Stack length	L_{stk}	170	mm
Stator slots	Q_s	48	-
Slot height	h_s	19	mm
Back-iron height	h_{bi}	15	mm
Tooth width	w_t	6	mm
Open Slot width	w_{so}	2	mm
Open slot height	h_{so}	1	mm
Wedge height	h_{wed}	2	mm
Stator slot area	$S_{s,slot}$	89	mm^2
Stator conductors in slot	$n_{s,c}$	4	-
Parallel stator paths	$n_{s,pp}$	2	-
Air gap	g	0.7	mm
Copper conductivity	$\sigma_{Cu,120°}$	37.5	MS/m
Iron specific weight	γ_{fe}	7800	kg/m^3

Flux density waveform influences also the EMF forces. Fig. 5.5 shows the line to line voltages. PMaExc shows a higher voltage magnitude compared to EESM machine and a slightly higher oscillation along the waveform.

The no-load analysis underlines that, adding PMs, EMF and flux density amplitudes slightly increase, but their waveform does not change significantly. Both these rotor excitation motors have the possibility to regulate the line to line voltage, by increasing or decreasing the excitation current. These machines can also achieve a very low short circuit current because the rotor flux can be reduced to zero.

Table 11: Rotor geometry

Parameter	Symbol	Value	Unit
Shaft diameter	R_{sh}	19	mm
PM thickness	t_m	3.5	mm
PM length	l_m	11	mm
PM tilt angle	α_{PM}	16	deg
Excitation slot area	$S_{r,slot}$	103	mm^2
Rotor and stator fill factor	k_{fill}	0.6	-

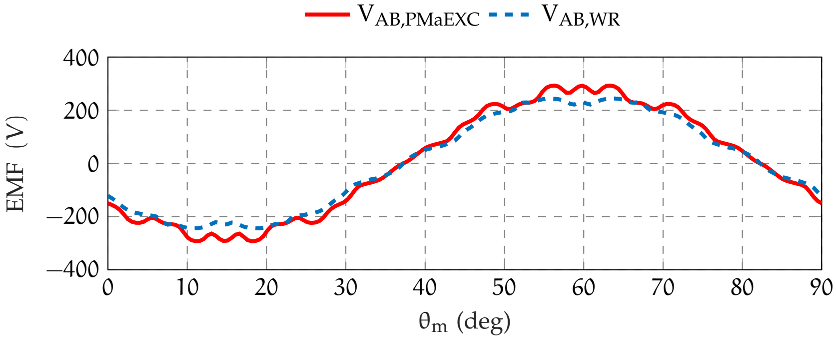

Figure 5.5: Back electro-magnetic force induced by EESM (dashed lines) and PMaExc (solid lines) machines.

Nevertheless, EESM voltage regulation is more flexible thanks to the absence of PMs.

5.2 LOAD ANALYSIS

This part deals with the load analysis with a current supplied in the (i_d, i_q) plane. Both electric motors have to satisfy the requirements reported in Tab.12. The study has been carried out adopting the maximum excitation current $J_{exc} = 4.5\,A/mm^2$ to achieve the highest torque. In addition, the stator current is controlled adopting the MTPA strategy.

Both EESM and PMaExc motor torque waveform is computed, to get mean value and ripple. The map along (i_d, i_q) plane has been deeply described for both machines to compare torque versus speed curves, MTPA, FW, MTPV trajectories, voltage limit ellipses and efficiency maps on the torque and current plane.

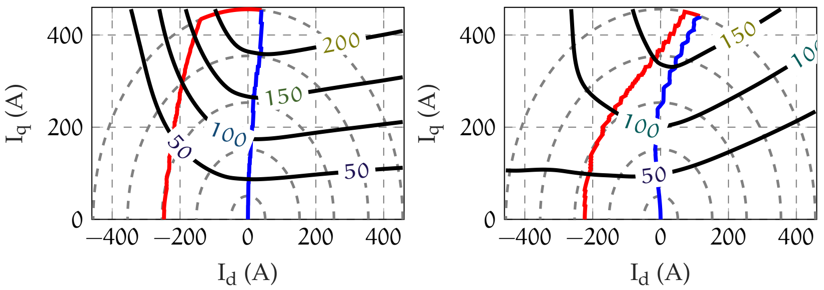

(a) PMaExc motor.
(b) EESM motor.

Figure 5.6: MTPA and MTPV trajectories in the (i_d, i_q) plane.

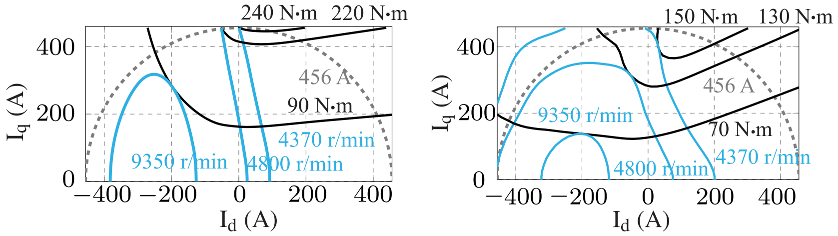

(a) PMaExc motor.
(b) EESM motor.

Figure 5.7: Torque (black solid line), voltage (light blue solid line) and current contour (gray dashed line) plot in (i_d, i_q) plane for PMaExc and EESM motors.

5.2.1 *Limit curves mapping*

In this subsection the motor performance along the (i_d, i_q) plane is analysed. In particular, current, voltage and torque limit curves are computed at various speeds, evaluating the highest possible torque for each speed working point. Fig. 5.6a and Fig. 5.6b show the working points as the motor speed increases. Current limit curves (grey dashed lines) are circumferences with radius equal to the current amplitude and with centre in (i_d, i_q) plane origin. Torque contour lines (black lines) correspond to hyperbolas distorted by the saturation.

First, the MTPA trajectory (blue line) can be followed, up to the rated speed. Then, to increase the operating speed, both motors operate in FW. In particular the stator current amplitude is maintained constant, while its electrical phase angle is increased. At a certain speed the MTPV operation becomes more convenient. Thus, the operating trajectory shifts within the current circle.

The PMaExc motor trajectory in the (i_d, i_q) plane is reported in Fig. 5.6a, while the EESM trajectory is shown in Fig. 5.6b. PMaExc motor develops MTPA trajectory for positive i_d values and reaches a torque of $T = 240\,\mathrm{N \cdot m}$ at the rated point (with the maximum current of $I_N = 456\,\mathrm{A}$). EESM motor exhibits a similar behavior, but its MTPA torque is much lower than the PMaExc torque. The EESM maximum

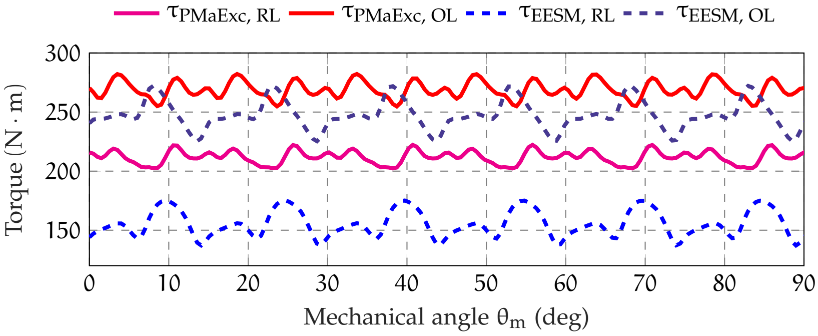

Figure 5.8: Torque ripple versus mechanical angle.

torque is reached at a higher positive value of i_d and it is approximately $T = 165\,\mathrm{N \cdot m}$ (about 30% lower).

As shown in Fig. 5.7, at motor speeds above the rated speed, voltage ellipses (blue lines) tend to collapse inside of the current limit circumference (grey dashed line). Most suitable working points are located where constant torque curve (black solid lines) is tangent to voltage curves. Thus, both motors move along MTPV trajectory for higher speeds. This is why in Fig. 5.6a and Fig. 5.6b the FW red line drifts within the current circumference at a certain speed.

It is worth noting that in Fig. 5.7 torque curves (black lines) are distorted hyperbolas, as well as the voltage ellipses (blue lines). This distortion is related to the interaction between rotor and stator flux. In fact, the rotor flux is not strictly bound to a fixed axis, but slightly oscillates as the position of stator current vector changes.

5.2.2 *Torque behavior and ripple*

Fig. 5.8 shows the torque behaviour of PMaExc and EESM computed in MTPA condition, with stator current $\hat{I}_s = 455$ A. PMaExc motor exhibits a higher torque than EESM, reaching an average torque of 210 $\mathrm{N \cdot m}$ and 270 $\mathrm{N \cdot m}$ with rated load (RL) current and overload (OL) current ($J_{exc} = 4.5 - 9 \mathrm{A/mm^2}$) in the excitation circuit. EESM exhibits an average torque of 155 $\mathrm{N \cdot m}$ and 245 $\mathrm{N \cdot m}$ corresponding to the same excitation currents. The introduction of the PM in the pole shoes has a double effect. At first, it reduces the stator q-axis current reaction, that is, the q-axis flux produced by the stator current, which is almost completely on the q-axis as observed in Fig. 5.6. Then, the PMs provide an additional rotor flux that is of great benefit, especially in overload operating conditions.

Fig. 5.8 shows that the torque ripple of the PMaExc motor is lower than in EESM. Torque ripple is 11% for the PMaExc motor, 28% for the EESM. This is due to the lower local saturation of the pole shoe edges. The smaller flux variation yields a reduction in torque oscillations. Anyway, it is worth remembering that the PM location and PM tilt angle have been selected considering also to reduce motor torque ripple.

5.2.3 *Mechanical characteristics*

Fig. 5.9 shows the maximum torque (and power) versus speed characteristics for PMaExc (solid lines) and EESM (dashed lines). Both motor configurations exhibit significant capabilities in a wide speed range, with the ability to reach up to 20 kr/min, which is five times the base speed. The PMaExc motor demonstrates superior torque and power throughout the entire speed range. The rotor current remains fixed at $N_e I_e = 720$ A (RL) and $N_e I_e = 1440$ A (OL) for both the PMaExc and EESMs, and this value is maintained constant. The motor mechanical characteristics are achieved by following specific trajectories in the (i_d, i_q) plane, as explained in the previous subsection (and in [34] for the EESM). The maximum torque can be delivered when the motor speed is lower or equal to the base speed. Then, the highest output torque decreases as the speed increases, as typically happens along the FW trajectory.

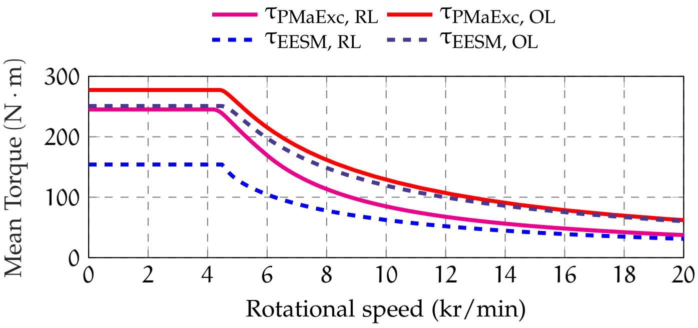

(a) Torque versus speed.

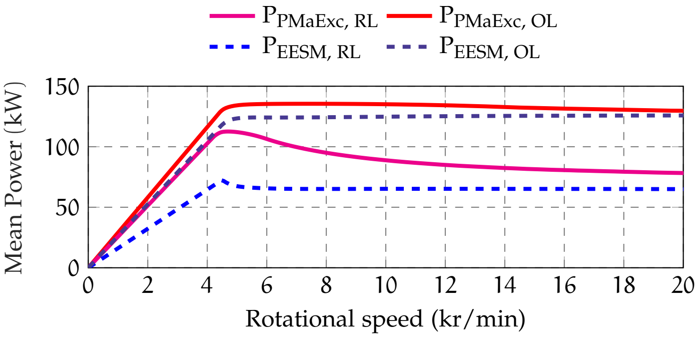

(b) Power versus speed.

Figure 5.9: Torque and power versus speed delivered by PMaExc motor with rated and overload excitation.

Consequently to the torque versus speed behaviour described, the maximum power versus speed characteristic is illustrated hereafter.

Based on a rotor current of $N_e I_e = 720$ A, the power of the PMaExc motor increases linearly with speed until reaching a maximum point. After the peak, the power slowly decreases during FW operation (particularly when it achieves the MTPV operation). This power decrease is due to the lower amplitude of the stator current vector during MTPV operation, resulting in reduced torque. On the other hand, the power of the EESM remains almost constant after reaching its peak, although it is consistently lower than the power of the PMaExc motor. This constant power characteristic is achieved without any significant reduction in rotor current, including the MTPV operation. This advantage is due to the fact that the excitation flux of the EESM does not follow any specific preferential paths. In particular, the rotor flux prefers the path of lowest reluctance, resulting in higher EESM flux linkages and an increase in the average delivered torque.

According to $N_e I_e = 1440$ A, the PMaExc motor power remains almost constant in the whole speed range as the EESM. Again, the curve is obtained without rotor current reduction. During the FW operations the stator current vector remains almost along the current limit circle, as shown in Fig. 5.6a.

For low torque request and motor speed higher than the rated, a possible control strategy is to maximize the torque as illustrated in [67]. Based on these considerations, efficiency maps for both motors have been calculated and will be discussed in the following subsection.

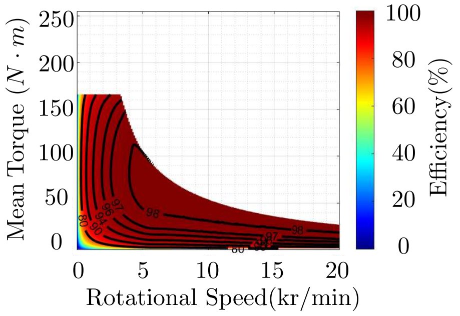

Figure 5.10: EESM rated torque versus speed efficiency maps.

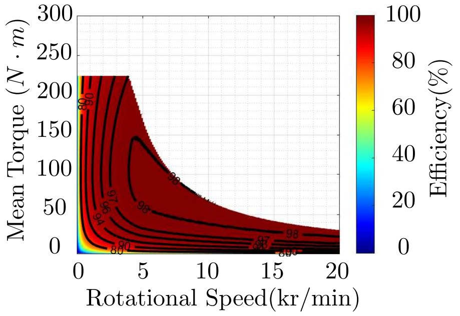

Figure 5.11: PMaExc rated torque versus speed efficiency maps.

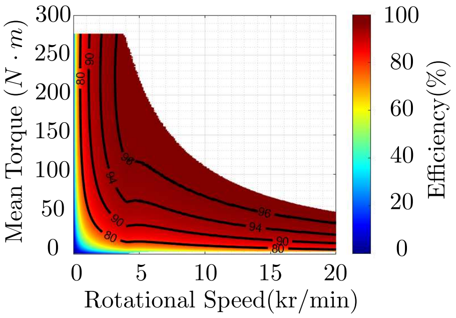

Figure 5.12: Torque versus speed efficiency maps of PMaExc according to rated excitation current and transient excitation over-current.

5.2.4 *Efficiency maps*

The efficiency map is contour plot representing the machine efficiency defined in the torque-speed plane, covering all possible operating points. Efficiency maps of the EESM is reported in Fig. 5.11 while PMaExc motor are reported in Fig. 5.11 and Fig. 5.12 according to excitation current N_eI_e = 720 A and N_eI_e = 1440 A. It is worth noticing that the efficiency is higher than $\eta = 90\%$ in most of the operating area. A comparison between EESM and PMaExc motor is given and it is shown that the PMaExc motor exhibits higher efficiency in a wider torque–speed range than the EESM [34].

5.3 DISCUSSION

This Chapter presents the study of the electromagnetic performance of two synchronous motors characterized by salient poles. One machine model is a typical salient-pole motor, while the other includes excitation winding and PMs to produce the overall rotor flux. It is achieved by modifying the traditional structure of a Wound Rotor motor, inserting PMs in the lateral parts of the pole shoes.

While in the past the analysis has been carried out with only the rated excitation current, comparing the performance to the traditional EESM, the analysis considering an excitation overcurrent as well. The purpose is to verify if the performance is modified according to higher field.

The analysis highlights and validates advantages of the PMaExc motor configuration. The PMaExc motor represents an improved configuration of the traditional EESM, obtained adding PMs to boost the rotor flux generated by excitation windings. Such a solution allows high torque density to be achieved in a wide speed range. Adding a few amount of PMs, the performance improvement is evident: torque, power and efficiency are higher in PMaExc motor a rather than the EESM.

This has been also verified during overload operations. The PMs limit the current reaction and keep a high rotor flux even in presence of high iron saturation. In comparison to the EESM, the PMaExc motor torque results to be about 50% and 10% higher with rated excitation current and overcurrent, respectively.

Power is kept constant in the whole operating speed range with the high excitation current. It slightly decreases with the speed with rated excitation current.

The next step is the thermal and mechanical analysis in order to highlight the corresponding limits.

6

FLUID DYNAMIC - THERMAL AND MECHANICAL ANALYSIS

In this Chapter thermal and mechanical limits are treated considering the presence of both PMs and excitation winding. Electric motor thermal and mechanical limits are mandatory for both EESM and HEPM motors. Traditionally are quickly computed through Lumped Parameters Thermal Networks (LPTNs). LPTNs are thermal circuits composed by several nodes (with an imposed or unknown temperature) connected together by thermal resistors [66].

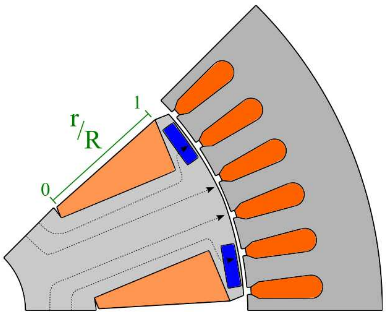

Figure 6.1: Partial HEPM motor.

In LPTNs network conductive resistances between different materials are easy to define because they depend on geometry and material properties. On the contrary, convective resistances are difficult to compute because they require the calculation of Heat Transfer Coefficients (HTCs). HTCs depend on the fluid motion field close to solid surfaces wetted by the fluid. In particular, the complexity of salient pole rotors geometry generates highly turbulent flows and possible stagnation points that can affect HTCs values. These parameters change with the rotor speed and they can be obtained by numerical simulations accounting for fluid-dynamic and thermal aspects. However, these tests are extremely time consuming.

Here an evaluation of HTCs values on the surface of the hybrid PM-salient pole machine. They are computed by 2-D thermal fluid-dynamic simulations at different rotational speeds. In literature there are some experimental and numerical studies on heat exchange for salient poles machines [20, 91]. This study focuses on accurate correlations and approaches for determining HTCs of the pole surface, especially at high rotational speed.

The fluid dynamic - thermal study gives precise and reliable results. Lumped parameters of the thermal network can be tuned on the basis of such results.

Table 12: Motor performance requirements.

Parameter	Symbol	Value	Unit
DC bus voltage inverter	V_{DC}	350	V
Rated torque	T_N	108	$N \cdot m$
Speed base	n_N	5000	r/min
Minimum power delivered	P_{out}	50	kW
Phase stator current	I_N	190	A
Continuous excitation current	I_e	90	A

The first part highlights most relevant simulation results and losses computation. Section 6.1.3 includes the thermal-fluid analysis numerical approach and simulation settings.

6.1 HEPM MOTOR

Traditional PM synchronous motors for automotive applications require high torque density and high speed range, thus, a high PM flux. However, a high PM flux reduces the motor maximum speed achievable.

The HEPM machine overcomes this limit adding excitation windings in the rotor core. PMs produce a constant flux, while excitation coils produce a variable flux. The total rotor flux can be either increased or decreased supplying an adequate excitation current.

Performance is improved in several speed regions: the constant torque region, up to a rated speed, and the constant power region, between rated and maximum speed. In the first region a higher torque is achieved increasing the rotor flux. In the second region a flux weakening control strategy yields higher speed and constant power.

This section presents a HEPM motor electromagnetic analysis employing the control strategy described in [18, 67]. In order to satisfy the torque, power and speed constrains of Tab.12, the geometry design is optimized as in Fig. 6.1.

The electromagnetic study of the HEPM motor designed is conducted through finite element analysis. 2D time domain magnetostatic simulations are carried out.

Fig. 6.2 shows both power and torque requirement versus speed values along the overall region. The maximum speed achieved is more than five times the base speed. For each FW working point losses are computed as described hereafter.

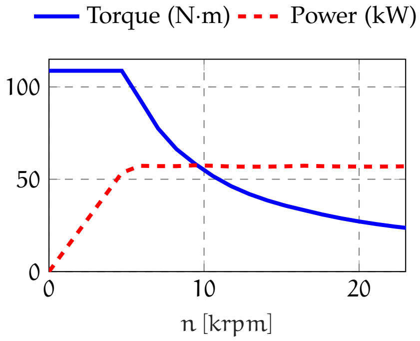

Figure 6.2: Torque and power versus speed.

6.1.1 *Joule losses*

The HEPM machine is characterized by both stator and rotor Joule losses, due to the presence of excitation windings. Considering geometric data and motor parameters summarized in Tab.10 and Tab.11, stator Joule losses are computed as:

$$P_{js} = J_{lim}^2 \cdot V_{cu,s} \cdot \frac{1}{\sigma_{Cu,120^\circ}} \tag{6.1}$$

The current density J_{lim} is calculated as:

$$J_{lim} = \frac{I_{slot}}{\sqrt{2}} \cdot \frac{1}{S_{slot} \cdot k_{fill}} \tag{6.2}$$

The windings fill factor k_{fill} is chosen equal to 0.6 assuming hairpin stator and rotor winding configurations. Considering the maximum current for each FW point $I_{slot} = n_{s,c} \cdot \sqrt{I_d^2 + I_q^2}$. The volume of copper material in the stator is evaluated considering an approximated end winding length $L_{ew} \approx 2.5 \cdot D_s/p$:

$$V_{cu,s} = k_{fill} \cdot S_{slot} \cdot Q_s \cdot (L_{stk} + L_{ew}) \tag{6.3}$$

Similarly, rotor Joule losses are computed by (6.1), considering excitation windings current density J_{exc} instead of J_{lim} and rotor copper volume $V_{cu,r}$ instead of $V_{cu,s}$. The current density depends on the excitation current supplied in the specific FW operating point I_e. The volume of rotor copper material is estimated as:

$$V_{cu,r} = k_{fill} \cdot S_{slot,exc} \cdot Q_{exc} \cdot (L_{stk} + L_{ew,exc}) \tag{6.4}$$

6.1.2 *Iron losses*

Iron losses are computed from Steinmetz formulation, considering both hysteresis and eddy currents effects. The iron losses in the back-iron are computed considering an increase coefficient $k_{magg,bi} = 1.5$, as:

$$P_{fe,bi} = k_{magg,bi} \cdot p_{s,bi} \cdot G_{bi} \tag{6.5}$$

Specific back-iron losses are computed considering the maximum flux density value in the back iron core and the specific FW frequency compared to the reference flux density $B^*_{fe} = 1.5$ T and frequency $f^* = 50$ Hz, respectively. For such reference values hysteresis accounts for 70 % of iron losses (hysteresis coefficient $k_h = 0.7$), while eddy currents for 30 % of iron losses (eddy current coefficient $k_{ec} = 0.3$). Thus, specific back-iron losses are calculated as:

$$p_{s,bi} = p_{s,fe} \cdot \left(\frac{\hat{B}_{bi}}{B^*_{fe}}\right)^2 \cdot \left[k_h \cdot \left(\frac{f}{f^*}\right) + k_{ec} \cdot \left(\frac{f}{f^*}\right)^2\right] \tag{6.6}$$

The back-iron weight is:

$$G_{bi} = \gamma_{fe} \cdot \pi\big(D_e - 2 \cdot h_{bi}\big) h_{bi} \cdot L_{stk} \tag{6.7}$$

Similarly, iron losses in teeth are computed considering an increase coefficient $k_{magg,t} = 2$, as:

$$P_{fe,bi} = k_{magg,t} \cdot p_{s,t} \cdot G_t \tag{6.8}$$

Specific back-iron losses are computed by (6.7) considering the maximum flux density value in the tooth $\hat{B}_t$ instead of $\hat{B}_{bi}$. Teeth weight is:

$$G_t = \gamma_{fe} \cdot Q_s \cdot h_s \cdot w_t \cdot L_{stk} \tag{6.9}$$

Fig. 6.3 shows losses versus speed waveform in the FW region. Stator Joule losses are constant, while rotor Joule losses decrease in the FW region because of the excitation current reduction. Iron losses increase quadratically with the frequency, becoming dominant during FW operations.

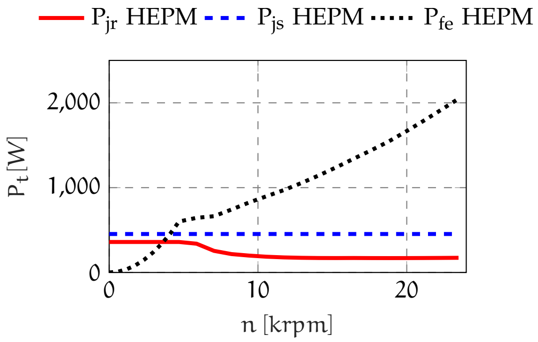

Figure 6.3: Stator and rotor losses.

6.1.3 *Thermal-fluid analysis*

Generally, knowing the thermal resistance R_{th} between two nodes and the thermal flux q that flows through one to the other, the temperature difference could be computed as follows:

$$\Delta T = R_{th} \cdot q \tag{6.10}$$

Thermal resistance evaluation depends on the nature of the heat transfer process between two nodes. It can occur by conduction, convection or radiation [46]. Considering the convective heat transfer, the thermal resistance can be computed as follows:

$$R_{th,conv} = \frac{1}{h \cdot A} \tag{6.11}$$

where h is the HTC relative to the surface of area A. This coefficient depends on the type of fluid flow occurring close the surface and on the fluid properties. The complex geometry of salient pole surfaces exhibits speed-dependent HTCs values. To gain more information about these coefficients for the HEPM motor under study, the 2-D thermal-fluid-dynamic analysis of the rotor is carried out. The 2D rotor assumption was made to focus on the convective heat transfer phenomena occurring on the rotor core surfaces, where the thermal effects of rotor end-windings are negligible. No axial air flow was considered to study the worst-case cooling scenario. No further assumptions were made on the external cooling system, since detailed stator geometry was not considered. A constant temperature of 100 °C has been set on the inner stator surface as boundary condition.

6.1.4 *Geometry, mesh and material properties*

Only one pole of the rotor is analysed through 2-D Computational Fluid Dynamic (CFD) simulations considering the proper boundary condition. The size of a generic element of the mesh is chosen equal to 0.2 mm. In the salient pole and the shaft the mesh element size is equal to 1 mm, while in the air domain it is equal to 0.1 mm. To adequately model the boundary layers next to rotor and stator walls a mesh inflation is considered (the first layer thickness is 0.002 mm, with a growth rate of 1.2 throughout 20 layers). The mesh realized has roughly 50000 elements and a detail is presented in Fig. 6.4.

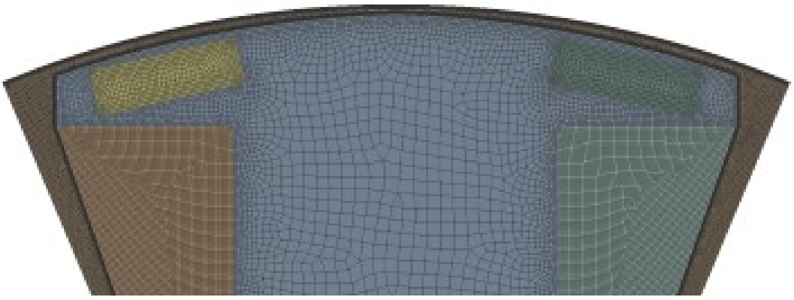

Figure 6.4: Mesh Detail.

Such a mesh is suitable for CFD computation also for high linear velocities reached. In fact, for maximum speed 22500 rpm, y+ value results to be equal to 0.35 (which also corresponds to the highest value obtained among all the simulations). Air is modeled as a fluid having temperature-dependent physical properties. Air parameters considered are: density ρ_{air}, thermal conductivity λ_{air} and dynamic viscosity μ_{air} at atmospheric pressure ($p_{ATM} = 101\,325\,Pa$). The temperature varies in the range from 100 °C to 200 °C and the specific heat c_p is equal to $1020\,\frac{kJ}{kgK}$. Equations regulating the dependence on temperature are obtained through interpolation of *Engineering Toolbox* [94] data. Thus, interpolation functions are:

$$\rho_{air} = \frac{353}{T} \tag{6.12}$$

$$\mu_{air} = -2.619 \cdot 10^{-11} T^2 + 6.206 \cdot 10^{-8} T + 2.230 \cdot 10^{-6} \tag{6.13}$$

$$\lambda_{air} = -2.625 \cdot 10^{-8} T^2 + 8.847 \cdot 10^{-5} T + 2.266 \cdot 10^{-3} \tag{6.14}$$

Since CFD temperatures are computed in Kelvin degree, also the obtained equations are valid considering absolute temperatures. Fig. 6.5a and Fig. 6.5b show *Engineering Toolbox* data and their interpolation.

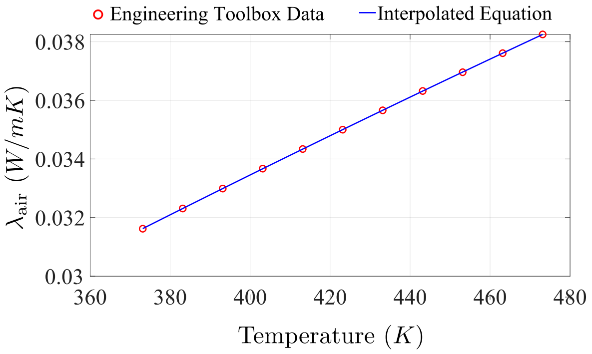

(a) Air thermal conductivity versus temperature.

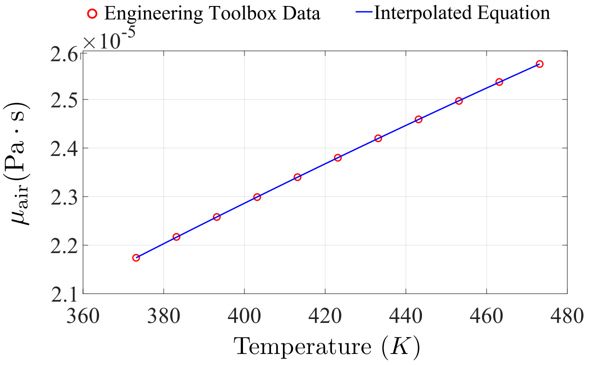

(b) Air dynamic viscosity versus temperature.

Figure 6.5: Air properties versus temperature.

Tab.13 summarizes physical properties of materials involved in the simulation. Winding properties are obtained as weighted values of copper and resin properties (considering a 70% Copper and 30% Resin re-partition). Only the thermal conductivity is set equal to the one of Resin $\left(0.3\frac{W}{m°C}\right)$. In particular, low value of thermal conductivity used for the equivalent slot allows a higher windings temperature compared to the one reached in the actual motor. This way thermal machine computation is in a safety condition with respect to the prototype. Moreover, thermal conductivity of insulated wires immersed into resin is hard to computed. In fact, it depends on the winding configuration and materials employed. H-thermal class has been chosen as upper thermal boundary for the windings insulation, i.e. a maximum absolute temperature of $T = 180\,°C$.

6.1.5 *Thermal problem modelling*

Concerning the numerical problem, periodic boundary conditions are set at the two sides of the domain. In addition, a fixed 100 °C temperature is set on the stator wall as a boundary condition. Considering the stator wall, a zero fluid velocity is set with respect to the absolute motion frame.

For the electrical machine under study, Joule losses are modelled as an energy source terms. The heat generated by winding per unit volume is computed as:

$$p = \frac{P_{jr} \cdot k_{fill}}{V_{cu,r}} = 3.23 \cdot 10^5 \frac{W}{m^3} \tag{6.15}$$

considering the maximum value of rotor Joule losses P_{jr}, even if they slightly decrease as the rotor speed increases. Nevertheless, the maximum value of rotor Joule losses is considered to compare heat exchange at different rotor speeds [36, 67]. All the radiation heat transfer phenomena are neglected.

The k-ϵ Re-Normalization Group (RNG) turbulence model is applied. The enhanced wall treatment allows to fully reproduce the fluid flow in the proximity of a wall. To reproduce the effect of rotor rotation, a frame motion source term is added to the air domain, while all the other rotor parts are considered as stationary, as proposed in [53]. That rotating speed has to be set as the of rotor speed value.

Table 13: Material properties.

Property	Iron	Steel	Windings	Magnet
$\rho\ \left(\frac{kg}{m^3}\right)$	7600	7850	5820	7700
$c_p\ \left(\frac{J}{kgK}\right)$	460	400	830	380
$\lambda\ \left(\frac{W}{m°C}\right)$	30	52	0.3	10

Fig. 6.6a and Fig. 6.6b show the temperature contour figures obtained from the thermal-fluid-dynamic simulations of the HEPM rotor at two different rotation rates. In both cases hotspots are located

close to winding surfaces, directly in contact with air. The heat concentration close to windings is related to the low efficiency of the heat transfer phenomena. In fact, the air close to windings is almost stationary.

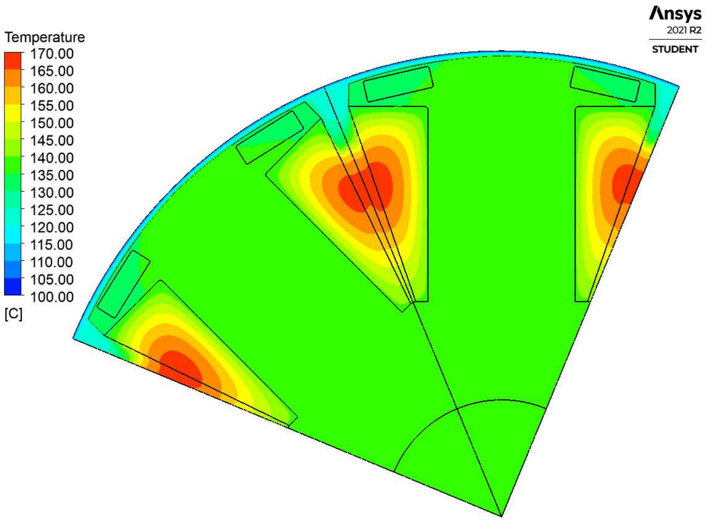

(a) Rotor speed 5000 r/min.

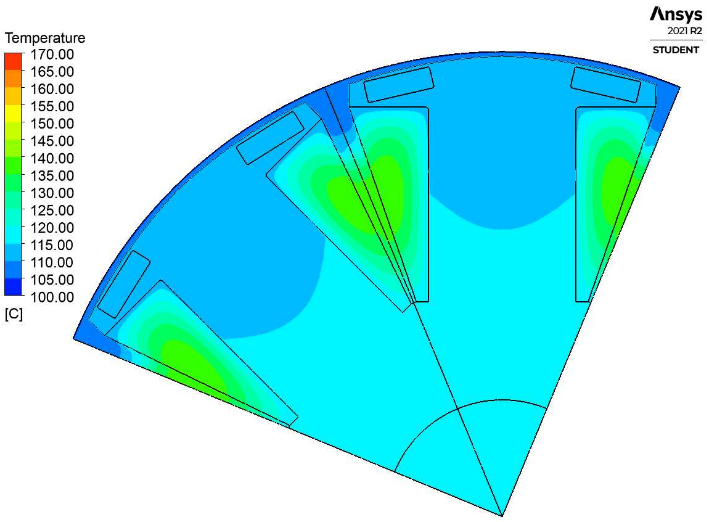

(b) Rotor speed 22500 r/min.

Figure 6.6: Temperature contour figures at different rotor speeds.

Comparing the two pictures, a general decrease of temperature can also be observed: this phenomenon is due to the difference in rotational speed. In fact, when the speed is higher (22500 r/min versus 5000 r/min) the turbulent air motion is enhanced and the relative velocity between air and rotor surfaces increases, improving the heat transfer.

Table 14: HTCs result at different rotational speed

$n\,(r/min)$	$h_{HP}\ \left(\frac{W}{m^2K}\right)$	$h_{RW}\ \left(\frac{W}{m^2K}\right)$	$h_{LW}\ \left(\frac{W}{m^2K}\right)$	$h_{SW}\ \left(\frac{W}{m^2K}\right)$
4500	155.81	88.20	37.32	136.73
9000	234.45	101.90	47.96	216.25
13500	307.47	117.43	53.95	285.09
18000	376.48	127.14	62.70	348.28
22500	442.11	125.81	73.79	407.22

Knowing the heat power emitted/absorbed q by a surface and the temperature difference between this surface and the adjacent air, the heat transfer coefficient is computed as:

$$h = \frac{q}{A \cdot |T_{surface} - T_{air,adj}|} \tag{6.16}$$

Four surfaces are considered as shown in Fig. 6.7a. Fig. 6.7a exhibits the head pole (HP) represented by the red curve and the stator wall (SW) by magenta line. The winding surface on the right (RW) side of the salient pole is figureted in green and the one on the left (LW) side with dark blue line.

As shown in Fig. 6.7b the air domain was divided into two sub volumes. The air-gap region is highlighted with light blue colour, where the air flow has high velocity, while the blue slot region is affected by slow air speed. This division has been carried out because the air proprieties, in particular the air temperature, are different from the air-gap to the air-slot. Thus, different mean temperature values have been used as reference for the two areas. Such temperatures have been used inside (6.16) to compute the HTCs of rotor head pole and stator walls. In particular, air-slot temperature is used for the computation of windings HTCs, while air-gap temperature is used for determining stator and head pole surfaces HTCs. Tab.14 summarizes the HTCs computed for such surfaces and Fig. 6.8 shows HTCs computed from five simulations at different rotor speeds.

It can be noticed that HTC values of left and right winding surfaces do not assume the same value. In particular, the right side winding exhibits higher heat transfer than the left side winding, for every rotational speed case considered. This is due to the anti-clockwise rotor rotation, which improves the right winding heat exchange. In fact, as shown in Fig. 6.9a and Fig. 6.9b, the air is pushed towards the right winding and it is pushed away from the left winding of the adjacent pole. However, the air velocity is higher toward the right winding top part, allowing higher heat exchange. Nevertheless, the convective heat exchange takes place mainly along the air gap, where speed is higher.

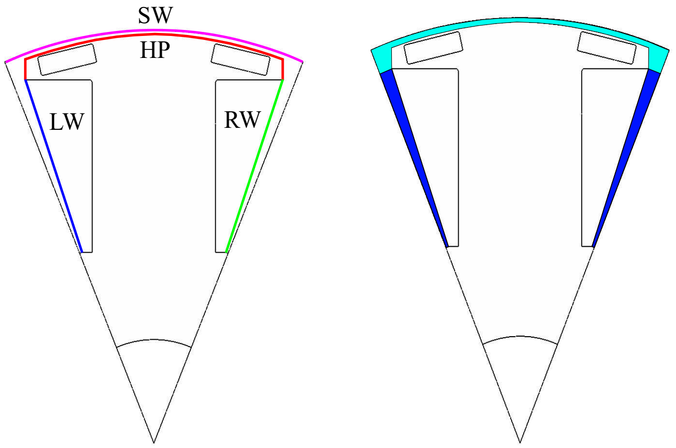

(a) HTCs surfaces computation.

(b) Air sub-regions division calculation.

Figure 6.7: HTC versus rotor speed.

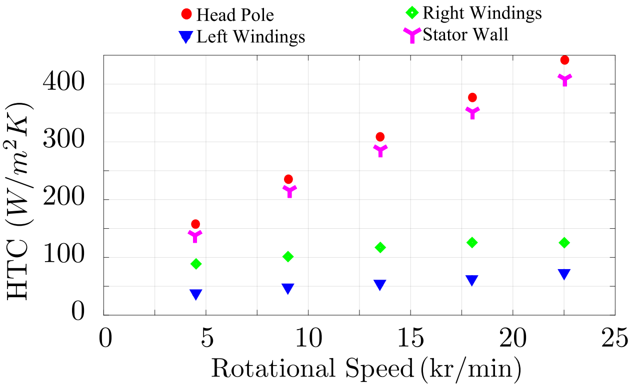

Figure 6.8: HTC versus rotor speed.

Fig. 6.10a and Fig. 6.10b show the heat flux versus per unit radial position r/R (with R maximum winding radius). For $r/R \geqslant 0.8$ the heat transfer due to convection is higher for both sides windings. In fact, the top is the only part of the winding surface where relative motion between air and walls allows heat removal. In the bottom part of the winding the air velocity is almost zero and does not allow heat exchange as shown in Fig. 6.9a and Fig. 6.9b.

As highlighted by the blue circle, streamlines near the left head pole wall sticks better to the wall at 22500 r/min than at 5000 r/min. The high rotor speed (high tangential velocity) helps in maintaining the air flux attached to the wall of leading winding. This causes an improvement in the heat transfer phenomena and consequently brings to the continuous raise of the HTC value as the rotor speed increases. On the contrary, the top part of the right head pole is affected by a sudden heat flux drop when speed reaches 22500 r/min. In fact, as highlighted by the red circle, the air flux detaches from the surface and reduces the local heat flux and, consequently, the HTC value.

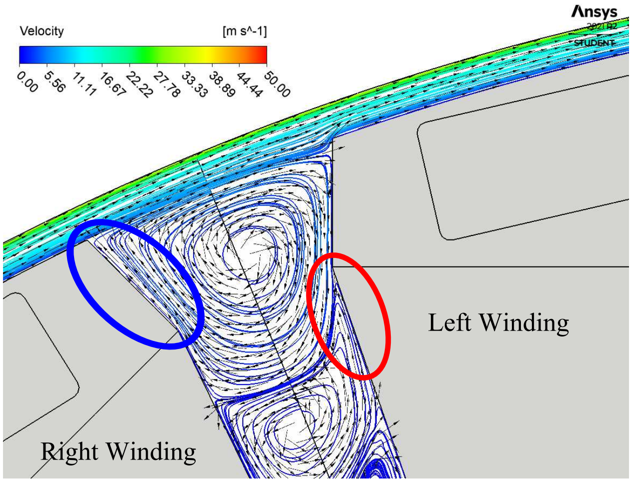

(a) Rotor speed 5000 r/min.

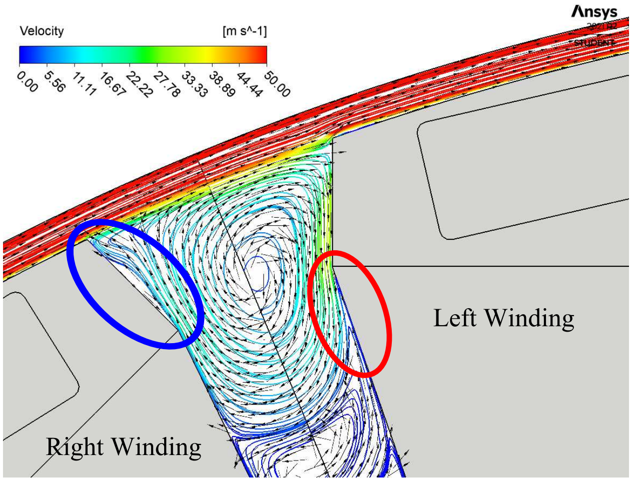

(b) Rotor speed 22500 r/min.

Figure 6.9: Relative air velocity map at different rotor speeds.

HTC values computed can be used in the thermal network [66]. The network becomes more detailed considering the dependence of the speed in HTC values without increasing the computational cost. In particular, thermal network continues to be easy and fast to compute also taking into account the fluid-dynamics air flow dependence on rotor speed. In this way the geometry can be represented with a simple thermal-fluid network also when if it is affected by air turbulent flow.

6.1.6 *Mechanical test*

The mechanical study shows that the fluid rotor geometry has a very low stress in the pole body but with high stress around the PM hole. Structural integrity is kept also considering the rotor winding contact

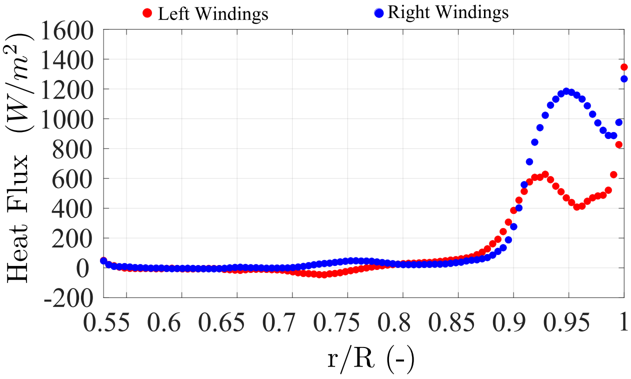

(a) Rotor speed 5000 r/min.

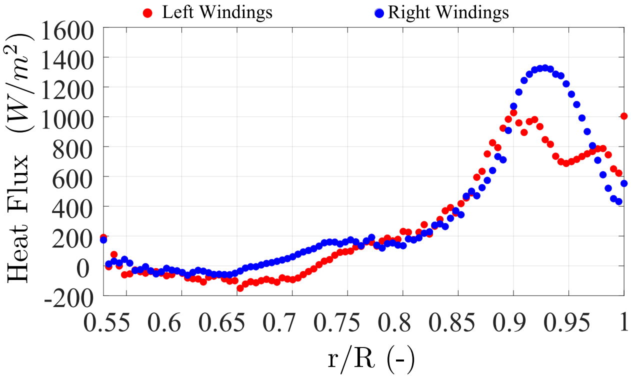

(b) Rotor speed 22500 r/min.

Figure 6.10: Heat flux versus per unit radial distance at different rotor speeds.

with the pole body and pole shoe. The maximum Von Mises stress are closer to 200 MPa.

6.1.7 *EESM analysis*

The EESM has lower mechanical issues than HEPM motor. This is due to the absence of the PM inside the rotor geometry. Just a small scale, low speed, example has been reported for both traditional and fluid rotor structures. The fluid structure will be explained in Chapter 8. The mechanical and fluid dynamic analysis has been carried out in order to understand limits and advantage of both rotor configurations analyzed.

The mechanical study shows that the fluid rotor geometry has a very low stress in the pole shaping due to the fluid geometry. The traditional salient pole has stress 4-5 times higher than the fluid rotor. The magnitude values of the simulation are low due to the fact that the geometry simulated has prototype laboratory size and can not reach the speed higher than 4500 r/min.

Finally, the fluid dynamic simulation has been computed under the turbulent model k-ϵ RNG. Both models have a rotational speed

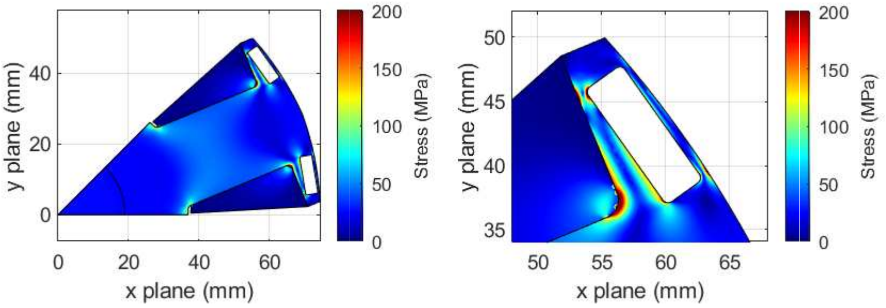

Figure 6.11: PMaExc Von Mises mechanical stress.

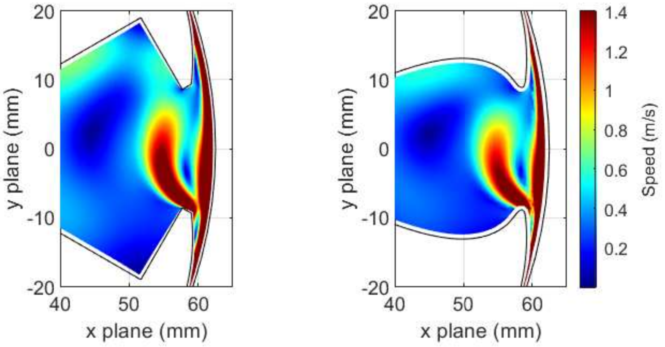

Figure 6.12: Airgap fluid dynamic comparison.

of 4500 rpm. The variation of the geometry does not influence the air flow between two adjacent poles. Under the fluid dynamic point of view, both geometries are equivalent, yielding the same heat transfer coefficients with no difference under the thermal point of view.

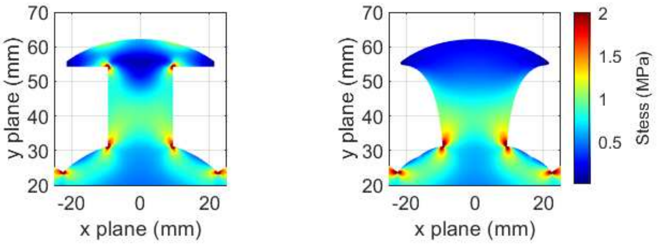

Figure 6.13: EESM traditional and fluid mechanical stress comparison.

6.2 DISCUSSION

This part focuses on the thermal and fluid-dynamic analysis of the turbulent convective heat transfer between air and rotor surfaces of a HEPM motor at different rotational regimes. The numerical simulations were performed using the k-ϵ RNG turbulence model considering only one pole of the real rotor 2-D geometry. Periodic boundary conditions were applied at the two sides of the domain and air properties were set as functions of temperature. Through CFD analysis the air turbulent flow has been studied and HTCs computed at different rotational speed. Such values can be employed in an equivalent thermal network. The mechanical issues must be treated but are under safety condition. From the results and discussions, the following conclusions can be drawn. First of all, the temperature hotspots affect the surface of both windings and they decrease as the rotational velocity increases. This means that HTCs at the windings walls generally increase as the rotational velocity increases because of the raise in turbulence and relative velocities between windings walls and air. At the same time, the HTCs of the two winding walls are not equal to each other, highlighting the non-symmetry of the problem. In particular, the trailing windings present higher values for the convective HTCs than those of the leading windings. The majority of the heat transfer through convection mechanism occurs in the upper part of both windings, close to the head of the pole. Finally, a slight decrease of the HTC occurs at the trailing windings for high velocity values. HEPM motors require both careful mechanical and thermal analysis as they can be dangerous for PMs buried in the rotor. EESM has less mechanical problem than HEPM motor and also the thermal problem can be different.

This is the end of the analysis part of the process and the start of the design part.

Part II

ELECTRICALLY EXCITED AND HYBRID EXCITED PERMANENT MAGNET: DESIGN

This part focus on the analytical sizing techniques for HEPM motor and EESM, FE and test bench validation. The initial part involves calculating parameters based on the operating point. A novel sizing approach is presented for the MTPA and FW working conditions. Various machine parameters are determined based on the specific operational region. Subsequently, an alternative sizing method is introduced, providing an approximate initial configuration for the optimal EESM and HEPM motor, reducing the spatial harmonic component. At the end, prototype test bench validation are carried out to validate the design and FE analysis.

7

HEPM DESIGN: MTPA AND FW REQUIREMENTS

This Chapter presents an analytical sizing procedure that take into account of MTPA and FW region. The machines are sized in a way to fulfill current and voltage limits imposed by thermal and dielectric electric fields, while considering whether the machine must be optimized to operate in MTPA or if it requires an extended FW region. Starting from these equations, machine parameters can be determined, allowing for the design of either an EESM or an HEPM motor to obtain these values and optimize the system.

7.1 DESIGN OF ELECTRIC MOTORS FOR GIVEN MTPA REQUIREMENTS

In PMSMs the optimal operating condition in the constant torque region is obtained following the MTPA trajectory. Its focus is to minimize the copper losses in the stator windings while providing the required torque. In HEPM motors, the excitation circuit has to be taken into account in order to provide a complete analysis [29]. Hence, the MTPA trajectory is defined as the set of optimal operating points $P_{opt} = (i_{d,opt}, i_{q,opt}, i_{e,opt})$ that minimize the overall copper losses of both stator and rotor windings. In particular, referring to the rotating reference frame, the copper losses can be computed as:

$$P_j(I_d, I_q, I_e) = \frac{3}{2} R_s (I_d^2 + I_q^2) + R_e \, I_e^2 \tag{7.1}$$

where R_e is the resistance of the excitation winding and R_s of the stator winding.

In the MTPA operating condition, the motor satisfies equation (4.1), i.e. it exhibits the desired output torque T^*. For this reason, the operating point P_{opt} is the solution of the following constrained optimization problem:

$$\min_{I_d, I_q, I_e} P_j(I_d, I_q, I_e) \quad \text{subject to} \quad g(I_d, I_q, I_e) = T - T^* = 0 \tag{7.2}$$

The method of Lagrange multipliers can be used to compute its solutions since the optimization problem has only one equality constraint.

Equation (4.1) is rewritten as:

$$T = \underbrace{\left(\frac{3}{2} p \Lambda_{PM}\right)}_{A} I_q + \underbrace{\left(\frac{3}{2} p M_e\right)}_{B} I_e \, I_q + \underbrace{\left[\frac{3}{2} p \left(L_d - L_q\right)\right]}_{C} I_d \, I_q \tag{7.3}$$

Then the Lagrangian function can be defined as:

$$\begin{aligned} \mathcal{L}(I_d, I_q, I_e, \lambda) &= P_j(I_d, I_q, I_e) + \lambda \cdot g(I_d, I_q, I_e) = \\ &= \frac{3}{2} R_s (I_d^2 + I_q^2) + R_e\, I_e^2 + \lambda \left[(A + B I_e + C I_d) I_q - T^*\right] \end{aligned} \tag{7.4}$$

To find the stationary points of $\mathcal{L}$, i.e. the maximum and minimum of $P_j(I_d, I_q, I_e)$, its partial derivative should be equal to zero:

$$\begin{cases} \dfrac{\partial \mathcal{L}}{\partial I_d} = 0 & \Rightarrow 3 R_s I_d + \lambda C I_q = 0 \\ \dfrac{\partial \mathcal{L}}{\partial I_q} = 0 & \Rightarrow 3 R_s I_q + \lambda (A + B I_e + C I_d) = 0 \\ \dfrac{\partial \mathcal{L}}{\partial I_e} = 0 & \Rightarrow 2 R_e I_e + \lambda B I_q = 0 \\ \dfrac{\partial \mathcal{L}}{\partial \lambda} = 0 & \Rightarrow (A + B I_e + C I_d) I_q - T^* = 0 \end{cases} \tag{7.5}$$

that yield the following variable dependencies:

$$\begin{cases} \lambda = -\dfrac{2\, I_e\, R_e}{B\, I_q} \\ I_d = \dfrac{2\, C\, I_e}{3\, B\, r_R} \\ I_q^2 = \dfrac{2(A + B\, I_e + C\, I_d)}{3 r_R C I_e} \\ I_q = \dfrac{t}{A + B\, I_e + C\, I_d}. \end{cases} \tag{7.6}$$

Solving the system lead to the following equation:

$$\begin{aligned} I_e \left[A + \left(B + \frac{2}{3} \frac{1}{r_R} \frac{C^2}{B}\right) I_e\right]^3 - \frac{3}{2} \frac{r_R}{1}\, B (T^*)^2 = 0 \\ I_e (a + b I_e)^3 - c = 0 \end{aligned} \tag{7.7}$$

that can be rewritten in polynomial form in order to highlight its coefficient:

$$\left(b^3\right) I_e^4 + \left(3ab^2\right) I_e^3 + \left(3a^2 b\right) I_e^2 + \left(a^3\right) I_e + (-c) = 0 \tag{7.8}$$

The rotor current I_e value can be computed just numerically.
If the PM flux component Λ_{PM} is equal to zero, there are no magnets, a closed formulation can be calculated.

By the way, EESM has I_e that minimize the joule losses equal to:

$$I_e = \sqrt[4]{\left(\frac{B\, r_R\, t^2}{(B + D)^3}\right)} \tag{7.9}$$

where $D = \dfrac{2\,C^2}{3\,B\,r_R}$ and $r_R = R_s/R_e$. Consequently the I_d and I_q direct and quadrature stator currents are:

$$\begin{aligned} I_d &= \frac{2\,C\left(\dfrac{3\,B\,r_R\,t^2}{2\,(B+D)^3}\right)^{1/4}}{3\,B\,r_R} \\ I_q &= \frac{2^{1/4}\,3^{3/4}\,B\,r_R\,t}{(3\,r_R\,B^2+2\,C^2)\left(\dfrac{B\,r_R\,t^2}{(B+D)^3}\right)^{1/4}} \end{aligned} \tag{7.10}$$

Starting from these considerations, analytical motor design is computed.

During the motor design, many constraints must be satisfied. Typically the bus voltage V_{dc}, the inverter current I_N, the DC/DC converter current $I_{e,N}$, the operating speed ω_N, the torque required T_N are imposed. Moreover, designer have to choose the pole pairs p, the saliency ratio ξ, the direct inductance L_d, the mutual inductance between rotor and stator M_e and the stator and rotor resistance R_s and R_e. The proposed design procedure yields the configuration that at the nominal point has the lowest joule losses according to the constraints imposed by the application.

7.1.1 *Design Procedure*

At the beginning of the design process the limits are imposed as:

- the nominal motor voltage $V_N = V_{dc}/\sqrt(3)$,
- the nominal stator and rotor motor currents I_N and $I_{e,N}$,
- the torque required T_N,
- the operating electrical speed $\omega_m^e = p\omega_N$.

Another designer choice is the pole pair p and the saliency ratio ξ. Adopting this assumptions, there is just one combination of the parameter M_e, L_d, and r_R that can satisfy the minimum joule losses at the rated point.

Machine EESM parameters are computed solving the system:

$$\begin{cases} I_N^2 = I_d^2 + I_q^2 \\ I_{e,N}^2 = I_e^2 \\ V_N^2 = \omega_m^{e^2}\left[(M_eI_e + L_dI_d)^2 + \left(\xi L_dI_q\right)^2\right]^2 \end{cases} \tag{7.11}$$

the currents I_e, I_d and I_q are computed in (7.9) and (7.10) for EESM while just numerically for HEPM motor. I_e, I_d and I_q contain the

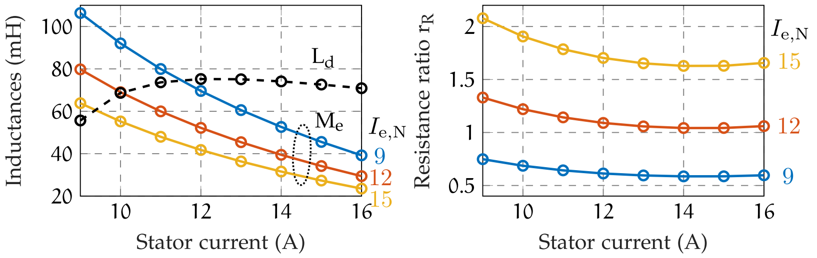

Figure 7.1: Mutual, direct inductance and resistance ratio for different $I_{e,N}$ and $\xi = 0.5$.

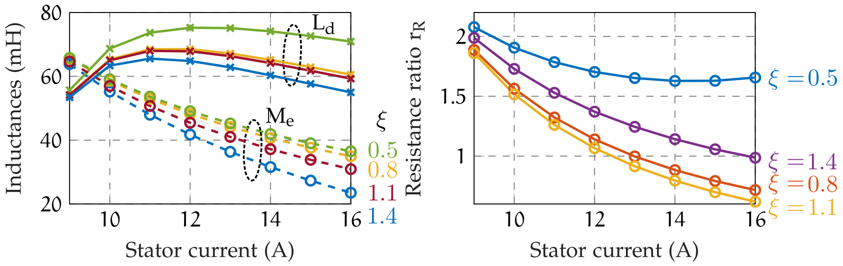

Figure 7.2: Mutual, direct inductance and resistance ratio for different ξ and $I_{e,N} = 15\,A$.

parameters unknown M_e, L_d, and r_R. For both machines, the system (7.11) is highly nonlinear and must be solved numerically.
The equation system complexity increases for the HEPM motor being I_e possible to computed just numerically.

A EESM design example is carried out adopting the following parameter: $V_N = 173\,V$, $I_N = 9$ - $16A$ and $I_{e,N} = 9$ - $16A$, $T_N = 40\,N \cdot m$, $p = 3$, $\xi = 0.5$ - 1.4 and $\omega_m^e = 2\pi\, p\, 4500/60$.

The system (7.11) is solved for different combination of saliency ratio ξ, stator and rotor currents limits I_N and $I_{e,N}$. Mutual inductance M_e, direct inductance L_d and resistance ratio r_R are reported.

Fig. 7.1 shows the variation of the mutual inductance M_e, direct inductance L_d and resistance ratio r_R imposing a constant saliency ratio $\xi = 0.5$ but varying the nominal excitation current from $I_{e,N} = 9, 12, 15\,A$. These values are reported for different values of stator current I_N.

In Fig. 7.1b the resistance ratio r_R is reported. It shown that the ratio has a minimum for a each rotor current I_e for a prescribed stator current I_N and this ratio decrease while the $I_{e,N}$ increase.

Another test has been done in Fig. 7.2 assuming a constant rotor current $I_{e,N} = 15\,A$ and changing the saliency ration $\xi = 0.5, 0.8, 1.1, 1.4$. It possible to appreciate in Fig. 7.2a L_d are lower increasing the ξ, while the mutual has a higher value for ξ values close to 1.

Fig. 7.2b shows the ratio r_R that has lower value for ξ values close to 1.

Lastly, Fig. 7.3 shows how the stator current component changes according to a variation of $I_{e,N}$ and ξ. In Fig. 7.3a it is possible to see

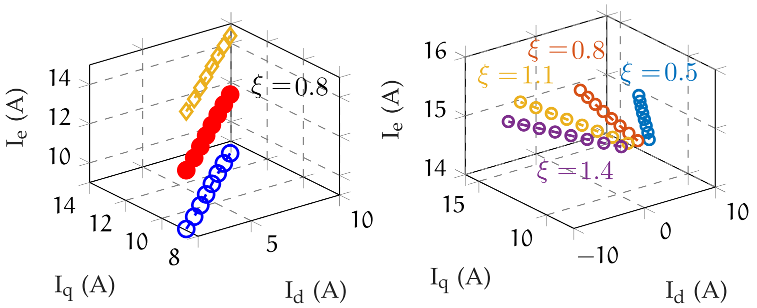

Figure 7.3: Stator current angle variation with parameter variation.

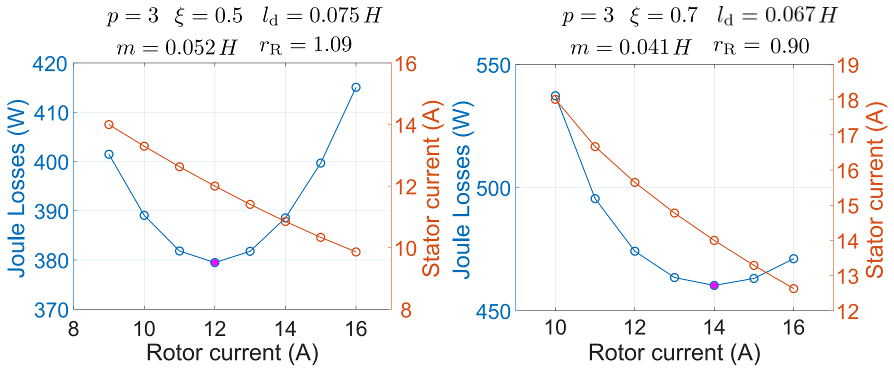

Figure 7.4: Minimum Losses validation for different saliency ratio $\xi = 0.5$ and $\xi = 0.7$ at the torque $T_N = 40\ \mathrm{N \cdot m}$ the voltage $V_N = 173\,\mathrm{V}$ and the electrical speed $\omega_m^e = 2\pi\, p\, 4500/60$.

that the ratio I_q/I_d is constant for different $I_{e,N}$ while Fig. 7.3b reports the variation of the angle according to the variation of ξ.

To validate the design process, the losses computation is carried out after having selected two motor design. In this case the process is different. The machine parameter are selected as: the pole pairs p, the mutual inductance M_e, direct inductance L_d, resistance ratio r_R and the saliency ratio ξ, solving (7.11). Then a losses computation considering different values of $I_{e,N}$ an I_N is done, in order to continue to satisfy the torque $T_N = 40\ \mathrm{N \cdot m}$, the voltage $V_N = 173\,\mathrm{V}$ and the electrical speed $\omega_m^e = 2\pi\, p\, 4500/60$.
At the end, it is necessary verify which values couple yields the minimum value. This check is reported in Fig. 7.4, where Fig. 7.4a has been done considering a saliency ration $\xi = 0.5$ while Fig. 7.4b $\xi = 0.7$. Both drawings exhibit a magenta dot that represents the losses computed assumed from the initial design process. Other points explore different combinations of stator and rotor currents to continue to delivered the same torque and rotate at the same speed.

The light blue lines of Fig. 7.4 show that the minimum losses are exactly reached for currents combination that has been used as constraints to design the machine. Indeed other combinations using low values of $I_{e,N}$ and higher of I_N or vice-versa yields higher joule losses. These results show that it is possible to obtain a machine that minimize losses starting from voltage and current constraints.

7.2 DESIGN OF ELECTRIC MOTORS FOR GIVEN FW REQUIREMENTS

This part involves calculating parameters based on the FW operation. Various machine parameters are determined based on the specific operational region. Subsequently, an similar EESM sizing method is reported, providing an approximate initial configuration for the optimal HEPM motors.

Analog procedure to EESM can be used starting from the FW requirements. Synchronous motor type and inverter Volt-Ampere ratings can be selected to meet a desired torque versus speed characteristic. Alternatively, the motor drive design can be optimized for a given nominal and FW requirement as proposed in [38]. This allows both the energy losses and the constraints on the power converter to be reduced. A proper combination of machine parameters of rotor PM and excitation flux linkage can be derived, in particular d-q axis inductances. The inverter current rating can be obtained, as well.

For the sake of generality, it is convenient to normalize all motor data with respect to the base quantities defined in the following. Normalized data are denoted by means of small letters. This permits to easily extend the considerations to motors of any power. Moreover, interesting comparisons can be carried out among different motor types, requiring fixed FW performances.

Torque, speed, and voltage under full load at the maximum speed of the constant torque region have been defined as base torque T_b, base angular frequency ω_N and base voltage V_N, respectively. The base values of the motor parameters and current are retrieved by using the power balance:

$$T_b \frac{\omega_N}{p} = \frac{3}{2} V_N I_b. \tag{7.12}$$

Then, the base current, inductance and flux linkage are computed as:

$$I_b = \frac{2T_b\omega_N}{3pV_N}, \qquad L_b = \frac{3pV_N^2}{2T_b\omega_N^2}, \qquad \Lambda_b = L_b I_b = \frac{V_N}{\omega_N}. \tag{7.13}$$

All the normalised motor data are resumed in Table 15.

Table 15: Normalised quantities.

P.U. quantities

Torque	$t = T/T_b$
Electrical speed	$\omega = \omega_m^e/\omega_N$
Phase current	$i = I/I_b$
Rotor flux linkage	$\lambda_R = (\Lambda_{PM} + \Lambda_e)/\Lambda_b$
Phase voltage	$v = V/V_N$
Synchronous inductance	$l = L/L_b$

The flux linkage, the d-q axis inductances and the inverter Volt-Ampere ratings are selected such that the drive exhibits the desired nominal torque T_b at the desired base speed ω_N. Moreover, the maximum p.u. speed and p.u. torque achievable in FW operating condition are defined, namely ω_{FW} and t_{FW}. They represent the maximum FW speed and torque for which the motor is designed, respectively. The motor has to guarantee all requirements in its operating conditions.

The design procedure works as follows:

1. Set the desired values of maximum FW speed ω_{FW} and torque t_{FW};
2. A suitable couple of rotor flux linkage λ_R and saliency ratio ξ must be selected;
3. In order to fulfill the specification at nominal point of base torque $t_N = 1$, voltage $v_N = 1$, and speed $\omega_N = 1$, only one value of direct inductance l_d and current i_N can assure the desired performance once λ_R and ξ are set;
4. Finally, the defined p.u. parameters can be reported to the absolute magnitude value and then the machine can be designed. These values must be realized with a proper motor design by taking into account practical limitation.

An example is reported in Fig. 7.5, considering a desired FW speed $\omega_{FW} = 4$ p.u. The requirement on FW torque t_{FW} at speed $\omega_{FW} = 4$ p.u. is 0.28 p.u. If $\xi = 2$ is defined, λ_R has to be chosen equal to 0.65, accordingly to the green line in Fig. 7.5. Once values of λ_R and ξ are selected, the values of l_d and i_N can be grabbed by exploiting Fig. 7.6 and 7.7. With the selected values, $l_d = 0.4$ p.u. and $i_N = 1.3$ p.u. It is worth noting that Fig. 7.5 shows that the FW torque t_{FW} does not exist at a desired speed for all couple of the rotor flux linkage λ_R and saliency ratio ξ. Moreover, there is only one peak for each saliency ratio ξ.

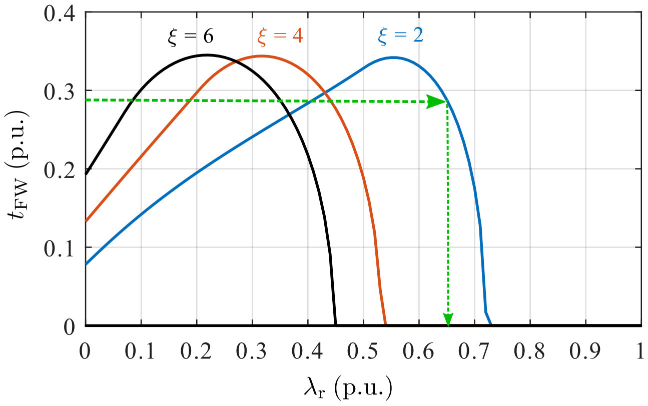

Figure 7.5: FW torque as a function of the saliency ratio ξ, with a FW speed of 4 p.u. [72].

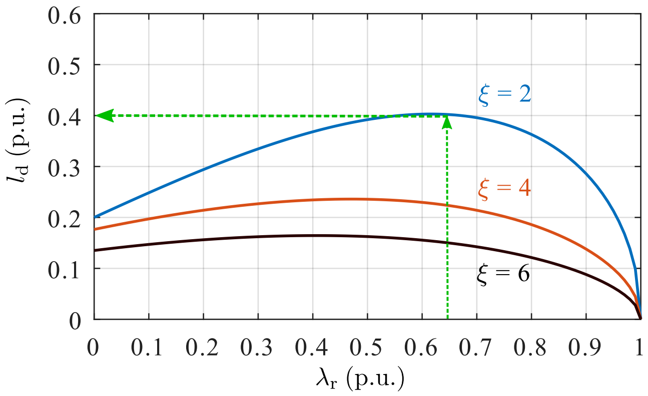

Figure 7.6: Normalized inductance as a function of the saliency ratio ξ [72].

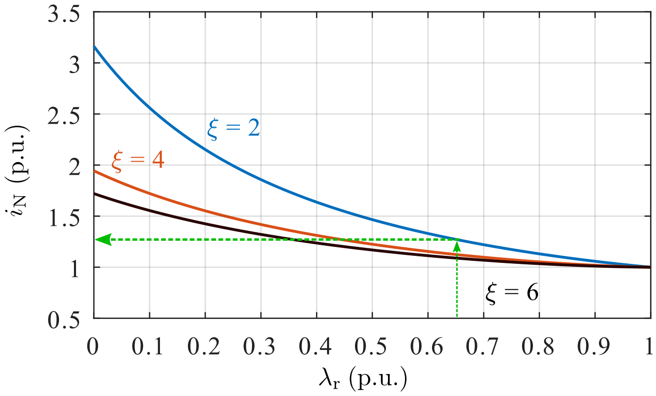

Figure 7.7: Normalized current as a function of the saliency ratio ξ [72].

7.2.1 *PM Motors*

In PM motors, the rotor flux linkage λ_R is equal to permanent magnet flux linkage λ_{PM} and it can change in the range between 0 and 1. Comparing Fig. 7.5–7.7, the maximum torque occurs with $\lambda_{PM} = l_d i_N$, or when the voltage limit ellipse center is exactly placed on the current limit circle. The corresponding maximum power is approximately equal to $\sqrt{2}$ p.u., i.e., the theoretical value when $\omega_{FW} = \infty$. A wide FW speed range can also be obtained with a lower ξ, provided that high inductances or additional external inductances are used. Moreover, comparing the FW torque in Fig. 7.5 with the current values in Fig. 7.7, it is always preferable to design synchronous motors with $\lambda_R > l_d\, i_N$ to minimize the losses. As far as joule losses are concerned, PM motors should be preferred rather than REL motors. Other examples of IPM design are reported in [14].

In case of SPM motors, the problem can be solved analytically, namely, l_d and i_N can be computed in closed form. This kind of motors have been studied in [15, 51, 57, 80]. An SPM motor is characterized by a unitary saliency ratio ξ. In addition, it is worth reminding that the MTPA locus corresponds to a current angle $\alpha_i^e = 90$ degrees. By fixing $t_N = 1$ p.u., $v_N = 1$ p.u., $\omega_N = 1$ p.u., and $\alpha_i^e = 90$ degrees, the motor inductance and the drive current result as [72]:

$$l_d = l_{qq} = \lambda_{PM}\sqrt{1-\lambda_{PM}^2}, \qquad i_N = \frac{1}{\lambda_{PM}}. \tag{7.14}$$

Then, the maximum FW speed can be evaluated as:

$$\omega_{max} = \frac{1}{\lambda_{PM} - \sqrt{1-\lambda_{PM}^2}}. \tag{7.15}$$

All speeds ω_{FW} can be reached, even if high values of current or inductances may be required for the highest speed. Since high inductances are not obtained with an SPM motor configuration, a wide FW speed range requires the use of external inductances.

7.2.2 *Pure Reluctance Motor*

In REL motors, the rotor flux linkage λ_R is zero. Thus, the MTPA angle is $\alpha_i^e = 135$ degrees (with the adopted convention $l_q > l_d$). The normalized values of the dq-axis inductances and drive current can be expressed analytically as a function of the motor saliency ratio ξ as follow:

$$l_d = \frac{\xi - 1}{\xi^2 + 1} \qquad i_N = \frac{\sqrt{2(\xi^2+1)}}{\xi - 1} \tag{7.16}$$

which is always greater than $\sqrt{2}$.

As regards the FW performance, the torque is always greater than zero at any speed ω_{FW}[1, 70, 98]. However, both the maximum torque and power decrease with ω_{FW}, while for an IPM motor the maximum power can be kept constant, close to $\sqrt{2}$.

7.2.3 *Motor with Rotor Excitation Windings*

Power generation and traction systems use motors with excitation windings. In these machines, the rotor flux linkage Λ_R is given by the sum of PM λ_{PM} and excitation λ_e flux linkages. The control of excitation current gives an additional degree of freedom that can improve the motor performance at high speeds. The formulation proposed in [67]:

$$\lambda_R^* = \frac{\xi(\omega_{FW}\ l_d\ i_N)^2 + \nu_N^2}{\omega_{FW}\sqrt{(\omega_{FW}\ \xi\ l_d\ i_N\ )^2 + \nu_N^2}} \tag{7.17}$$

computes the rotor flux linkage λ_R^* that maximizes the delivered motor torque at each motor speed. The control strategy is valid if $\lambda_R^* < \lambda_R$. In order to keep the power constant, its value increases as the motor speed decreases. However, to guarantee the nominal motor behavior, the actual rotor flux linkage λ_R must be limited to its base point value. Fig. 7.8 shows an example of the rotor flux linkage trend as a function of motor speed with a rotor flux linkage at base point of λ_R = 0.85 p.u. The rotor flux linkage is constant and equal to its base value for motor speed smaller than ω_{th}. For higher speed, the excitation flux linkage λ_e decreases to assure a total rotor flux linkage equal to λ_R^*. The speed ω_{th} is the threshold speed at which excitation must decreases. It is worth noting that ω_{th} is greater than unity indeed stator currents are already flux weakening the machine when the excitation flux linkage λ_e start decreasing. During that FW operations, the rotor flux λ_R and the corresponding stator current are regulated so as to achieve a torque as high as possible according to that speed ω_{FW}. For different values of λ_R, ξ, l_d, i_N and ν_N, it is possible to verify that the reduction of rotor flux is convenient only if $\lambda_R > l_d i_d$ as described in [18, 67].

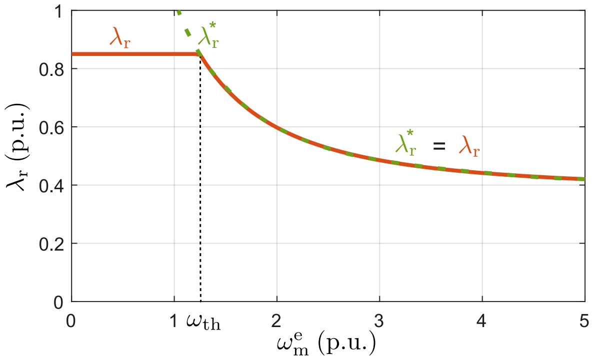

Figure 7.8: Rotor flux linkages as a function of various electrical speed.

Similarly to Fig. 7.5, Fig. 7.9 shows the FW torque at $\omega_{FW} = 4$ p.u. for different values of λ_R in a HEPM motor, considering the strategy of rotor flux linkage reduction as in (7.17). The maximum delivered torque by the machine at speed $\omega_{FW} = 4$ p.u. is represented as a function of the rotor flux linkage at base point that changes from 0 to 1 p.u. Motor with an excited rotor allows for operating at high speed, e.g., $\omega_{\mathrm{FW}} = 4$ p.u., even if the base rotor flux linkage is high as in the aforementioned example. This is a important difference with respect to classical motor configuration where a trade-off between rotor flux linkage magnitude and maximum achievable speed must be found (see Fig. 7.5). This difference allows for reducing the base motor current and, in turn, the motor losses.

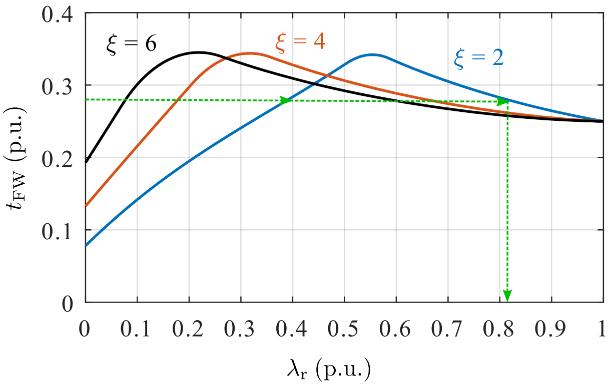

Figure 7.9: FW torque as a function of excitation control for a FW speed of 4 p.u. [67].

The motor design procedure is the same already described in Section 7.2. The ratio between λ_e and λ_{PM} must be defined and it can be chosen according to the machine application. The described strategy can be applied in HEPM and EESM configurations. It was compared to conventional IPM motors in terms of torque, speed capabilities and efficiency in [33, 36, 52, 84].

7.3 DISCUSSION

This chapter presents an analytical sizing procedure tailored to achieve MTPA and FW ranges in motor design. The aim is to size machines in such a way that the current and voltage constraints imposed by the thermal and dielectric electric fields are met. The sizing process depends on the decision whether the machine should be optimised for MTPA operation or whether an extended FW range is required.

The equations presented in this chapter can be used to determine essential machine parameters. These parameters allow the design of both an EESM or an HEPM motor. By optimising the motor configuration and design to these values, the overall system performance can be improved.

This analytical approach provides a systematic way to tailor motor designs for specific operating characteristics, striking a balance between efficiency, torque and the flexibility to operate over a wide range of conditions, ultimately contributing to improved motor performance and system efficiency.

The effective sizing of both the EESM motor and the HEPM motor will now be presented.

8

EESM SIZING: SIZING BY MEANS OF MAGNETIC NETWORK

This Chapter reports the analytical design. A detailed explanation of the magnetic network used and the rotor configuration is given. The aim is to provide a step-by-step procedure to obtain a rough size of the ESM machine. EESM rotor design is crucial for achieving high performance and efficiency [42]. A proper approach to achieve optimal pole shaping in EESMs is necessary. Traditional methods for pole shaping in EESMs focus on electromagnetic considerations, aiming to maximize the flux density while minimizing the harmonic content. To do that, analytical magnetic network for EESM design will be presented Fig. 8.1, along with the corresponding reluctance values that vary according to the pole shape is used. The pole shapes follow sinusoidal component shapes, considering a 1^{st}, 3^{rd}, 5^{th}, and 7^{th} order harmonics.

The validation of the analytical model is reported to validate the procedure. A parametric computation will be carried out to obtain a Pareto front for the selection of better solutions. The design wellness will be evaluated considering the low order harmonic and the maximum values of no-load flux density. The results presented for a described geometry considering shaping with two variable changes (1^{st} and 3^{rd} harmonic shaping) and with four variables (1^{st}, 3^{rd}, 5^{th}, and 7^{th} harmonic shaping).

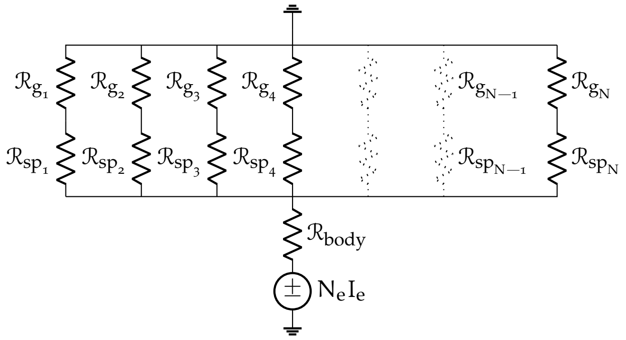

Figure 8.1: EESM model configuration and magnetic circuit.

The aim of the shaping is to minimize losses, cogging and ripple effects. It is important to ensure that both the stator and rotor magnetic potentials are as sinusoidal as possible. To achieve this, the rotor pole shaping has been designed to minimize the harmonic distortion (HD), with a particular emphasis on the 3^{rd}, 5^{th}, and 7^{th} harmonics.

One example of EESM is reported in Fig. 8.2a and Fig. 8.2b. In Fig. 8.2a the dashed light blue line shows the pole shaping calcu-

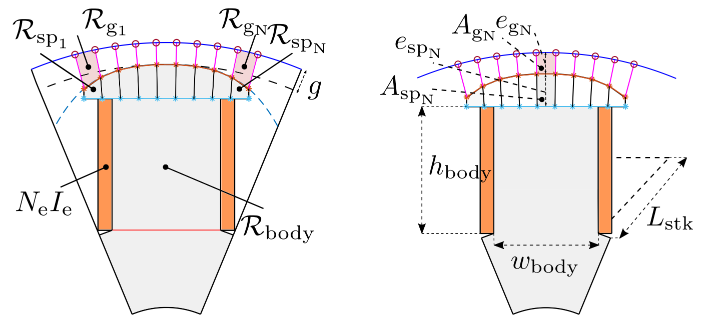

(a) EESM rotor reluctance division.

(b) EESM rotor reluctance division.

Figure 8.2: EESM sketch.

lated adopting combination of different harmonic while the dashed black line the original shape without any addition on harmonics. In a mathematical approach this shape can be described by a function f(x) defined as:

$$f(x) = \sum_{i=1,3,5,7} A_i \cos(p\nu_i(\theta + \phi_i)) \tag{8.1}$$

This function is used to models the pole shaping in order to minimizes the harmonic content while increasing the fundamental component. Specifically, changing the parameters amplitude A_i and phase shift ϕ_i, with $i = 1, 3, 5, 7$, different geometries are carried out with the aim of optimizing the rotor design. The magneto motive force on the stator/rotor exhibits odd harmonics content, for this reason symmetric adds waves have been used to shaping the pole. Moreover due to this hypotheses just two phase shift are admitted: 0 and π. In this way, the phase shift can be considered adopting coefficient lower than zero compacting (8.1) into:

$$f(x) = \sum_{i=1,3,5,7} A_i \cos(p\nu_i\theta) \tag{8.2}$$

where the coefficients A_i can be negative. A graphical representation is reported in Fig. 8.3, Fig. 8.3a shows and example of harmonic summation with positive coefficients, while Fig. 8.3b with negative coefficients. In blue is plotted the 1^{st} harmonic, in red the 3^{rd}, in yellow the 5^{th}, in violet the 7^{th} and in black the sum of the various components. It is worth noting that Fig. 8.3 exhibits very different global shapes switching the coefficients from positive to negative.

In order to properly study influence of this function on the airgap rotor shape, both analytical and FE analysis are be carried out. The FE analysis is time-computationally expensive, so the analytical method is preferable used for the parametric computation study. Of course the analytical model requires a magnetic network that takes into account the variation of the rotor shape and that have an accuracy close to the FE analysis.

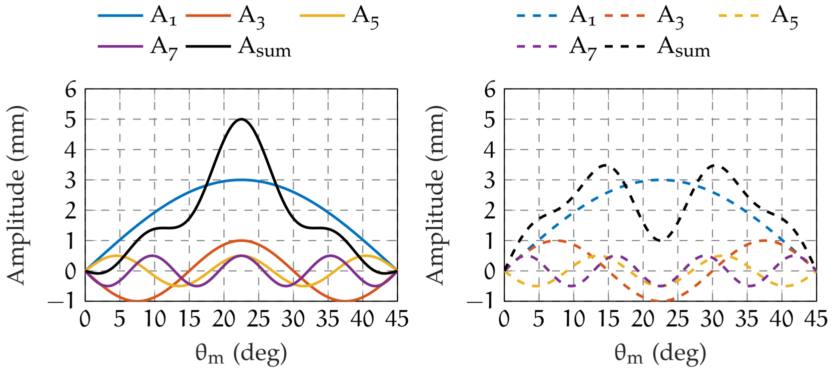

(a) Pole shape with positive coefficients. (b) Pole shape with negative coefficients.

Figure 8.3: Harmonic shape addiction.

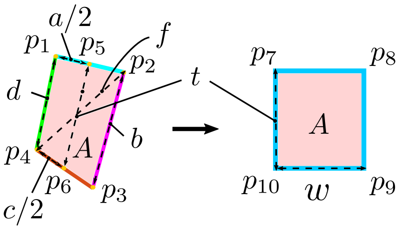

Figure 8.4: EESM reluctance surface calculation.

The complete magnetic network is shown in Fig. 8.1, and it is supplied by $N_e I_e$ ampere turns that provide an iron path composed of the pole salient body $\mathcal{R}_{body}$ and the polar shoe subdivision $\mathcal{R}_{sp_k}$, as well as an air path composed of an airgap subdivision $\mathcal{R}_{g_k}$. The corresponding reluctance have been reported also in Fig. 8.2a. Fig. 8.2a shows the magnetic reluctance on the rotor, which is composed by $k = N$ steps corresponding to the polar shoe and airgap subdivision. The polar shoe and airgap divisions have different lengths and surfaces depending on the geometric position θ. To perform analytical calculations, each reluctance must be represented by an equivalent

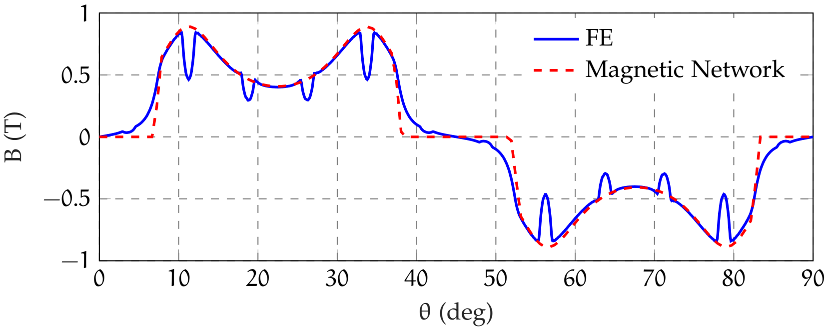

Figure 8.5: Pole shape with positive coefficients.

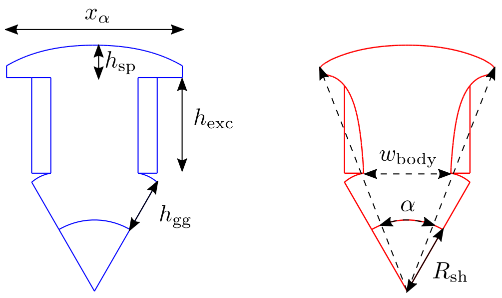

Traditional Fluid

Figure 8.6: Traditional vs fluid pole shaping salient pole.

block volume that takes into account of the particulate shape of the subdivision. Fig. 8.4 illustrates how an irregular airgap or pole shoe surface is transformed into a rectangular surface with an equivalent area and vertical rectangular edge $t(k)$ equal to the distance between the midpoint of the inner stator radius and the outer external radius. The equivalent thickness, $t(k)$, is given by:

$$t(k) = \| p(x,y)_5 - p(x,y)_6 \|$$

where $p(x,y)_5(k)$ and $p(x,y)_6(k)$ are the middle point of the segment $(p(x,y)_1(k) + p(x,y)_2(k))/2$ and $(p(x,y)_3(k) + p(x,y)_4(k))/2$. The equivalent surface area, $A(k)$, is given by:

$$A(k) = A_1(k) + A_2(k)$$

where the area is divided in two triangle area:

$$A_1(k) = \sqrt{p_1(p_1 - a)(p_1 - b)(p_1 - f)}$$
$$A_2(k) = \sqrt{p_2(p_2 - c)(p_2 - d)(p_2 - f)}$$

where a, b, c, d are the edges of the quadrilateral and f is one of the two diagonals. The semi-perimeters of the two triangles that compose the quadrilateral, p_{n1} and p_{n2}, can be calculated as follows:

$$p_1 = \frac{a + b + f}{2}$$
$$p_2 = \frac{c + d + f}{2}$$

Once computed the area $A(k)$ and the equivalent height $t(k)$ can be computed the width of the equivalent rectangle $w(k) = A(k)/t(k)$ and then is possible compute the equivalent reluctance. In details the reluctance component can be computes as :

- $\mathcal{R}_{\text{body}} = \dfrac{h_{\text{body}}}{\mu_r \mu_0 S_{\text{body}}}$ $S_{\text{body}} = w_{\text{body}} L_{\text{stk}}$, for the body;
- $\mathcal{R}_{\text{sp}}(k) = \dfrac{t_{\text{sp}}(k)}{\mu_{\text{fe}} \mu_0 S_{\text{sp}}}(k)$ $S_{\text{sp}}(k) = w_{\text{sp}}(k) L_{\text{stk}}$ for the pole shoe subdivision;

- $\mathcal{R}_g(k) = \dfrac{t_g(k)}{\mu_0 S_g}(k)\ S_g(k) = w_g(k) L_{stk}$ for the airgap subdivision.

With these reluctance is possible to solve the magnetic network imposed magnetic voltage source of $N_e I_e$ ampere turns. The analytical network return the fluxes $\phi(k)$ that can be showed to the flux density $B(k)$. According to the aim to reduce the harmonic content and increase the flux density the analytical procedure has been validated by FE analysis. Fig. 8.5 shows a comparison between the results obtained from the analytical magnetic network and those obtained from the FE flux density analysis. It is important to note that the FE analysis considers a non-linear material and also includes the presence of slots, which can significantly impact the accuracy of the results. However, despite these differences, the accuracy between the two models is shown to be very high. This outcome provides strong evidence to validate the analytical circuit that can be used for a deeper analysis of the effect of pole shaping on the flux density. In other words, the high accuracy obtained from the comparison of the analytical model with the FE analysis reinforces the idea that the analytical method can be a reliable and efficient tool for analyzing the effects of pole shaping on the performance of EESMs.

8.1 TRADITIONAL EESM ANALYSIS

A traditional geometry has been considered as shown in Fig. 8.6 and a parametric study has been done by changing the pole shape while considering only two variables, A_1 and A_3. This study has been carried out to underline harmonic flux density components in a graphical plot that can be possible to plot with two variables but not in four.

8.1.1 *Two variables Parametric analysis*

Here and example of EESM has been analyzed and some additional data are reported in Tab.16. The rotor airgap shapes follow the function:

$$f(x) = A_1 \cos(p\theta) + A_3 \cos(3p\theta) \tag{8.3}$$

In order to have a good approximation of the airgap rotor curve, an discretization of the airgap and pole shoes of $k = N = 100$ has been chosen. The parametric study has been carried out considering a design of experiment that consider all the possible degree of freedom of the function f(x) and the geometry constraint. That way the study was conducted by considering a variation of A_1 and A_3 ranging from $-[D_r - D_{sh}]$ to $[D_r - D_{sh}]$. Fig. 8.7, 8.8, and 8.9 show a zoomed-in view where A_1 is included between $-25\,\mathrm{mm}$ and $25\,\mathrm{mm}$, while A_3 is between $-5\,\mathrm{mm}$ and $5\,\mathrm{mm}$.

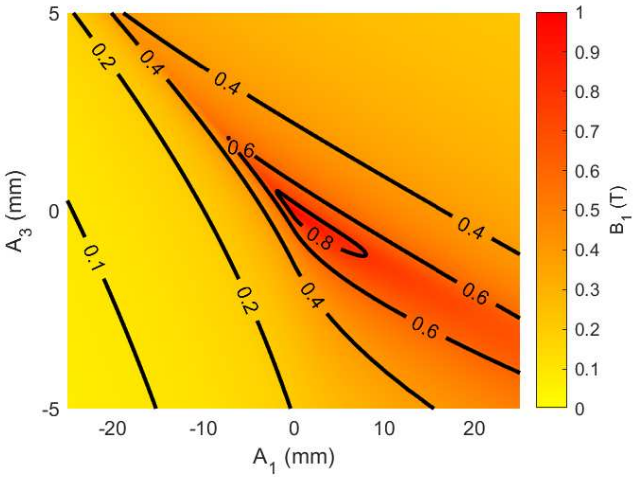

(a) Fundamental harmonic component amplitude.

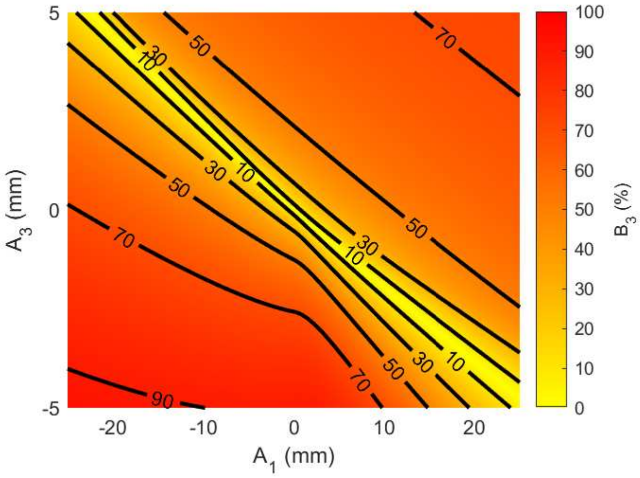

(b) 3rd harmonic component amplitude.

Figure 8.7: 1st and 3rd flux density harmonic component.

Fig. 8.7 and 8.8 show the 1st, 3rd, 5th, and 7th harmonic components of the flux density for the variation of the parameters A_1 and A_3. High values of the flux density are plotted in red while low values in yellow. In each point the 3rd, 5th and 7th harmonics are reported respect to the fundamental amplitude in percentage.

Fig. 8.7a exhibits the contour plot of the 1st flux density harmonic content. The goal from this plot is to choice the couple of A_1 and A_3 that maximize the 1st harmonic component. It shows that the maximum values of the flux density are achieved when A_1 is between $0\,\mathrm{mm}$ and $10\,\mathrm{mm}$, and A_3 is between $-3\,\mathrm{mm}$ and $3\,\mathrm{mm}$. The maximum value reached considering all the possible shaping is $B_1 = 0.88\,\mathrm{T}$. The minimum is obtained for negative values of A_1 and A_3, this happened because with these values the airgap at the middle of the pole increases, make falling down the 1st harmonic component.

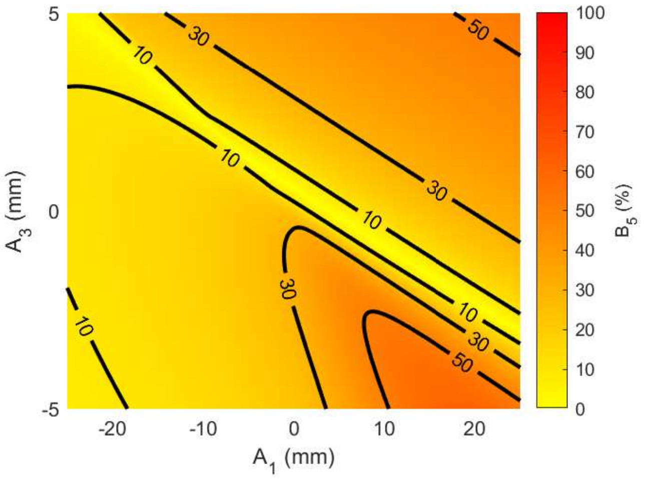

(a) 5th harmonic component amplitude in percentage.

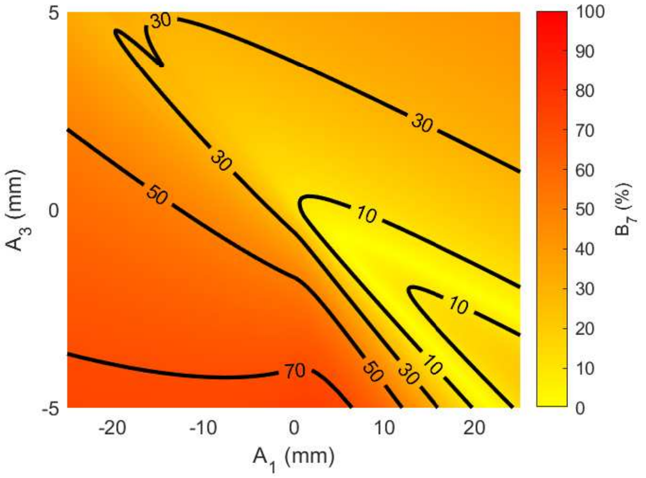

(b) 7th harmonic component amplitude in percentage.

Figure 8.8: 5th and 7th flux density harmonic component.

Fig. 8.7b shows the 3rd harmonic, which has very low values for the values of A_1 and A_3 mentioned above. The lowest values of this harmonic happened when A_1 and A_3 have different sign. Far away from this condition its value are quite important. The 5th and 7th harmonics are shown in Fig. 8.8a and Fig. 8.8b, respectively.

Their values have a low impact in the region where A_1 is between $0\,\mathrm{mm}$ and $10\,\mathrm{mm}$, and A_3 is between $-3\,\mathrm{mm}$ and $3\,\mathrm{mm}$. The minimum values for the 5th and 7th harmonic are obtained both close to $A_1 = 10\,\mathrm{mm}$ and $A_3 = -1\,\mathrm{mm}$. 3rd, 5th, and 7th give an harmonic content equal to the sum of the least squares, this amplitude has been shown in Fig. 8.9a. It shows that there is a minimum region close to the $A_1 = 5\,\mathrm{mm}$ and $A_3 = -1\,\mathrm{mm}$, that is very close to the region where the fundamental harmonic is on the highest value.

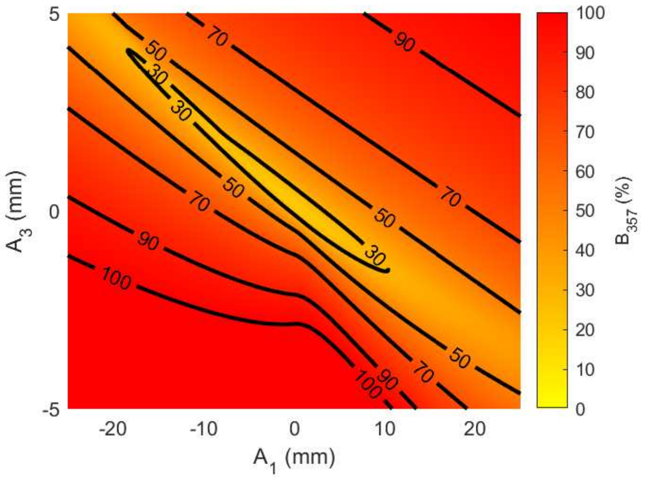

(a) Harmonic component considering 3rd harmonic contribute.

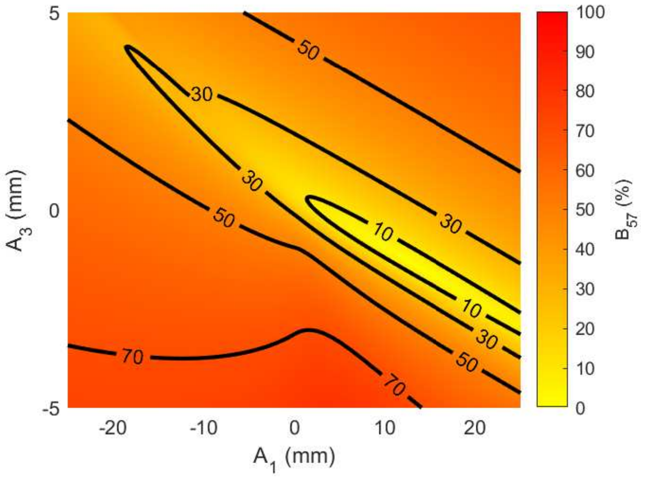

(b) Harmonic component without considering 3rd harmonic.

Figure 8.9: HD with and without 3rd harmonic contribution.

If the contribution of the 3rd harmonic component is neglected, considering, for example, star connection stator winding, other consideration are treated. Under this hypothesis the sum of the 5th and 7th contributions is reported in Fig. 8.9b. Here, the minimum different from Fig. 8.9a. In particular the values of A_1 have higher amplitude and A_3 lower amplitude if when what to minimize that harmonics. To have a complete idea of which configuration has the lowest harmonic content with the highest fundamental flux density a Pareto front has been carried out. These front has been obtained considering both cases, with 3rd harmonic and without 3rd harmonic component.

The results are reported in Fig. 8.10. Is it possible to note that according to the level of the HD that is possible to have higher flux density can be archived. For example, if the constraint are a low harmonic content with star connection different choice can be take compared to the triangle connection. Anyway some configurations exhibit a higher values of flux density.

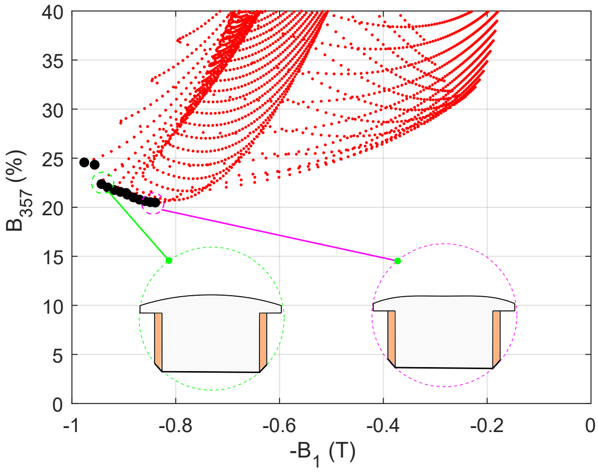

(a) Pareto front considering 3rd,5th and 7th harmonic content.

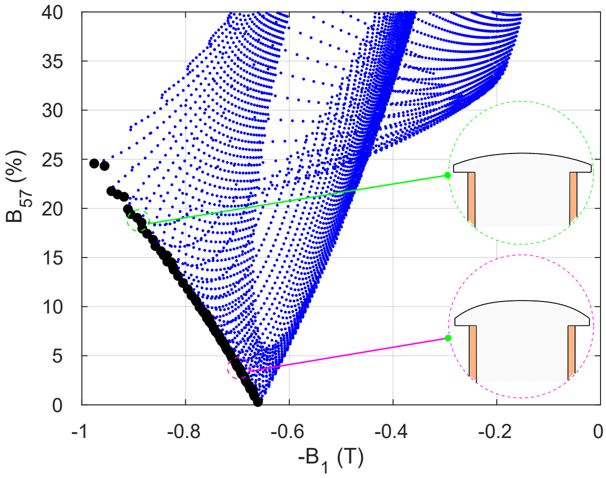

(b) Pareto front considering 5th and 7th harmonic content.

Figure 8.10: Two variables Pareto front.

8.1.2 *Four variables Parametric analysis*

In the previous section has been used the variation of the parameters A_1 and A_3, while in this section are making variate the parameters A_1, A_3, A_5 and A_7.
The airgap shape follows the function:

$$f(x) = A_1 \cos(p\theta) + A_3 \cos(3p\theta) + A_5 \cos(5p\theta) + A_7 \cos(7p\theta)$$

This shaping function take into account of also of the 5th and 7th harmonics. This aspect modify the shape of the salient pole that help

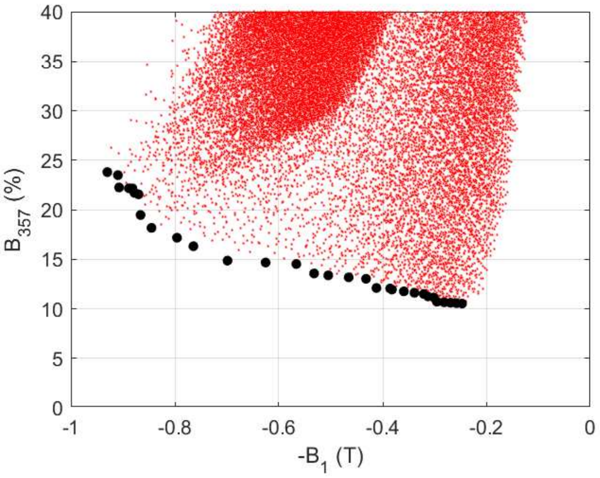

(a) Pareto front considering 3^{rd}, 5^{th} and 7^{th} harmonic content.

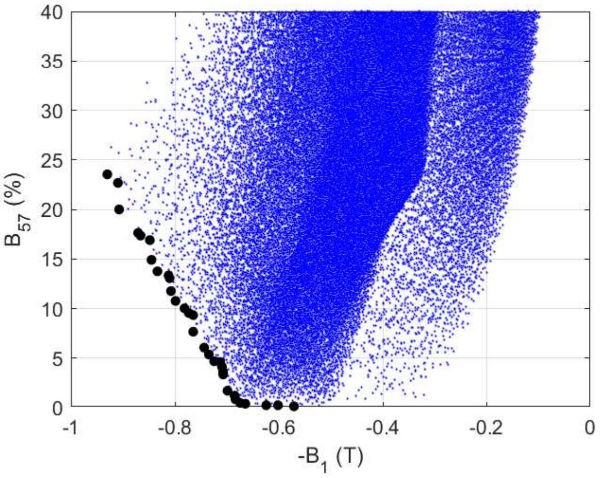

(b) Pareto front considering 5^{th} and 7^{th} harmonic content.

Figure 8.11: Four variables Pareto front.

the reduction of the corresponding harmonics. With the variation of all these parameters just the Pareto front can be shown in Fig. 8.11. As aspect, the values of the HD are lower adopting four parameter variation compared to the two variable. This effect is due to the fact that increasing the degree of freedom of the pole shaping also the effect of the harmonic content is different.

Table 16: Data motor

Data motor			
Iron Type	M530 50A	-	-
Iron Relative permeability	μ_r	4000-7000	-
Pole pair	p	4	-
Outer diameter	D_e	210	mm
Inner diameter	D_r	150	mm
Shaft diameter	D_{sh}	60	mm
Axial length	L_{stk}	50	mm
Air gap	g	0.7	mm
Pole excitation angle	θ_{exc}	15	deg
Ampere turns	$N_e I_e$	1000	A

8.2 FLUID EESM SIZING AND ANALYSIS

Up to now, traditional rotor pole sizing approach is carried out. Here, a novel approach to achieve optimal pole shaping in EESMs is presented. Traditional methods for pole shaping in EESMs focus on electromagnetic considerations, aiming to maximize the flux density while minimizing the harmonic content. Differently, this study proposes a new excitation pole design that includes fluid dynamic equations to shape the rotor pole body and pole shoe and combining them into the traditional electromagnetic design procedure. Fluid rotor is showed in Fig. 8.6.

The integration of fluid dynamics into the pole shaping process is motivated by the potential benefits it offers. By utilizing fluid dynamic equations the objective is to minimize the rotor saturation and reduce mechanical issues.

The implementation of the electromagnetic design equations are used in a network to satisfy flux density limits at the rotor yoke, salient pole body, air gap, and rotor current density requirements. Then the fluid dynamics laws that have been used during the pole body and pole shoe - air gap connection design process.

Finally, a traditional rotor and a fluid rotor geometry are compared, focusing on the electromagnetic behavior. Fluid dynamics and mechanical performance are reported in Chapter 6. Results obtained from finite element simulations show the advantages of the proposed innovative solution. The novel fluid dynamic-based pole shaping geometry exhibits improved performance and higher efficiency compared to an equivalent traditional pole shaping motor geometry.

8.2.1 *Fluid Model*

The rotor design incorporates fluid-dynamic assumptions that can be extended to electromagnetic theory. The analogy between fluid flow and magnetic flow has been previously employed to size the rotor of synchronous reluctance motors [9, 37]. For these reason, the rotor geometry is sized using a combination of fluid dynamics and electromagnetic equations.

The pole shaping technique is described in the following. The sizing procedure of the air gap - pole shoe follows the magnetic network approach reported in [31], with the fact that the rotor body changes according to the fluid dynamic laws. The rotor pole body is computed based on the fluid-dynamic theory of the Rankine Half-Body [104]. The lateral connection of the pole shoe is not achieved through a straight line but following a fluid iso-potential curve. This design choice aims at smoothing the surface of the lateral pole shoe, reducing the number of corner points. This connection follows the fluid current stream law of an incompressible fluid stream that flow be-

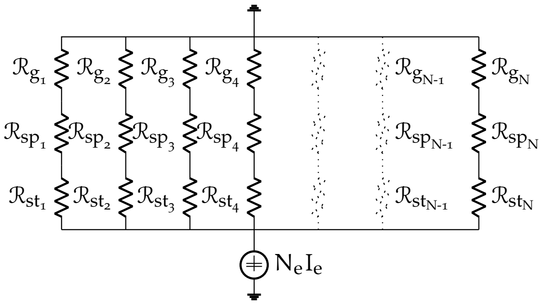

(a) EESM model configuration and magnetic circuit.

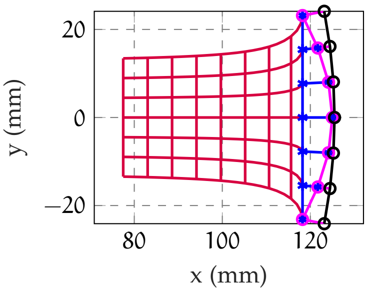

(b) Fluid rotor pole subdivision.

Figure 8.12: Fluid rotor model and geometry discretization.

tween two walls with a variable alpha angle. This design choice aims to smooth the surface of the lateral pole shoe, reducing the number of corner points.

The objective is to obtain a geometry that exhibits lower rotor saturation, reduced mechanical stress, and enhanced rotor speed exchange. By combining fluid dynamics and electromagnetic considerations in the rotor design, the proposed approach aims at optimizing various aspects of motor performance. The resulting geometry exhibits improved rotor flux-density distribution, reduced mechanical stress, and enhanced rotor speed range, leading to enhanced overall motor efficiency and reliability.

8.2.2 *Main pole rotor*

The main design of the air gap and the pole shoes are carried out in order to increase the electromagnetic performance, that means to maximize the first harmonic flux density and to reduce the current spatial harmonic components. The model used to size rotor geometry is an improvement of the one reported in [31]. Fig. 8.12a shows the circuit model (on the left) and the novel fluid pole model (on the right).

The design requires some starting parameters as air gap peak flux density $\widehat{B}_g$, current density J_{exc}, yoke flux density B_{gg}, pole body flux

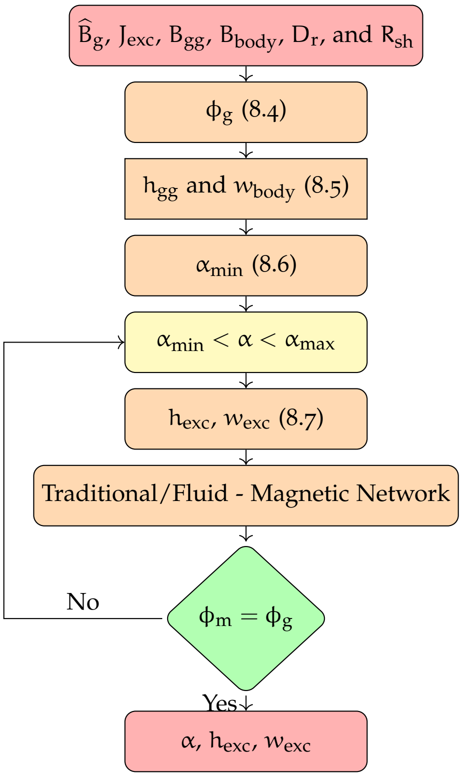

Figure 8.13: Electromagnetic flowchart design process.

density B_{body}. The procedure returns the required rotor opening angle α, the excitation height h_{exc} and the excitation width w_{exc}.

First of all, the flux per pole is computed after the selection of the rotor diameter D_r, the stack length L_{stk} and the pole pair p as:

$$\phi_g = \frac{\widehat{B}_g D_r L_{stk}}{p} \tag{8.4}$$

then the rotor yoke h_{gg} and the pole body width w_{body} are calculated:

$$\begin{aligned} h_{gg} &= \frac{\phi_g}{2B_{gg} L_{stk} k_{pack}} \\ w_{body} &= \frac{\phi_g}{B_{body} L_{stk} k_{pack}} \end{aligned} \tag{8.5}$$

Once computed the w_{body}, the rotor pole angle minimum α_{min} is obtained with:

$$\alpha_{min} = 2 \arcsin\left(\frac{w_{body}}{D_r}\right). \tag{8.6}$$

At this point, an iterative loop changes the pole angle α between α_{min} and $\alpha_{max} = \pi/p$. According to the airgap pole shaping function [31] a corresponding pole shoe height $h_{sp}(A_1, A_3, A_5, A_7)$ is calculated.

Consequently the rotor excitation height h_{exc} and width w_{exc} are be computed as:

$$\begin{aligned} h_{exc} =& D_r/2 - h_{gg} - R_{sh} - h_{sp}(A_1, A_3, A_5, A_7) \\ w_{exc} =& (x_\alpha - w_{body})/2 \end{aligned} \tag{8.7}$$

where x_α is the amplitude distance between the two airgap external points and R_{sh} is the shaft radius. The rotor geometry parameters computed are reported in Fig. 8.6.

The equivalent circuit can be solved computing the corresponding magnetic reluctance. The iterative loop continues until the flux computed from the magnetic network ϕ_m is equal to the flux per pole imposed ϕ_g. The model used for the fluid geometry is shown in Fig. 8.12a. This model is an extension of [31], where the pole body reluctance is distributed and take into account of the fluid curvature of the pole body that will be explained. A fluid rotor sketch geometry is reported in Fig. 8.12b. The red surfaces affected $\mathcal{R}_{st_k}$, the blue area the $\mathcal{R}_{sp_k}$ and the magenta the $\mathcal{R}_{g_k}$. All parts are discretized according to the k number subdivision imposed. The flowchart used for rotor design is reported in Fig. 8.13.

8.2.3 *Body and air gap - pole shoe connection*

The main novelties of the fluid rotor compared to the traditional salient pole motor are:

- pole body shaping;
- connection between the air gap and the pole shoe.

Both shaping techniques have been developed starting from fluid dynamic equations as follows.

The rotor body configuration has been designed through the fluid dynamic equation of the Rankine Half Body (RHB). RHB current stream is the compositions of a sink and a uniform flow and can be described by:

$$\gamma = Ur\sin(\theta) + m\theta \tag{8.8}$$

where γ is the current stream, U the fluid speed, r the distance from the sink point (0,0), θ the point angle and m the volumetric flow rate. Moreover the distance between the stagnation point and the sink point is labeled with a. Fluid dynamic current function (8.8) is plotted in Fig. 8.14 in p.u. values. The contour plot shows the current stream plot at different speeds. The magenta dot represented the sink, while the red dot the stagnation point. The idea is to size the rotor body following the dashed curve that has the current stream $\gamma = m\pi$.

This sizing is included in the electromagnetic design procedure and it is done after computing h_{exc} and w_{exc}. The current stream line is

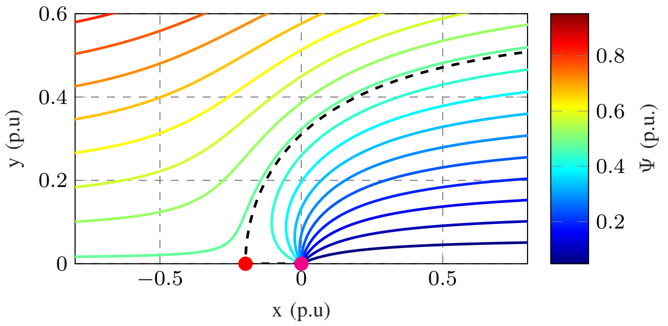

Figure 8.14: Rankine Half Body flow rate.

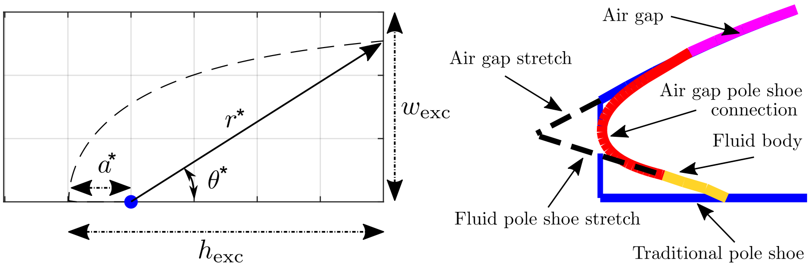

(a) Body pole shaping computation.
(b) Pole shoe connection.

Figure 8.15: Body pole shaping and Pole shoe connection computation.

calculated in order to satisfy h_{exc} and w_{exc} as shown in Fig. 8.15a. This computation is done fixing the speed U and varying the sink position a^* in order satisfy the limits. Fig. 8.15a shows the link between the unknown angle θ^* and the limits that can be expressed as:

$$\theta^* = \arctan\left(\frac{w_{\text{exc}}}{h_{\text{exc}} - a^*}\right) \tag{8.9}$$

that yields the radius r^*:

$$r^* = \frac{h_{\text{exc}} - a^*}{\cos(\theta)}, \tag{8.10}$$

and the corresponding volumetric flow rate m^*

$$m^* = \frac{U r^* \sin(\theta)}{\pi - \theta} \tag{8.11}$$

After few iterations, it is possible to compute a^* that, fixed the fluid speed U, satisfy the constraints h_{exc} and w_{exc}.

The curve is used like rotor pole body and from that computed the corresponding magnetic reluctance $\mathcal{R}_{st_k}$, the rotor excitation slot $S_{\text{slot,exc}}$, and the ampere turn $N_e I_e = J_{\text{exc}}/S_{\text{slot,exc}}$.

After the pole body computation, the connection between the air gap and the pole shoes is computed and drawn. Fig. 8.15b shows the two approach used to draw that connection. In magenta line is drawn the airgap, in blue the traditional salient pole, in red the fluid

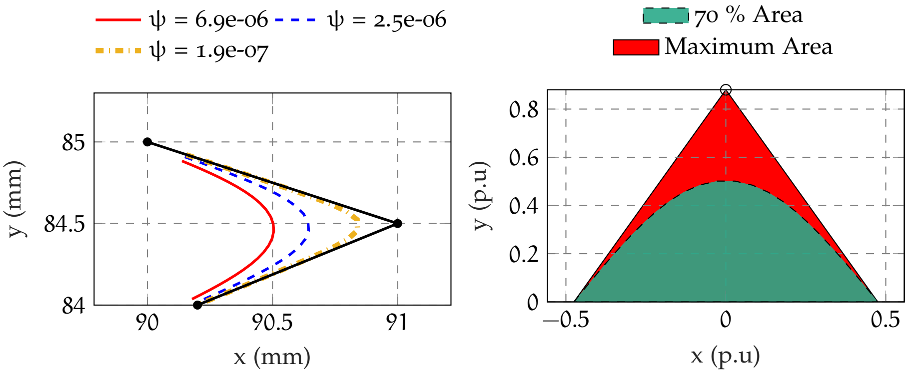

(a) Example of different pole shoes connection.

(b) Area criterio of the iso-potential curve selection.

Figure 8.16: Harmonic shape addiction.

proposed connection and in yellow the beginning of the fluid body. The proposed strategy to connect the airgap and the pole follow the fluid current stream law of an incompressible fluid stream that flow between two walls with a variable alpha angle.
The law equation is:

$$\psi = Ar^{\pi/\alpha} \sin\left(\frac{\pi\theta}{\alpha}\right) \tag{8.12}$$

where ψ is the current flow, A is an arbitrary constant, r is the radius distance from (0,0), α is the angle between the two walls and θ is the evaluation angle. In the excitation pole shoes the most lateral point on the air gap and on the higher part of the pole body are stretched, as shown in Fig. 8.15b, in order to have two walls and build a iso-potential curve between them.

Fig. 8.16a shows different iso-potential curves with different current flow ψ. The higher the ψ value, the higher the distance of the curve from the walls. Under this hypothesis the curves with lower ψ looks promising being closer to the walls. However they exceed the pole rotor angle that was imposed to obtain the flux per pole required. Moreover, a single specific curve must be selected, and the criteria used is the one reported in Fig. 8.16b. This figure shows the selection of the curve based on the portion of the area under that curve compared to the overall triangle area. In the example has been chosen 70% of the triangle area. Values higher that 50% of the triangle area yield curves with a distance to the walls that is less than 50 times the length of the segments walls. Anyway, the pole rotor angle increases. For this reason a convergent loop must be done slightly varying the starting angle to obtain the rotor pole angle that satisfy the flux per pole.

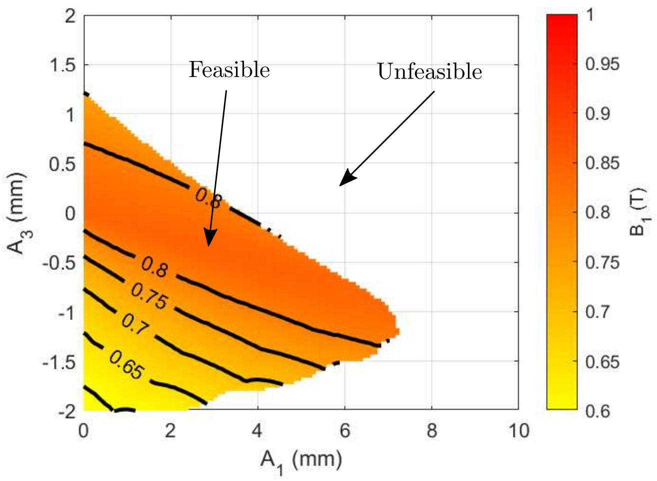

(a) Fundamental harmonic component amplitude.

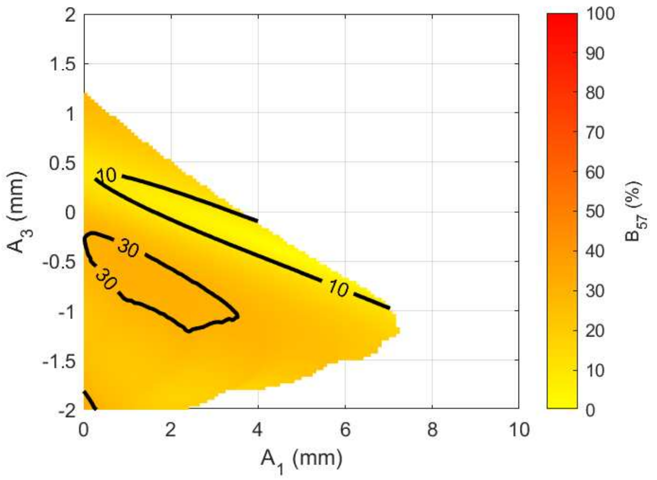

(b) 3^{rd} harmonic component amplitude.

Figure 8.17: A_1 and A_3 flux density harmonic component.

8.2.4 *Performance result*

The design flowchart has been used to size both traditional and fluid rotor pole, then the one of the optimal geometries has been chosen and compared with the same but adopting the fluid rotor configuration. The input variables used are: $\widehat{B}_g = 0.8\,\mathrm{T}$, $J_{exc} = 5\,\mathrm{A/mm^2}$, $B_{gg} = 1.2\,\mathrm{T}$, $B_{body} = 1.5\,\mathrm{T}$, $D_r = 60.9\,\mathrm{mm}$, and $R_{sh} = 18\,\mathrm{mm}$. The study has been considering different values for A_1 and A_3 as harmonic airgap shaping function. The results are reported in Fig. 8.17. The main and fifth-seventh harmonic amplitude component contour plot are reported for various combination of A_1 and A_3 values adopting in the airgap shaping function. The variable input limit the plane A_1 - A_3 making a feasible and an unfeasible area. Starting from this parametric study it is possible to find some geometry that can deliver higher

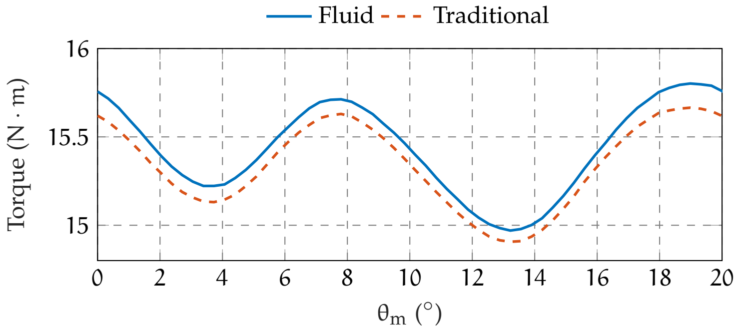

Figure 8.18: Rated torque comparison.

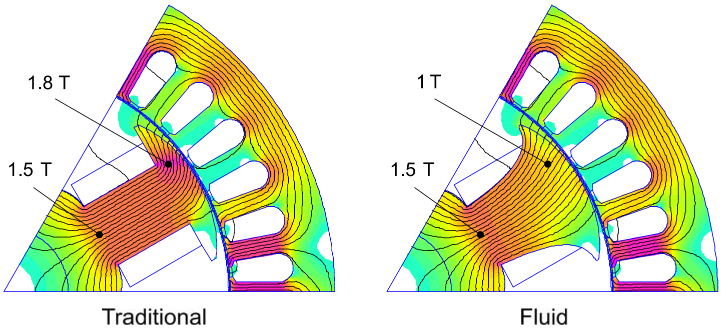

Figure 8.19: Flux density comparison.

main harmonic with a lower ripple. The parameters chosen in our case are $A_1 = 6\,\mathrm{mm}$ and $A_3 = -0.4\,\mathrm{mm}$. The main geometry parameters are reported in Tab.17.

Traditional and fluid rotor geometry have been drawn and compared at load performance, during the Maximum Torque Per Ampere working condition. Electronic and thermal limitations determine the current limits for the stator and rotor. The MTPA current angle $\alpha_i^e = 68\,\mathrm{deg}$ for both geometries but there is a slight difference in the average torque and ripple as shown in Fig. 8.18. The traditional geometry has a lower average torque that is $T_{trad} = 15.4\,\mathrm{N \cdot m}$, while $T_{fluid} = 15.2\,\mathrm{N \cdot m}$. They exhibit the same torque ripple equal to 5%. Another advantage of the rotor fluid is the lower rotor saturation as shown in Fig. 8.19. The rotor saturation pole shoe level changes from $B = 1.8\,\mathrm{T}$ to $B = 1\,\mathrm{T}$. The main geometry parameters are reported in Tab.17. Finally, some practical considerations are that traditional rotor structure helps in maintaining the rotor conductors against the centrifugal force, while the fluid shape does not presenting such feature, favoring the conductor's movement. Moreover the rotor winding when a fluid rotor is used instead of a conventional structure impact on the rotor current density. Indeed the area available for the rotor conductors is reduced when the fluid design is considered.

Table 17: Data motor

Stator winding			
Slot conductors	n_c	46	-
Machine parallel	n_{pp}	1	-
Rated rms current	I_{lim}	7	A
Voltages DC Bus	V_{dc}	300	V
Pole pair	p	3	-
Rotor excitation winding			
Ampere turns	$N_e I_e$	370	A
Stator geometry			
Air gap	g	0.8	mm
Outer diameter	D_e	184	mm
Inner diameter	D_s	126	mm
Axial length	L_{stk}	40	mm
Slot gap height	h_{so}	0.7	mm
Wedge height	h_{wed}	0.66	mm
Slot height	h_s	13.8	mm
Gap slot	w_{so}	2.5	mm
Slot area	S_{slot}	66.8	mm^2
Slots number	Q_s	36	-
Rotor geometry			
Inner diameter	D_r	95.2	mm
Shaft diameter	D_{sh}	36	mm
Excitation angle	ϑ_{exc}	14.4	deg

8.3 DISCUSSION

Traditional and innovative analytical design approach for Electrically Excited Synchronous Motors are presented, in particular focusing on the rotor pole shaping. Traditional methods for pole shaping focus just on the electrical aspects of the motor, while this study suggests a different approach. It combines fluid dynamics equations with the electromagnetic laws to design the rotor. By using fluid dynamics theory, the goal is to reduce saturation and increase mechanical resistance. Unlikely some drawback affected fluid geometry, as lower space for the rotor winding, less Electromagnetic design equations are used to meet certain requirements, and then fluid dynamics laws are used to shape the poles and the space between them. Finally, a comparison between the traditional pole design with the new fluid design is carried out through finite element simulation. The results show that the new design improves the motor's mechanical performance without affecting efficiency compared to the traditional design. This approach can be extended to HEPM motor. In the next Chapter HEPM motor effective design and optimization details will be described.

9

HEPM MOTOR SIZING: ROTOR DESIGN

This Chapter reports another possible analytical design that can be used for HEPM motor. As EESM, HEPM motor can be firstly designed and analyzed adopting a magnetic network. Fig. 9.1a and Fig. 9.1b show the main components of a fast magnetic network. The excitation coil and the equivalent magnetic lumped parameters are shown in Fig. 9.1a. The excitation coil can be represented by a continuous magnetic voltage source with an amplitude equal to $N_e I_e$, which are the ampere-turns of the excitation coil. The reluctance of air-gap $\mathcal{R}_{air}$ is in series with the excitation coil.

Fig. 9.1b represents the PM. The equivalent circuit is a continuous flux source with an amplitude ϕ_{PM} in parallel to the PM reluctance $\mathcal{R}_{PM}$, where the quantity $\mathcal{R}_{PM}$ is obtained from:

$$\mathcal{R}_{PM} = \frac{t_m}{\mu_r \mu_o S_{PM}}$$

The parameter t_m is the PM thickness, μ_r is the relative differential permeability, μ_o is the vacuum permeability, S_{PM} the cross-area section of the PM.

The reluctance of air gap $\mathcal{R}_{air}$ is:

$$\mathcal{R}_{air} = \frac{g}{\mu_o S_{air}}$$

where g is the thickness of air gap and S_{air} is the air gap surface.

The PM flux Λ_{PM} is equal to:

$$\phi_{PM} = B_{rem} h_m L_{stk}$$

where B_{rem} is the residual flux density and is obtained from:

$$B_{rem} = \mu_r \mu_o H_c$$

and H_c is the coercive magnetic field. The iron reluctances $\mathcal{R}_{fe}$ can be neglected because they are not significant with respect to the other quantities.

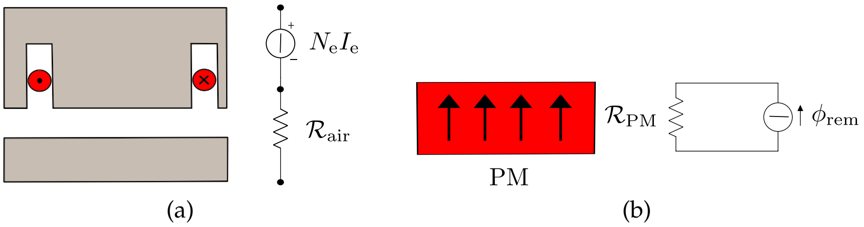

Figure 9.1: Elements of magnetic network. (**a**) Excitation winding and magnetic network. (**b**) PM and magnetic network.

Starting from these considerations a minimal and fast magnetic network has been built for both EESM and HEPM motors.

Under that theory and assumption, the flux Λ_{he} can also be expressed as:

$$\Lambda_{he} = \frac{k_w N}{2} \left(\frac{N_e I_e}{\mathcal{R}_{eq}} + \phi_{PM} \right) \tag{9.1}$$

where the reluctance of the pole $\mathcal{R}_{eq}$ is the magnetic reluctance corresponding to the rotor excitation winding only, k_w is the winding factor, N is the number of phase stator turns, $N_e I_e$ are the ampere-turns of the excitation coil. These values are different in series and parallel architecture. In HEPM motors series configurations have an $\mathcal{R}_{eq}$ higher than the air gap reluctance $\mathcal{R}_{air}$. On the contrary, HEPM motors parallel configurations and EESM have an $\mathcal{R}_{eq}$ close to $\mathcal{R}_{air}$.

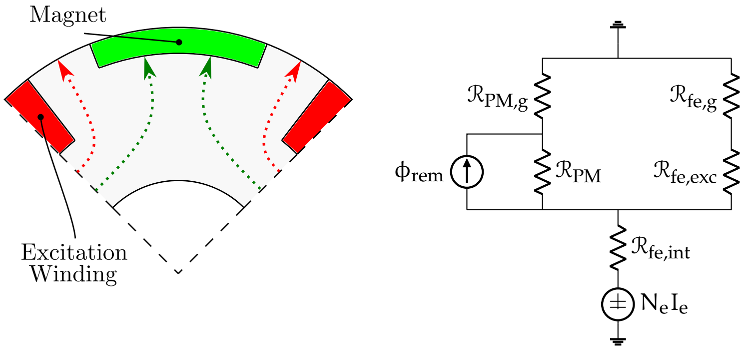

(a) Simplified motor. (b) HEPM magnetic circuit

Figure 9.2: HEPM model configuration and magnetic circuit.

9.1 FAST ANALYTICAL DESIGN

As mentioned above, a similar approach to EESM has been carried out also for the HEPM motor, adopting a different magnetic network that include the permanent magnets. According to [8, 30], parallel configuration has better performance, for this reason parallel configurations have been selected and studied. Just one configuration has been studied analytically, but the same magnetic con be extended to all the network that yields PMs and rotor excitation winding.

The reported prototype analytical sizing started from the requirements that are concerned, the torque required is around $T_{em} = 5\ \mathrm{N \cdot m}$ and the constant power speed range is fixed to be equal to 3.

The preliminary stator geometry has been determined based on the following considerations. The electric loading is chosen between $\widehat{K}_{el} = 20$ to $40\ \mathrm{kA/m}$ and the airgap flux density is fixed at $\widehat{B}_g = 0.7\ \mathrm{T}$.

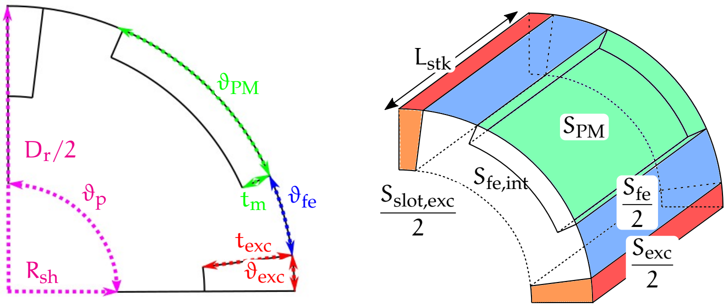

(a) Rotor angle sketch.

(b) Rotor surface sketch.

Figure 9.3: HEPM rotor parameter sketch.

In order to avoid complex cooling system a motor with a higher diameter compared to the axial length is preferred. As a consequence the ratio between the axial length L_{stk} and the inner stator diameter D_s is chosen around $L_{stk}/D_s = 0.3 - 0.5$. According to these data, a preliminary stator size is derived from the equations:

$$\begin{cases} T_{em} = \frac{4}{\pi}\widehat{B}_0\widehat{K}_{el}D_s^2L_{stk} \\ L_{stk}/D_s = 0.4 \end{cases} \tag{9.2}$$

where the variables are L_{stk} and D_s.

A possible design is given by commercial solution available on the market with:

$$L_{stk} = 40\ \mathrm{mm} \quad \text{and} \quad D_s = 96\ \mathrm{mm}$$

As far as the rotor is concerned, the sizing procedure requires a magnetic flux study as described hereafter. Different HEPM motors could be investigated, according to the rotor flux path [7, 29]. Hereafter, the parallel-type HEPM motor is analyzed. A sketch of such a configuration is reported in Fig. 9.2a. The rotor exhibits two iron paths in parallel to PM flux path represented with dotted red lines. The PM flux flows directly through the air gap without crossing any iron path as shown by dotted green lines. Starting from these magnetic considerations, an equivalent magnetic circuit can be arranged and implemented to describe the HEPM configuration as reported in Fig. 9.2b.

The magnetic network includes:

- a PM that is represented by the residual PM flux generator ϕ_{rem} and the corresponding PM reluctance $\mathcal{R}_{PM}$ connected in parallel;
- an excitation winding that is represented by a magneto-motive force generator of N_eI_e ampere-turns and the iron reluctance $\mathcal{R}_{fe,exc}$ and $\mathcal{R}_{fe,int}$ connected in series.

The other reluctances $\mathcal{R}_{PM,g}$ and $\mathcal{R}_{fe,g}$ are the corresponding magnetic reluctance of the air gap in front of PM and Excitation Winding paths. The rotor parameter graphical representation is reported in Fig. 9.3 and how to determine them is described in the Tab.18.

Let ϕ_g be the total flux per pole, ϕ_{exc} the flux developed by the excitation windings, and ϕ_{PM} the flux developed by the PM. Of course, the total flux per pole is given by

$$\phi_g = \phi_{exc} + \phi_{PM} \tag{9.3}$$

and it is computed from the stator pole surface and from the value of the air gap flux density, that is fixed to $\widehat{B}_g = 0.7$ T.
According to [67], for achieving a speed range equal to 3, the ratio γ between ϕ_{exc}/ϕ_{PM} is chosen close to 0.45, that is

$$\phi_{exc} = \gamma\ \phi_{PM} \approx 0.45\ \phi_{PM} \tag{9.4}$$

which is useful to determine the Amperturns of the excitation winding, $N_e I_e$. For such a winding a current density $J_{exc} = 6\ A/mm^2$ is chosen.

According to the magnetic circuit of Fig. 9.2b, it is possible to determine an initial estimate of rotor winding and PM size, carried out by imposing the following equality:

$$\begin{aligned} \phi_{exc} &= \frac{N_e I_e}{\mathcal{R}_{eq}} = \gamma \\ \phi_{PM} &= \frac{\gamma}{\gamma + 1} \phi_g \end{aligned} \tag{9.5}$$

where $\mathcal{R}_{eq}$ is equivalent magnetic reluctance.

The fluxes ϕ_{PM} and ϕ_{exc} depend on the span angles ϑ_{PM} and ϑ_{exc}, as shown in Fig. 9.3a. Therefore, solving (9.5) the span angle of the excitation ϑ_{exc} and the span angle of the PM ϑ_{PM} are obtained.

The equations reported in Tab.18 linking the motor geometry to the magnetic quantities have to be used. Once such angles are determined, the other rotor parameters are achieved, thus completing the preliminary rotor geometry, which is therefore ready for the FE analysis and a geometry optimization.

Table 18: HEPM motor magnetic network parameters.

$S_{PM} = \frac{D_r L_{stk}}{2} \vartheta_{PM}$	$S_{exc} = \frac{D_r L_{stk}}{2} \vartheta_{exc}$
$S_p = \frac{D_r L_{stk}}{2p}$	$S_{fe} = S_p - S_{exc} - S_{PM}$
$S_{fe,int} = \left(\frac{D_r}{2} - t_{exc}\right) L_{stk} \left(\frac{\pi}{p} + \vartheta_{exc}\right)$	$\phi_g = \widehat{B}_g S_p$
$S_{slot,exc} = t_{exc} \frac{D_r - t_{exc}}{4} \vartheta_{exc}$	$\mathcal{R}_{PM,g} = \frac{g}{\mu_0 S_{PM}}$
$\mathcal{R}_{PM} = \frac{t_m}{\mu_{PM} \mu_0 S_{PM}}$	$\mathcal{R}_{fe,exc} = \frac{t_m}{\mu_{fe} \mu_0 S_{fe}}$
$\mathcal{R}_{fe,int} = \frac{t_{exc} - t_m}{\mu_{fe} \mu_0 S_{fe,int}}$	$\mathcal{R}_{fe,g} = \frac{g}{\mu_0 S_{fe}}$
$\mathcal{R}_{eq} = \frac{[\mathcal{R}_{fe,int} + (\mathcal{R}_{fe,g} + \mathcal{R}_{fe,exc})](\mathcal{R}_{PM,g} + \mathcal{R}_{PM})}{[\mathcal{R}_{fe,int} + (\mathcal{R}_{fe,g} + \mathcal{R}_{fe,exc})] + (\mathcal{R}_{PM,g} + \mathcal{R}_{PM})}$	$N_e I_e = J_{exc} S_{slot,exc} k_{fill}$
$\phi_{PM} = \phi_{rem} \frac{\mathcal{R}_{PM}}{\mathcal{R}_{PM} + \mathcal{R}_{PM,g}}$	$\phi_{rem} = B_{rem} S_{PM}$

10

HEPM OPTIMIZATION AND PROTOTYPE RESULTS

The preliminary sizing yields the main dimensions but a geometrical refining is carried out, with the aim of improving the magnetic paths. In this Chapter , particular care is taken in selection of the flux barrier geometry so as to get the proper PM flux without limiting the excitation flux. On the other hand, the rotor slot is shaped to achieve a higher cross-area section keeping a proper width of the path for the excitation flux. This procedure originates the slot shape drawn in Fig. 10.1a. At last, an optimization carried out through a differential evolution (DE) algorithm was carried out whose objectives were the maximization of the average torque and the minimization of the torque ripple. The final stator and rotor geometry details are shown in Fig. 10.1 and the main data are reported in Tab.16.

The FE analysis has been developed by means of FEMM. Only one fourth of the the machine was modeled, as shown in Fig. 10.1b, introducing the anti-periodicity boundary conditions. The machine periodicity can be calculated as the maximum common divisor between total number of the motor slots Q_s and the pole pairs p, resulting equal to 4, thus one fourth of the machine is analyzed, as shown in Fig. 10.1b. The anti-periodic boundary conditions are imposed on the lines that divides one pole from the other. This greatly reduces the FE analysis computational time.

Dirichlet boundary condition is imposed on the outer circumference of the motor and on the inner circumference of the rotor. The value of the vector magnetic potential is set equal to zero $A_z = 0$. This means that the flux lines remain within these two circumferences.

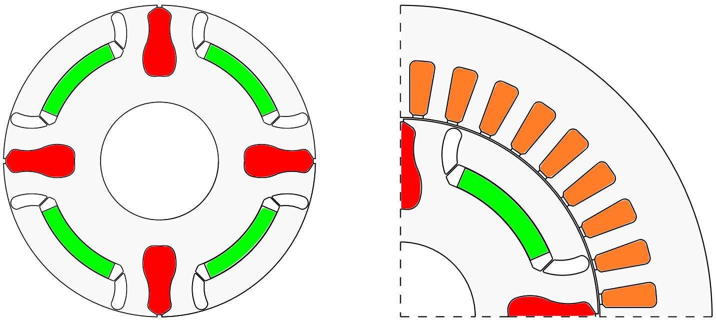

(a) Complete rotor.

(b) Partial stator and rotor.

Figure 10.1: Optimized geometry realized.

10.1 NO-LOAD TEST

The no-load test deals with the motor analysis where the stator winding is considered to be open-circuited. In particular, the main goal is the alignment of the $d-$axis of the rotor and the axis of the stator of the $a-$phase winding. The second goal is the evaluation of the flux linked by the stator due to the rotor.

10.1.1 *No-Load Flux Evaluation*

The flux linkage can be computed by integrating the magnetic vector potential over the stator slots. For a generic jth phase ($j = a, b, c$), it is:

$$\Lambda_j = \sum_{i=1}^{Q_{sim}} \frac{Q_s}{Q_{sim}} \frac{n_c k_j(i)}{n_{s,pp} S_{slot}} \int_{S_{slot}} A_z S_{slot}, \tag{10.1}$$

where A_z is the vector magnetic potential, Q_{sim} is the number of simulated slots, S_{slot} is the cross-area section of the slot, n_c is the number of conductors in the slot and $n_{s,pp}$ the number of the parallel paths. Then, $k_j(i)$ is a coefficient reporting how much the ith slot is filled by conductors of the jth phase. Its value is 0, ± 1, or ± 0.5 [16]. It is 1 if the slot contains only conductors of that phase. It is 0 if the slot contains no conductors of that phase. It is 0.5 in case of double layer winding, and the slot contains only one coil side of that phase. The sign $\pm$ define the conventional direction of the conductors. Once obtained the flux linkages Λ_a, Λ_b and Λ_c, the flux linkages Λ_d and Λ_q can be computed by means of the Clark-Park transformation.

$$\bar{\Lambda} = \Lambda_d + j\Lambda_q = \frac{2}{3}\left[\Lambda_a + \Lambda_b e^{-j2/3\pi} + \Lambda_c e^{-j4/3\pi}\right]. \tag{10.2}$$

10.1.2 *Impact of the excitation winding*

The no-load flux linkage Λ_o is given by two components, Λ_{PM} (constant) and Λ_e (variable) which are the PM and excitation winding flux linkage contributions, respectively. Later on, Λ_{he} will be used to indicate the rotor flux linkage of the Hybrid Excitation motor.

$$\Lambda_o = \Lambda_{he} = \Lambda_{PM} + \Lambda_e. \tag{10.3}$$

Once the rotor is aligned, the rotor flux linkage of the machine can be computed by a set of magnetostatic FE analysis varying the excitation current I_e. Of course, if $I_e = 0$, the only contribution of the magnets Λ_{PM} is obtained.

Fig. 10.2 illustrates the behavior of the total rotor flux linkage Λ_{he} (solid red line) varying the excitation current I_e. The blue marker

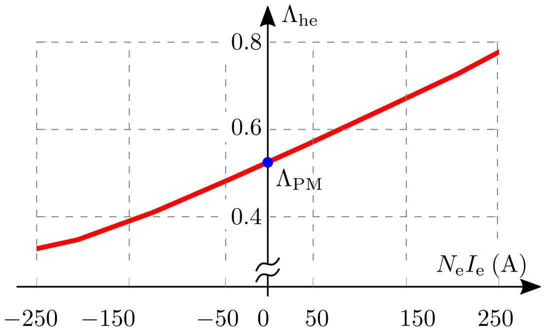

Figure 10.2: No-load flux linkages varying the excitation current HEPM motor.

refers to the PM flux linkage contribution, this value is obtained for I_e= 0 A. In this particular case study $\Lambda_{PM} = 0.524\,V \cdot s$. The contribution of the excitation winding varies from $\Lambda_{he} = 0.360\,V \cdot s$ with $N_e I_e = -216\,A$ to $\Lambda_{he} = 0.737\,V \cdot s$ with $N_e I_e = 216\,A$.

It is worth noticing that the flux linkage trend is almost linear along all the range. It is also possible to observe that the ratio between the flux linkage due to the excitation current Λ_{he} and that due to the PMs Λ_{PM} is about 0.41, that is slightly lower than expected.

10.1.3 *Cogging Torque*

Cogging torque is an effect caused by the interaction between the magnet flux due to the PMs buried into the rotor and the stator teeth, independently whether the machine is supplied or not. This attraction force between permanent magnets and teeth depends on their location and on the number of pole pairs and teeth.

As well known, the cogging torque can be minimized skewing the stator or the rotor, shaping conveniently the PMs or optimizing the number of the magnetic poles and teeth. Cogging torque can be computed by means of Maxwell weight stress tensor thanks to a set of FE analysis. The rotor is rotated from the initial position up to a mechanical angle of $30°$.

Fig. 10.3a shows the cogging torque of the motor under analysis. It can be noticed that its waveform is periodic and the period is equal to $10°$ mechanical degrees as expected ($Q_s = 36$). In Fig. 10.3b the cogging torque has been plotted according to the same motor with a stator skewed of $360°/Q_s$. The torque peak is reduced from a values of $0.3\,N \cdot m$ to $0.06\,N \cdot m$.

According to the high effect of the skewing, it is almost mandatory to adopt a skewed rotor. However, a remark is necessary. The skewing yields no issue for the excitation winding, however, attention has to be paid to the PMs which have to be inset in the rotor barriers. The adopted solution is illustrated in Fig. 10.4: the PMs have parallel lateral surface, they have a width lower than the barrier width, so that

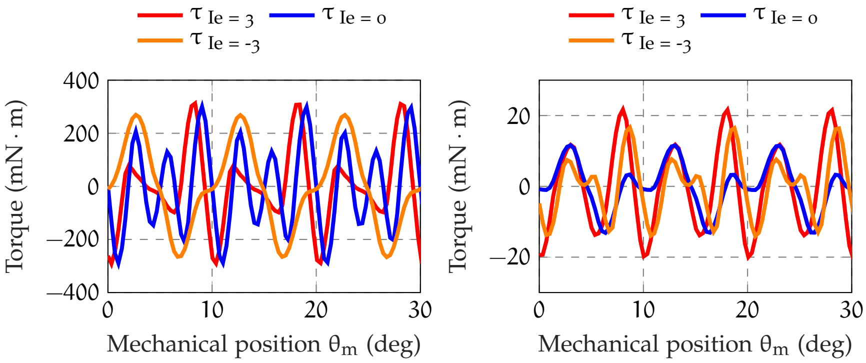

(a) Cogging torque without skewing

(b) Cogging torque with 10deg of skewing

Figure 10.3: Cogging torque without and with skewing.

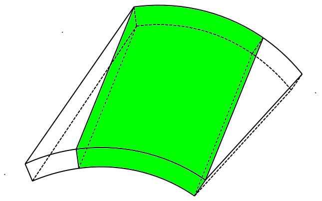

Figure 10.4: PM buried in the skewed flux barrier.

they can be addressed even if the barrier is skewed. Two avoid an excessive PM width reduction, the rotor is formed in two parts.

10.2 TEST UNDER RATED LOAD

The test under load is used to determine the rated capability and the parameters of the machine, in particular: the electromechanical torque of the motor T_{em}, the inductance L_d and L_q, the saliency ratio $\xi = L_q/L_d$, the rated flux linkage Λ_N, the rated speed $\omega^e_{m,N}$ according to the nominal voltage V_N. Moreover the flux-weakening is explored implementing a control system that maximized the power delivered in this region.

10.2.1 *MTPA trajectory*

Eqn (10.4) represents the q−axis current as a function of d−axis current and motor parameters which guarantees the motor to work on the MTPA trajectory.

$$I_q = \pm\sqrt{I_d^2 + \frac{\Lambda_{he}}{L_d - L_q} I_d} \tag{10.4}$$

This equation is useful to compute I_d and I_q on MTPA condition, however the parameters are not known and change with the current.

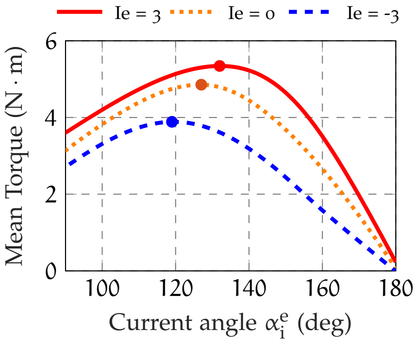

Figure 10.5: Operating region and MTPA trajectory for different excitation current and evaluation of the torque in MTPA.

The rotor flux Λ_{he} was only computed previously under no-load test. To find this particular working point, an iterative procedure is used.

The peak value of the stator current I_N is corresponding to the current limit I_{lim} ($I_N = \sqrt{2} I_{lim}$). The motor torque is computed for different values of the current vector angle α_i^e. The stator current limit is the maximum admissible current value, fixed by the motor designer according to the available cross-area section of the stator slots and the capability of the cooling system. Once obtained the torque $T_{em}\left(\alpha_i^e\right)$ as a function of α_i^e and nominal current the MTPA working point corresponds to the working point which exhibits the maximum torque. The corresponding value of I_d and I_q on the MTPA trajectory are computed as:

$$\begin{aligned} I_d &= I_N \cos\left(\alpha_i^e\right) \\ I_q &= I_N \sin\left(\alpha_i^e\right). \end{aligned} \tag{10.5}$$

Fig. 10.5 illustrates the trend of the torque versus the current phase angle α_i^e referred to HEPM motor for different values of excitation current I_e = 3 A, I_e = 0 A and I_e = -3 A. It can be noticed that α_i^e allowing the motor to work on MTPA condition at different I_e changes and is equal to 119° electrical degrees when I_e = -3 A, 127° electrical degrees I_e = 0 A and 132° electrical degrees I_e = 3 A. The maximum torque changes almost linearly with the excitation current I_e, with $I_e = -3\,\mathrm{A}$ the mean torque reached is equal to $T_{em} = 4\,\mathrm{N \cdot m}$, with $I_e = 0\,\mathrm{A}$ $T_{em} = 4.8\,\mathrm{N \cdot m}$ and with $I_e = \ 3\,\mathrm{A}$ $T_{em} = 5.3\,\mathrm{N \cdot m}$.

10.2.2 *Parameter Estimation*

The parameters of the motor correspond to the respective value computed analysing the motor on MTPA condition (rated working point). The values of I_d and I_q which guarantee the motor to work on MTPA trajectory calculated previously are converted into I_a, I_b and I_c by means of the inverse Clark-Park transformation. Once the three phase current I_a, I_b and I_c are calculated, the total current in each slot is:

$$I_{slot}(i) = \frac{n_c}{n_{s,pp}} \left[k_a(i)I_a + k_b(i)I_b + k_c(i)I_c\right] \tag{10.6}$$

where k_a, k_b and k_c are the corresponding fill coefficients of each phase. Λ_d and Λ_q are computed using (10.2). To estimate the electromechanical torque, the inductance L_d and L_q, the saliency ratio ξ, and the total rated flux are:

$$T_{em} = \frac{3}{2}p\left(\Lambda_d I_q - \Lambda_q I_d\right) \tag{10.7}$$

$$L_d = \frac{\Lambda_d - \Lambda_{he}}{I_d} \qquad L_q = \frac{\Lambda_q}{I_q} \qquad \xi = \frac{L_q}{L_d} \tag{10.8}$$

$$\Lambda_N = \sqrt{\Lambda_d^2 + \Lambda_q^2} \tag{10.9}$$

Once fixed the required rated speed it is possible to estimate the RMS line-to-line voltage V_N necessary to the motor to reach that specific speed:

$$V_N = \sqrt{3/2}\,\omega_m^e \Lambda_N \tag{10.10}$$

where ω_m^e is the electrical speed given by $\omega_m^e = p\omega_m \left(\mathrm{rad\,s^{-1}}\right)$. The coefficient $\sqrt{3/2}$ is used to convert the amplitude of the space vector of the phase voltage $\left(V_N = \sqrt{2/3}V_N\right)$.

Tab. 19 reports the nominal parameters of the HEPM motor .

10.3 MEASUREMENT VALIDATION

Hereafter the comparison between FE simulations and measures on the prototype have been reported. The prototype is shown in Fig. 10.6. The prototype rotor has been skewed as described above. The motor has been addressed on a test bench and mechanically coupled to a brake. The rotor excitation winding has been fed by slip ring and brushes, which allow the current direction to be reversed. The current control has been implemented adopting the dSPACE MicroLabBox 1202.

Some representative measures can validate the goodness of the procedure described above. The first one is the flux linkages comparison, the second is the mean torque in the plane I_d-I_q for different excitation current and finally the torque/power versus speed characteristic at nominal point.

Fig. 10.7 shows direct and quadrature flux linkages for different value of excitation current. The direct flux linkage Λ_d is strongly influenced from the excitation current I_e, being the excitation rotor flux

Figure 10.6: HEPM motor prototype.

oriented along the d-axis. Anyway also the q-axis flux linkage feel some variation changing the excitation current but with reduced amplitude. In Fig. 10.7 the solid lines represented the simulated values and the dashed the measured data. This figure shows the flux linkage Λ_d versus the current I_d when the quadrature current I_q is equal to zero, and the flux linkage Λ_q versus the current I_q when the direct current I_d is equal to zero. The match between the measured and simulated data is satisfactory in the overall operating range for both the flux linkages.

In Fig. 10.8 the torque comparison with different values of excitation current is carried out. The torque is reported equal to $6\,\mathrm{N}\cdot\mathrm{m}$ and $2\,\mathrm{N}\cdot\mathrm{m}$ for different excitation currents and a different combination of stator current I_d and I_q. There is a satisfactory match between simulated and measures. The average difference between the FE prediction and experimental results is about 5%.

It is interesting noticing the moving of the torque hyperbolas with the excitation current. The non linear FE model shows a good accuracy with the measurement also for different excitation currents.

Fig. 10.9 shows the torque and power versus speed curves developed by means of FE and measures on the test bench. The test has been carried out until 1600 r/min, about 3 times the rated speed. The correspondence between the torque and power delivered versus the rotational speed is good. As aspect the maximum torque at steady state is close to $5.3\ \mathrm{N}\cdot\mathrm{m}$ and the maximum power is around 330 W. It is kept fixed along all the FW region. The correspondence between the FE results and the test bench measurements is satisfactory also during a variation of the excitation current together with the rotation of the angle of the stator current vector. Fig. 10.10 shows the corresponding efficiency. This is the total efficiency of the drive: it is computed considering the inverter input power and the output power at the motor shaft. It is a reasonable efficiency, considering the small scale motor under test which is available in laboratory.

Finally, the effectivity of the excitation current in the event of a three-phase circuit is verified. The stator winding is short-circuited

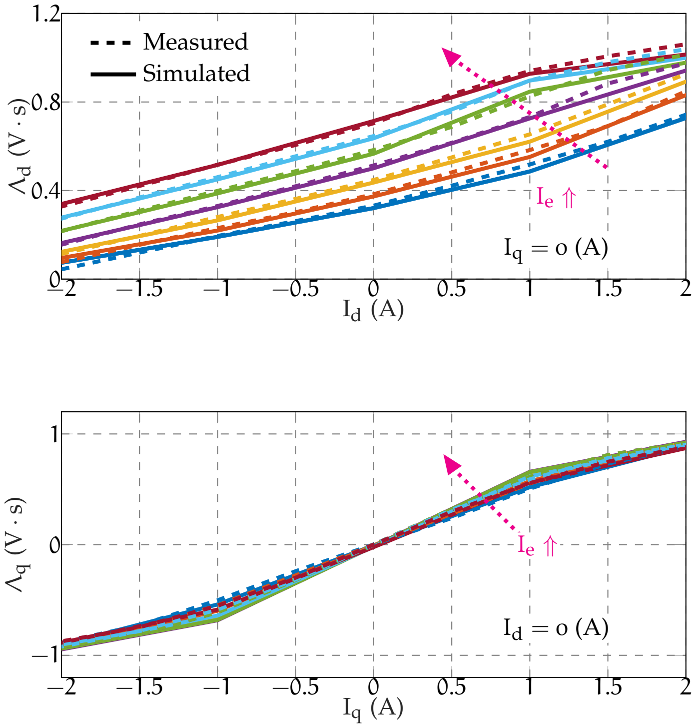

Figure 10.7: Comparison between the flux linkage simulated and measured.

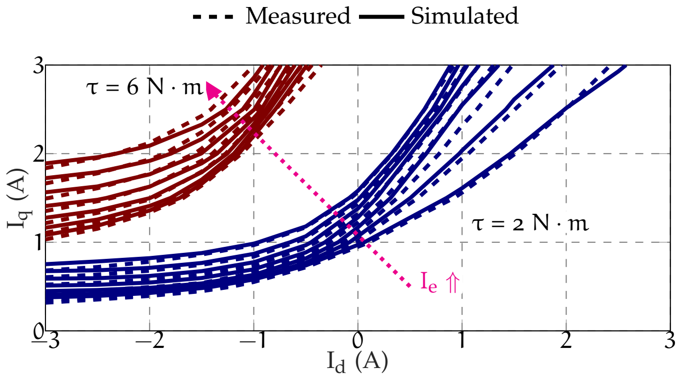

Figure 10.8: Torque comparison.

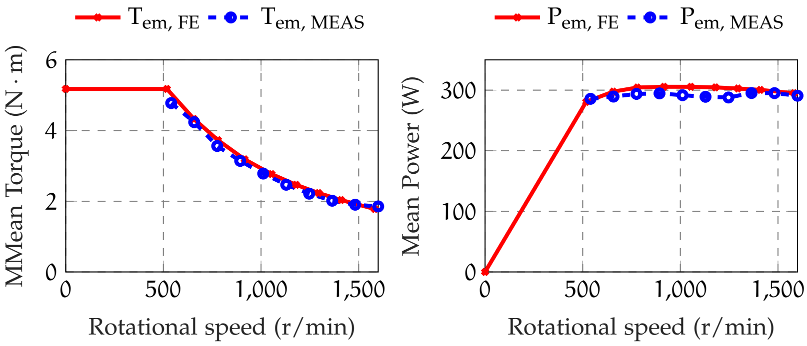

Figure 10.9: FE and measured torque and power versus speed during MTPA and FW conditions controlling the rotor flux linkages.

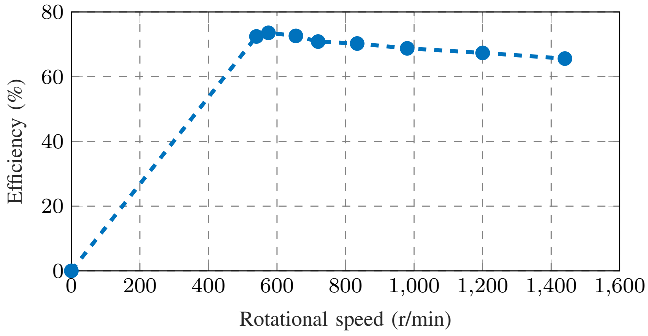

Figure 10.10: Measured efficiency versus speed corresponding to the tests of Fig. 10.9.

and the rotor is dragged at a speed as to achieve the short-circuit current equal to the nominal current (to avoid overheating during the test). Both stator current and braking torque are measured Then the excitation current is reduced to zero and then completely reversed. Fig. 10.11 shows the measured stator current and braking torque during the test corresponding to different excitation currents. As expected, both short-circuit current and braking torque reduce when the excitation current is supplied to decrease the rotor flux.

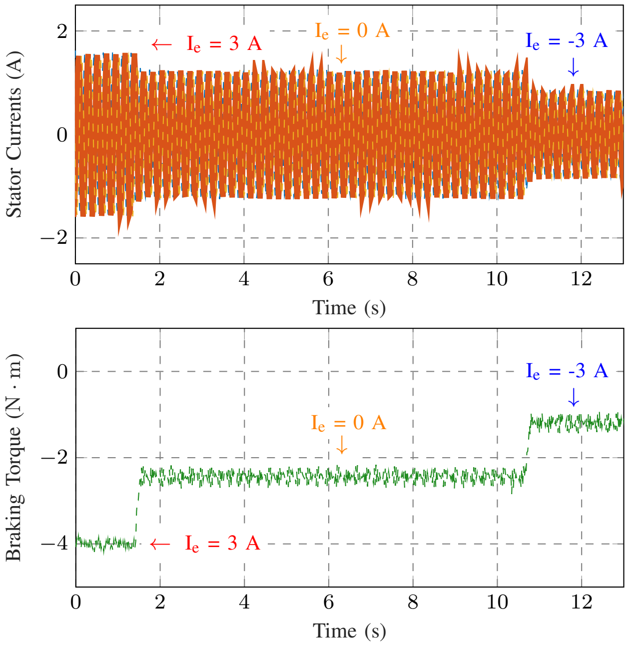

Figure 10.11: Measured stator current and braking torque during short circuit corresponding to different rotor excitation currents.

10.4 DISCUSSION

At first a preliminar analytical approach is proposed to determine the main motor size. Then, a finite element analysis is carried out to refine the motor geometry accounting the effect of the non-linearity, mainly due to iron saturation, so that to improve its torque versus speed capability. Preliminary considerations are introduced about the geometry, and the magnetic circuit is shown. Both pre- and post-processing procedures are described, including how setting the phase currents and boundary conditions, how quickly computing the flux linkages and obtaining the rotor alignment. The two main analysis procedures have been illustrated, the no-load test and the test under load. Finally, some experimental measurements are presented to validate the predictions.

By means of the no-load analysis, it is possible to compute the constant component of the flux linkage Λ_{PM} due to the permanent magnets the variable component Λ_e due to excitation winding. The ratio between Λ_e and Λ_{PM} is strongly linked to the constant power speed range that is a requirement of the application. The analysis under load is used to compute the nominal parameters of the motor, to determine the nominal working condition of the motor (the maximum torque per Amps strategy is applied) and then voltage, current, torque and power behaviour versus rotor speed.

The finite element analysis highlights that the analytical computation of the excitation current behaviour has to be refined, to improve the motor capability. In particular, a higher weakening of the rotor flux is required at higher speeds. To validate the model a comparison has been done adopting a HEPM motor prototype. Simulated and measured flux and torques have been compared for various excitation currents. Moreover torque versus speed and power versus speed curves up to 1600 rpm (3 times the rated speed) have been measured to validate the excitation control strategy. The good match between simulations and measures has been obtained. An almost constant power during flux weakening operations has been obtained.

The proposed procedure proves to be a proper guide in designing the Hybrid Excited Permanent Magnet Synchronous motors.

Table 19: Nominal parameters HEPM motor

PMs flux linkage	Λ_{PM}	0.524	$V \cdot s$
Excitation winding flux linkage	Λ_e	0.213	$V \cdot s$
Total rotor flux linkage	Λ_{he}	0.737	$V \cdot s$
Direct synchronous inductance	L_d	141	mH
Quadrature synchronous inductance	L_q	540	mH
Saliency ratio	ξ	3.83	-
Nominal torque	T_N	5.3	$N \cdot m$
Nominal speed	n_n	540	r/min

Part III

HYBRID EXCITED PERMANENT MAGNET: CONTROL

This part describes the HEPM motors with a focus on electric control. Initially, PM control strategies used in literature are reported, then the HEPM motor model is discussed, considering the nonlinearity that affected the machine. Subsequently, low-speed techniques such as the MTPA technique and sensorless control and high-speed algorithms used during the FW are described. Lastly, an extension of the implicit Model Predictive Control (MPC) current control, considering voltage and current constraints for HEPM is reported.

11

SYNCHRONOUS MOTOR BACKGROUND

This Chapter presents the most common synchronous motors model, the operational working regions, control strategies and related relevant literature.

At first, the focus is on explaining and discussing the essential equations used to determine the size and behavior of synchronous motors across various operating conditions. Following this, an outline of classical control approaches that are suitable for achieving optimal performance in these scenarios is provided.

Finally, the theoretical study for conducting a more detailed analysis of EESM and HEPM motors is explained.

11.1 PMSM: MODEL AND CONTROL SCHEME

Steady-state voltage equations of a synchronous motor in the *dq* rotating reference frame are:

$$V_d = R_s I_d - \omega_m^e L_q I_q \qquad V_q = R_s I_q + \omega_m^e \left(\Lambda_{PM} + L_d I_d\right), \tag{11.1}$$

where V_d, V_q are the stator voltages, I_d, I_q are the stator currents, L_d, L_q are the motor apparent inductances, R_s is the stator resistance, Λ_{PM} is the PM flux linkage and $\omega_m^e = p\omega_m$ are the electromechanical speed, pole pairs and mechanical speed, respectively. To describe all synchronous motors by (11.1), the *d*-axis of the rotating reference frame is aligned to PM flux linkage. To simplify the notation and the dissertation, magnetic saturation, iron losses and PM demagnetisation effects are neglected. However, the aforementioned effects can be included as in [39, 108]. Finally, the steady-state torque of a synchronous motor can be computed as follows:

$$T = \frac{3}{2} p \left[\Lambda_{PM} I_q + \left(L_d - L_q\right) I_d I_q\right], \tag{11.2}$$

where two terms can be recognized, namely, the PM and the reluctance torque components.

Operating motor conditions are studied by drawing Equations (11.1) and (11.2) in the *dq* current plane as in Fig. 11.1a, 11.1b [69, 89]. Before analyzing the motor operating regions, some relevant curves are introduced in the *dq* plane, in particular the current limit locus, the voltage limit loci and the constant torque loci. The motor current limit describes a circle centered in the origin in the *dq* plane, given by:

$$I_N^2 = I_d^2 + I_q^2, \tag{11.3}$$

where I_b is the nominal current of the motor. The current limit is represented by a red blue line in Fig. 11.1a, 11.1b.

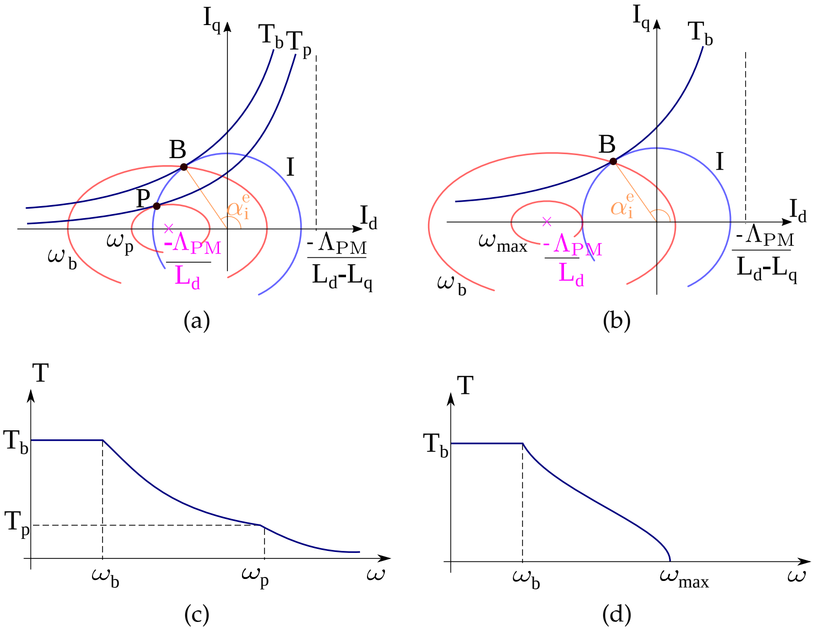

Figure 11.1: Circle diagrams and torque versus speed characteristic when electric motors have $\Lambda_{PM} > L_d I_b$ or $\Lambda_{PM} < L_d I_b$. (**a**) Circle diagram with $\Lambda_{PM} < L_d I_b$. (**b**) Circle diagram with $\Lambda_{PM} > L_d I_b$. (**c**) Torque vs. speed $\Lambda_{PM} < L_d I_b$. (**d**) Torque vs. speed with $\Lambda_{PM} > L_d I_b$.

The voltage limit is retrieved from (11.1), by imposing a maximum voltage magnitude equal to the nominal value V_N. The resulting equation describes elliptical trajectories in the *dq* current plane, which depend on the actual motor speed as:

$$V_N^2 = \omega_m^{e^2} \left[(\Lambda_{PM} + L_d I_d)^2 + (L_q I_q)^2 \right] . \tag{11.4}$$

The curve ellipticity is equal to the motor saliency ratio $\xi = L_q/L_d$. Moreover, the ellipses are centered in $(-\Lambda_{PM}/L_d, 0)$, where the ratio Λ_{PM}/L_d is equal to the magnitude of the steady-state three-phase short-circuit current. Furthermore, the ellipse major semi-axis length is equal to $V_N/(\omega_m^e L_d)$, thus it is inversely proportional to the operating speed.

As limit cases, the voltage limit curves of SPM machines are circular, having an unitary saliency ratio.

Voltage ellipses of REL motors are centered in the origin, having a zero steady-state short-circuit current. Voltage limit curves are depicted by red solid line in Fig. 11.1a, 11.1b. It is remarked that (11.4) holds at high speeds and for medium-high power machines. In fact, the resistive voltage drop is not negligible for low power motors and it has to be accounted in the machine description, as in [44].

The constant torque loci shape is obtained by inspecting (11.2). In particular, constant torque curves are described by hyperbola, whose asymptotes are the *d* axis and the vertical straight line defined by the equation $I_d = -\Lambda_{PM}/(L_d - L_q)$. Since the *d* axis is assumed to be aligned with the PM flux, the vertical asymptote lies in the positive I_d semiplane, indeed $L_d < L_q$.

Constant torque loci are the black solid line hyperbolas in Fig. 11.1a, 11.1b.

As particular case, SPM motors are characterized by horizontal straight lines constant loci as in Fig. 11.2a, having an unitary saliency ratio, whereas REL machines are characterized by hyperbolic constant torque curves centered in the origin, mounting no PMs (Fig. 11.2b.)

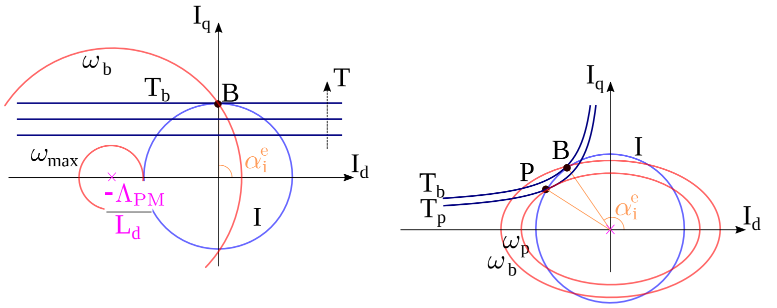

(a) (b)

Figure 11.2: Circle diagrams of the SPM and REL motors. (**a**) SPM circle diagram. (**b**) REL circle diagram ($L_q > L_d$).

11.1.1 *Constant Maximum Available Torque Region*

At the standstill condition, the only constraint that limits the motor torque capabilities is the current limit circle (11.3). The voltage ellipse constraint described by (11.4) expands, covering the entire *dq* current plane. Indeed, the ellipse size is inversely proportional to the speed. In this condition, the motor is controlled along the MTPA strategy. In particular, given a desired torque T, the *dq* currents magnitude I and phase α_i^e are computed such that the desired torque is guaranteed and the Joule losses in the machine are minimized. For any current amplitude, the current angle α_i^e should be chosen equal to:

$$\cos\alpha_i^e = \frac{-\Lambda_{PM} + \sqrt{\Lambda_{PM}^2 + 8\left(L_d - L_q\right)^2 I^2}}{4(L_d - L_q)I}. \tag{11.5}$$

Considering Fig. 11.1a, 11.1b, the MTPA trajectory is obtained as the tangent points between current circles and torque hyperbola. The maximum available torque is retrieved from (11.5) by substituting the nominal current magnitude I_b, and it represents the nominal motor torque.

The nominal torque remains the maximum available one until the voltage constraint ellipse, which shrinks for increasing speeds, crosses the MTPA current locus at the nominal current circle. This condition occurs in the points denoted as B in Fig. 11.1a, 11.1b. Above such a speed, known as nominal speed and denoted as ω_N, the motor is not longer able to deliver its nominal torque, since the voltage ellipse constraint forces the working point to lie on a lower torque hyperbola, given the nominal current [2].

11.1.2 *Flux-Weakening: Constant Maximum Available Volt-Ampere Region*

FW operation begins above the nominal speed [85]. Since the MTPA strategy can not be implemented, the nominal torque can not be obtained. The maximum available torque for a given speed and a rated current is retrieved by the intersection of the current limit circle with the voltage limit ellipse. This intersection starts moving the working points from the base ones B (Fig. 11.1a, 11.1b) along the limit circle towards the point $(I_b, 0)$, keeping a constant Volt-Ampere rating.

Two main possibilities can occur while moving along the current limit circle, depending on the position of the voltage ellipse center with respect to the nominal motor current. If the ratio Λ_{PM}/L_d is greater than the nominal current I_N, the ellipse center lies outside the current limit circle. In this condition, the movement of the motor current along the current limit circle can proceed till the point $(-I_b, 0)$, where the motor exhibits zero torque. From a geometrical point of view, it implies that the ellipse voltage limit is tangent to the current limit circle. This condition is depicted in Fig. 11.1b and it corresponds to the smallest voltage ellipse. Moreover, in this condition the voltage limit corresponds to a higher achievable speed:

$$\omega_{max} = \frac{V_N}{\Lambda_{PM} - L_d I_N}. \tag{11.6}$$

The motor is not able to operate above such speed, since there are no longer intersections between the current limit and voltage limit locus. In other words, the electric drive has a maximum operating speed. This behavior is often retrieved in SPM machines, characterized by small synchronous inductances and, consequently, high Λ_{PM}/L_d ratios, as shown in Fig. 11.2a.

On the contrary, a different behavior characterizes machines with the ellipse voltage limit center placed inside the current limit circle. The behavior is shown in Fig. 11.1a. In this case, the movement of the current point along the limit circle reaches the point P in the same figure, where the torque hyperbola is tangent to the voltage limit ellipse. In this operating point P, the drive exhibits its maximum torque-to-voltage ratio and the corresponding electrical speed ω_p represents the maximum speed of the FW constant Volt-Ampere region. Above such speed the control strategy needs to be changed to guarantee a feasible working condition.

11.1.3 *Flux-Weakening: Decreasing Volt-Ampere Region*

The third operating region exists only for those machines whose ellipse center lies within the current circle, as in Fig. 11.1a. This is also the case of REL motor [13, 89] whose circle diagram is reported in Fig. 11.2b. SPM machines achieve rarely such operating mode, if not supported by external inductances. Above the speed ω_p, torque performances are limited by the voltage limit ellipse. In particular, it is not possible to proceed moving the current along the current limit circle. The maximum drive current must decreased in order to respect the voltage limit ellipse, describing the Maximum Torque per Voltage (MTPV) trajectory as reported in Fig. 11.1c. Since the ellipse axis is inversely proportional to the speed, the drive can theoretically reach an infinite maximum speed, i.e., till the ellipse collapses in a single point. Of course, mechanical effects limit the maximum achievable speed operation.

11.2 FLUX WEAKENING CONTROL STRATEGIES

MTPA strategy is commonly implemented for PMSM control up to the nominal speed. This strategy allows for a constant maximum available torque up to the nominal speed, thus maximizing the available power. In addition, an efficient operation of the drive is assured by minimizing the joule losses. Achieving high torque in a wide speed range is an essential feature. However, most of PMSMs are characterized by a limited speed range since the EMF of such machines increases linearly with the speed. Thus, the voltage limit of the converter is quickly reached [88].

The feasible speed working region of e-motors can be extended by means of several solutions. First, it is possible by acting on the design of the overall mechanical system. Considering EV applications, the introduction of multiple gear-ratios can address the issue. However, this solution involves significant costs, increasing weights, and it may reduce the reliability of the system. As an alternative, the motor control strategy can be modified, leaving the MTPA operation above the nominal speed. In this condition, the FW mode represents the most widespread solution [48, 49]. Such strategy allows for a constant deliverable maximum power and it is achieved by decreasing the motor stator current component aligned with the PM flux or by acting on the rotor windings excitation. This solution has a limited impact on the overall system where the electric motor is mounted. Depending on the PM flux linkage and on the direct axis inductance, PMSM can have a finite or infinite theoretical maximum operating speed. In the latter case, a constant available maximum power can not be guaranteed in the whole speed range. Above a defined speed, a new strategy must be implemented for the motor control, namely, the MTPV [87, 105]. It allows all the current and voltage constraints of the system to be met, at the cost of a reduction in the delivered power.

An effective FW operation of PMSM drives requires particular care both during the electric machine design and the control scheme design one. Machine designers are required to enhance the FW capability of electric motors by changing the motor structures [106] or by using excitation rotor windings. For example, annular iron mounted on the surface of the PM and flux barriers can be used to reduce the direct flux demagnetization and to increase the machine operation speed range, as in [106].

A proper control strategy is needed to extract the maximum output torque given the converter voltage constraint [78], once a PMSM with satisfactory FW capabilities is designed. Several challenges need to be overcome in the selection of the most effective motor control architecture [41, 75, 95]. Different FW techniques are available in the literature depending on the PMSM controller type. Synchronous PID current controllers, DTCs, MPCs and flux-based controls are considered in this review. Robustness against motor parameters uncertainties, computational burden, anti-windup handling, and maximum deployment of the motor feeding converter are some of the aspects that the control designer needs to take into account. The most widespread architectures in the literature are presented, including feed-forward, feedback and mixed FW control structures. For sake of completeness, some cutting-edge solutions which couples, for instance sensorless and FW operations, are included in this review, as well.

FW operation of synchronous motors has been investigated for all the most widespread control architectures, including current controllers, flux-based controllers and model predictive control schemes. All these three structures are considered in this review. More attention is paid on FW operation with synchronous PI current regulators, since it is by far the most common solution. FW control strategies are clustered according to the presence or absence of a feedback of the motor voltage. Actually, the feedback is obtained by using the inverter reference voltage, since the actual motor voltage is not available in industrial drives. According to the voltage feedback criterion, three main categories of FW strategies are identified:

- feed-forward architectures, which do not implement any voltage feedback;
- feedback schemes, where only a voltage feedback provides the FW operation;
- hybrid methods, which couple both a voltage feedback and feed-forward action.

All these topologies have been deeply investigated in the literature and each of them has its own benefits. In the following, each category is reviewed, considering first drives which implement synchronous current PIs.

11.2.1 *Feed-Forward Schemes*

Feed-forward schemes are known also as model-based methods. In fact, this technique consists of computing the FW d-axis current reference by exploiting an accurate analytical model of the motor, e.g., the voltage balance equation as in [69]. A block scheme representation of feed-forward structures is reported in Fig. 11.3, including some aspects that may be taken into consideration when the feed-forward term is computed. The required inputs by the algorithm are the torque reference, which comes from a speed regulator, the motor speed and all the electric motor parameters, i.e., the stator windings resistance and, possibly, the current to flux linkages relationship [13]. All the asterisks in Fig. 11.3 denote reference variables. The same notation is used hereinafter.

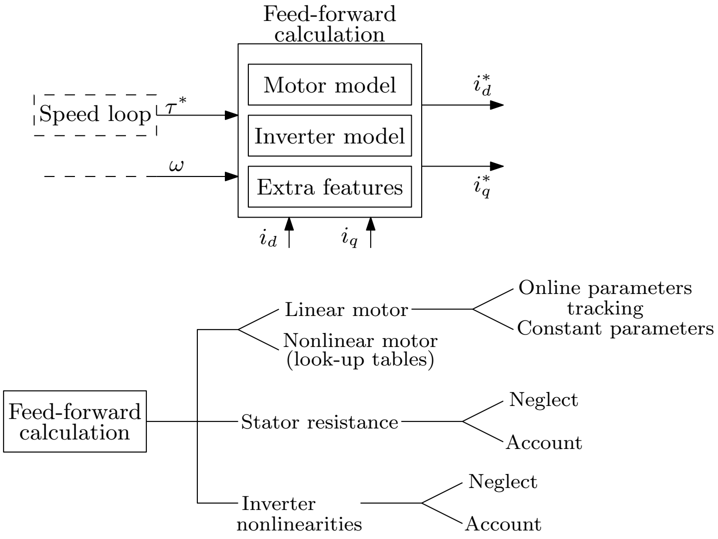

Figure 11.3: Scheme of a standard feed-forward FW control architecture and an overview of the most common features available in the literature for the feed-forward term calculation.

The most relevant advantage of this approach is a superior behavior during fast transients. Indeed, the dynamic performances of feedback type schemes are slow down by the closed-loop dynamic of the voltage loop. Moreover, as further merits, feed-forward methods are not affected by significant stability problems [47] and no tuning parameters are necessary.

However, a pure open-loop computation of the FW current reference can be badly affected by any parameter mismatch. Since FW operation is often required in demanding applications, such as the automotive, the parameter sensitivity issue needs to be addressed. Most of the works on feed-forward schemes of the last two decades aim to overcome this problem. In particular, the temperature effect on the stator resistance and the nonlinear magnetic characteristic have been deeply analyzed.

In [10], the iron saturation effect is addressed by an online estimation of the electric motor inductive parameters. The paper focuses on an IPM machine, but the method can be easily implemented for other highly saturated motor topologies, e.g., pure REL machines or PM assisted REL motors. However, the work neglects the effect of the stator resistance.

The latter is studied in [97], where the stator resistance is included in the computation of the current set points during the FW operation. Moreover, the computational burden of the scheme is reduced by approximating the elliptical voltage constraint in a piece-wise linear manner. The latter method appears indeed as the benchmark for feed-forward solutions. Look-up-tables may be too small because of hardware limitations. In this case, advanced computational tools are available to expand small tables to larger ones, such as the second-order bilinear interpolation method [102]. More and more detailed model [28] may be implemented in order to improve the current reference generation. For example, the inverter nonlinear voltage drop are included in [105], too. However, the computation burden increases with the complexity of the model. Thus, the main advantages of the feed-forward architecture is its simplicity. When the model becomes too cumbersome, it is convenient to prefer feedback-based solutions. Despite all the improvements, it is worth reminding also that the available DC-bus of the inverter is rarely entirely exploited by feed-forward algorithms, since a small derating needs to be introduced to deal with the parameter sensitivity issue.

11.2.2 *Feedback Schemes*

Feedback schemes [45, 99] implement a feedback on the inverter reference voltages to reach the FW operation. This topology is also known as robust, to further highlight the key benefit with respect to feed-forward architectures. The plant model is not explicitly exploited by feedback algorithms. However, the electric model is required for tuning the voltage loop regulator. In addition, an accurate model knowledge results mandatory to linearise the loop, as will be clear in the following. The two merits of the feedback solutions are the enhanced parametric robustness and a higher exploitation of the available inverter DC-bus voltage. However, the voltage control loop introduces a delay in the FW response. Thus, dynamic performances are slightly penalized. Moreover, the additional control loop poses many challenges, e.g., tuning, linearisation and selection of a reasonable bandwidth.

Feedback topologies are subdivided in two subcategories, depending on how the loop acts on the current references coming from the speed loop. In particular, it is possible to distinguish between solutions acting on the angle of the MTPA current references [81, 111] and solutions acting on the d-current reference [68, 74]. The control schemes are reported in Fig. 11.4 whereas their operating principle is depicted in Fig. 11.5. The two different approaches affect both control effectiveness and regulator tuning. It is worth noting that the voltage loop linearization deeply differs between the two schemes.

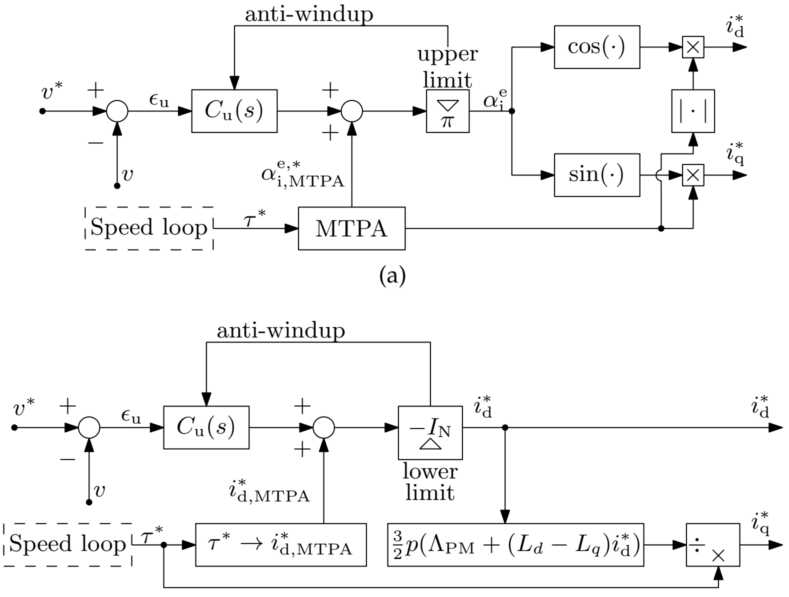

(a)

(b)

Figure 11.4: Feedback flux weakening control architectures. (**a**) Flux weakening voltage loop with angle control. (**b**) Flux weakening voltage loop with i_d control.

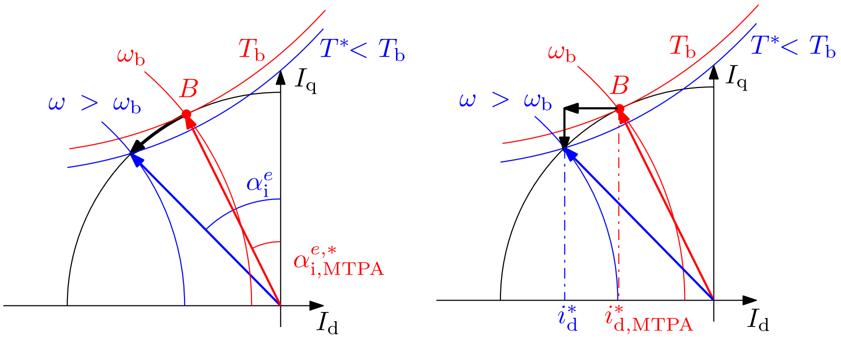

(a) (b)

Figure 11.5: Principle of angle and current correction in feedback FW schemes. (**a**) Angle current vector diagram control scheme. (**b**) Direct current vector diagram control scheme.

An interesting configuration was proposed in [63] where the voltage error generates two auxiliary control variables. The former acts on the MTPA current reference angle, increasing the FW current component. The latter is used when the current amplitude needs to be limited if the MTPV operation is reached. The voltage loop is often designed in a model-based fashion to accomplish the desired specifications in terms of bandwidth and phase margin. Alternatively, the tuning can be performed using a modified relay feedback tuning, as proposed in [92]. This method represents a promising solution for general purpose applications, where motor parameters are partially or completely unknown and an online auto-tuning procedure is needed.

Unfortunately, the dynamic of the current angle is strongly nonlinear. Moreover, a linearization of the angle loop would require the computation of a non trivial linearizing gain. From this point of view, the d-axis current strategy appears more convenient [23]. The loop linearization requires an accurate knowledge of the electric motor model and system parameters and the operating speed as auxiliary input of the voltage loop.

Feedback based strategies are adopted for HEPM motors [24], as well. However, the voltage loop is used to regulate the rotor excitation current, instead of the d-axis stator windings current. This is still an open research topic since new motor topologies combining PM and current winding to generate the rotor flux linkage have been proposed. Different hybridization ratio leads to an additional degree of freedom in the control that it can be exploited. Moreover, in HEPM motors, the excitation current affects the motor voltage equation than the linearization approach [23] is no longer valid and a different dissertation must be studied.

Particular attention needs to be paid to avoid the wind-up phenomenon in the voltage loop. Thus, a back-calculation anti-windup strategy is proposed in [107]. As a further relevant contribution, the same paper proposes an adaptive velocity particle swarm optimization algorithm to optimize the control parameters of the anti-windup proportional and integral controller. Once the desired architecture is selected, a proper bandwidth of the voltage loop needs to be chosen. In case of d-axis current compensation schemes, shown in Fig. 11.4b, three different approaches are proposed in [47]. In a nutshell, the bandwidth can be selected based on specifications of torque disturbance transients, fast acceleration transients or quick variation of the grid voltage.

11.2.3 *Hybrid FW Schemes*

Finally, mixed or hybrid FW schemes are shortly reviewed. Hybrid architectures include both a voltage control loop and a feed-forward term. As feed-forward schemes, the feed-forward contribute is computed by means of the motor model. As feedback structures, the reference d-axis current or current angle is then modified accordingly to the output of the voltage loop.

This allows us to reinforce the feed-forward action. Not surprisingly, mixed schemes aim to guarantee the benefits of both aforementioned structures, namely, fast dynamic and robustness against parameter variations. Examples of hybrid FW schemes can be found in [54, 96, 113].

11.2.4 *Model Predictive Control*

An emerging and promising control structure in electric motor drives is represented by the model predictive control. Few preliminary works are found in the literature concerning the FW operation, e.g., [71], resulting an appealing topic for academic research. Model predictive control is mostly used to replace the d- and q-axis current regulators, rather than acting on the generation of the FW current references as in [58]. The d-axis FW current reference is generated by a standard feed–forward algorithm, whereas the model predictive control takes care of the current reference tracking, as shown in Figure 11.6. A model predictive control is designed for the voltage control loop of a feedback strategy in [27]. The authors believe that the complexity and non linearity of the problems have not entirely been addressed yet.

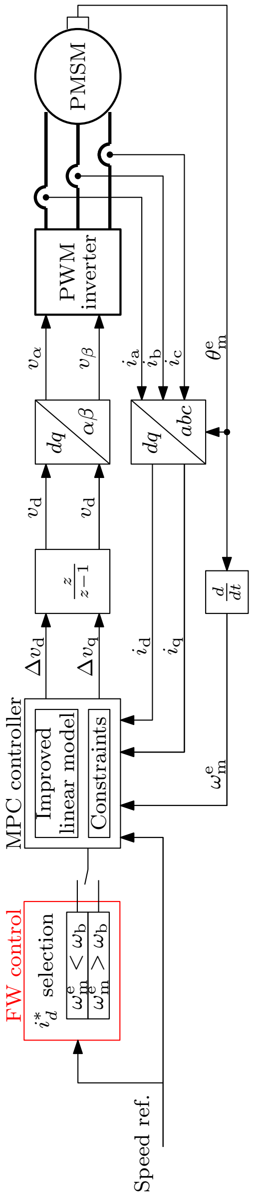

Figure 11.6: FW scheme of a MPC drive.

11.2.5 *Sensorless Control*

Nowadays, a crucial requirements for industrial drives is the sensorless operation capability. In other words, the motor needs to be controlled without the position sensor to increase the reliability of the system and to reduce the product costs. Interesting and challenging issues occur when a drive operates in the FW region without position sensor. For example, the delay introduced by position estimation algorithms could influence FW loops. Indeed, a Luenberger observer is proposed in [55] to replace the low-pass filter in the rotor position estimation. Thanks to the proposed observer, the motor speed estimation delay was reduced. The delay can be further reduced by means of even more sophisticated position estimators, such as the extended Kalman filter [22]. However, attention must be taken to keep the computation burden at bay when coupling a voltage loop, a position observer and, possibly, current-flux linkage look-up tables.

Instability problems of sensorless FW operation are analyzed recently in [109], considering both feedback and feed-forward strategies. In particular, it has been analytically proven that the limited bandwidth of the position estimation can induce speed oscillations, which increase when approaching the FW operation. The system may even become unstable. This is mainly due to the position estimation error and it is worsened in fast transients. Thus, from this point of view, low-inertia drives result to be particularly challenging.

Some of these control startegies will be tested and validated on HEPM motor. The next step will focus on the validation of the HEPM model.

12

HEPM MODEL

In this Chapter the HEPM model is described. Rotor coordinates are adopted for the analysis of HEPM motors, namely the *dq* reference frame, synchronous to the rotor position and aligned along the permanent magnet axis. The quantities are all marked with small symbols to indicate the time variant. The effects of spatial flux-linkage harmonics and temperature are omitted. Under such hypotheses, the dynamic voltage balance model of the HEPM motor results:

$$\begin{aligned}\frac{d\lambda_d(i_d, i_q, i_e)}{dt} &= v_d - R_s i_d - \omega_m^e \lambda_q(i_d, i_q, i_e)\\ \frac{d\lambda_q(i_d, i_q, i_e)}{dt} &= v_q - R_s i_q + \omega_m^e \lambda_d(i_d, i_q, i_e) \\ \frac{d\lambda_e(i_d, i_q, i_e)}{dt} &= v_e - R_e i_e\end{aligned} \qquad (12.1)$$

where v_d, v_q and i_d, i_q are the *dq* stator voltage and current components, v_e and i_e are the rotor excitation voltage and current, respectively. R_s and R_e represent the stator and rotor windings resistances, while ω_m^e is the angular electric frequency. Finally, $\lambda_d(\cdot)$, $\lambda_q(\cdot)$ and $\lambda_e(\cdot)$ are the stator and rotor flux linkages, which all depends on the operating current set-point. The explicit dependence of flux linkages from stator currents and vice-versa will be reported only when necessary to highlight the nonlinear magnetic relationship. The (12.1) can be condensed in the following compact matrix expression:

$$\frac{d\boldsymbol{\lambda}(\boldsymbol{i})}{dt} = \boldsymbol{v} - \mathbf{R}\boldsymbol{i}(\boldsymbol{\lambda}) - \omega_m^e \mathbf{J}\boldsymbol{\lambda}(\boldsymbol{i}), \qquad (12.2)$$

being $\boldsymbol{v} = [v_d,\, v_q,\, v_e]^T$, $\boldsymbol{\lambda} = [\lambda_d,\, \lambda_q,\, \lambda_e]^T$, $\boldsymbol{i} = [i_d,\, i_q,\, i_e]^T$,

$$\boldsymbol{R} = \begin{bmatrix} R_s & 0 & 0 \\ 0 & R_s & 0 \\ 0 & 0 & R_e \end{bmatrix}, \text{ and } \boldsymbol{J} = \begin{bmatrix} 0 & 1 & 0 \\ -1 & 0 & 0 \\ 0 & 0 & 0 \end{bmatrix}.$$

It is worth highlighting the explicit dependency of flux linkages $\boldsymbol{\lambda}(\boldsymbol{i})$ and currents $\boldsymbol{i}(\boldsymbol{\lambda})$.

Fig. 12.1 shows the current-to-flux linkage characteristics of a HEPM motor, obtained by FE and available as look-up tables (LUTs). It is worth remarking that the figure shows the flux-linkage surfaces for the minimum and maximum excitation current values, namely, $i_e = -3\,A$ and $i_e = 3\,A$ respectively. A current set-point $\boldsymbol{i} = [i_d,\, i_q,\, i_e]^T$ is mapped in the *d*-axis flux linkage set point $\Lambda_d(i_d,\, i_q,\, i_e)$ lying in the volume between the two surfaces depicted in Fig. 12.1, with

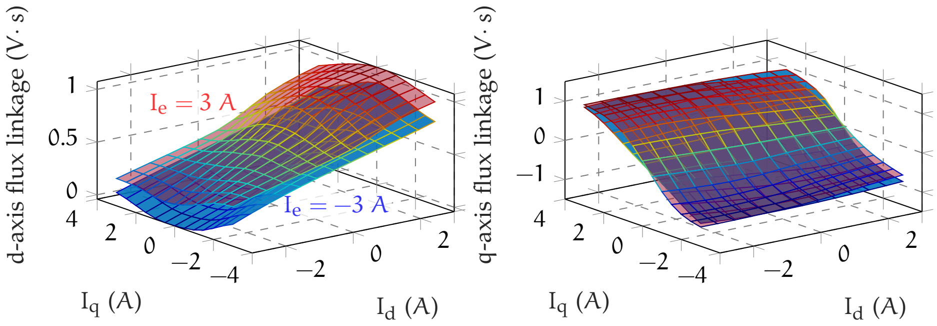

(a) *d*-axis flux linkage.

(b) *q*-axis flux linkage.

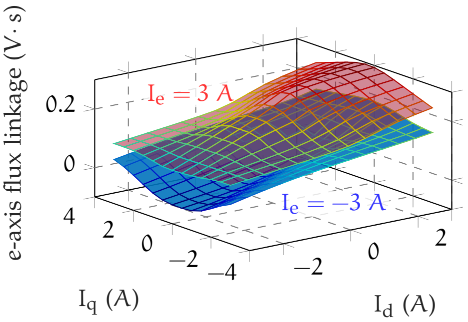

(c) *e*-axis flux linkage.

Figure 12.1: HEPM motor current-to-flux linkage characteristics for the minimum and maximum rotor excitation current i_e.

$\sqrt{i_d^2 + i_q^2} \leqslant I_N$ and $\|i_e\| \leqslant I_{e,N}$ where I_N and $I_{e,N}$ are the stator and rotor rated current values, respectively. A closer look to the curves reveals that the cross magnetic coupling is not negligible both between the *d* and *q*-axis, and between the *e* and *q*-axis. The λ_d and λ_e surfaces are function of the *q*-axis current. Moreover, concerning the λ_e map, the effect of i_e is strongly nonlinear. Indeed, i_e does not simply increase λ_e, but it significantly changes the shape of the flux surfaces, too. As a further remark, considering the low reluctance axis (*q*-axis), the iron saturation effect on the λ_q characteristic is relevant, leading to non planar surfaces.

12.1 HEPM MOTOR INVERSE MODEL

Reproducing the HEPM motor electrical behavior means solving the ordinary differential equation (ODE) (12.2) in a simulation environment. Since currents and flux-linkages appear on both sides of the equations, the equation solution is not trivial. For this reason, flux-based and current-based models have been proposed. Regardless of the adopted approach, the input information is always the current-to-flux characteristics $\boldsymbol{\lambda}(\boldsymbol{i})$ since it can be easily obtained by means of FE simulations or experimental measurements. However, it is worth re-

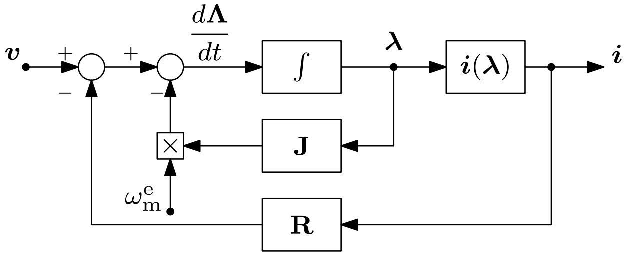

Figure 12.2: Flux-linkage model of a HEPM motor.

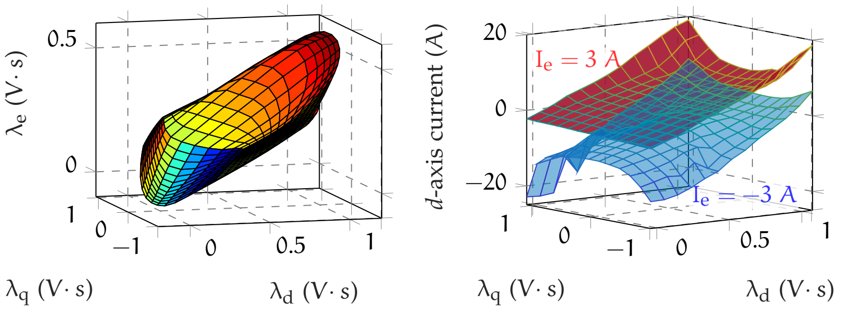

(a) Flux linkage map in $\lambda_d, \lambda_q, \lambda_e$ coordinates.

(b) i_d map for maximum and minimum i_e.

Figure 12.3: HEPM motor flux linkage-to-current characteristics for the minimum and maximum rotor excitation current i_e.

membering that is not trivial to directly measure the excitation rotor flux λ_e.

12.1.1 *Flux-based description*

A flux-linkage based model for HEPM motor can be implemented in a simulation environment by solving equation (12.1), as reported in Fig. 12.2. The ODE model (12.2) is solved adopting the flux-linkages as unknown, while the static nonlinear 3D map $\boldsymbol{i}(\boldsymbol{\lambda})$ permits to retrieve the motor currents. Even if one nonlinear map is required only, the $\boldsymbol{i}(\boldsymbol{\lambda})$ map turns out to be hard to compute given the available currento-to-flux linkage $\boldsymbol{\lambda}(\boldsymbol{i})$ characteristics.

Direct LUTs (Fig. 12.1) provide the flux-linkage set-points for a 3D i_d, i_q, i_e input current grid with $\|i_d\| \leqslant I_N$, $\|i_q\| \leqslant I_N$ and $\|i_e\| \leqslant I_{e,N}$. Hence, the input current domain has a cubic shape. It is mapped into a flux-linkage output solid domain shown in Fig. 12.3a in $\Lambda_d - \Lambda_q - \Lambda_e$ coordinates. The output domain results very thin and tilted. The inverse $\boldsymbol{i}(\boldsymbol{\lambda})$ static map should have the domain of Fig. 12.3a as support. Defining a regular mesh grid on such a nonlinear support is not trivial. In order to compute $\boldsymbol{i}(\boldsymbol{\lambda})$ as LUTs, a mesh grid need to be defined anyway.

Two approaches are adoptable for defining a suitable mesh grid. On one side, one could find the biggest cuboid inscribed in the solid

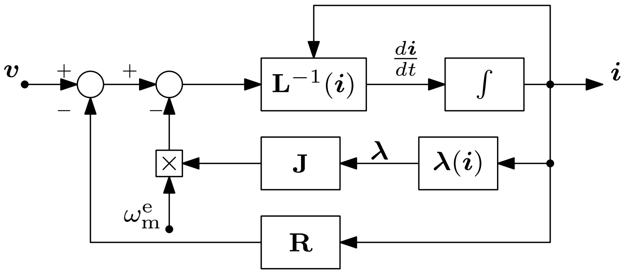

Figure 12.4: Current model of a HEPM motor.

of Fig. 12.3a. Then, the inverse characteristics $i(\boldsymbol{\lambda})$ could be reconstructed within such a cuboid. This approach assures that the resulting currents $i(\boldsymbol{\lambda})$ belong to the domain for which the direct current-to-flux-linkage map $\boldsymbol{\lambda}(i)$ is available. However, it has a relevant drawback, as a small cuboid would be found, being the solid of Fig. 12.3a particularly thin and stretched. A current map with a reduced domain is achievable, covering only partially the HEPM motor current operating region. Moreover, plenty of information carried by the direct maps (Fig. 12.1) is discarded. On the other side, one could choose instead the smallest cuboid containing the solid of Fig. 12.1, aiming to exploit all the available flux-linkage set-points. As a drawback, not all points belonging to the defined domain lie in the original function $i(\boldsymbol{\lambda})$ domain, so it is not possible to obtain the corresponding value by interpolation. The lack of information about the HEPM motor behavior in those regions, lead the extrapolations as unique strategy to get the remaining values, without any guarantee on the model reliability. This issue is visualized by means of Fig. 12.3b, reporting the inverse $i_d(\lambda_d, \lambda_q, \lambda_e)$ characteristic. Current values span a much larger domain with respect to the one for which the direct current-to-flux map is available (Fig. 12.1). In particular, Fig. 12.1 is obtained for $i_d \in [-3\,\text{A}, 3\,\text{A}]$, while the interpolated inverse characteristic outputs $i_d \in [-20\,\text{A}, 20\,\text{A}]$. Larger direct maps could mitigate the issue. However, larger maps may be obtained via FE only, since experimental measurements are precluded, as high current load are dangerous for the motor.

12.1.2 *Current-based description*

The current-based representation of HEPM motors is obtained by applying the chain rule to (12.1) and by substituting the flux linkages with a function of the motor currents:

$$\frac{d\boldsymbol{\lambda}(i)}{di}\frac{di}{dt} = \mathbf{L}(i)\frac{di}{dt} = v - \mathbf{R}i - \omega_m^e \mathbf{J}\boldsymbol{\lambda}(i), \tag{12.3}$$

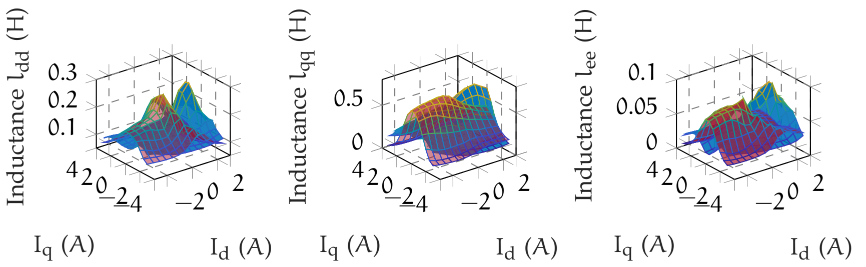

(a) *d*-axis incremental inductance.

(b) *q*-axis incremental inductance.

(c) *e*-axis incremental inductance.

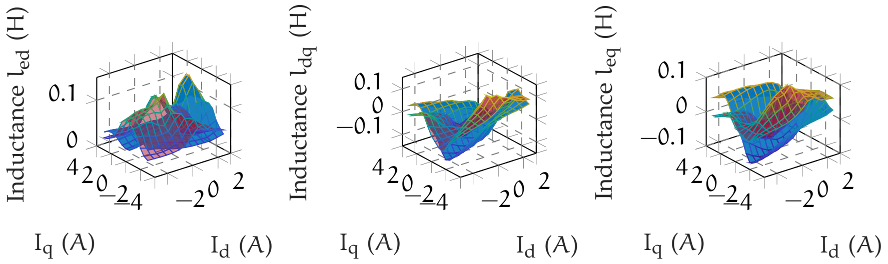

(d) *e-d* cross incremental inductance.

(e) *d-q* cross incremental inductance.

(f) *e-q* cross incremental inductance.

Figure 12.5: Current model of a HEPM motor. Fig 12.5a-12.5c show the incremental auto inductances, whereas Fig 12.5d-12.5f show the incremental cross inductances. All the inductances are provided for the minimum and maximum i_e values.

where $\mathbf{L}(\boldsymbol{i})$ is the incremental inductance matrix, i.e. the Jacobian matrix containing the gradient of the flux-linkage curves with respect to the motor currents:

$$\mathbf{L}(\boldsymbol{i}) = \begin{bmatrix} l_{dd} = \dfrac{\partial \lambda_d}{\partial i_d} & l_{dq} = \dfrac{\partial \lambda_d}{\partial i_q} & l_{de} = \dfrac{\partial \lambda_d}{\partial i_e} \\ l_{qd} = \dfrac{\partial \lambda_q}{\partial i_d} & l_{qq} = \dfrac{\partial \lambda_q}{\partial i_q} & l_{qe} = \dfrac{\partial \lambda_q}{\partial i_e} \\ l_{ed} = \dfrac{\partial \lambda_e}{\partial i_d} & l_{eq} = \dfrac{\partial \lambda_e}{\partial i_q} & l_{ee} = \dfrac{\partial \lambda_e}{\partial i_e} \end{bmatrix} \tag{12.4}$$

Being the current-to-flux linkage characteristics nonlinear, all the matrix components depend on the current operating set-point. Such dependence is omitted in the equations to ease the notation. Fig. 12.4 reports the resulting dynamic model. In particular, the ODE model (12.3) is solved with respect to the motor currents. Two nonlinear static maps are needed in the solution, i.e. $\mathbf{L}(\boldsymbol{i})$ and $\boldsymbol{\lambda}(\boldsymbol{i})$.

The major advantage of the current approach consists in the fact that inverse $\boldsymbol{\lambda}(\boldsymbol{i})$ maps are not required, avoiding all the issues discussed in the previous section. The inversion of a nonlinear 3D function is replaced by the inversion of the incremental matrix $\mathbf{L}(\boldsymbol{i})$ (see Fig. 12.4), which is more affordable, provided that a good and smooth approximation of the incremental inductances is available. The law of

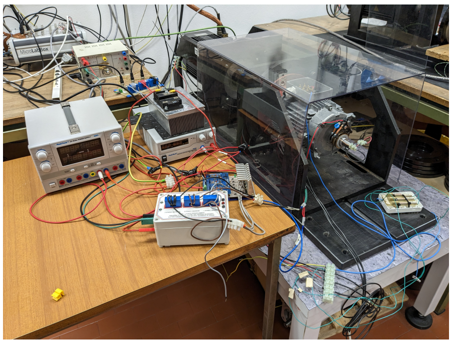

Figure 12.6: Test bench layout.

conservation of energy eases the computation of $\mathbf{L}(\boldsymbol{i})$ matrix, exploiting its reciprocity. In fact, it turns out that $l_{dq} = l_{qd}$, $l_{de} = \frac{2}{3} l_{ed}$ and $l_{qe} = \frac{2}{3} l_{eq}$.

Fig. 12.5 shows all the incremental inductances of the considered HEPM motor. It is remarkable that both l_{dq} (Fig. 12.5e) and l_{eq} (Fig. 12.5f) share the same order of magnitude with l_{ed} (Fig. 12.5d). However, state-of-the-art current-based models [65] neglect the effects of the latter two inductances, whereas only the former one is always included in the modeling. In other words, only the excitation winding and direct axis coupling is taken into account and $l_{dq} = l_{eq} = 0$ is assumed. Differently from the state-of-the-art, the proposed current-based model accounts for all the incremental inductances.

12.2 MODEL VALIDATION

The analysis of Sec. 12.1 revealed that the current-based model is preferable for describing the electric behavior of HEPM machines. The encoding of $\boldsymbol{i}(\boldsymbol{\Lambda})$ remains an open issue for the flux-linkage based representation. Thus, the current-based model of Sec. 12.1.2 is considered in the validation. In particular, two ad-hoc experiments were designed to highlight the presence of magnetic cross-coupling in HEPM motors, usually neglected in the conventional models. The motor under test was controlled in current mode during both tests, while a load motor keeps the system at standstill. Fig. 12.6 shows the test-bed layout. The HEPM motor stator winding was fed by a three-phase two-level converter, while an H-bridge regulates the rotor winding current. Tab.20 reports some relevant HEPM motor parameters.

12.2.1 *Effect of the cross magnetic coupling*

The first experiment was aimed at verifying the non-negligible cross coupling between all system axes, namely, direct, quadrature and excitation one. It is composed by two tests in which the reference system used for injection changes. First, a sinusoidal voltage is injected on

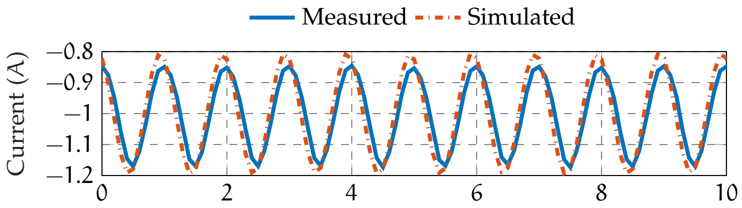

(a) *d*-axis current.

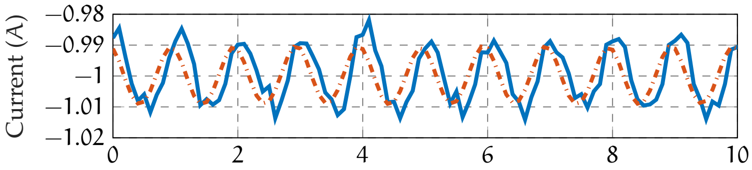

(b) *q*-axis current.

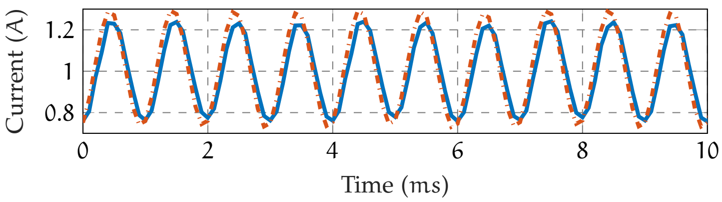

(c) *e*-axis current.

Figure 12.7: Measured current response of the HEPM motor to a sinusoidal voltage excitation on the *d*-axis. Dashed waveforms represent the expected responses, obtained by applying the same sinusoidal voltage to the current model of Sec. 12.1.2, whereas continuous line were measured on the test bench.

the *d*-axis of the motor, having a 1 kHz frequency and an amplitude of 100 V. According to state-of-the-art models, the injection would induce sinusoidal oscillations only on the *d*-axis and rotor currents. These oscillations are shown in Fig. 12.7a and 12.7c, representing indeed the two most evident effects of the voltage injection. However, Fig. 12.7b reveals that the *q*-axis current oscillates, as well. Thus, the hypothesis $l_{dq} = 0$ needs to be waived to accurately describe the machine behavior. Fig. 12.7 reports the estimated motor currents, obtained by applying the same voltage of the experiment to a simulation model as the one shown in Fig. 12.4, including the l_{dq} and l_{eq} characteristics obtained by FE. The proposed simulation model accurately predicts the amplitudes of all the current oscillations. In particular, the magnetic cross-coupling is properly estimated. Small discrepancies are justified by the measurement noise and by differences between the actual HEPM motor behavior and the curves computed by means of FE.

The second test consists of a quadrature axis voltage injection. A lower injection frequency was adopted, i.e. 500 Hz, to increase the induced currents, since the *q*-axis incremental inductance is higher than the *d*-axis one (see Fig. 12.5a and 12.5b). According to the state-of-the-

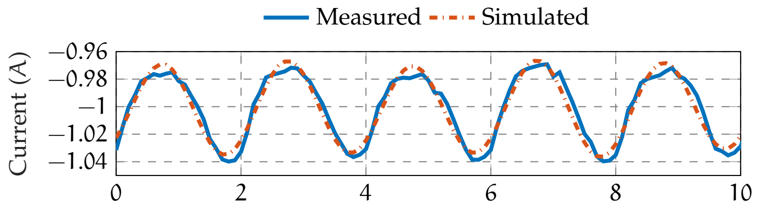

(a) *d*-axis current.

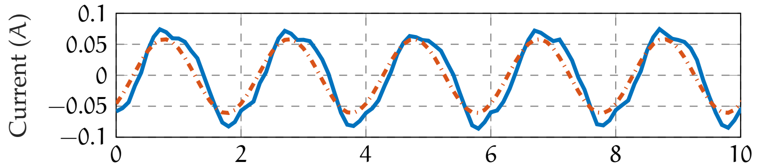

(b) *q*-axis current.

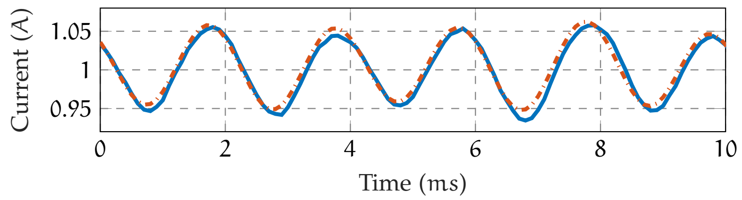

(c) *e*-axis current.

Figure 12.8: Measured current response of the HEPM motor to a sinusoidal voltage excitation on the *q*-axis. Dashed waveforms represent the expected responses, obtained by applying the same sinusoidal voltage to the current model of Sec. 12.1.2, whereas continuous line were measured on the test bench.

art models, the expected effect is only a sinusoidal oscillating of *q*-axis current. Similarly to the previous case, this effect is indeed the dominant one. However, due to the magnetic cross-coupling, the effects of the voltage injection are evident both on the *d*-axis (Fig. 12.8a) and on the excitation winding (Fig. 12.8c). Thus, both l_{dq} and l_{eq} need to be modeled to simulate the observed behavior.

12.2.2 *Low speed sensorless application*

Sinusoidal high-frequency voltage signals are widely used in low-speed sensorless applications [76, 103] to estimate the electric motor angular position, allowing the position sensor removal. However, when synchronous motors operate in sensorless mode, the estimated rotor position differs from the actual one due to magnetic cross saturation. The induced open-loop estimation error $\widetilde{\vartheta}_{me}$ is critical and it could lead performance degradation as well as stability issues. The models developed in this paper allow the analyze these effects.

With HEPM motor topology, a high-frequency voltage signal can be injected either on the stator winding [103] or on the rotor winding.

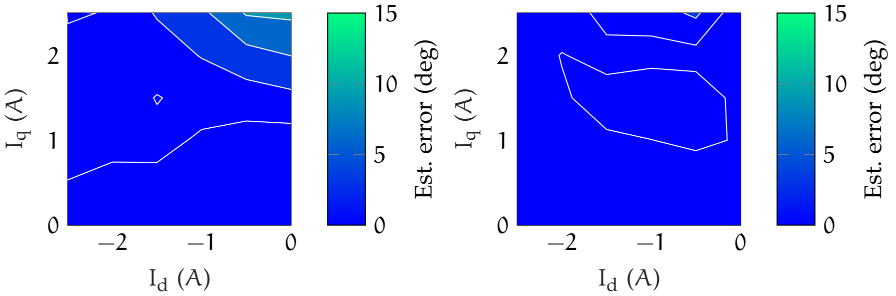

(a) Position estimation error, $I_e = 0\,A$.

(b) Position estimation error, $I_e = 3\,A$.

Figure 12.9: Open-loop position estimation error with high-frequency stator injection-based position estimators.

In the former case, the position estimation error $\tilde{\vartheta}_{me}$ can be computed as [11]:

$$\tilde{\vartheta}^e_m = \frac{1}{2}\arctan\frac{2l_{dq}l_{ee} - 3l_{de}l_{qe}}{\left(3/2(l^2_{de} - l^2_{qe}) - (l_{dd} - l_{qq})l_{ee}\right)}. \tag{12.5}$$

Fig. 12.9 reports the computed error starting from the current-to-flux-linkage characteristics for two different excitation current values. In the latter case, the error becomes [32]:

$$\tilde{\vartheta}^e_m = \arctan\frac{l_{dd}l_{qe} - l_{de}l_{dq}}{l_{de}l_{qq} - l_{dq}l_{qe}}. \tag{12.6}$$

Fig. 12.10 shows the error in the same operating condition as Fig. 12.9, assuming a rotor voltage signal injection. It is worth highlighting that both the *d*-*q* and *e*-*q* cross-couplings are relevant for the error expressions (12.5) and (12.6). Thanks to the proposed current-based model, practitioners can evaluate the sensorless capability of the HEPM machine starting from the incremental inductance values (Fig. 12.5). In particular, comparing Fig. 12.9 and Fig. 12.10, designers realize that a stator excitation is more suitable for the considered machine, since lower position estimation errors are achieved in most of the *dq* current plane for both the analyzed excitation current rates.

12.3 DISCUSSION

Current and flux-based dynamic model are investigated in this chapter for the analysis and simulation of hybrid excited permanent magnet motors. The current-to-flux linkage characteristics inversion issues are discussed, which are related to the inversion of a three-dimensional nonlinear map. A current-based model is found to be more suitable for the considered motor topology, since it allows the avoidance of the inversion issue.

Magnetic cross-couplings are not negligible for hybrid excited permanent magnet machines, compared to conventional model in the

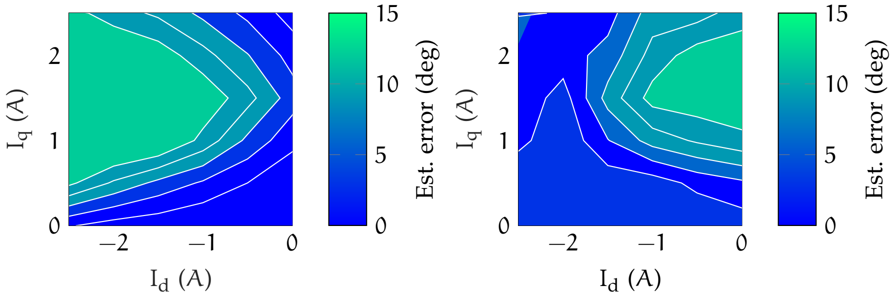

(a) Position estimation error, $I_e = 0$ A. (b) Position estimation error, $I_e = 3$ A.

Figure 12.10: Open-loop position estimation error with high-frequency rotor injection-based position estimators.

Parameter	Value
PM flux-linkage	0.524 V· s
Excitation winding flux-linkage	0.213 V· s
Total rotor flux-linkage	0.737 V· s
d-axis inductance (unsaturated)	141 mH
q-axis inductance (unsaturated)	540 mH
Saliency ratio	3.83 -
Nominal torque	5.3 N· m
Nominal speed	540 r/min
Nominal stator current	2 A
Nominal rotor current	3 A

Table 20: HEPM motor parameters.

literature. Experiments on a prototype machine validate the presence of these couplings. Moreover, a good agreement is found between the proposed current-based model and measured quantities. Finally, a low-speed sensorless control is considered as case-study for the application of the proposed model. In particular, thanks to the accurate motor description, the sensorless capabilities of hybrid excited permanent magnet motors can be evaluated in advance, helping the designers selecting of the more suitable sensorless technology.

13

MTPA CONTROL ALGORITHMS

HEPM motors are characterized by stator current-to-flux linkages characteristics which strongly rely on the excitation currents. For a given excitation current, stator current-to-flux linkage map is non-linear and affected by a remarkable magnetic coupling, thus high cross-differential inductances. The relevant magnetic saturation and the excitation current dependency on the stator flux linkages make the sensorless operation particularly challenging.

In literature, compensation methods have been proposed to address the position error due to the cross-differential inductances and to extend the stable operating region of the position estimator [62]. However, HEPM machines have an additional degree of freedom, i.e. the excitation winding current, that can be exploited for improving the self-sensing capabilities. To improve the dynamic motor performance, the excitation current reference is commonly set at its rated values, regardless the torque request. Then, to minimize the stator windings Joule losses, the HEPM torque is delivered by using the MTPA control policy [7].

This Chapter proposes: as first, the Maximum Torque Per Ampere control policy minimizing both stator and rotor Joule losses for each torque load requirement, then, secondly, an innovative control policy for HEPM machines has been developed. Such strategy aims first to maximize the self-sensing capabilities of the motor, i.e. to minimize the sensorless position error due to the cross-differential inductance, then to minimize the overall Joule losses. This control strategy is colled optimal sensorless policy (OSP). Both MTPA and OSP are built by using a two-step procedure. Given a reference torque, MTPA policy find the minimum stator and rotor current that gives the lower losses,for several excitation currents. While OSP method optimizes the stator currents reference in terms of position estimation error, for several excitation currents. In the second step, a further optimization is performed among the outcomes set-points of the first step, focusing on the maximization of the drive efficiency in terms of stator and rotor windings Joule losses.

13.1 MTPA POLICY

The MTPA trajectory, considering the stator and rotor losses minimization, is particulary interesting for HEPM motors.
Starting from analytical motor equations, a numerical solution that minimized the HEPM motor losses can be computed, as reported in

(7.8). The analytical equations provide a significant solution, but they do not consider the intricate no-linearity intrinsic to the system. No-linearity affected the real prototypes, and are included through FE analysis or test bench measurement inside the model, as illustrated in Fig. 12.1. This model reports the steady state relationship between stator current and magnetic flux for each rotor current.

Recognizing this, the no-linear behavior of the system must be considered. To this end, new trajectories considering the measured maps are computed, considering both magnetic saturation and cross-coupling effects.

13.1.1 *Benchmark Control Policy*

The delivered torque by an HEPM motor is computed as:

$$T = \frac{3}{2} p \boldsymbol{\Lambda}_{\mathbf{dq}}^{T} \mathbf{J}^{T} \boldsymbol{I}_{dq}. \tag{13.1}$$

where $\boldsymbol{\Lambda}_{\mathbf{dq}} = [\Lambda_d, \Lambda_q]$, $\boldsymbol{I}_{dq} = [I_d, I_q]$ and the superscript $\cdot^T$ denotes the vector transposition. As for other synchronous motor topologies, the MTPA policy can be adopted for HEPM machines [101]. The maximum torque is achieved by setting the excitation current to its rated value. Then, the stator current reference is selected in order to minimize the stator Joule losses. For a given torque request T^*, the stator currents reference $\boldsymbol{I}_{dq}^*$ is found by solving:

$$\min_{\boldsymbol{I}_{dq}^*} \|\boldsymbol{I}_{dq}^*\|, \text{ s.t. } T = T^*, \tag{13.2}$$

where the operator $\|\cdot\|$ denotes the euclidean norm,. The problem can be solved by exploiting the nonlinear magnetic maps shown in Fig. 13.3 and Fig. 13.4 [40]. Then, the resulting current trajectory can be implemented in the electric drive by means of a look-up table. It is worth noticing that the MTPA control policy does not guarantee the maximum efficiency in the torque delivery, since the excitation winding losses are neglected in the optimization problem (13.2). The proposed simplification reduces the tuning effort for the excitation current, as it is kept constant.

An example of the MTPA control policy is presented in Fig. 13.1. This figure displays the relationship between the rotor current (I_e) and the stator currents (I_d and I_q) necessary to achieve a prescribed torque (T). Notably, the rotor current starts with low values and progressively increases as the torque requirement rises. These current combinations are optimized to minimize losses for a given torque selection.

The computation process behind each data point combination is showed in Fig. 13.2. Specifically, an instance with $T = 5\,\mathrm{N \cdot m}$ is depicted, showcasing five different rotor current values. The calculation

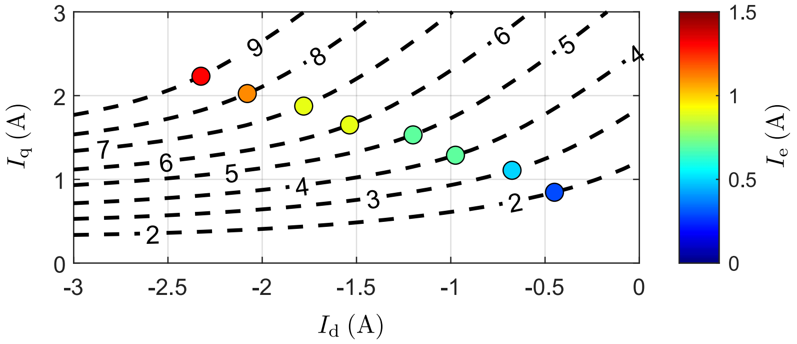

Figure 13.1: I_e, I_d I_q optimal combination to achieve a selected torque T in (i_d, i_q) current plane.

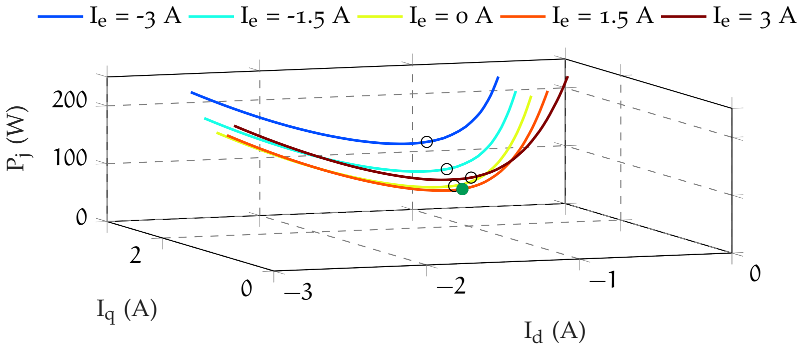

Figure 13.2: Overall joule losses computation for different I_e, considering a torque $T = 5\,N \cdot m$.

of Joule losses for all data points capable of producing a torque of $T = 5\,N \cdot m$ is carried out for five rotor current values: I_e = [-3, -1.5, 0, 1.5, 3] A. Each set of excitation currents defines a unique curve line, with the point of minimum losses indicated by an open circle. The filled green circle corresponds to the configuration that yields the lowest Joule losses considering all the planes. By extending this procedure across multiple rotor current planes and various torque references, the resulting plot is shown in Fig. 13.1. This process is widely documented in the literature [7]. However, it's based on the knowledge of the rotor's position. This is why an innovative MTPA-Sensorless policy, OSP, has been introduced to address this limitation.

13.2 SENSORLESS TRACKING CAPABILITY

Magnetic maps show the stator current-to-flux linkage curve, considering both magnetic saturation and cross-coupling effects. Fig. 13.3 shows the measured d-axis flux Λ_d curves as function of I_d. The curves are reported for two excitation current values, i.e., its minimum and its maximum ones, and for two q-axis currents, namely, zero and nominal rates. Fig. 13.4 reports the measured Λ_q curves as

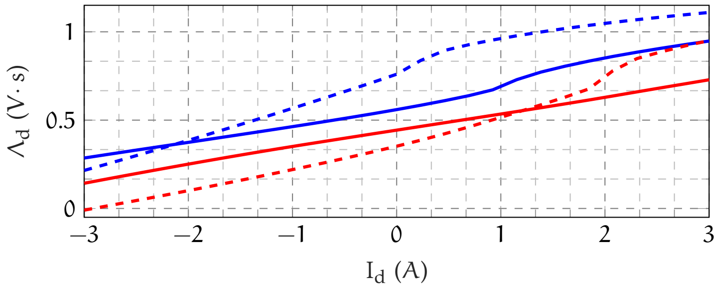

Figure 13.3: *d*-axis flux linkage characteristics for different excitation current and *q*-axis current values.

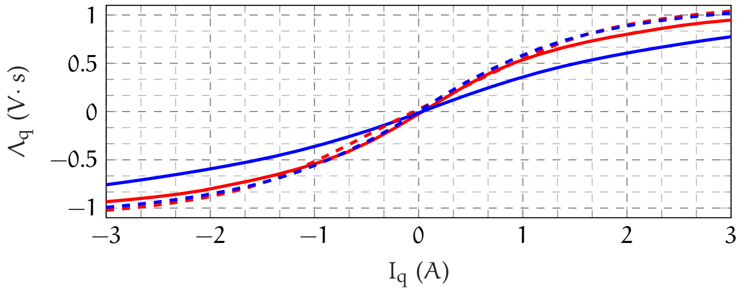

Figure 13.4: *q*-axis flux linkage characteristics for different excitation current and *d*-axis current values.

function of I_q and for two values of excitation currents and *d*-currents as in Fig. 13.3. The minimum and maximum values of excitation current are reported, and zero and nominal I_d current are depicted.

In both figures, the relevant flux linkages dependency on both stator currents and excitation current is evident. The equivalent PM flux linkage, namely the contribution of permanent magnet and excitation winding, can be grasped in Fig. 13.3. Moreover, the *d*-axis is affected by a strong magnetic cross-saturation, i.e. Λ_d varies with I_q for a given I_d. Graphically, solid and dashed Λ_d curves of the same color in Fig. 13.3 are significantly different. In addition, the cross-saturation is influenced by the excitation current, too. The two solid Λ_d curves of Fig. 13.3 differ. The noteworthy dependency of the magnetic cross-saturation from the excitation current is exploited to improve the sensorless capability of HEPM machines. Concerning the *q*-axis flux, the iron saturation effect is certainly the most evident, since the curves in Fig. 13.4 are nonlinear.

The nonlinear magnetic model of HEPM machine implies that the voltage balance equations (12.1) are nonlinear, as well. The linearized version of such equations are obtained by using the chain rule and, in

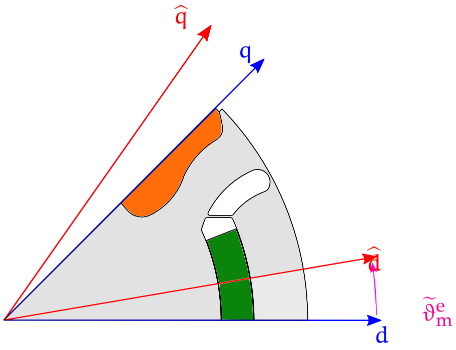

Figure 13.5: Motor *dq* reference frame vs estimated $\widehat{dq}$ reference frame.

particular, the rate of change of the flux linkages can be approximated as:

$$\begin{aligned}\frac{d\Lambda}{dt} &= \begin{bmatrix} \frac{\partial\lambda_d}{\partial i_d} & \frac{\partial\lambda_d}{\partial i_q} & \frac{\partial\Lambda_d}{\partial i_e} \\ \frac{\partial\lambda_q}{\partial i_d} & \frac{\partial\lambda_q}{\partial i_q} & \frac{\partial\Lambda_q}{\partial i_e} \\ \frac{\partial\lambda_e}{\partial i_d} & \frac{\partial\lambda_e}{\partial i_q} & \frac{\partial\lambda_e}{\partial i_e} \end{bmatrix} \frac{d}{dt} \begin{bmatrix} i_d \\ i_q \\ i_e \end{bmatrix} \\ &= \begin{bmatrix} l_{dd} & l_{dq} & l_{de} \\ l_{dq} & l_{qq} & 0 \\ \frac{3}{2} l_{de} & 0 & l_e \end{bmatrix} \frac{d}{dt} \begin{bmatrix} i_d \\ i_q \\ i_e \end{bmatrix}\end{aligned} \tag{13.3}$$

where l_{dd} and l_{qq} are the self-differential inductances, l_{de} is the mutual inductance between the excitation winding and the stator *d*-axis, l_e is the excitation winding self-inductance, while l_{dq} is the cross-differential inductance. It is worth reminding that all the differential inductances depend on the operating point of the HEPM motor, i.e., on $\boldsymbol{I}_{dq}$ and I_e. The cross-coupling between excitation winding and the stator *q*-axis is neglected in the analysis.

13.2.1 *Injection-based Sensorless Scheme*

In low speed region, the rotor position can be retrieved by exploiting rotor anisotropy and high frequency (HF) signal injection. Two different injection schemes can be adopted, namely, the rotating [12] or the pulsating one [77]. In this paper, the latter one is exploited as it exhibits superior performance. It is worth remembering that both injection schemes suffer of cross-differential inductance error equally.

To retrieve the rotor position, a HF sinusoidal voltage signal is injected along the estimated $\widehat{d}$-axis:

$$\widehat{u}_{h,d} = U_h \cos(\omega_h t) \tag{13.4}$$

where U_h and ω_h are the amplitude and the pulsation of the injected voltage signal, respectively. Superscript $\widehat{\cdot}$ denotes variables in the estimated rotor reference frame, depicted in Fig. 13.5. Denoting $\widetilde{\vartheta}^e_m = \widehat{\vartheta}^e_m - \vartheta^e_m$ the position estimation error, the induced HF *q*-axis current due to the voltage injection (13.4) is:

$$\begin{aligned}\widehat{\imath}_{h,q} =& I_h\Big((2l_e l_\Delta - \frac{3}{2}l^2_{de})\sin(2\widetilde{\vartheta}^e_m) \\ &- 2l_e l_{dq}\cos(2\widetilde{\vartheta}^e_m)\Big)\sin(\omega_h t)\end{aligned} \tag{13.5}$$

where $l_\Sigma = (l_{dd} + l_{qq})/2$ is the mean self-differential inductance, $l_\Delta = (l_{qq} - l_{dd})/2$ is the semi-difference of self-differential inductances, and $I_h = U_h/\big(\omega_h(3l_{qq}l^2_{de} + 2l_e l^2_{dq} - 2l_{dd}l_e l_{qq})\big)$.

The rotor position can be obtained by zeroing the HF current along the estimated $\widehat{q}$-axis, namely, $\widehat{\imath}_{h,q}$. It is carried out by exploiting the heterodyne principle and a phase locked loop (PLL) scheme. The HF pulsating current $\widehat{\imath}_{h,q}$ is multiplied by $\sin(\omega_h t)$, and the obtained signal is fed into a regulator which nullifies it. Once the regulator input is driven to zero, the rotor position is estimated.

If cross-differential inductance is neglected, the expression of $\widehat{\imath}_{h,q}$ in (13.5) becomes:

$$\widehat{\imath}_{h,q} = I'_h\left(2l_e l_\Delta - \frac{3}{2}l^2_{de}\right)\sin(2\widetilde{\vartheta}^e_m)\sin(\omega_h t), \tag{13.6}$$

where $I'_h = U_h/\big(\omega_h l_{qq}(3l^2_{de} - 2l_{dd}l_e)\big)$. Thus, zeroing $\widehat{\imath}_{h,q}$ implies that the rotor position is accurately estimated.

The aforementioned hypothesis holds for a reduced group of synchronous motors, i.e., those motors characterized by a negligible magnetic saturation. Motors that shows an accentuate anisotropy, thus suitable for low speed sensorless operation, usually suffer of self and cross magnetic saturation. HEPM machines exhibit a remarkable saturation as can be inferred by flux linkages curves depicted in Fig. 13.3 and Fig. 13.4. When cross-inductance l_{dq} is considered in (13.6), the estimator converges to a wrong position. The steady-state angular error between estimated $\widehat{dq}$ and motor dq reference frame results:

$$\widetilde{\vartheta}^e_m = -\frac{1}{2}\arctan\left(\frac{2l_e l_{dq}}{2l_e l_\Delta - \frac{3}{2}l^2_{de}}\right). \tag{13.7}$$

Such estimation error appears since the zero of the demodulated HF current $\widehat{\imath}_{h,q}$ in (13.5) occurs for an estimated position different from the actual one of (13.7). If the excitation winding is opened, i.e. l_{de} is null, the error expressions collapses into the one of an interior-permanent magnet machine [50].

The estimation error in (13.7) is shown by the estimator in open-loop mode, namely, when control loops are closed with the measured position. If the estimated quantities are used by current and speed loops, the estimation error differs from $\widetilde{\vartheta}^e_m$ and instability issues could arise in sensorless operation. It is worth noting that $\widetilde{\vartheta}_m^e$ depends on the operating current point as inductances vary.

The position error is influenced by the control policy adopted for the generation of currents set-point, given a torque request. HEPM motors suffer of a relevant magnetic saturation, but the availability of an additional degree of freedom in the control, namely the excitation current, it can be exploited to improve sensorless operation. Indeed, the currents set-point is defined by both $\boldsymbol{I}_{dq}$ and I_e for a HEPM motor. If the reference current operating point shows a null estimation error $\widetilde{\vartheta}_m^e$ in open-loop mode, even in closed-loop mode the actual operating point will follow the reference one with $\widetilde{\vartheta}_m^e = 0$.

13.3 MAXIMIZATION OF HEPM SENSORLESS CAPABILITIES

A novel control policy is derived for HEPM motors in this section, aiming to maximize the sensorless capabilities of the motor, without lost the minimum losses policy. The idea consists into exploiting the additional degree of freedom that HEPM offers, namely the excitation current I_e, to improve the HEPM sensorless operation. The method finds the motor current set-points which minimize or eliminate the estimation position error (13.7) due to cross-differential inductances, while keeping a good efficiency in the torque delivery.

The proposed control policy can be achieved by a two-step procedure. The optimization inputs are the torque reference T^* and a set of n_e *dq* flux curves (as Fig. 13.3 and Fig. 13.4), for n_e excitation current rates. An accurate identification of the stator current-to-flux characteristics is mandatory by the proposed algorithm. Flux curves can be obtained either by means of finite element simulations or by an experimental characterization. The number n_e of measured magnetic maps is defined as a trade-off between two opposing objectives, namely, the accuracy of the final trajectory and the required time to obtained them.

13.3.1 *First Step*

The first step of the procedure consists into finding the T^* iso-torque level in the *dq* current plane. Since such curve depend on the excitation current, n_e iso-torque loci exist. Then, the minimum sensorless position error (13.7) is found along each iso-torque curve by solving n_e constrained optimization problems as:

$$\min_{\boldsymbol{I}_{dq}^*} \widetilde{\vartheta}_m^{e,2}, \text{ s.t. } T = T^*, \ \|\boldsymbol{I}_{dq}^*\| \leqslant I_N \tag{13.8}$$

where I_N is the nominal stator current. It is worth noting that (13.8) can have several solutions. The MATLAB solver *fmincon* was used to handle the optimizations. The aforementioned constrained minimization may output three different kind of results:

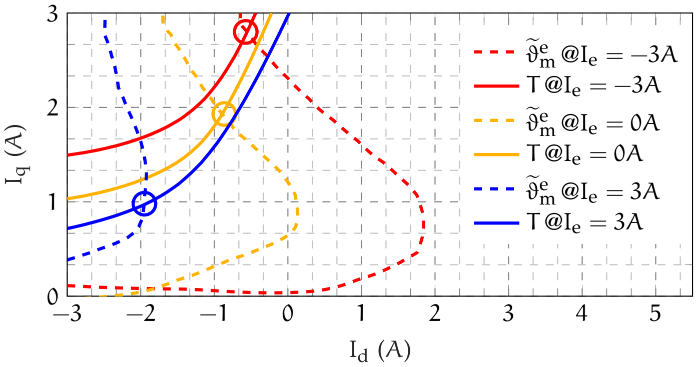

Figure 13.6: Solid lines depict isotorque loci with $T^* = 5\,\mathrm{N}\cdot\mathrm{m}$, while the dashed lines show the zero position error $\widetilde{\vartheta}^e_m$ loci. Three different values of excitation current I_e are considered. The circles depict the desired working point, which will be the input for the second step of the procedure.

- a feasible $\boldsymbol{I}^*_{dq}$ reference is found, which allows a zero $\widetilde{\vartheta}^e_m$, as shown in Fig. 13.6. Solid curves depict $T = 5\,\mathrm{N}\cdot\mathrm{m}$ iso-torque loci for three excitation current levels while dashed lines shows the corresponding $\widetilde{\vartheta}^e_m = 0$ loci for the same excitation currents. Circles represent the solutions of (13.8) for each excitation currents;

- a feasible $\boldsymbol{I}^*_{dq}$ reference is found, which minimizes $\widetilde{\vartheta}^e_m$ without zeroing it, as occurs in Fig. 13.7 for $I^*_e = 3\,\mathrm{A}$ where the nominal torque is achieved only in the top-left corner. For high torque values, the intersection between the two iso-values curves is not guaranteed. The current vector able to provide the requested torque does not guarantee $\widetilde{\vartheta}^e_m = 0$.

- no feasible $\boldsymbol{I}^*_{dq}$ references are found for the considered excitation current values. In Fig. 13.7, the iso-torque curve at $I^*_e = 0\,\mathrm{A}$ and $I^*_e = -3\,\mathrm{A}$ are not reported, since the motor is not able to provide the nominal torque with a stator current smaller than the nominal current I_N. No solution of (13.8) exists.

All the feasible current set-points are denoted as $[\boldsymbol{I}^*_{dq}, I^*_e]^T_{subopt}$, and they are stored in an auxiliary vector u. Thus, all candidate current set-points able to deliver the requested torque and to guarantee the smallest position estimation error are found after this first optimization step.

13.3.2 *Second Step*

The second step of the control policy optimization is devoted to the maximization of the drive efficiency. For a given torque reference, the current set-points that minimizes the Joule losses must be selected.

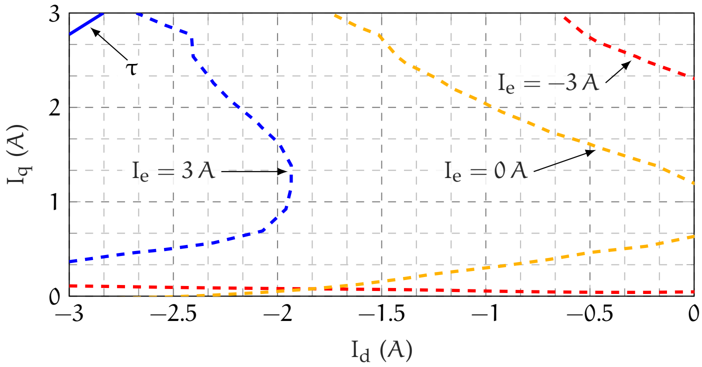

Figure 13.7: Solid line depicts the isotorque locus with $T^* = T_N$ while the dashed lines show the zero position error $\widetilde{\vartheta}^e_m$ loci. Three different values of excitation current I_e are considered. The nominal torque can be achieved only with the maximum positive excitation current.

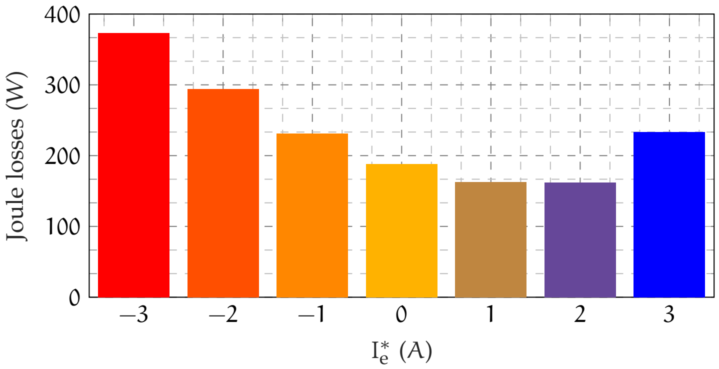

Figure 13.8: Overall HEPM motor Joule losses for several excitation current levels. In each test, the delivered torque is $T = 5\,\mathrm{N\,m}$.

Thus, a second optimization step is carried out among the feasible set-points stored in $\mathfrak{u}$. The new cost function penalizes the overall Joule losses of the HEPM motor as:

$$\min_{\boldsymbol{I}^*_{dq}, I^*_e} \left(\frac{3}{2} R_s \|\boldsymbol{I}^*_{dq}\|^2 + R_e I_e^{*2} \right), \quad \begin{bmatrix} \boldsymbol{I}^*_{dq} \\ I^*_e \end{bmatrix} \in \mathfrak{u}. \tag{13.9}$$

An example of such optimization is shown in Fig. 13.8, where the total Joule losses are reported as a function of the excitation current references I_e^* in $\mathfrak{u}$ for a torque reference of $T = 5\,\mathrm{N \cdot m}$. It is worth noticing that both stator and rotor Joule losses are minimized by the proposed optimization problem, differently from what happens for the MTPA problem stated in (13.2). The outcome of this second step represents the final current set-point $[\boldsymbol{I}^*_{dq}, I^*_e]^T_{opt}$ used to deliver the desired torque reference T^*. The proposed two-step method to find the optimal current set-point given τ^* is resumed in Algorithm 1.

The full HEPM motor control policy is built by applying Algorithm 1 for different torque requests, spanning the entire operating

Algorithm 1 Calculate optimal self-sensing currents set-point

```
Require: $T^*$ torque reference, stator current-to-flux linkages characteristics for $n_e$ excitation current rates.
function POSITION ERROR MINIMIZATION (SEC. 13.3.1)
    for $I_e^* = 1 : n_e$ do
        Find $T = T^*$ level-set
        $\boldsymbol{I}_{dq}^* \leftarrow$ solve (13.8)
        $u \leftarrow [\boldsymbol{I}_{dq}^*, I_e^*]_{subopt}^T$
    end for
end function
return $u$
function DRIVE EFFICIENCY OPTIMIZATION (SEC. 13.3.2)
    $[\boldsymbol{I}_{dq}^*, I_e^*]_{opt}^T = u(1)$
    $J_{min} \leftarrow$ solve (13.9) for $u(1)$
    for $[\boldsymbol{I}_{dq}^*, I_e^*]^T \in u$ do
        $J \leftarrow$ solve (13.9) for $[\boldsymbol{I}_{dq}^*, i_e^*]^T$
        if $J < J_{min}$ then
            $J_{min} \leftarrow J$
            $[\boldsymbol{I}_{dq}^*, I_e^*]_{opt}^T \leftarrow [\boldsymbol{I}_{dq}^*, I_e^*]^T$
        end if
    end for
end function
return Optimal currents set-point $[\boldsymbol{I}_{dq}^*, I_e^*]_{opt}^T$
```

region from zero to the nominal torque value. The resulting current set-points are stored in a 3D look-up-table, suitable for an embedded real-time implementation.

13.4 RESULTS

The main purpose of the proposed control policy is the minimization of the position estimation error in sensorless operation. Fig. 14.1 shows the considered HEPM motor ready for the commissioning, while Tab.21 resumes its parameters. In particular, both the stator windings contacts and the sliding rotor winding contacts are shown.

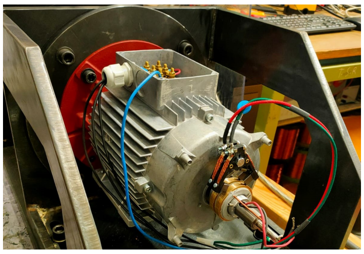

Figure 13.9: HEPM motor prototype. Sliding contacts can be noted.

Table 21: Overview of the HEPM motor parameters.

Parameter	Symbol	Value
Pole pairs	p	2
Stator over rotor winding resistance	R_s/R_e	5
Saliency at nominal point	l_{qq}/l_{dd}	3
Nominal stator current	I_N	3 A
Nominal excitation current	I_e	3 A
Nominal speed	ω_N	500 rpm
DC bus voltage	V_{dc}	300 V
Nominal torque	T_N	10 N · m

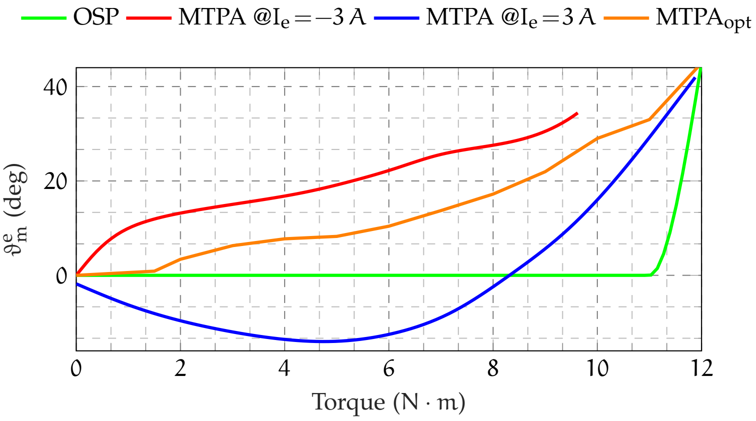

Figure 13.10: Position estimation error (13.7) versus torque under different control policies.

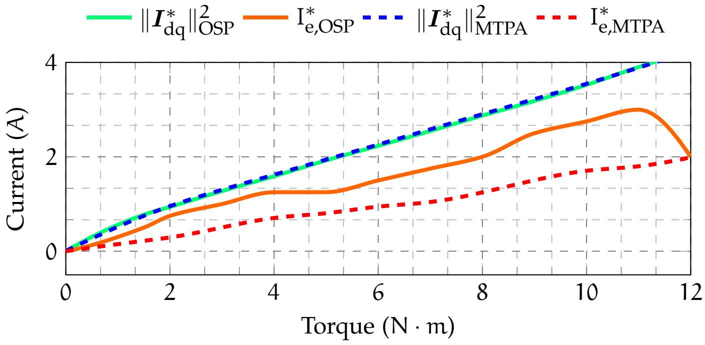

Figure 13.11: Stator current amplitude and excitation current magnitude under the optimized self-sensing control policy (OSP)

The error (13.7) is evaluated for four different control policies, in particular the MTPA locus with maximum I_e^* and with the minimum I_e^*, with the optimal I_e^* that minimize the stator and rotor losses ($\mathrm{MTPA_{opt}}$) and the proposed policy called OSP (optimal sensorless policy). Results are shown in Fig. 13.10 for the four strategies. The OSP allows for keeping the estimation position error $\widetilde{\vartheta}_m^e$ equal to zero for a wide torque range. In the high torque range, the error increases as no intersection between iso-torque and $\widetilde{\vartheta}_m^e = 0$ level occurs. The delivered torque must be guaranteed at the cost of a non-zero estimation error. For the nominal torque, the proposed strategy converges to the maximum excitation current MTPA curve as it is the only condition able to guarantee the requested torque. Three MTPA strategies result critical for sensorless control, due to the significant cross-saturation inductances of the considered HEPM machine. Finally, it is worth noting that the MTPA curve at $I_e = -3\,A$ exists only below $T = 10\,N \cdot m$.

Fig. 13.11 shows the current references generated by the OSP and $\mathrm{MTPA_{opt}}$ as a function of the requested torque. In particular, it is evident the relevant role of the rotor excitation current. If common MTPA strategies would be adopted, the reference I_e^* would be constant and equal to its nominal value regardless the torque. On the opposite, the OSP and $\mathrm{MTPA_{opt}}$ requires a variable excitation to track a low position error in sensorless operation and minimize the overall losses. It is worth noting that in the OPS policy the excitation current saturates before it maximum value and then converge to the $\mathrm{MTPA_{opt}}$ value. This aspect is due to the impossibility of the OPS to track the zero error, so the minimum error estimation is used until only a few points remain and converge to the $\mathrm{MTPA_{opt}}$.

Since the rotor excitation current changes depending on the torque operating point, stator current reference angle $\alpha_i^e = \mathrm{atan}(i_q^*/i_d^*)$ in OSP is different with respect to both MTPA policies. Fig. 13.12 reports such angles for the four considered control strategies. Major differences are observed at low torque ratings. On the opposite, at nominal torque the OSP collapses on the MTPA strategy $\mathrm{MTPA_{opt}}$, since the nominal torque needs a rated excitation current to be delivered. It is worth remembering that even if the stator current angle may result similar between the MTPA curve at $I_e = -3\,A$ and MTPA curve at $I_e = 3\,A$ locus, they are actually significantly different because of the different excitation currents. Indeed, a certain current set-point needs to be graphically represented in the three-dimensional space $[\boldsymbol{I}_{dq}^*, I_e^*]^T$.

The drive efficiency probably plays the most important role in industrial applications. Thus, a comparative analysis is performed among the four policies in terms of total stator and rotor Joule losses. Results are reported in Fig. 13.8. As expected, the $\mathrm{MTPA_{opt}}$ guarantees the lowest losses among the four strategies. This is mainly due to the fact that both MTPA strategies are optimized only in terms of

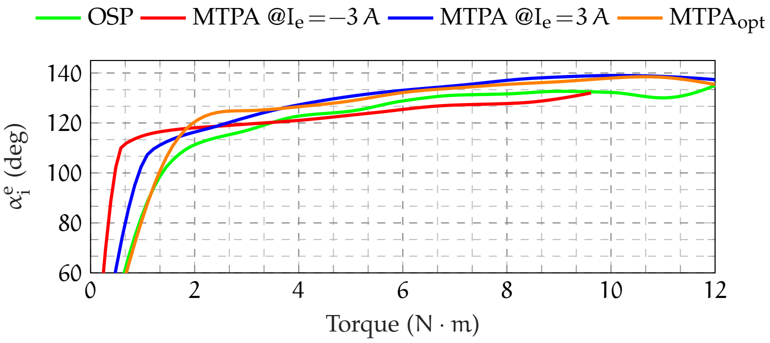

Figure 13.12: Stator currents references angle versus torque under different control policies.

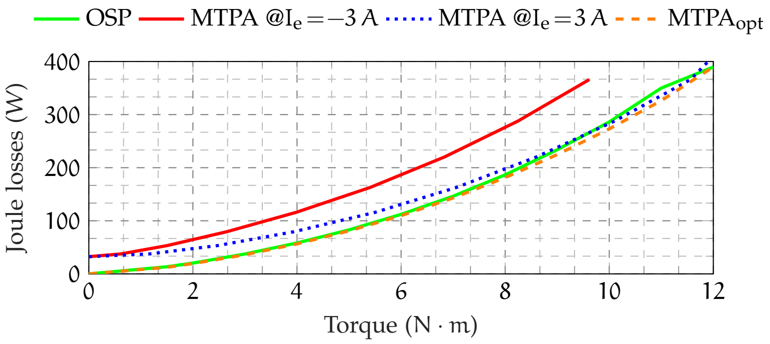

Figure 13.13: Total stator and rotor Joule losses versus torque under different control policies.

stator Joule losses while OPS need to track the zero error position estimation. The MTPA with $I_e = -3$ A strategy is significantly less efficient than the other MTPA, since the excitation current produces an opposite flux contribution with respect to the permanent magnet. The greatest improvement achieved by the OSP and MTPA$_{opt}$ is obtained at low torque rates, where the rotor excitation currents of both considerably differs from the one of MTPA with $I_e = 3$ A and $I_e = -3$ A.

The efficiency considerations could change depending on the HEPM stator and the rotor excitation windings, i.e. on the ratio R_s/R_e. The lower the ratio, the higher the rotor excitation winding weights on the overall efficiency.

13.5 DISCUSSION

This part describes a novel control strategy for hybrid excited permanent magnet motors focused on the minimization of the joule losses and the maximization of their sensorless capabilities. The strategy results from a two-step optimization, the first one devoted to the minimization of the position error under sensorless operation, the second one to the drive efficiency maximization. The new control policy allows for a zero position error in a wide torque operating region for low-speed HF-injection based sensorless schemes, without any additional compensation. The low estimation error is achieved by a proper design of the stator and rotor current reference set-point. Moreover, the overall efficiency of the drive is found to be higher than the one achieved by a conventional maximum-torque-per-ampere strategy. This feature derives from the second step of the optimization, which takes into account both stator and rotor Joule losses. The proposed approach was verified on an the HEPM motor prototype. In the next Chapter high speed operation will be treated and analyzed.

14

FW CONTROL ALGORITHM

FW operation represents a crucial feature of electric motor drives in several applications, including electric vehicle drives and spindles. IPM synchronous motor are preferred by industries for such applications [79]. In fact, such motors exhibit excellent dynamic performance, high torque density, and a maximum operating speed up to three times the nominal one [19]. However, industries would be interested in achieving even higher maximum speeds, e.g. five times the rated one, without compromising the other advantageous features of IPM machines.

The maximum operating speed of IPM motors is mainly limited by the PM flux linkage. In particular, the lower the PM flux linkage, the higher the maximum achievable speed, assuming an equal supplying voltage. Conversely, the torque density and the dynamic performance decrease with the reduction of magnetic material in the rotor [43, 60]. As a result, it is hard to find a convenient trade-off among the desired specifications using such a motor technology. Other synchronous motor topologies have been investigated in literature. In particular, WR machines [84] represent a favorable solution for increasing the maximum speed. The rotor flux can be regulated [82] by means of the excitation winding. Thus, the stator back-electro-motive force can be reduced, decreasing the voltage required to supply the stator winding. However, the absence of PMs in the rotor reduces the motor torque density. Moreover, the rotor excitation winding represents an additional source of losses, which affects the overall efficiency.

An interesting trade-off between torque performance and favorable FW behavior is achieved by HEPM motors [8]. The distinguishing feature of such machine topology is a double rotor flux excitation. In particular, both PMs and an excitation winding are mounted on the rotor [5]. The excitation winding adds a further degree of freedom to the motor control algorithm, allowing a fine regulation of the rotor flux, similarly to WR machines. The presence of PMs permits to achieve a higher torque density and a higher efficiency with respect to WR motors. When compared to IPM machines, the presence of an excitation winding allows the reduction of the PMs sizes, which is beneficial from the point of view of the manufacturing costs.

Proper control schemes need to be designed in order to exploit the HEPM features. Flux regulation control policies for HEPM motors were investigated in [18, 24, 52, 67], with the main aim of achieving a wide constant-power speed range. Considering [24], FW operation was achieved by means of a voltage magnitude and a voltage phase

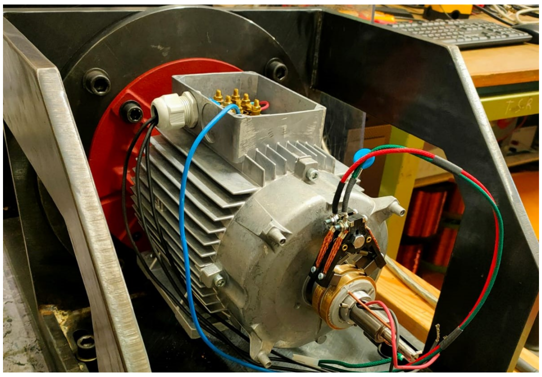

Figure 14.1: Rotor and stator of a HEPM motor prototype. Rotor winding is missing to highlight the PMs layout, but sliding contacts can be noted.

control loops which generate the excitation current and the d-current references, respectively. The method is suitable for isotropic HEPM motors, characterized by small stator inductances. However, only a few works are found in literature about the design of the FW control scheme of HEPM motors. Thus, several aspects have not been investigated yet.

This Chapter proposes a new FW control scheme, suitable for anisotropic HEPM motors with high motor inductances. A hybrid FW architecture is developed, including a feed-forward generation of the excitation current reference and a voltage loop for the direct-axis current reference. On one hand, the feed-forward excitation current reference generation aims to maximize the output power. On the other hand, the voltage loop for the direct axis current is inspired by conventional IPM sensorless schemes [47]. The presence of a feed-back on the voltage magnitude improved the robustness of the overall architecture, preventing the feeding converter from running out of voltage. The design and the linearization of the voltage loop requires particular care, since the HEPM motor model has an additional degree of freedom, with respect to IPM machines.

14.1 HEPM MOTOR MODEL

The rotating *dq* reference frame is adopted to describe the HEPM motor model. In particular, such reference frame is synchronous with the rotor PM flux, which rotates at the angular speed $\omega_m^e = p\omega_m$, being ω_m the rotor speed and p the pole pairs. The direct *d*-axis is aligned with the PM flux. Considering such reference frame, the stator and rotor windings voltage balance equations of a HEPM motor results:

$$\begin{aligned} v_d &= R_s i_d + \frac{d\lambda_d}{dt} - \omega_m^e \lambda_q \\ v_q &= R_s i_q + \frac{d\lambda_q}{dt} + \omega_m^e \lambda_d, \\ v_e &= R_e i_e + \frac{d\lambda_{e,rot}}{dt} \end{aligned} \tag{14.1}$$

where λ_d and λ_q, v_d and v_q, i_d and i_q are the *dq* stator flux linkage, voltage, and current components, respectively. Moreover, λ_e, v_e, and i_e are the excitation flux linkage, voltage, and current, respectively. Finally, R_s and R_e represent the stator and rotor winding resistance, respectively. In order to ease the presentation of the proposed flux-weakening algorithm, linear current-to-flux linkage characteristics are assumed:

$$\lambda_d = \Lambda_{PM} + L_d i_d + \lambda_e = \Lambda_{PM} + L_d i_d + M_e i_e \tag{14.2a}$$

$$\lambda_q = L_q i_q, \tag{14.2b}$$

$$\lambda_{e,rot} = L_e i_e + \frac{3}{2} M_e i_d \tag{14.2c}$$

where L_d, L_q and M_e are the direct, quadrature and excitation-to-direct axis mutual inductances, respectively. Λ_{PM} represents the no-load flux linkage due to the PMs. Finally, the HEPM motor torque equation results:

$$\begin{aligned} T &= \frac{3}{2} p(\lambda_d i_q - \lambda_q i_d) \\ &= \frac{3}{2} p(\Lambda_{PM} + M_e i_e + (L_d - L_q) i_d) i_q. \end{aligned} \tag{14.3}$$

For sake of compactness, the contribution of the PMs and the excitation winding to the flux linkage, namely $\Lambda_{PM} + M_e i_e$, will be denoted as λ_{he}. The considered HEPM machine prototype in this paper is reported in Fig. 14.1. In particular, the PMs layout in the rotor is shown, as well as the sliding contacts required to supply the rotor winding.

14.2 FLUX-WEAKENING CONTROL OF HEPM MOTORS

Differently from other synchronous machines, HEPM motors are characterized by an additional degree, i.e. the excitation winding current. Such current contributes to the *d*-axis flux linkage regulation (see (14.2)). Consequently, the stator voltage (14.1) magnitude can be properly modified at high speed to achieve a wider constant-power operating region, with respect to other motor topologies.

The behavior of HEPM motors for increasing operating speeds is discussed taking a classical IPM machine as benchmark (Fig. 14.2). In particular, the considered IPM and a HEPM motors share equal

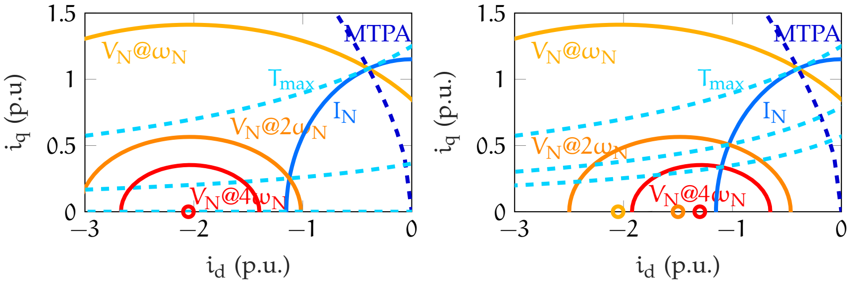

(a) IPM motor. (b) HEPM motor.

Figure 14.2: Current, voltage limit region and maximum torque loci at different motor speed. The MTPA loci and the voltage ellipses centres are shown, as well.

nominal torque T_{max} and nominal speed ω_N. In addition, the electric parameters R_s, L_d and L_q are the same for the two machines. The two motors differ in the d-axis components of the flux linkage. In fact, no excitation winding is installed in the rotor of IPM machines. Thus, the IPM motor current-to-flux linkage model is defined by only the first two equations of (14.2), i.e. (14.2a) and (14.2b). Moreover, equation (14.2a) collapses into $\lambda_d = \Lambda_{PM} + L_d i_d$.

Below the nominal speed, the excitation current of the HEPM motor is always regulated at its rated value. Indeed, the MTPA trajectories of the two machines are similar, i.e. the dark blue dashed curves of Fig. 14.2. Above the nominal speed, the maximum deliverable torque decreases both for HEPM and IPM motors, because the required voltage exceeds the maximum one available from the inverter. The voltage constraint for the two motors at ω_N describes the two outer ellipses of Fig. 14.2a and Fig. 14.2b. Feasible current operating points lie in the intersection area within the current limit circle of I_N radius, defined by the equation

$$i_d^2 + i_q^2 = I_N^2, \tag{14.4}$$

and the voltage limit ellipse, defined by the equation

$$V_N^2 = R_s^2(i_d^2 + i_q^2) + \omega_m^{e2}\Big((\Lambda_{he} + L_d i_d)^2 + (L_q i_q)^2\Big). \tag{14.5}$$

V_N denoted the amplitude of the maximum voltage vector that can be synthesized by the power converter feeding the HEPM machine.

In the IPM motor case, i.e. Fig. 14.2a, the intersection area shrinks with increasing speeds, until it collapses in the point where the two boundary curves are tangent and the maximum speed of the drive is achieved. On the opposite, in the HEPM machine case, i.e. Fig. 14.2b, a feasible operating area is preserved by shifting the center of the voltage ellipse constraint. Indeed, the center lies on the d-axis, and the expression of its d coordinate is $-(\Lambda_{PM} + M_e i_e)/L_d$. Thus, the center can be moved on the right side by applying a decreasing excitation

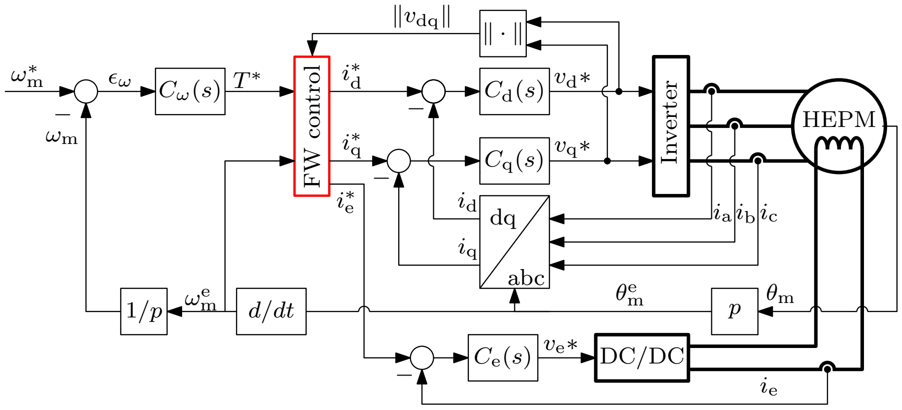

Figure 14.3: Control scheme of the HEPM motor.

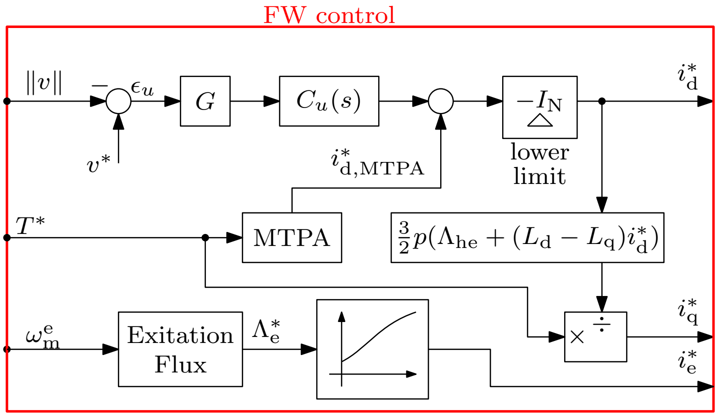

Figure 14.4: Detail of Fig. 14.3 - Flux weakening block.

winding current. As a result, the maximum speed of the drive is theoretically increased up to infinity. Frictions and mechanical issues limit the maximum achievable speed in real world applications.

14.2.1 *Control scheme*

The overall control scheme of the HEPM motor is reported in Fig. 14.3, and it is characterized by a conventional cascaded structure. An outer speed loop steers the HEPM motor speed ω_{m} to the desired reference ω_{m}^*. The speed regulator $C_\omega(s)$ consists of a conventional PI controller, which zeros the speed reference tracking error ϵ_ω and generates the torque reference T^*. The FW block in the scheme elaborates the torque reference signal to derive the stator current references i_{d}^* and i_{q}^*, and the excitation current reference i_{e}^*. Three PI regulators, namely $C_{\mathrm{d}}(s)$, $C_{\mathrm{q}}(s)$, and $C_{\mathrm{e}}(s)$, are designed for the internal current loops. The first two regulators, i.e. $C_{\mathrm{d}}(s)$ and $C_{\mathrm{q}}(s)$, output the stator voltage references v_{d}^* and v_{q}^* for a three-phase two-levels inverters. $C_{\mathrm{e}}(s)$ outputs the voltage command v_{e}^* and a DC/DC converter supplies the excitation winding.

The FW block represents the core of the proposed FW methodology, which consists of a feed-forward excitation current reference generation and a feed-back control of the stator voltage magnitude. Thus, Fig. 14.4 is reported to provide a deeper insight.

The excitation current control is discussed in Section 14.2.3. Such excitation winding current control aims to maximize the output power of the machine at each operating speed by moving the center of the voltage ellipse constrain (Fig. 14.2b) when needed. Stator currents references are generated according to conventional FW scheme [47]. An MTPA strategy is employed as long as the inverter provides the required voltage. It is worth noting that the stator voltage vector magnitude threshold is set to 90% of the maximum available voltage to ensure a proper margin in the current control. Once the voltage error signal ϵ_u in Fig. 14.4 becomes negative, the control strategy enters in the FW operating mode. The MTPA d-axis current reference $i^*_{d,MTPA}$ is decreased by the output of the voltage controller $C_u(s)$. Then, the q-axis current reference is obtained to guarantee a safe magnitude of the current vector.

The relationship between the *d*-current and the voltage vector magnitude is strongly nonlinear. Thus, the following section is entirely devoted to the characterization of such nonlinearity and its compensation.

14.2.2 *Voltage loop linearization*

The design and tuning of the voltage loop results troublesome. A promising approach to address such issue is described in [47]. In order to compensate the variation in the nonlinear gain of the voltage loop, such gain is analytically computed and the loop is linearized. Consequently, a desired bandwidth for the voltage loop can be guaranteed.

Since for the considered HEPM motor the *d*-axis current has strong effect on the total *d*-axis flux, the voltage loop is exploited to adjusts the *d*-axis MTPA current reference during the FW, differently from [24]. The voltage magnitude expression results:

$$\|v\| = \sqrt{v_d^2 + v_q^2}. \tag{14.6}$$

Thus, from a small signal perspective, i_d produces nonlinear effects on $\|v\|$, in fact:

$$\begin{aligned}\frac{\partial\|v\|}{\partial i_d} &= \frac{1}{V}\left(V_d\frac{\partial v_d(i_q)}{\partial i_q} + V_q\frac{\partial v_q(i_d)}{\partial i_d}\right)\\ &= \frac{1}{V}\left(V_d\frac{\partial v_d(i_q)}{\partial i_q}\frac{\partial i_q}{\partial i_d} + V_q\frac{\partial v_q(i_d)}{\partial i_d}\right),\end{aligned} \tag{14.7}$$

where lowercase letters stand for the total quantities, while uppercase letters stand for large-signal dc quantities. $\frac{\partial}{\partial(*)}$ represents the partial derivative operator.

Following the idea of [47], the nonlinear effect $\frac{\partial\|\nu\|}{\partial i_d}$ is compensated by including the following linearizing gain

$$G = \frac{1}{\dfrac{\partial\|\nu\|}{\partial i_d}} \tag{14.8}$$

in the voltage loop, as shown in Fig. 14.4. The computation of such gain is slightly different with respect to the case of an IPM machine because of the excitation winding. In particular, the expressions of the three partial derivatives $\frac{\partial \nu_d}{\partial i_q}$, $\frac{\partial \nu_q}{\partial i_d}$ and $\frac{\partial i_q}{\partial i_d}$ are required.

Concerning the computation of the *dq* voltage partial derivatives, the voltage balance equations (14.1) are simplified assuming negligible resistive voltage drops:

$$\begin{aligned} \nu_d &\approx -\omega_m^e L_q i_q \\ \nu_q &\approx \ \ \omega_m^e \left(\Lambda_{PM} + L_d\, i_d + M_e\, i_e\, (i_d)\right). \end{aligned} \tag{14.9}$$

The assumption is well motivated by the fact that the motional terms are prominent with increasing speed, i.e. in FW operation. Under such an hypothesis, the voltage partial derivatives in (14.7) result:

$$\begin{aligned} \frac{\partial \nu_d}{\partial i_q} &= -\omega_m^e L_q \\ \frac{\partial \nu_q}{\partial i_d} &= M_e \frac{\partial i_e(i_d)}{\partial i_d} + L_d \end{aligned} \tag{14.10}$$

An additional partial derivative needs to be computed, namely $\dfrac{\partial i_e}{\partial i_d}$. From a small signal point of view, the effect of a variation of i_d on i_e is derived from the flux model equation (14.2c):

$$\frac{\partial i_e}{\partial i_d} = -\frac{3}{2}\frac{M_e}{L_e}. \tag{14.11}$$

Concerning the partial derivative $\dfrac{\partial i_q}{\partial i_d}$, its expression is derived assuming a constant delivered torque, as in [47]. The *q*-current expression for a given torque is obtained from (14.3). Then, substituting (14.8) in the i_q expression, the following equivalence holds:

$$\begin{aligned} \left.\frac{\partial i_q}{\partial i_d}\right|_T &= -\frac{2T\left(L_d - L_q - M_e \dfrac{\partial i_e}{\partial i_d}\right)}{3p\left(\Lambda_{PM} + M_e i_e + (L_d - L_q) i_d\right)^2} \\ &= -\frac{I_q\left(L_d - L_q - \dfrac{3}{2}\dfrac{M_e^2}{L_e}\right)}{\Lambda_{PM} + M_e I_e + (L_d - L_q) I_d} \end{aligned} \tag{14.12}$$

The nonlinear behavior of the voltage loop can be finally described by substituting equations (14.10) and (14.12) into (14.7):

$$\frac{\partial\|v\|}{\partial i_d} = \frac{\omega_m^e}{V}\left(V_d \frac{L_q I_q \left(L_d - L_q - \frac{3}{2}\frac{M_e^2}{L_e}\right)}{\Lambda_{PM} + M_e i_e + (L_d - L_q) i_d} + V_q \left(L_d - \frac{3}{2}\frac{M_e^2}{L_e}\right)\right) \tag{14.13}$$

Such expression is evaluated each control period to compute the linearizing gain G in Fig. 14.4. The gain computation requires currents ans speed measurement, as well as the values of the input voltages applied in the previous control period.

14.2.3 *Excitation current control in FW operation*

The excitation current reference of HEPM motors is kept constant below the nominal speed. Once overcome the base point, the value of such current can be selected in order to maximize the output torque and power, given the working speed. The excitation current expression that optimize such control objective is derived hereinafter.

When the HEPM machine works at the boundaries of the voltage and current feasible regions, the *dq* stator currents fulfill the following relationships:

$$\begin{aligned} i_d &= \frac{-\Lambda_{he} \pm \sqrt{\xi^2 \Lambda_{he}^2 - (1-\xi^2)(\xi^2 L_d^2 I_N^2 - \frac{\overline{V_N}^2}{\omega_m^{e2}})}}{(1-\xi^2) L_d} \\ i_q &= \sqrt{I_N^2 - i_d^2}, \end{aligned} \tag{14.14}$$

where ξ represents the motor saliency ratio, namely the ratio L_q/L_d and $\overline{V_N}$ stands for the nominal voltage magnitude decurted by the nominal resistive voltage drop, i.e. $\overline{V_N} = \sqrt{V_N^2 - R_s^2 I_N^2}$. The positive solution of i_d is considered hereinafter, since it allows to maximize the torque for a given speed. It is worth highlighting that the two currents depend only on the excitation flux Λ_{he}. The just derived relationships are substituted in the torque equation (14.3). Then, the HEPM motor torque is maximized with respect to the excitation flux Λ_{he}, obtaining:

$$\Lambda_{he} = \frac{\overline{V_N}^2 + \xi I_N^2 L_d^2 \omega_m^{e2}}{\omega_m^e \sqrt{\overline{V_N}^2 + \xi^2 I_N^2 L_d^2 \omega_m^{e2}}} \tag{14.15}$$

The excitation winding current reference can be finally retrieved reminding that $\Lambda_{he} = M_e i_e + \Lambda_{PM}$:

$$i_e^* = \frac{1}{M_e}\left(\frac{\overline{V_N}^2 + \xi I_N^2 L_d^2 \omega_m^{e2}}{\omega_m^e \sqrt{\overline{V_N}^2 + \xi^2 I_N^2 L_d^2 \omega_m^{e2}}} - \Lambda_{PM}\right). \tag{14.16}$$

Such expression of i_e^* maximizes the torque at each operating speed under FW operation. The equation can be easily implemented in the real-time controller by means of a 1D look-up-table.

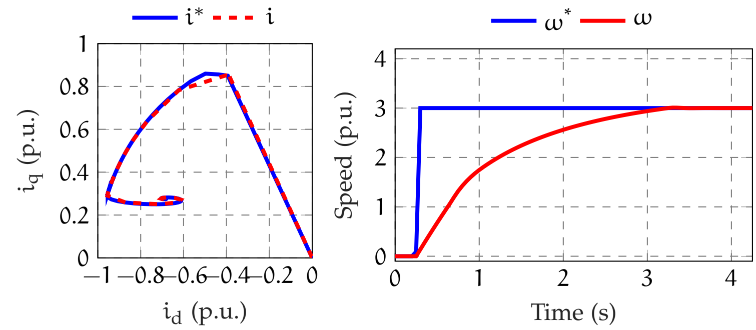

(a) Stator currents. (b) Speed.

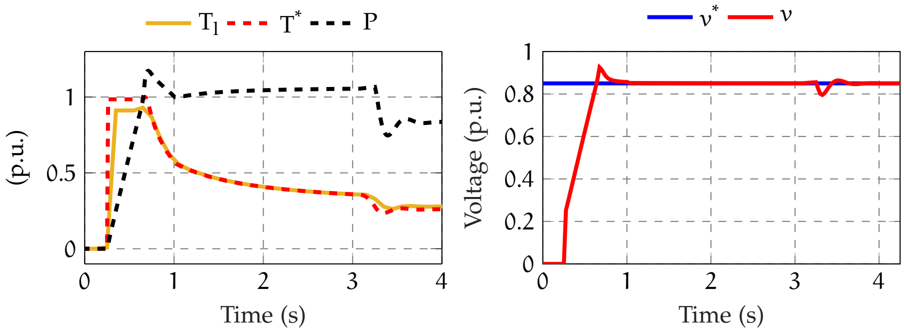

(c) Torque and power. (d) Stator voltage.

Figure 14.5: Motor *dq* currents, speed, torque and power of the HEPM motor when a speed reference was step-wise changed from 0 to 4p.u.: variable load torque case. Both constant torque and power region are shown.

14.3 RESULTS

Simulations had twofold aim. The former one was to validate the proposed control strategy and the latter one was to highlight the superior performance achievable by HEPM motors with respect to IPM ones. The considered motors share the same rated parameters that are reported in Tab.22. Fig. 14.5 and Fig. 14.6 show, instead, the simulation results obtained for the two motors in case of a variable load torque.

All the simulations are carried out assuming linear flux-to-current characteristics.

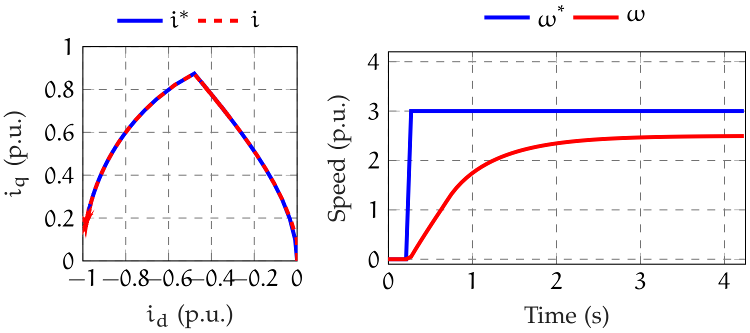

(a) Stator currents.

(b) Speed.

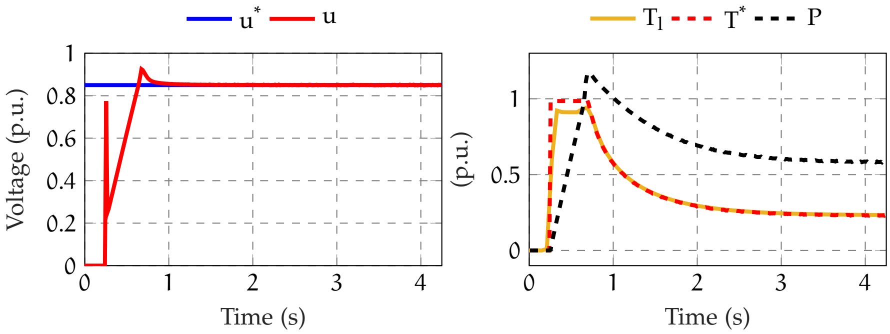

(c) Stator currents.

(d) Torque and power.

Figure 14.6: Motor *dq* currents, speed, torque and generated power of the IPM motor when a speed reference was step-wise changed from 0 to 4p.u.: variable load torque case. Both constant torque and power region are shown.

14.3.1 *Inertial load*

The first test consists in a step-wise change of the speed reference from standstill to three times the rated speed for both the considered machines. Both motors are loaded with inertial variable torque load conditions. The speed reference was changed step-wise from zero to three times the rated speed. The load torque was decided by the motor inertia and the viscous friction.

Fig. 14.5a and Fig. 14.6a shows the currents trajectories in the *dq* plane. In particular, stator currents moved accurately through the MTPA locus and the current limit circle. Thanks to the reduction of the Λ_{he} flux, the HEPM motor never ran out of voltage, and it reached the steady-state operation at speed 3p.u. after $t = 3.25\,s$ as shown in Fig. 14.5b. Conversely, the IPM motor ran quickly out of voltage and it stopped to accelerate during the test, reaching a maximum operating speed lower 2.5 p.u. (Fig. 14.6b). This fact is confirmed by the analysis of the motors output torques, too. In Fig. 14.5c the HEPM motor delivered torque T^* is higher or equal than the load T_L one during the transient. The balancing of the motor and load torques was achieved both during transient and steady-state.

From the output power point of view, the HEPM motor delivered the maximum admissible power, as proved by Fig. 14.5c. After $t = 0.6\,s$, there is a power spike due to the time delay required for the voltage loop to react to keep the absolute module constant. The IPM machine exhibits a significantly lower power performance, due to the limitations in terms of maximum achievable speeds. This fact further proves the superiority of HEPM motor drives during the FW operation.

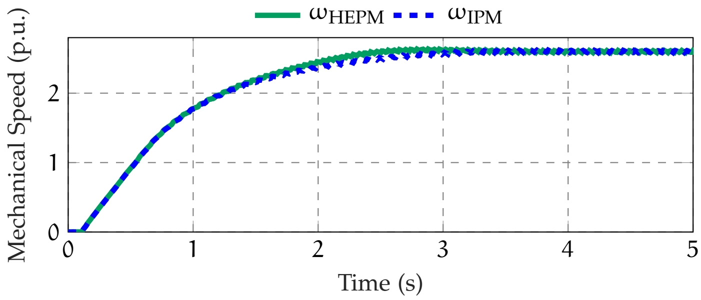

(a) Speed vs time.

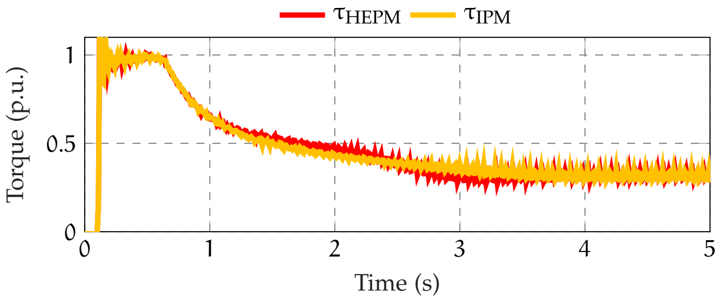

(b) Delivered torque vs time.

Figure 14.7: Speed and Torque delivered during experimental test at 2.5 nominal speed in p.u.

14.4 EXPERIMENTAL ASSESSMENT

Finally, experimental tests were carried out to validate the HEPM superior performance results on the prototype. First, a step up to 2.5 times the rated speed was performed to compare the HEPM and IPM motor transients with the same inertial load. This test is done considering that both motor can reach 2.5 times the rated speed and than evaluate the rising time. The HEPM motor rising time is lower than the IPM motor as shown in Fig. 14.7a. This transient increasing is due to the higher torque developed during the FW operation thanks

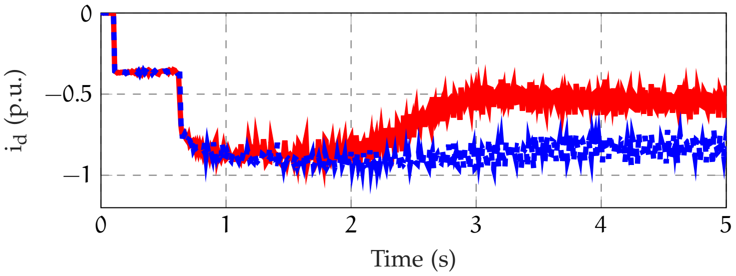

(a) Direct current vs time.

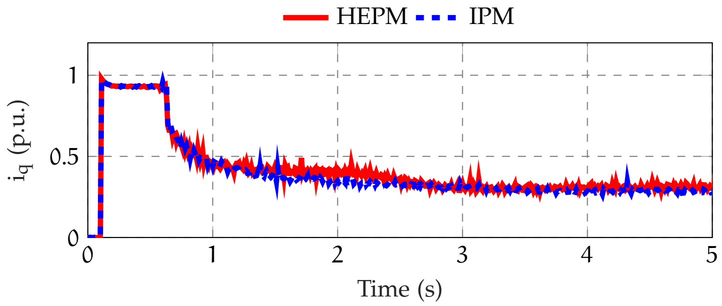

(b) Quadrature current vs time.

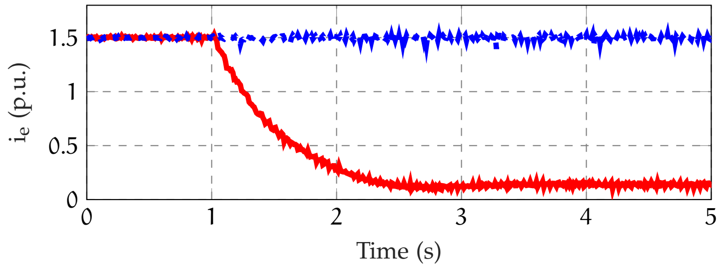

(c) Excitation current vs time.

Figure 14.8: Experimental test at 2.5 nominal speed in p.u.

to the rotor control current which, combined with a proper i_d and i_q stator current, can give the maximum torque for each speed. After $t = 0.6\,s$, the FW operation begins. The torque delivered is reported in Fig. 14.7b. The difference between the torque delivered by the two motors are only during the FW operation.

Figs. 14.8a and 14.8b show direct and quadrature currents. Until $t = 1\,s$ both HEPM and IPM motor have the same speed and stator current behavior. After $t = 1\,s$ the excitation current i_e is reduced according to (14.16), to achieve the maximum torque for each speed. After this point the torque delivered by HEPM motor is always higher than IPM motor until the steady state condition. This test highlights a slight faster transient dynamic of the HEPM motor compared to IPM motor. This occurs after overcoming the nominal speed when the flux is decreased by the rotor current. Anyway both motors reach the same reference speed.

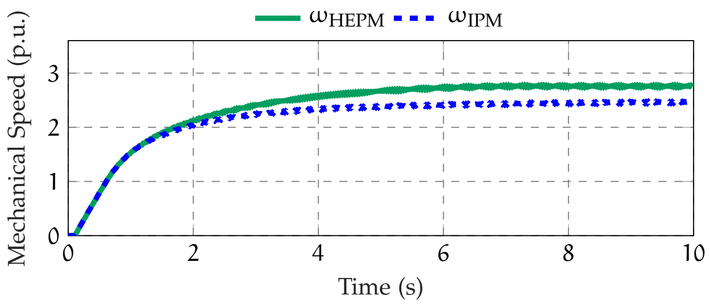

(a) Rotor speed vs time.

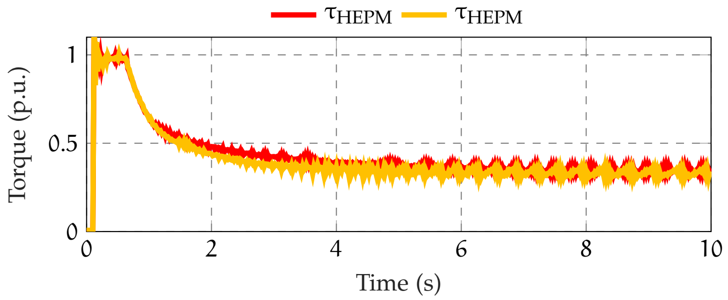

(b) Torque delivered vs time.

Figure 14.9: Maximum speed experimental test.

Another test was carried out and the result is shown in Fig. 14.9. A four p.u speed step is imposed to verify which is the highest speed that each motor can reach. The test is carried out with the same inertial load. Fig. 14.9a shows HEPM motor speed that exhibits faster transient dynamic and higher maximum speed value adopting the same current and voltage limits. The maximum speed of the HEPM motor is 15% higher than IPM motor. The increasing of the torque during the transient can be appreciate in Fig. 14.9b. Besides the small size of the prototype, that works in high saturation condition, these tests validate the effective superiority of the HEPM motor compared to the IPM motor in terms of performance during FW operation.

14.5 DISCUSSION

The proposed flux-weakening scheme consists of a voltage loop for the stator direct axis current reference generation and a feed-forward generation of the excitation current reference. Concerning the voltage loop, the direct current effect on the voltage vector magnitude exhibits a strong nonlinear behavior. Its linearization was computed and the obtained gain was exploited to guarantee a constant voltage-loop bandwidth. The gain computation includes the effect of the excitation winding current. Concerning the feed-forward excitation current reference generation, a method was proposed to reduce rotor flux linkage for increasing working speeds. The proposed control strategy

Table 22: HEPM motor parameters.

Parameter	Symbol	Value
Pole pairs	p	2
Stator over rotor winding resistance	R_s/R_e	5
Saliency at nominal point	$\xi = L_q/L_d$	3
Nominal stator current	I_N	$2\,A$
Nominal excitation current	$I_{e,N}$	$3\,A$
Nominal speed	n_N	$540\,rpm$
DC bus voltage	V_{dc}	$300\,V$
Nominal torque	T_N	$5.3\,N \cdot m$

was validated by means of simulations and experimental test, comparing the FW capability of an HEPM motor and an IPM with same dimension and rated parameters. HEPM motor shows superior capability during the flux weakening operation compared to the IPM motor. At the end of this part on control strategies, a mention of model predictive control has been reported and is under test on the HEPM machine.

15

MPC CONTROL ALGORITHM

15.1 HEPM MOTOR MODEL

The HEPM motor prototype is shown in Fig. 15.1, and the considered electric drive scheme is depicted in Fig. 15.2. The voltage equations of an HEPM motor in the rotating reference frame are:

$$\begin{aligned} v_d &= R_s i_d + L_d \frac{di_d}{dt} + M_e \frac{di_e}{dt} - L_q i_q \omega_m^e, \\ v_q &= R_s i_q + L_q \frac{di_q}{dt} + \omega_m^e \left(\Lambda_{PM} + L_d i_d + M_e i_e\right), \\ v_e &= R_e i_e + L_e \frac{di_e}{dt} + \frac{3}{2} M_e \frac{di_d}{dt}, \end{aligned} \tag{15.1}$$

where $v_{d,q,e}$, $i_{d,q,e}$ and $L_{d,q,e}$ are respectively the direct, quadrature, excitation voltages, currents and inductances, $R_{s,e}$ are the stator and excitation resistances, Λ_{PM} is the PM flux linkage, and ω_m^e is the electromechanical speed. Finally, note that the mutual inductance M_e is multiplied by $3/2$ in the excitation winding voltage equation to take into account the transformation effect. The motor is considered magnetically linear and cross saturation effects are neglected. The motor parameters are reported in Tab.21.

Figure 15.1: HEPM motor prototype. The excitation winding can be observed.

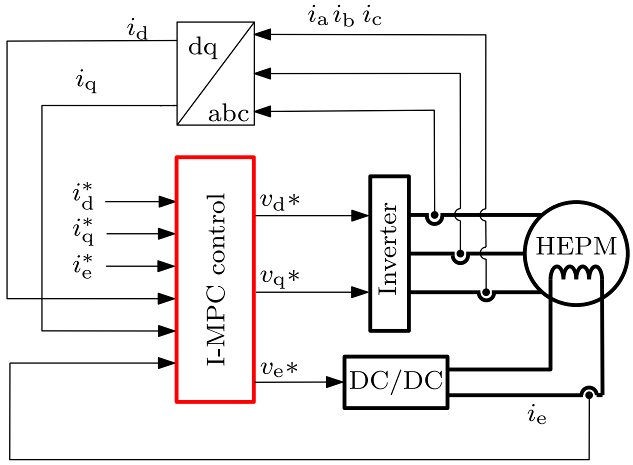

Figure 15.2: HEPM motor drive and the proposed control algorithm is highlighted.

Reformulating (15.1) yields:

$$\begin{aligned}
\frac{di_d}{dt} &= \frac{v_d - R_s i_d + L_q i_q \omega_m^e - \dfrac{M_e v_e}{L_e} + \dfrac{M_e R_e i_e}{L_e}}{L_d - \dfrac{3M_e^2}{2L_e}}, \\
\frac{di_q}{dt} &= \frac{v_q - R_s i_q - \omega_m^e(\Lambda_{PM} + L_d i_d + M_e i_e)}{L_q}, \\
\frac{di_e}{dt} &= \frac{v_e}{L_e} + \frac{3M_e v_d - R_s i_d}{2(3M_e^2/2 - L_d L_e)} + \frac{3M_e^2 v_e - 3M_e^2 R_e i_e}{\sigma_1} + \\
&+ \frac{3L_q M_e i_q \omega_m^e}{2(3M_e^2/2 - L_d L_e)} - \frac{R_e i_e}{L_e},
\end{aligned} \tag{15.2}$$

with $\sigma_1 = 2L_d L_e^2 - 3L_e M_e^2$. Finally, the continuous-time dynamics of the HEPM motor (15.2) are discretized by using the forward Euler approximation with the sampling interval T_s and arranged in the following state-space representation:

$$\begin{aligned}
\boldsymbol{x}(k+1) &= \boldsymbol{A}\boldsymbol{x}(k) + \boldsymbol{B}\boldsymbol{u}(k) + \boldsymbol{D}(k) \\
\boldsymbol{y}(k) &= \boldsymbol{C}\boldsymbol{x}(k)
\end{aligned} \tag{15.3}$$

where $\boldsymbol{x} = [i_d, i_q, i_e]^T$ is the state vector, $\boldsymbol{v} = [v_d, v_q, v_e]$ is the input vector, and $\boldsymbol{y}$ is the output vector. The matrices $\boldsymbol{A}$, $\boldsymbol{B}$, and $\boldsymbol{D}$ are:

$$\boldsymbol{A} = \begin{bmatrix} 1 - \dfrac{R_s T_s}{L_d - \dfrac{3M_e^2}{2L_e}} & \dfrac{L_q \omega_m^e T_s}{L_d - \dfrac{3M_e^2}{2\,L_e}} & \dfrac{M_e R_e T_s}{L_d L_e - \dfrac{3}{2} M_e^2} \\ -\dfrac{L_d \omega_m^e T_s}{L_q} & 1 - \dfrac{R_s T_s}{L_q} & -\dfrac{M_e \omega_m^e T_s}{L_q} \\ -\dfrac{3M_e R_s T_s}{3M_e^2 - 2L_d L_e} & \dfrac{3L_q M_e \omega_m^e T_s}{3M_e^2 - 2L_d L_e} & \sigma_2 \end{bmatrix},$$

$$\boldsymbol{B} = \begin{bmatrix} \dfrac{T_s}{L_d - \dfrac{3M_e^2}{2L_e}} & 0 & -\dfrac{M_e T_s}{L_e \left(L_d - \dfrac{3M_e^2}{2L_e} \right)} \\ 0 & \dfrac{T_s}{L_q} & 0 \\ \dfrac{3M_e T_s}{3M_e^2 - 2L_d L_e} & 0 & \dfrac{3M_e^2 T_s}{\sigma_1} + \dfrac{T_s}{L_e} \end{bmatrix},$$

$$\boldsymbol{D} = \begin{bmatrix} 0 \\ -\dfrac{\Lambda_{PM} \omega_m^e T_s}{L_q} \\ 0 \end{bmatrix},$$

where $\sigma_2 = 1 - \dfrac{R_e T_s}{L_e} - \dfrac{3M_e^2 R_e T_s}{\sigma_1}$, while $\boldsymbol{C} = \boldsymbol{I}_{3\times3}$, with $\boldsymbol{I}_{3\times3}$ being the 3×3 identity matrix.

15.2 MPC CURRENT CONTROL

Indirect MPC (I-MPC) computes the optimal voltage vector $\boldsymbol{v}_{opt}(k)$ that is subsequently applied to the power converter by means of a modulator. The controller predicts the system behavior for the next N_p steps on the basis of the system model (15.3) and the applied voltage vector $\boldsymbol{v}(k-1)$. The optimal voltage input $\boldsymbol{v}_{opt}(k)$ is the vector that minimizes a performance index, or cost function, by taking into account system constraints. The chosen cost function is:

$$J(k) = \sum_{l=k}^{k+N_p-1} \|\boldsymbol{y}^*(l+1) - \boldsymbol{C}\boldsymbol{x}(l+1)\|_2^2 + \lambda_u \|\boldsymbol{v}(l) - \boldsymbol{v}(l-1)\|_2^2, \quad (15.4)$$

which quantifies the defined control objectives, namely, the tracking of the stator and excitation current references and the minimization of control input variation. The control priority between the opposing goals is set by the weighting factor λ_u, which defines the trade-off between the tracking ability of the controller and response time during transients. The optimal control input $\boldsymbol{v}_{\text{opt}}(k)$ is the solution of the following quadratic program (QP):

$$\begin{aligned} \boldsymbol{v}_{\text{opt}}(k) = \arg \underset{\boldsymbol{v} \in \mathbb{R}^3}{\text{minimize}}\ & J(k) \\ \text{subject to}\ & \text{- motor model (15.3),} \\ & \text{- voltage constraints,} \\ & \text{- current constraints.} \end{aligned} \tag{15.5}$$

It is worth noting that for (15.5) to be a convex QP the current and voltage constraints need to be written as linear inequality constraints. To this end, a new formulation to include a current constraint is proposed in the sequel.

15.3 VOLTAGE AND CURRENT CONSTRAINTS

An inherent MPC feature is the capability to include state and/or input constraints in the optimization problem. Successfully handling such constraints can improve the system performance, in particular when critical operation is desired, e.g., flux-weakening. In electric drives, there are physical constraints that relate to the available voltage provided by the converter and the nominal motor current, which are hereafter described. It is worth remembering that a HEPM motor is characterized by an additional excitation winding, supplied by a dc/dc converter, implying that the relevant constraints must be properly handled.

15.3.1 *Voltage Constraint*

The maximum available voltage for a three-phase two-level inverter can be modeled with a vector that lies in a fixed hexagon in the $\alpha\beta$ reference frame where its size depends on the available dc-bus voltage. Any voltage vector lying within the hexagon can be generated by the converter coupled with a modulator. The hexagon represents the voltage constraint and it can be described by its sides, which in turn can be presented as linear inequality constraints. In doing so, the stator voltage constraints, considering the dq rotating frame, are given by:

$$\begin{gathered}\begin{bmatrix}\sqrt{3} & 1 & 0\\ -\sqrt{3} & 1 & 0\\ 0 & 1 & 0\\ 0 & -1 & 0\\ \sqrt{3} & -1 & 0\\ -\sqrt{3} & -1 & 0\end{bmatrix}\boldsymbol{P}^{-1}\begin{bmatrix}v_d\\ v_q\\ v_e\end{bmatrix}\leqslant\frac{V_{dc}}{\sqrt{3}}\begin{bmatrix}2\\2\\1\\1\\2\\2\end{bmatrix}\\ \begin{bmatrix}0 & 0 & 1\\ 0 & 0 & -1\end{bmatrix}\boldsymbol{P}^{-1}\begin{bmatrix}v_d\\ v_q\\ v_e\end{bmatrix}\leqslant\begin{bmatrix}v_{e,\mathrm{lim}}\\ v_{e,\mathrm{lim}}\end{bmatrix}\end{gathered} \tag{15.6}$$

where $\boldsymbol{P}^{-1}$ is the inverse of the Park transformation and it is reported in Appendix A.1. Moreover, (15.6) shows the rotor voltage constraint. Note that the inequality constraints (15.6) define the "voltage constraints" in the QP (15.5).

15.3.2 *Current Constraint*

Both the stator and excitation currents must be kept below their nominal values to ensure the safe operation of the motor. To achieve this, additional constraints can be added to the MPC formulation, similarly to the voltage one. By translating the current (i.e., output) constraints into voltage (i.e., input) constraints an ellipsoidal feasible area results in the dq voltage frame. This implies that the current-related voltage constraints are nonlinear, and as such cannot be directly added to the QP (15.5). Hence, the current constraints must be linearized so that they can be added to the optimization problem. A conventional method suitable for the QP formulation is called linear piecewise method (LPM) [64] and it approximates the nonlinear constraints with a polygon. In doing so, however, the number constraints can increase significantly, making the constrained MPC problem more computationally demanding. In this paper, the equivalent tangent method (ETM) is proposed to mitigate the aforementioned issue. The ETM calculates the tangent line of the nonlinear constraints closest to the last applied voltage vector $\boldsymbol{u}(k-1)$. As a result, the nonlinear constraints can be approximated with only one linear constraint.

As mentioned above, the stator current constraint is a nonlinear function:

$$i_d(k+1)^2 + i_q(k+1)^2 \leqslant i_{\mathrm{lim}}^2 \tag{15.7}$$

where $i_{\text{lim}} = I_N$ is the stator current limit. Expression (15.7) can be rearranged as a function of the corresponding voltage limits $v_{d,\text{lim}}$ and $v_{q,\text{lim}}$ by exploiting (15.3), yielding:

$$(c\, v_{d,\text{lim}} + a(k))^2 + (d\, v_{q,\text{lim}} + b(k))^2 \leqslant i_{\text{lim}}^2 \tag{15.8}$$

where the time-varying coefficients $a(k)$ and $b(k)$, and the constants c and d are:

$$\begin{aligned}
a(k) &= i_d(k) - T_s \frac{R_s\, i_d(k)}{L_d - \dfrac{3\, {M_e}^2}{2\, L_e}} + T_s \frac{M_e\, v_e(k) - M_e\, R_e\, i_e(k)}{\dfrac{3\, {M_e}^2}{2} - L_d\, L_e} \\
&\quad + T_s \frac{L_q\, i_q(k)\, \omega_m^e}{L_d - \dfrac{3\, {M_e}^2}{2\, L_e}} \\
b(k) &= i_q(k)\left(1 - \frac{R_s T_s}{L_q}\right) + \frac{T_s \omega_m^e}{L_q}\left(\Lambda_{PM} - L_d i_d(k) - M_e i_e(k)\right) \\
c &= \frac{T_s}{L_d - \dfrac{3\, {M_e}^2}{2\, L_e}}, \qquad d = \frac{T_s}{L_q}
\end{aligned} \tag{15.9}$$

As can be seen, (15.8) depicts an ellipsoid in the dq voltage plane, the center and radii of which change according to the operating point. Note that to simplify the mathematical notation, the explicit time-step dependency is omitted hereafter.

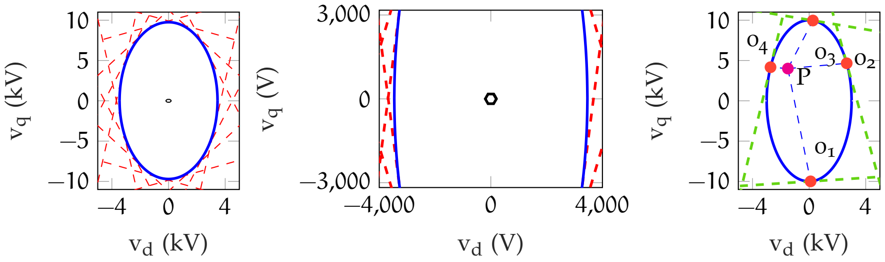

(a) Voltage and current constraints with LPM.

(b) Zoom-in on Fig. 15.3a.

(c) Voltage and current constraints with ETM.

Figure 15.3: Visualization of the LPM and ETM.

15.3.2.1 *Linear Piecewise Method*

The LPM approximates (15.8) with n_a straight lines, each of which is tangent to the ellipse while all tangency points are equally spaced. According to this method, a generic ellipse (15.8) can be approximated as follows:

$$\sum_{k=1}^{n_a} c\, v_d \cos(k\alpha) + d\, v_q \sin(k\alpha) \leqslant i_{\text{lim}} - a\cos(k\alpha) - b\sin(k\alpha), \tag{15.10}$$

with the approximation angle $\alpha = 2\pi/n_a$ and k is a integer number. It is worth noting that the value of n_a can be selected according to the desired level of approximation accuracy. Increasing n_a results in a higher degree of accuracy, but also in a bigger number of summation terms, and thus constraints.

The linearization method (15.10) can be applied to the voltage constraint (15.8), yielding the following linear constraints for the QP (15.5):

$$\boldsymbol{L}\begin{bmatrix} v_{d,\mathrm{lim}} \\ v_{q,\mathrm{lim}} \\ v_{e,\mathrm{lim}} \end{bmatrix} \leqslant \boldsymbol{I}_{\mathbf{lim}} \tag{15.11}$$

where

$$\boldsymbol{L} = \begin{bmatrix} c\cos(\alpha) & d\sin(\alpha) & 0 \\ \vdots & \vdots & \vdots \\ c\cos\Big((n_a-1)\alpha\Big) & d\sin\Big(n_a-1)\alpha\Big) & 0 \\ c & 0 & 0 \end{bmatrix}, \tag{15.12}$$

$$\boldsymbol{I}_{\mathbf{lim}} = \begin{bmatrix} i_{\mathrm{lim}} - a\cos(\alpha) - b\sin(\alpha) \\ \vdots \\ i_{\mathrm{lim}} - a\cos\Big((n_a-1)\alpha\Big) - b\sin\Big((n_a-1)\alpha\Big) \\ i_{\mathrm{lim}} - a \end{bmatrix}. \tag{15.13}$$

The linearized constraints with the LPM are reported in Fig. 15.3a with the actual current-based voltage elliptical constraint. The voltage limit (the hexagon) is depicted as well. The number of approximating lines was set equal to $n_a = 18$ as trade-off between accuracy and the number of constraints, i.e., complexity of the MPC problem. It is worth noting the different dimension of the voltage and current-based constraints shown in the zoomed-in dq voltage plane in Fig. 15.3b. Indeed, the former one is more strict.

15.3.2.2 *Equivalent Tangent Method*

The proposed method exploits the different dimension of the voltage and current-based constraint in the dq reference frame and the fact that only a small part of the ellipsoidal constraint is actually involved in the optimization problem when the current constraint is active. Specifically, the LPM introduces several constraints, most of which are not necessary in the optimization as they set a less restrictive constraint than that imposed by the voltage hexagon. Moreover, the tangent lines are uniformly distributed along the ellipse and, in case of a reduced number of them, the approximation will be very

coarse, and thus less effective, meaning that a violation of the actual ellipsoidal constraint becomes more likely.
To overcome this issue, the ETM replaces the ellipse trace with the tangent line closest to the last applied voltage vector. As a result, only one constraint must be included in the QP (15.5) instead of n_a introduced by the LPM. Fig. 15.3c illustrates the ETM principle. The point P represents the last applied voltage vector, the ellipse is the current-based constraint and the dashed segments are the four tangent lines orthogonal to the vector Po_x, with $x \in \{1, 2, 3, 4\}$. The only constraint included in the optimization problem (15.5) is the tangent line to the point o_4.

The desired tangent line closest to the last applied voltage vector can be obtained by rewriting the ellipsoidal current constraint (15.8) in its canonical, i.e.,:

$$\frac{\left(v_{d,\text{lim}} + \dfrac{a}{c}\right)^2}{\left(\dfrac{i_{\text{lim}}}{c}\right)^2} + \frac{\left(v_{q,\text{lim}} + \dfrac{b}{d}\right)^2}{\left(\dfrac{i_{\text{lim}}}{d}\right)^2} = 1. \tag{15.14}$$

This expression corresponds to an ellipse centered at $\left(v_{d,\text{lim}}, v_{q,\text{lim}}\right) = (a/c, b/d)$. This ellipse can be shifted such that its center is the origin of the dq voltage plane, resulting in:

$$\frac{v_{d,\text{lim}}^2}{\Psi^2} + \frac{v_{q,\text{lim}}^2}{\Theta^2} = 1, \tag{15.15}$$

where $\Psi = i_{\text{lim}}/c$ and $\Theta = i_{\text{lim}}/d$. A tangent line to the shifted ellipse (15.15) at a generic point o (v_{do}, v_{qo}) can be computed with the help of:

$$\frac{v_{d,\text{lim}} v_{do}}{\Psi^2} + \frac{v_{q,\text{lim}} v_{qo}}{\Theta^2} = 1. \tag{15.16}$$

Finally, (15.16) can be rewritten in the explicit form as:

$$v_{q,\text{lim}} = \frac{\Theta^2}{v_{qo}} - \frac{\Theta^2}{\Psi^2}\frac{v_{do}}{v_{qo}} v_{d,\text{lim}} = q_r + m_r v_{d,\text{lim}}, \tag{15.17}$$

where m_r and q_r are the angular coefficient and the intercept of the tangent line, respectively.

The angular coefficient of the line segment that connects point P (v_{dP}, v_{qP}) inside the ellipse with point o is:

$$m_{Po} = \frac{v_{qP} - v_{qo}}{v_{dP} - v_{do}}. \tag{15.18}$$

With (15.18), the coordinates of the desired point o (v_{do}, v_{qo}) can be found by solving the following system of equations:

$$\begin{cases} m_r = -\dfrac{1}{m_{Po}} \\ \dfrac{v_{do}^2}{\Psi^2} + \dfrac{v_{qo}^2}{\Theta^2} = 1 \end{cases} \Rightarrow \begin{cases} -\dfrac{\Theta^2}{\Psi^2}\dfrac{v_{do}}{v_{qo}} = \dfrac{v_{do} - v_{dP}}{v_{qP} - v_{qo}} \\ \dfrac{v_{do}^2}{\Psi^2} + \dfrac{v_{qo}^2}{\Theta^2} = 1 \end{cases} \tag{15.19}$$

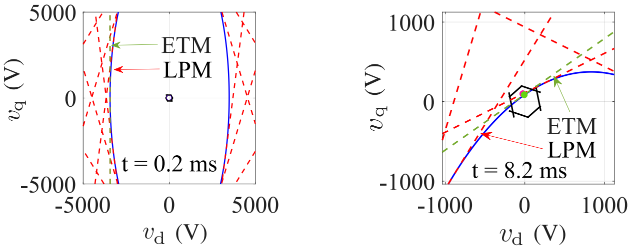

(a) Problem snapshot at 0.2 ms. (b) Problem snapshot at 8.2 ms.

Figure 15.4: Voltage and current constraints. Both LPM and ETM are shown.

where the first equation imposes the perpendicularity condition between line segment P0 and the tangent lines belonging to the ellipse, while the second equation represents the location of point o on the ellipse.

System (15.19) has four solutions, as depicted in Fig. 15.3c. Indeed given a point P inside the ellipse, four tangent lines perpendicular to the segment Po exist. However, the proposed method takes into account only the solution closest to point P. It is worth remembering that the ellipsoidal current constraint has been shifted, meaning that the computed solution must be properly displaced. Hence, Point o (v_{do}, v_{qo}) computed with (15.19) must be relocated to the original reference system. Given this, the tangent line coefficients in the original dq reference frame can be obtained as follows:

$$\begin{aligned} m_r' &= m_r, \\ q_r' &= \left(v_{qo} - \frac{b}{d}\right) - m_r \left(v_{do} - \frac{b}{d}\right). \end{aligned} \tag{15.20}$$

With the above, the proposed linearized current constraint tailored for the QP (15.5) is:

$$\begin{bmatrix} m_r' & -1 & 0 \end{bmatrix} \begin{bmatrix} v_{d,\mathrm{lim}} \\ v_{q,\mathrm{lim}} \\ v_{e,\mathrm{lim}} \end{bmatrix} < q_r', \tag{15.21}$$

where the coefficients m_r' and q_r' are computed at each discrete time step. Finally, it is worth mentioning that the aforementioned procedure is with regards to the stator currents. Nevertheless, a similar approach can be applied to the excitation current, as reported in Appendix A.2.

15.4 PERFORMANCE ASSESSMENT

The proposed ETM was tested by means of simulations. Two different tests were carried out. The first one compares the conventional LPM with the proposed one, whereas the latter examines the capability of the proposed MPC scheme to handle the magnetic mutual coupling between the rotor and stator windings of a HEPM motor. Both tests were carried out at steady-state operating conditions with a speed equal to one third of the nominal one. The stator current references were set equal to $i_d^* = -0.5\,\text{A}$, $i_q^* = 1.5\,\text{A}$, whereas the current limits were set equal to $i_{\text{lim}} = 2\,\text{A}$ and $i_{e,\text{lim}} = 2.1\,\text{A}$. Other relevant control parameters were $N_p = 7$, $\lambda_u = 1 \cdot 10^{-3}$ and $n_a = 18$. The switching frequency was $f_s = 10\,\text{kHz}$, while the inverter and dc/dc converter voltage buses were set to $V_{dc} = 300\,\text{V}$ and $U_{dc,\,dc/dc} = 50\,\text{V}$, respectively.

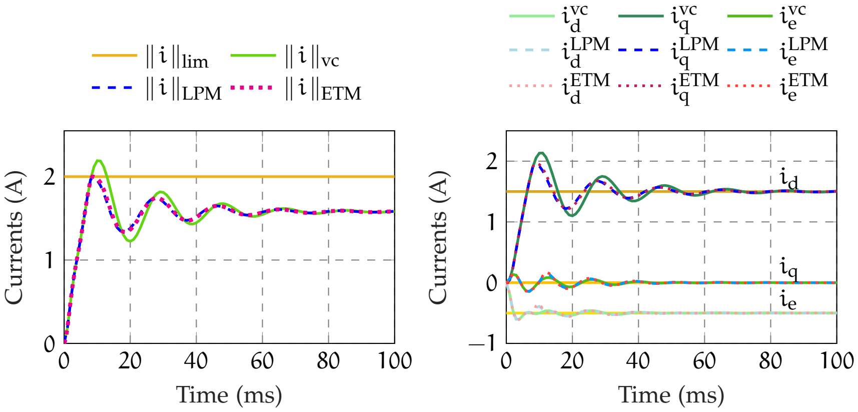

(a) Stator current vector magnitude. (b) Stator and excitation current response.

Figure 15.5: Comparison between voltage (vc) and current constrained MPC solution, both with LPM and the proposed ETM without rotor current.

15.4.1 *Comparison Between LPM and ETM*

In this test, the LPM and ETM current constraints are compared while the excitation current reference was set to zero. Fig. 15.4 shows the dq voltage plane with the voltage and current limits in two different time instants of the test depicted in Fig. 15.5, namely, when the current limit is not active and when it is activated and thus affecting the optimal solution accordingly. Fig. 15.4a and Fig. 15.4b show the dq voltage plane when the current constraint affects the optimal solution, namely, the ellipse intersects the voltage hexagon. All linearized trajectories are depicted as well. The ETM segment better approximates the ellipse, whereas the LPM segments are less accurate. As a result, a violation of the original (i.e. ellipsoidal) current-based constraint is avoided with the proposed method. Moreover, the proposed algorithm keeps the computational burden at bay since only one—instead of n_a—linear constraint is computed.

Fig. 15.5 shows the current transient and the magnitude of current vector for three different cases, i.e., (a) when only the voltage (hexagon) constraint is used, (b) when the voltage and current-based constraints as approximated with the LPM are used, (c) the same as 'b', but the current-based constraint is approximated with the proposed ETM. In Fig. 15.5 the voltage constraint is always respected but the current can exceed its limit if the constraint is not included in the optimization problem (see Fig. 15.5a with $\| i \|^{vc}$). On the contrary, the current almost fully respects the defined limit when its constraint is included in (15.5). However, it is worth noting that the stator current slightly exceeds its maximum allowable value when the LPM is implemented compared to the proposed method, since the linearized ellipse is not accurate enough at the depicted point. The current limitation allows for a smoother transient without affecting the rising time, while the excitation current i_e oscillations are due to the mutual inductances between the stator end excitation windings. Specifically, the HEPM motor exhibits a noteworthy rotor-stator interaction which reflects on currents and torque dynamics. Hence, the motor controller must be able to reject these oscillations as much as possible to improve performance.

15.4.2 *Mutual Inductance Effect*

To analyze the MPC ability to handle the mutual coupling between the stator and rotor windings, an additional test was carried out. More specifically, this test investigates the system behavior when the excitation current reference is zero or close to its limit, namely, $i_e^* = 2\,A$. At the beginning of the test, all currents are initialized to zero and the current constraints are linearized with the proposed ETM. Fig. 15.6a shows the dynamic behavior of the currents for both considered cases. As can be seen, the quadrature current is not affected by the operating conditions as dictated by the excitation current reference. On the contrary, the direct and excitation currents are strongly coupled, as changes in the excitation current i_e have a great impact on the direct current i_d amplitude. It is worth noting that the direct current overshoot increases with an increasing excitation current. For the first $3\,ms$, namely, until the direct current reaches its minimum value, the excitation current increases almost linearly. Indeed, the applied voltage is saturated (see Fig. 15.6b). After the i_d negative peak, and even though the excitation voltage remains saturated, the excitation current i_e rate of change decreases since is is affected by the direct current transient. Hence, as MPC tries to track the the direct current reference, it cannot keep the same excitation current slope since the dc/dc voltage is fully exploited. Nevertheless, both the magnitude of the stator current (see Fig. 15.6c) as well as of the excitation one (see Fig. 15.6a) remain below the imposed limits, thus clearly demonstrating the effectiveness of the proposed current constraint linearization method.

15.5 DISCUSSION

This paper proposed an indirect MPC control algorithm for HEPM motors. The proposed MPC method is designed based on the HEPM motor model, which, as shown, has intrinsic differences compared with conventional synchronous motors. Moreover, the developed control algorithm accounts for both the voltage and stator and rotor current limits. To achieve this, the nonlinear current constraints are included into the derived QP, after being transformed into equivalent voltage constraints, and linearized by means of the tangent segment closest to the last applied voltage vector. Thanks to this linearization method, the proposed control scheme is computationally efficient, and thus suitable for an on-chip implementation. Simulation results highlight the efficacy and the reliability of the proposed MPC algorithm as well as the strong coupling between the stator and excitation windings of the HEPM motor.

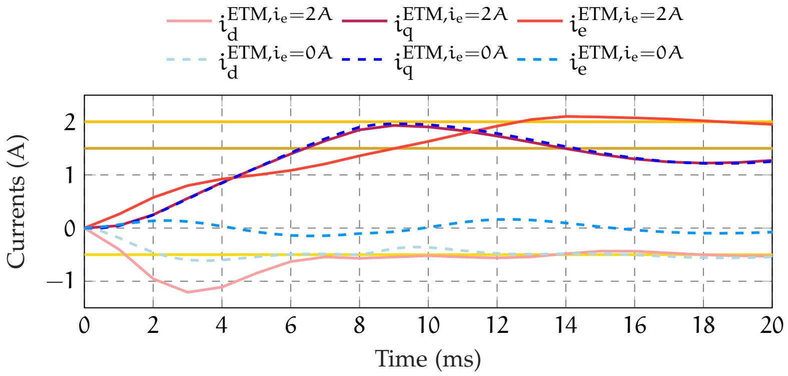

(a) Stator and excitation current response.

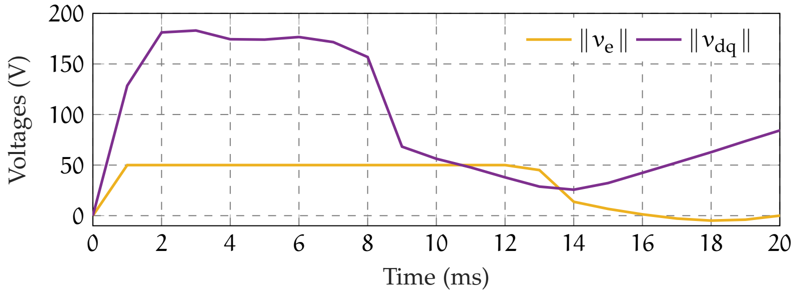

(b) Stator and excitation voltage magnitude.

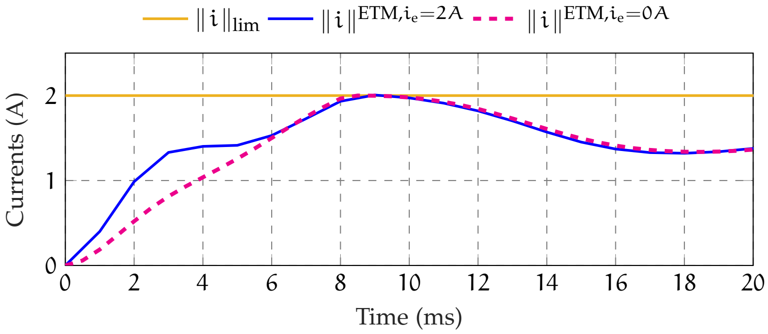

(c) Stator current vector magnitude.

Figure 15.6: Dynamic response considering the mutual inductance effect.

16

CONCLUSION

This thesis presents a comprehensive investigation about analysis, design and control of electrically excited synchronous motors (EESM) and hybrid excited permanent magnet motors (HEPM) for electric drive applications. These motor configurations are promising due to their high torque and power density, their capability to operate in a wide speed range and a reduced dependence on rare earth permanent magnets.

Various HEPM motor structures are investigated, including series and parallel configurations, and their performance under both no-load and load conditions is deeply analysed. Parallel configurations have been validated as more convenient than series topology. Various studies are carried out comparing permanent magnet motor capabilities to EESM and HEPM motors capabilities, for given machine sizes. Comparing to the interior permanent magnet motor, the HEPM motor exhibits similar performance, while comparing to the EESM, it exhibits higher performance. Thermal and mechanical issues are a possible bottleneck for the HEPM motor. Such issues are analyzed and suggestions are given to overcome the limits adopting proper designs.

The design process focuses on both theoretical approach and practical design considerations. Analytical methods are used to calculate the main machine parameters, with particular emphasis on optimizing performance at both low-speed (maximum torque per ampere) and high speed (flux weakening) operating points. Detailed design and optimisation processes are outlined for EESM and HEPM motors, culminating in the selection of an optimum motor geometry.

Different electrical control strategies suited for HEPM motors are implemented. A control range of many techniques including Maximum Torque Per Amps control, sensorless control and Flux Weakening control is reported. In addition, an extension of implicit Model Predictive Control is explored considering voltage and current constraints.

In addition to the design of both motor geometry and the definition of the control algorithms, a prototype is built. Systematic experimental tests are carried to validate the electromagnetic analysis and the drive control strategies.

Part IV

APPENDIX

A

APPENDIX

A.1 INVERSE PARK TRANSFORMATION

The inverse Park transformation is the following 3×3 matrix:

$$\boldsymbol{P}^{-1} = \begin{bmatrix} \cos(\omega_m^e t) & -\sin(\omega_m^e t) & 0 \\ \sin(\omega_m^e t) & \cos(\omega_m^e t) & 0 \\ 0 & 0 & 1 \end{bmatrix}. \tag{A.1}$$

A.2 EXCITATION CURRENT CONSTRAINT

The rotor current has to satisfy the current constraint $\| i_e(k+1) \| \leqslant \| i_{e,\lim} \|$ and it can be written as:

$$\left(\frac{3\,{M_e}^2}{\sigma_1} + \frac{T_s}{L_e}\right) v_{e,\lim} + a_e(k) \leqslant i_{e,\lim}, \tag{A.2}$$

where:

$$\begin{aligned} a_e(k) = i_e(k) + T_s \Bigg[& \frac{3\,M_e\,v_d(k)}{2\left(\frac{3\,{M_e}^2}{2} - L_d\,L_e\right)} - \frac{R_e\,i_e(k)}{L_e} + \\ & - \frac{3\,M_e\,R_s\,i_d(k)}{2\left(\frac{3\,{M_e}^2}{2} - L_d\,L_e\right)} - \frac{3\,{M_e}^2\,R_e\,i_e(k)}{\sigma_1} + \\ & + \frac{3\,L_q\,M_e\,i_q(k)\,\omega_m^e}{2\left(\frac{3\,{M_e}^2}{2} - L_d\,L_e\right)} \Bigg]. \end{aligned} \tag{A.3}$$

The rotor current constraint can be written for both positive and negative values as:

$$\begin{bmatrix} 0 & 0 & \frac{3T_s\,{M_e}^2}{\sigma_1} + \frac{T_s}{L_e} \\ 0 & 0 & -\frac{3T_s\,{M_e}^2}{\sigma_1} - \frac{T_s}{L_e} \end{bmatrix} \begin{bmatrix} v_{d,\lim} \\ v_{q,\lim} \\ v_{e,\lim} \end{bmatrix} \leqslant \begin{bmatrix} i_{e,\lim} - a_e(k) \\ i_{e,\lim} - a_e(k) \end{bmatrix}, \tag{A.4}$$

and can be included in the QP (15.5). It is worth noting that only one of the two constraints needs to be used in order to reduce the size of the optimization problem. Specifically, if the current reference is positive, the upper limit is used, otherwise the lower one.

BIBLIOGRAPHY

[1] Indula Prasad Abeyrathne, Mohammad Sedigh Toulabi, and Shaahin Filizadeh. “Design Optimization and Performance Prediction of Synchronous Reluctance Motors.” In: *2018 21st International Conference on Electrical Machines and Systems (ICEMS)*. 2018, pp. 576–581. doi: `10.23919/ICEMS.2018.8548975`.

[2] Undeland ; adnanes1991-Tor Adnanes, A Adnanes, and T Undeland. “newblock Optimum torque performance in PMSM drives above rated speed.” In: *Proceedings of the Conference Record of the 1991 IEEE Industry Applications Society Annual Meeting*. Vol. 1. Dearborn, MI, USA, Sept. 28, 1991, pp. 169–175. doi: `10.1109/IAS.1991.178150detokenize{10.1109/IAS.1991.178150}`.

[3] *Advanced Synchronous Motor (ASM) Technology*. url: `https://evkx.net/technology/motors/asm/`.

[4] Piergiorgio Alotto, Massimo Barcaro, Nicola Bianchi, and Massimo Guarnieri. “Optimization of Interior PM Motors With Machaon Rotor Flux Barriers.” In: *IEEE Transactions on Magnetics* 47.5 (2011), pp. 958–961. doi: `10.1109/TMAG.2010.2073450`.

[5] Amara, Vido, Gabsi, Ben ahmed Hoang, Y Amara, L Vido, M Gabsi, E Hoang, A Ben ahmed, and M Lecrivain. “newblock Hybrid Excitation Synchronous Machines: Energy-Efficient Solution for Vehicles Propulsion. newblock em, journal = IEEE Trans. Emergy Sel. Top. Power Electron. bf, date = 2009, year = 2009, pages = 2137–2149, volume = 58, doi = 10.1109/TVT.2008.2009306detokenize10.1109/TVT.2
In: ().

[6] Yacine Amara, Hamid Ben Ahmed, and Mohamed Gabsi. *Hybrid Excited Synchronous Machines: Topologies, Design and Analysis*. John Wiley & Sons, 2023.

[7] Yacine Amara, Sami Hlioui, Hamid Ben Ahmed, and Mohamed Gabsi. “Power Capability of Hybrid Excited Synchronous Motors in Variable Speed Drives Applications.” In: *IEEE Trans. on Magnet.* 55.8 (2019), pp. 1–12. doi: `10.1109/TMAG.2019.2911599`.

[8] Yacine Amara, Lionel Vido, Mohamed Gabsi, Emmanuel Hoang, A. Hamid Ben Ahmed, and Michel Lecrivain. “Hybrid Excitation Synchronous Machines: Energy-Efficient Solution for Vehicles Propulsion.” In: *IEEE Trans. Emerg. Sel. Topics Power Electron.* 58.5 (2009), pp. 2137–2149. doi: `10.1109/TVT.2008.2009306`.

[9] Giacomo Bacco and Nicola Bianchi. “Design Criteria of Flux-Barriers in Synchronous Reluctance Machines.” In: *IEEE Transactions on Industry Applications* 55.3 (2019), pp. 2490–2498. DOI: `10.1109/TIA.2018.2886778`.

[10] Massimo Barcaro, Nicola Bianchi, and Freddy Magnussen. “Rotor Flux-Barrier Geometry Design to Reduce Stator Iron Losses in Synchronous IPM Motors Under FW Operations.” In: *IEEE Trans. on Ind. Appl.* 46.5 (2010), pp. 1950–1958. DOI: `10.1109/TIA.2010.2060175`.

[11] Matteo Berto, Luigi Alberti, Virginia Manzolini, and Silverio Bolognani. “Computation of Self-Sensing Capabilities of Synchronous Machines for Rotating High Frequency Voltage Injection Sensorless Control.” In: *IEEE Trans. on Ind. Electron.* 69.4 (2022), pp. 3324–3333. DOI: `10.1109/TIE.2021.3071710`.

[12] Matteo Berto, Paolo Gherardo Carlet, Virginia Manzolini, and Luigi Alberti. “An Effective Ellipse Fitting Technique of the Current Response Locus to Rotating HF Voltage Injection in IPMSM for Sensorless Rotor Position Estimation.” In: *IECON 2018 - 44th Ann. Conf. of the IEEE Ind. Electron. Soc.* 2018, pp. 391–396. DOI: `10.1109/IECON.2018.8591855`.

[13] Jovanovic Betz, Lagerquist Betz, R Jovanovic, M Lagerquist, R Miller, and T. “newblock Aspects of the control of synchronous reluctance machines including saturation and iron losses.” In: *newblock In Proceedings of the Conference Record of the 1992 IEEE Industry Applications Society Annual Meeting*. Vol. 1. Houston, TX, USA, Oct. 1992, pp. 456–463. DOI: `10.1109/IAS.1992.244360detokenize{10.1109/IAS.1992.244360}`.

[14] N. Bianchi and S. Bolognani. “Unified approach to the analysis and design of an AC motor drive for flux-weakening operations.” In: *Conf. Record of 1998 IEEE Ind. Appl. Conf. Thirty-Third IAS Ann. Meet.* Vol. 1. 1998, 95–102 vol.1. DOI: `10.1109/IAS.1998.732265`.

[15] N. Bianchi, S. Bolognani, and P. Frare. “Design criteria for high-efficiency SPM synchronous motors.” In: *IEEE Transactions on Energy Conversion* 21.2 (2006), pp. 396–404. DOI: `10.1109/TEC.2005.853720`.

[16] N. Bianchi and T.M.Jahns. *Design,analysis, and control of interior PM syncronous machines*. Vol. 1. Clarendon, 2004.

[17] Nicola Bianchi, Alessandro Castagnini, Pietro Savio Termini, and Giulio Secondo. “The nature of the torque ripple in fractional-slot synchronous PMAREL machines.” In: *2016 IEEE Energy Conversion Congress and Exposition (ECCE)*. 2016, pp. 1–8. DOI: `10.1109/ECCE.2016.7855505`.

[18] Nicola Bianchi, Daniele Michieletto, and Luca Cinti. "Hybrid Excitation PM Synchronous Motors: Part II - Finite Element Analysis." In: *IEEE Trans. on Energy Convers.* 37.1 (2021), pp. 1–1. DOI: `10.1109/TEC.2021.3107957`.

[19] Claudio Bianchini, Giovanni Franceschini, and Ambra Torreggiani. "Improvement on Flux Weakening Control Strategy for Electric Vehicle Applications." In: *Applied Sciences* 11.5 (2021). ISSN: 2076-3417. URL: `https://www.mdpi.com/2076-3417/11/5/2422`.

[20] Aldo Boglietti, Andrea Cavagnino, Mircea Popescu, and Dave Staton. "Thermal Model and Analysis of Wound-Rotor Induction Machine." In: *IEEE Transactions on Industry Applications* 49.5 (2013), pp. 2078–2085. DOI: `10.1109/TIA.2013.2261444`.

[21] Ion Boldea, Vasile Coroban-Schramel, Gheorghe-Daniel Andreescu, Frede Blaabjerg, and Sever Scridon. "BEGA Starter/Alternator—Vector Control Implementation and Performance for Wide Speed Range at Unity Power Factor Operation." In: *IEEE Transactions on Industry Applications* 46.1 (2010), pp. 150–158. DOI: `10.1109/TIA.2009.2036534`.

[22] S. Bolognani, L. Tubiana, and M. Zigliotto. "EKF-based sensorless IPM synchronous motor drive for flux-weakening applications." In: *IEEE Trans. on Ind. Appl.* 39.3 (2003), pp. 768–775. DOI: `10.1109/TIA.2003.810666`.

[23] Silverio Bolognani, Sandro Calligaro, and Roberto Petrella. "Adaptive Flux-Weakening Controller for Interior Permanent Magnet Synchronous Motor Drives." In: *IEEE Trans. Emerg. Sel. Topics Power Electron.* 2.2 (2014), pp. 236–248. DOI: `10.1109/JESTPE.2014.2299153`.

[24] Gabriele Borocci, Fabio Giulii Capponi, Giulio De Donato, and Federico Caricchi. "Closed-Loop Flux-Weakening Control of Hybrid-Excitation Synchronous Machine Drives." In: *IEEE Trans. on Ind. Appl.* 53.2 (2017), pp. 1116–1126. DOI: `10.1109/TIA.2016.2639031`.

[25] R. Cao, X. Zhang, and X. Yuan. "A New Three-Phase Hybride Excitation Flux-Switching Motor for EV/HEV Applications." In: *2019 IEEE International Electric Machines Drives Conference (IEMDC)*. San Diego, CA, USA, May 2019, pp. 1398–1403. DOI: `10.1109/IEMDC.2019.8785097`.

[26] Ritvik Chattopadhyay, Md Sariful Islam, Ion Boldea, and Iqbal Husain. "FEA Characterization of Bi-Axial Excitation Machine for Automotive Traction Applications." In: *2021 IEEE International Electric Machines Drives Conference (IEMDC)*. Hartford, CT, USA, May 20, 2021, pp. 1–7. DOI: `10.1109/IEMDC47953.2021.9449514`.

[27] Ningning Chen, Zedong Zheng, Jun Zhou, Yongdong Li, and Kui Wang. "A novel MPC flux weakening method for induction motor applied in electric wheel." In: *2013 Inter. Conf. on Electr. Machin. and Syst. (ICEMS)*. 2013, pp. 113–118. DOI: `10.1109/ICEMS.2013.6754533`.

[28] Yuzheng Chen, Xiaoyan Huang, Jun Wang, Feng Niu, Jian Zhang, Youtong Fang, and Lijian Wu. "Improved Flux-Weakening Control of IPMSMs Based on Torque Feedforward Technique." In: *IEEE Transactions on Power Electronics* 33.12 (2018), pp. 10970–10978. DOI: `10.1109/TPEL.2018.2810862`.

[29] Carlucci Cinti, Bianchi, L Bertoluzzo]cl2021structural Cinti, M Carlucci, N Bianchi, and M Bertoluzzo. *newblock Electro-Magnetic and Structural Analysis of Six-Pole Hybrid-Excited Permanent Magnet Motors. newblock em Electronics bf 2021, em 10*. Ed. by bibitem[Cinti emet al. 2021. DOI: `10.3390/electronics10172051detokenize{10.3390/electronics10172051}`.

[30] Luca Cinti and Nicola Bianchi. "Hybrid-Excited PM Motor for Electric Vehicle." In: *Energies* 14.4 (2021), p. 916. ISSN: 1996-1073. DOI: `10.3390/en14040916`. URL: `https://www.mdpi.com/1996-1073/14/4/916`.

[31] Luca Cinti and Nicola Bianchi. "Optimal Shaping for Electrically Excited Synchronous Motor." In: *2023 IEEE International Conference on Electrical Systems for Aircraft, Railway, Ship Propulsion and Road Vehicles & International Transportation Electrification Conference (ESARS-ITEC)*. IEEE. 2023, pp. 1–6.

[32] Luca Cinti, Paolo Gherardo Carlet, Ludovico Ortombina, and Nicola Bianchi. "Maximization of Sensorless Capabilities of Hybrid Excited Permanent Magnet Motors." In: *2022 Int. Conf. on Electrical Machines (ICEM)*. 2022, pp. 2234–2241. DOI: `10.1109/ICEM51905.2022.9910877`.

[33] Luca Cinti, Mattia Carlucci, Nicola Bianchi, and Manuele Bertoluzzo. "Electro-Magnetic and Structural Analysis of Six-Pole Hybrid-Excited Permanent Magnet Motors." In: *Electronics* 10.17 (2021). ISSN: 2079-9292. DOI: `10.3390/electronics10172051`. URL: `https://www.mdpi.com/2079-9292/10/17/2051`.

[34] Luca Cinti, Chiara Contò, and Nicola Bianchi. "A Comparison between Hybrid Excited Permanent Magnet and Wound Rotor Motor." In: *International Symposium on Power Electronics, Electric Drives, Automation and Motion (Speedam), Sorrento, Italy*. Vol. 1. June 22-24, 2022, pp. 14–19.

[35] Luca Cinti, Daniele Michieletto, Nicola Bianchi, and Manuele Bertoluzzo. "A Comparison between Hybrid Excitation and Interior Permanent Magnet Motors." In: *2021 IEEE Workshop on Electrical Machines Design, Control and Diagnosis (WEMDCD)*.

Modena, Italy, 8, Apr. 9, 2021, pp. 10–15. DOI: `10.1109/WEMDCD51469.2021.9425634`.

[36] Michieletto Cinti, Bianchi, L Bertoluzzo]cl2021mod Cinti, D Michieletto, N Bianchi, and M Bertoluzzo. "A Comparison between Hybrid Excitation and Interior Permanent Magnet Motors." In: *Proceedings of the 2021 IEEE Workshop on Electrical Machines Design, Control and Diagnosis (WEMDCD)*. Ed. by bibitem[Cinti emet al. Modena, Italy, Apr. 2021, pp. 10–15. DOI: `10.1109/WEMDCD51469.2021.9425634detokenize{10.1109/WEMDCD51469.2021.9425634}`.

[37] Andrea Credo, Giuseppe Fabri, Marco Villani, and Mircea Popescu. "Adopting the Topology Optimization in the Design of High-Speed Synchronous Reluctance Motors for Electric Vehicles." In: *IEEE Transactions on Industry Applications* 56.5 (2020), pp. 5429–5438. DOI: `10.1109/TIA.2020.3007366`.

[38] Linh Dang, Nicolas Bernard, Nicolas Bracikowski, and Gérard Berthiau. "Design Optimization with Flux Weakening of High-Speed PMSM for Electrical Vehicle Considering the Driving Cycle." In: *IEEE Transactions on Industrial Electronics* 64.12 (2017), pp. 9834–9843. DOI: `10.1109/TIE.2017.2726962`.

[39] A. Dianov, F. Tinazzi, S. Calligaro, and S. Bolognani. "Review and Classification of MTPA Control Algorithms for Synchronous Motors." In: *IEEE Trans. on Power Electron.* 37.4 (2022), pp. 3990–4007. DOI: `10.1109/TPEL.2021.3123062`.

[40] Tinazzi Dianov, Calligaro Bolognani]dianov2022 Dianov, A Tinazzi, F Calligaro, S Bolognani, and S. "newblock Review and Classification of MTPA Control Algorithms for Synchronous Motors. newblock em IEEE Trans, booktitle = Power Electron. bf 2022, em 37." In: pp. 3990–4007. DOI: `10.1109/TPEL.2021.3123062detokenize{10.1109/TPEL.2021.3123062}`.

[41] Andrea Favato, Paolo Gherardo Carlet, Francesco Toso, Riccardo Torchio, and Silverio Bolognani. "Integral Model Predictive Current Control for Synchronous Motor Drives." In: *IEEE Trans. on Power Electron.* 36.11 (2021), pp. 13293–13303. DOI: `10.1109/TPEL.2021.3081827`.

[42] Federica Graffeo, Silvio Vaschetto, Marco Cossale, Michael Kerschbaumer, Edson C. Bortoni, and Andrea Cavagnino. "Cylindrical Wound-Rotor Synchronous Machines for Traction Applications." In: *2020 International Conference on Electrical Machines (ICEM)*. Vol. 1. 2020, pp. 1736–1742. DOI: `10.1109/ICEM49940.2020.9270992`.

[43] Aiyu Gu, Yiwei Guo, Jianan Dong, Bo Ruan, Yingzhan Lian, Shiquan Zhang, and Xiaofeng Song. "Modeling and Analysis of the Flux-Weakening Range of Interior Permanent Magnet

Synchronous Machines with Segmented Permanent Magnets." In: *2020 8th International Conference on Power Electronics Systems and Applications (PESA)*. Hong Kong, China, 7, Dec. 10, 2020, pp. 1–6. DOI: `10.1109/PESA50370.2020.9343986`.

[44] Christoph M. Hackl, Julian Kullick, Hisham Eldeeb, and Lorenz Horlbeck. "Analytical computation of the optimal reference currents for MTPC/MTPA, MTPV and MTPF operation of anisotropic synchronous machines considering stator resistance and mutual inductance." In: *2017 19th European Conference on Power Electronics and Applications (EPE'17 ECCE Europe)*. 2017, P.1–P.10. DOI: `10.23919/EPE17ECCEEurope.2017.8099040`.

[45] Khoa Dang Hoang and Hawa K. A. Aorith. "Online Control of IPMSM Drives for Traction Applications Considering Machine Parameter and Inverter Nonlinearities." In: *IEEE Transactions on Transportation Electrification* 1.4 (2015), pp. 312–325. DOI: `10.1109/TTE.2015.2477469`.

[46] Frank P. Incropera and David P. DeWitt. *Fundamentals of Heat and Mass Transfer*. 1996.

[47] Jose Jacob, Omar Bottesi, Sandro Calligaro, and Roberto Petrella. "Design Criteria for Flux-Weakening Control Bandwidth and Voltage Margin in IPMSM Drives Considering Transient Conditions." In: *IEEE Trans. on Ind. Appl.* 57.5 (2021), pp. 4884–4900. DOI: `10.1109/TIA.2021.3085535`.

[48] T.M. Jahns. "Flux-weakening regime operation of an interior permanent-magnet synchronous motor drive." In: *IEEE Trans. on Ind. Appl.* 23.July/Augus (1987), pp. 681–689.

[49] Thomas M. Jahns, Gerald B. Kliman, and Thomas W. Neumann. "Interior Permanent-Magnet Synchronous Motors for Adjustable-Speed Drives." In: *IEEE Trans. on Ind. Appl.* IA-22.4 (1986), pp. 738–747. DOI: `10.1109/TIA.1986.4504786`.

[50] Rupesh Kumar Jha, Giuseppe Buja, Manuele Bertoluzzo, Stefano Giacomuzzi, and Kishore Naik Mude. "Performance Comparison of the One-Element Resonant EV Wireless Battery Chargers." In: *IEEE Transactions on Industry Applications* 54.3 (2018), pp. 2471–2482. DOI: `10.1109/TIA.2018.2796058`.

[51] Kota Kawanishi, Keisuke Matsuo, Takayuki Mizuno, Koji Yamada, Takashi Okitsu, and Kouki Matsuse. "Development and Performance of High-Speed SPM Synchronous Machine." In: *2018 International Power Electronics Conference (IPEC-Niigata 2018 -ECCE Asia)*. 2018, pp. 169–176. DOI: `10.23919/IPEC.2018.8507781`.

[52] Laid Kefsi, Youssef Touzani, and Mohamed Gabsi. "Hybrid Excitation Synchronous Motor control with a new flux weakening strategy." In: *2010 IEEE Vehicle Power and Propulsion Conference*. Lille, France, Sept. 2010, pp. 1–5. DOI: `10.1109/VPPC.2010.5729181`.

[53] Anil Kumar. "Electric motor internal heat convection modelling and analysis - A Computational Fluid Dynamics Approach." In: (2018).

[54] Tae-Suk Kwon, Seung-Ki Sul, Luigi Alberti, and Nicola Bianchi. "Design and Control of an Axial-Flux Machine for a Wide Flux-Weakening Operation Region." In: *IEEE Trans. on Ind. Appl.* 45.4 (2009), pp. 1258–1266. DOI: `10.1109/TIA.2009.2023390`.

[55] Tae-Sung Kwon, Myoung-Ho Shin, and Dong-Seok Hyun. "Speed sensorless stator flux-oriented control of induction motor in the field weakening region using Luenberger observer." In: *IEEE Trans. on Power Electron.* 20.4 (2005), pp. 864–869. DOI: `10.1109/TPEL.2005.850939`.

[56] Ludmila Lavrinovicha and Janis Dirba. "Comparison of permanent magnet synchronous motor and synchronous reluctance motor based on their torque per unit volume." In: *2014 Electric Power Quality and Supply Reliability Conference (PQ)*. Rakvere, Estonia, June 2014, pp. 233–236. DOI: `10.1109/PQ.2014.6866817`.

[57] Yingjie Li, Dheeraj Bobba, and Bulent Sarlioglu. "Design and Optimization of a Novel Dual-Rotor Hybrid PM Machine for Traction Application." In: *IEEE Transactions on Industrial Electronics* 65.2 (2018), pp. 1762–1771. DOI: `10.1109/TIE.2017.2739686`.

[58] Jinglin Liu, Chao Gong, Zexiu Han, and Haozheng Yu. "IPMSM Model Predictive Control in Flux-Weakening Operation Using an Improved Algorithm." In: *IEEE Trans. on Ind. Electron.* 65.12 (2018), pp. 9378–9387. ISSN: 0278-0046. DOI: `10.1109/TIE.2018.2818640`.

[59] Jinhai Liu and Wei Chen. "Generalized DQ model of the permanent magnet synchronous motor based on extended park transformation." In: *2013 1st International Future Energy Electronics Conference (IFEEC)*. 2013, pp. 885–890. DOI: `10.1109/IFEEC.2013.6687627`.

[60] Xiangdong Liu, Hao Chen, Jing Zhao, and Anouar Belahcen. "Research on the Performances and Parameters of Interior PMSM Used for Electric Vehicles." In: *IEEE Transactions on Industrial Electronics* 63.6 (2016), pp. 3533–3545. DOI: `10.1109/TIE.2016.2524415`.

[61] *MAHLE Develops the Most Durable Electric Motor*. URL: `https://www.mahle-powertrain.com/en/news-and-press/press-releases/mahle-develops-the-most-durable-electric-motor-91264`.

[62] V. Manzolini and S. Bolognani. "On the Rotor Position Self-Sensing Capability of Reluctance and IPM Synchronous Motors." In: 56.4 (2020), pp. 3755–3766. DOI: `10.1109/TIA.2020.2984406`.

[63] Virginia Manzolini, Davide Da Rù, and Silverio Bolognani. "An Effective Flux Weakening Control of a SyRM Drive Including MTPV Operation." In: *IEEE Trans. on Ind. Appl.* 55.3 (2019), pp. 2700–2709. DOI: `10.1109/TIA.2018.2886328`.

[64] Sébastien Mariethoz, Alexander Domahidi, and Manfred Morari. "High-Bandwidth Explicit Model Predictive Control of Electrical Drives." In: *IEEE Trans. on Ind. Appl.* 48.6 (2012), pp. 1980–1992. DOI: `10.1109/TIA.2012.2226198`.

[65] Rita Mbayed, Georges Salloum, Lionel Vido, Eric Monmasson, and Mohamed Gabsi. "Hybrid excitation synchronous generator in embedded applications: Modeling and control." In: *Mathematics and Computers in Simulation* 90 (2013). ELECTRIMACS 2011- PART I, pp. 60–73. ISSN: 0378-4754. DOI: `https://doi.org/10.1016/j.matcom.2012.07.018`.

[66] PH Mellor, D Roberts, and DR Turner. "Lumped parameter thermal model for electrical machines of TEFC design." In: *IEE Proceedings B (Electric Power Applications)*. Vol. 138. 5. IET. 1991, pp. 205–218.

[67] Daniele Michieletto, Luca Cinti, and Nicola Bianchi. "Hybrid Excitation PM Synchronous Motors: Part I Per Unit Analysis." In: *IEEE Transactions on Energy Conversion* 37.1 (2021), pp. 1–8. DOI: `10.1109/TEC.2021.3107937`.

[68] Carlos Miguel-Espinar, Daniel Heredero-Peris, Gabriel Gross, Marc Llonch-Masachs, and Daniel Montesinos-Miracle. "Maximum Torque per Voltage Flux-Weakening Strategy With Speed Limiter for PMSM Drives." In: *IEEE Transactions on Industrial Electronics* 68.10 (2021), pp. 9254–9264. DOI: `10.1109/TIE.2020.3020029`.

[69] S. Morimoto, Y. Takeda, T. Hirasa, and K. Taniguchi. "Expansion of operating limits for permanent magnet motor by current vector control considering inverter capability." In: *IEEE Trans. on Ind. Appl.* 26.Sept./Oct. (1990), pp. 866–871. DOI: `10.1109/28.60058`.

[70] Shigeo Morimoto, Shohei Ooi, Yukinori Inoue, and Masayuki Sanada. "Experimental Evaluation of a Rare-Earth-Free PMASynRM With Ferrite Magnets for Automotive Applications." In: *IEEE Transactions on Industrial Electronics* 61.10 (2014), pp. 5749–5756. DOI: `10.1109/TIE.2013.2289856`.

[71] Zbynek Mynar, Libor Vesely, and Pavel Vaclavek. "PMSM Model Predictive Control With Field-Weakening Implementation." In: *IEEE Transactions on Industrial Electronics* 63.8 (2016), pp. 5156–5166. DOI: `10.1109/TIE.2016.2558165`.

[72] N.Bianchi and S.Bolognani. "Parameters and volt-ampere ratings of a synchronous motor drive for flux-weakening applications." In: *IEEE Trans. on Power Electronics* 12.5 (895-903), pp. 895–903. DOI: `10.1109/63.623008`.

[73] N.Bianchi, S.Bolognani, F.Parasiliti, and M.Villani. "Prediction of overload and flux-weakening performance of an IPM motor drive: analytical and finite element approach." In: *Proc. of Electrical Drives Design and Applications* 1.EPE'99, Lausanne, (1999).

[74] Radoslaw Nalepa and Teresa Orlowska-Kowalska. "Optimum Trajectory Control of the Current Vector of a Nonsalient-Pole PMSM in the Field-Weakening Region." In: *IEEE Transactions on Industrial Electronics* 59.7 (2012), pp. 2867–2876. DOI: `10.1109/TIE.2011.2116755`.

[75] Ludovico Ortombina, Petros Karamanakos, and Mauro Zigliotto. "Robustness Analysis of Long-Horizon Direct Model Predictive Control: Permanent Magnet Synchronous Motor Drives." In: *2020 IEEE 21st Work. on Control and Model. for Power Electron. (COMPEL)*. 2020, pp. 1–8. DOI: `10.1109/COMPEL49091.2020.9265855`.

[76] Ludovico Ortombina, Dario Pasqualotto, Fabio Tinazzi, and Mauro Zigliotto. "Comprehensive Analysis and Design of a Pulsating Signal Injection-Based Position Observer for Sensorless Synchronous Motor Drives." In: *IEEE J. of Emerg. and Sel. Topics in Power Electron.* 10.2 (2022), pp. 1925–1934. DOI: `10.1109/JESTPE.2021.3053467`.

[77] Tinazzi Ortombina, L Ortombina, F Tinazzi, and M Zigliotto. "newblock An effective start-up algorithm for sensorless synchronous reluctance and IPM motor drives." In: *newblock In Proceedings of the 2017 IEEE 12th International Conference on Power Electronics and Drive Systems (PEDS)*. Honolulu, HI, USA, Dec. 2017, pp. 1062–1067. DOI: `10.1109/PEDS.2017.8289167`.

[78] Gianmario Pellegrino, Eric Armando, and Paolo Guglielmi. "Direct Flux Field-Oriented Control of IPM Drives With Variable DC Link in the Field-Weakening Region." In: *IEEE Trans.*

on Ind. Appl. 45.5 (2009), pp. 1619–1627. DOI: `10.1109/TIA.2009.2027167`.

[79] Gianmario Pellegrino, Alfredo Vagati, Barbara Boazzo, and Paolo Guglielmi. "Comparison of Induction and PM Synchronous Motor Drives for EV Application Including Design Examples." In: *IEEE Trans. on Ind. Appl.* 48.6 (2012), pp. 2322–2332. DOI: `10.1109/TIA.2012.2227092`.

[80] Gianmario Pellegrino, Alfredo Vagati, Paolo Guglielmi, and Barbara Boazzo. "Performance Comparison Between Surface-Mounted and Interior PM Motor Drives for Electric Vehicle Application." In: *IEEE Transactions on Industrial Electronics* 59.2 (2012), pp. 803–811. DOI: `10.1109/TIE.2011.2151825`.

[81] N. Pothi. "Improvement of flux-weakening control of surface mounted permanent magnet synchronous machine considering inverter nonlinearity." In: *2017 International Electrical Engineering Congress (iEECON)*. 2017, pp. 1–4. DOI: `10.1109/IEECON.2017.8075736`.

[82] Maria Raluca Raia, Mircea Ruba, Razvan Alexandru Inte, Claudia Martis, Gabriel Mihai Sirbu, and Calin Husar. "Modelling and Virtual Testing of a Wound Rotor Synchronous Machine for Electrical Vehicles Propulsion System." In: *2021 International Aegean Conference on Electrical Machines and Power Electronics (ACEMP) 2021 International Conference on Optimization of Electrical and Electronic Equipment (OPTIM)*. 2021, pp. 129–134. DOI: `10.1109/OPTIM-ACEMP50812.2021.9590075`.

[83] *Renault Redesigns EV Electric Motor*. URL: `https://www.just-auto.com/news/renault-redesigns-ev-electric-motor/`.

[84] Claudio Rossi, Domenico Casadei, Alessio Pilati, and Matteo Marano. "Wound Rotor Salient Pole Synchronous Machine Drive for Electric Traction." In: *Conference Record of the 2006 IEEE Industry Applications Conference Forty-First IAS Annual Meeting*. Vol. 3. 2006, pp. 1235–1241. DOI: `10.1109/IAS.2006.256689`.

[85] R.F. Schiferl and T.A. Lipo. "Power capability of salient pole permanent magnet synchronous motors in variable speed drive applications." In: *IEEE Trans. on Ind. Appl.* 26.1 (1990), pp. 115–123. DOI: `10.1109/28.52682`.

[86] Tomy Sebastiangordon and Gordon R. Slemon. "Operating Limits of Inverter-Driven Permanent Magnet Motor Drives." In: *IEEE Trans. on Ind. Appl.* IA-23.2 (1987), pp. 327–333. DOI: `10.1109/TIA.1987.4504909`.

[87] Léopold Sepulchre, Maurice Fadel, Maria Pietrzak-David, and Guillaume Porte. “MTPV Flux-Weakening Strategy for PMSM High Speed Drive.” In: *IEEE Transactions on Industry Applications* 54.6 (2018), pp. 6081–6089. DOI: `10.1109/TIA.2018.2856841`.

[88] B. Sneyers, D.W. Novotny, and T.A. Lipo. “Field weakening in buried permanent magnet AC motor drives.” In: *IEEE Trans. on Ind. Appl.* 21.2 (1985), pp. 398–407. DOI: `10.1109/TIA.1985.349661`.

[89] Miller ; soong1993-The Soong, W Soong, and T Miller. “newblock Theoretical limitations to the field-weakening performance of the five classes of brushless synchronous AC motor drive.” In: *Proceedings of the 1993 Sixth International Conference on Electrical Machines and Drives*. Oxford, UK, 8, Sept. 10, 1993, pp. 127–132.

[90] W.L. Soong and T.J.E. Miller. “Practical field-weakening performance of the five classes of brushless synchronous AC motor drive.” In: *1993 Fifth Europ. Conf. on Power Electron. and Appl.* Vol. 5. 1993, pp. 303–310.

[91] David A. Staton and Andrea Cavagnino. “Convection Heat Transfer and Flow Calculations Suitable for Electric Machines Thermal Models.” In: *IEEE Transactions on Industrial Electronics* 55.10 (2008), pp. 3509–3516. DOI: `10.1109/TIE.2008.922604`.

[92] Wesam Taha and Ali Emadi. “Online Non-Parametric Auto-Tuning of Flux Weakening Controller for IPMSM Drives using Modified Relay Feedback Test.” In: *2021 IEEE Transportation Electrification Conference Expo (ITEC)*. 2021, pp. 309–314. DOI: `10.1109/ITEC51675.2021.9490113`.

[93] M. Takei, Y. Minoya, N. Kumagai, and K. Sakurai. “Analysis of IPM current oscillation under short circuit condition.” In: *Proceedings of the 10th International Symposium on Power Semiconductor Devices and ICs. ISPSD’98 (IEEE Cat. No.98CH36212)*. 1998, pp. 89–93. DOI: `10.1109/ISPSD.1998.702642`.

[94] *The Engineering ToolBox*. URL: `https://www.engineeringtoolbox.com/`.

[95] Francesco Toso, Paolo Gherardo Carlet, Matthias Preindl, and Silverio Bolognani. “Active-Flux-Based Motion-Sensorless Control of PMSM Using Moving Horizon Estimator.” In: *2018 IEEE 9th Int. Symp. on Sensorl. Control for Electr. Drives (SLED)*. 2018, pp. 78–83. DOI: `10.1109/SLED.2018.8486107`.

[96] Elena Trancho, Edorta Ibarra, Antoni Arias, Iñigo Kortabarria, Jonathan Jurgens, Luca Marengo, Antonio Fricassè, and Johannes V. Gragger. “PM-Assisted Synchronous Reluctance

Machine Flux Weakening Control for EV and HEV Applications." In: *IEEE Transactions on Industrial Electronics* 65.4 (2018), pp. 2986–2995. doi: `10.1109/TIE.2017.2748047`.

[97] Marco Tursini, Enzo Chiricozzi, and Roberto Petrella. "Feedforward Flux-Weakening Control of Surface-Mounted Permanent-Magnet Synchronous Motors Accounting for Resistive Voltage Drop." In: *IEEE Trans. on Ind. Electron.* 57.1 (2010), pp. 440–448. doi: `10.1109/TIE.2009.2034281`.

[98] A. Vagati, G. Pellegrino, and P. Guglielmi. "Comparison between SPM and IPM motor drives for EV application." In: *2010 International Conference on Electrical Machines (ICEM)*. 2010, pp. 1–6.

[99] Jing Wang, Jianhua Wu, Chun Gan, and Qingguo Sun. "Comparative study of flux-weakening control methods for PMSM drive over wide speed range." In: *2016 19th International Conference on Electrical Machines and Systems (ICEMS)*. 2016, pp. 1–6.

[100] Q. Wang and S. Niu. "A Novel Hybrid-Excited Dual-PM Machine With Bidirectional Flux Modulation." In: *IEEE Transactions on Energy Conversion* 32.2 (2017), pp. 424–435. doi: `10.1109/TEC.2017.2649574`.

[101] Shuo Wang, Michele Degano, Jinsong Kang, Alessandro Galassini, and Chris Gerada. "A Novel Newton-Raphson-Based Searching Method for the MTPA Control of PMASYNRM Considering Magnetic and Cross Saturation." In: *2018 Int. Conf. on Elect. Mach. (ICEM)*. Sept. 2018, pp. 1360–1366. doi: `10.1109/ICELMACH.2018.8506853`.

[102] Shuo Wang, Jinsong Kang, Michele Degano, Alessandro Galassini, and Chris Gerada. "An Accurate Wide-Speed Range Control Method of IPMSM Considering Resistive Voltage Drop and Magnetic Saturation." In: *IEEE Trans. on Ind. Electron.* 67.4 (2020), pp. 2630–2641. doi: `10.1109/TIE.2019.2912766`.

[103] Yueqi Wang, Ying Fan, Junlei Chen, and Ke Yu. "Sensorless Control of Synchronous Reluctance Motors for Low-Speed Operation Considering Cross-Saturation Effect." In: *2021 24th Int. Conf. on Elect. Mach. and Systems (ICEMS)*. 2021, pp. 1968–1972. doi: `10.23919/ICEMS52562.2021.9634584`.

[104] Frank M White. *Fluid mechanics*. The McGraw Hill Companies, 2008.

[105] Nalakath Xia, Tarvirdilu-Asl, Sun, Wiseman, Z Emadi]emadi2020onlineoptimaltrac Xia, ; Tarvirdilu-Asl, R Sun, Y Wiseman, and J. "Emadi, A. newblock Online Optimal Tracking Method for Interior Permanent Magnet Machines With Improved MTPA and MTPV in Whole Speed and Torque Ranges. newblock em IEEE Trans,

booktitle = Power Electron. bf 2020, em 35." In: 2020, pp. 9753–9769. DOI: `10.1109/TPEL.2020.2970111detokenize{10.1109/TPEL.2020.2970111}`.

[106] Longya Xu, Lurong Ye, Li Zhen, and A. El-Antably. "A new design concept of permanent magnet machine for flux weakening operation." In: *IEEE Trans. on Ind. Appl.* 31.2 (1995), pp. 373–378. DOI: `10.1109/28.370287`.

[107] Wei Xu, Moustafa Magdi Ismail, Yi Liu, and Md Rabiul Islam. "Parameter Optimization of Adaptive Flux-Weakening Strategy for Permanent-Magnet Synchronous Motor Drives Based on Particle Swarm Algorithm." In: *IEEE Trans. on Power Electron.* 34.12 (2019), pp. 12128–12140. DOI: `10.1109/TPEL.2019.2908380`.

[108] K. Yamazaki and Y. Seto. "Iron loss analysis of interior permanent-magnet synchronous motors-variation of main loss factors due to driving condition." In: *IEEE Transactions on Industry Applications* 42.4 (2006), pp. 1045–1052. DOI: `10.1109/TIA.2006.876080`.

[109] Jiwon Yoo, Joohyun Lee, and Seung-Ki Sul. "Analysis of Instability in Torque Control of Sensorless PMSM Drives in Flux Weakening Region." In: *IEEE Trans. on Power Electron.* 36.9 (2021), pp. 10815–10826. DOI: `10.1109/TPEL.2021.3063720`.

[110] *ZF Develops One of the World's Most Compact Magnet-Free Motors.* URL: `https://newatlas.com/automotive/zf-most-compact-magnet-free-motor/`.

[111] Zisui Zhang, Babak Nahid-Mobarakeh, and Ali Emadi. "Adaptive Voltage Controller for Flux-weakening Operation in PMSM Drives." In: *IECON 2021 – 47th Annual Conference of the IEEE Industrial Electronics Society*. 2021, pp. 1–6. DOI: `10.1109/IECON48115.2021.9589782`.

[112] Z. Q. Zhu, W. Q. Chu, and Y. Guan. "Quantitative comparison of electromagnetic performance of electrical machines for HEVs/EVs." In: *CES Transactions on Electrical Machines and Systems* 1.1 (2017), pp. 37–47. DOI: `10.23919/TEMS.2017.7911107`.

[113] Z.Q. Zhu, Y.S. Chen, and D. Howe. "Online optimal flux-weakening control of permanent-magnet brushless AC drives." In: *IEEE Trans. on Ind. Appl.* 36.6 (2000), pp. 1661–1668. DOI: `10.1109/28.887219`.

ACKNOWLEDGMENTS

And now, it's time to express my gratitude.

I would like to thank my supervisor Nicola Bianchi for guiding me along these PhD studies. His ideas have inspired me in my research. He has always shown confidence teaching me a lot as a person inside and outside the academic field. I could not have asked for a better supervisor.

I am also grateful to Prof. Petros Karamanakos for his guidance during my visit to the TUNI. The discussions with him provided me with valuable technical advice and new ideas.

I'm also thankful to Mosè Castiello, EDLab technician. He was always available to set-up the test benches, to solve theory, software and hardware problems. You was a main part of the EDLab family.

I would like to thank my colleagues and friends Paolo, Chiara, Ludovico and Riccardo. They helped me to achieve many results reported in this dissertation. I hope I have left you with some interesting and stimulating insights for your own research. But above all, more about the human being.

Thanks to Mattia, Riccardo and Simone, master students who, with their questions, smile and mistake, taught me to see things from different points of view.

I thank you the sharks Giuseppe, Elia, Daniele and Matteo for being with me during these three crazy years.

I think that many people should be mentioned, forgive me if can not mention you all. In any case, I must thank you all for the priceless time and emotions we shared, such as my friends Andrea, Francesco, Diego, Lefteris, Mattia, Manuel, Brando, Michael, Leonardo, Charlie and Spillo, my aunt Teresa, my mother Paola and my father Alberto.

Finally, I would like to thank one person who is the most important to me. Without her I would not be who I am now. No words would be enough to express my gratitude, a special thank you is for you, Alessia.

COLOPHON

This document was typeset using the typographical look-and-feel `classicthesis` developed by André Miede. The style was inspired by Robert Bringhurst's seminal book on typography *"The Elements of Typographic Style"*. `classicthesis` is available for both LaTeX and LyX:

`https://bitbucket.org/amiede/classicthesis/`

Happy users of `classicthesis` usually send a real postcard to the author, a collection of postcards received so far is featured here:

`http://postcards.miede.de/`

Final Version as of November 29, 2023 (`classicthesis` version 2.0).